



HAL
open science

Study of growth mechanism of conducting polymers by pulse radiolysis

Cecilia Coletta

► **To cite this version:**

Cecilia Coletta. Study of growth mechanism of conducting polymers by pulse radiolysis. Theoretical and/or physical chemistry. Université Paris-Saclay, 2016. English. NNT : 2016SACLS288 . tel-01552290v1

HAL Id: tel-01552290

<https://theses.hal.science/tel-01552290v1>

Submitted on 2 Jul 2017 (v1), last revised 7 Jul 2017 (v2)

HAL is a multi-disciplinary open access archive for the deposit and dissemination of scientific research documents, whether they are published or not. The documents may come from teaching and research institutions in France or abroad, or from public or private research centers.

L'archive ouverte pluridisciplinaire **HAL**, est destinée au dépôt et à la diffusion de documents scientifiques de niveau recherche, publiés ou non, émanant des établissements d'enseignement et de recherche français ou étrangers, des laboratoires publics ou privés.

NNT : 2016SACLS288

THESE DE DOCTORAT
DE
L'UNIVERSITE PARIS-SACLAY
PREPAREE A
L'UNIVERSITE PARIS SUD

ECOLE DOCTORALE N° 571
Sciences chimiques : molécules, matériaux, instrumentation et biosystèmes
Spécialité de doctorat Chimie

Par

Cecilia Coletta

Study of growth mechanism of conducting polymers by pulse radiolysis

Thèse présentée et soutenue à Orsay, le 6 Octobre 2016 :

Composition du Jury :

M. P. Audebert	Professeur	ENS Cachan	Président
M. J.-M. Jung	Professeur	Université de Strasbourg	Rapporteur
M. J. Roncali	Directeur de Recherche	Université d'Angers, CNRS	Rapporteur
M. A. Vieira	Professeur	Universidade Nova de Lisboa	Examineur
M. S. Remita	Professeur	CNAM, Université Paris-Sud	Directeur de thèse
M. J.-L. Marignier	Chercheur	Université Paris-Sud, CNRS	Co-directeur de thèse
M. P. Archirel	Chercheur	Université Paris-Sud, CNRS	Invité

NNT : 2016SACLS288

THESE DE DOCTORAT
DE
L'UNIVERSITE PARIS-SACLAY
PREPAREE A
L'UNIVERSITE PARIS SUD

ECOLE DOCTORALE N° 571
Sciences chimiques : molécules, matériaux, instrumentation et biosystèmes
Spécialité de doctorat Chimie

Par

Cecilia Coletta

Study of growth mechanism of conducting polymers by pulse radiolysis

Thèse présentée et soutenue à Orsay, le 6 Octobre 2016 :

Composition du Jury :

M. P. Audebert	Professeur	ENS Cachan	Président
M. J.-M. Jung	Professeur	Université de Strasbourg	Rapporteur
M. J. Roncali	Directeur de Recherche	Université d'Angers, CNRS	Rapporteur
M. A. Vieira	Professeur	Universidade Nova de Lisboa	Examineur
M. S. Remita	Professeur	CNAM, Université Paris-Sud	Directeur de thèse
M. J.-L. Marignier	Chercheur	Université Paris-Sud, CNRS	Co-directeur de thèse
M. P. Archirel	Chercheur	Université Paris-Sud, CNRS	Invité

Alle mie nonne

Remerciements

Bien que la thèse reste l'œuvre d'un unique auteur, ce travail n'aurait jamais pu être réalisé sans le soutien d'un grand nombre de personnes qui en ont pris parti directement ou indirectement.

En premier lieu, je tiens à remercier mes deux directeurs de thèse : Samy Remita et Jean-Louis Marignier.

Je suis reconnaissante à Samy Remita pour m'avoir proposé cette thèse sur un sujet si intéressant et d'avoir trouvé le temps de suivre mon travail, et ce malgré ses nombreux engagements. Je le remercie pour sa grande disponibilité.

Je tiens à remercier Jean-Louis Marignier pour tous ses enseignements, ses multiples conseils et pour toutes les heures qu'il a consacré à mon travail. Je lui suis reconnaissante de m'avoir fait bénéficier, tout au long de ce travail, de sa grande compétence, de sa rigueur intellectuelle, de son dynamisme, et de son efficacité certaine que je n'oublierai jamais.

Mes plus sincères remerciements vont également à M. Jean Roncali, directeur de recherche au Laboratoire d'Ingénierie moléculaire d'Anger et M. Jean-Marc Jung, Professeur à l'Université de Strasbourg qui m'ont fait l'honneur d'être rapporteurs de cette thèse. J'associe à ces remerciements M. Abel Vieira, Professeur à l'Universidade Nova de Lisboa, et M. Pierre Audebert, Professeur à l'ENS Cachan pour avoir accepté d'examiner mon travail avec un si grand intérêt.

J'adresse de sincères remerciements aux directeurs, passés et présents, du laboratoire M. Mehran Mostafavi et M. Philippe Maitre pour m'avoir accueilli au sein du Laboratoire Chimie Physique.

Je tiens à remercier M. Pierre Archirel pour avoir accepté d'être dans mon jury de thèse, pour son aide précieuse à la réalisation de ce travail et pour le temps qu'il m'a dédié à m'initier à la chimie théorique.

Je tiens à remercier également M. Pascal Pernot notamment pour son aide à

l'interprétation des données, pour sa sympathie et sa disponibilité.

J'exprime également ma gratitude aussi à Hynd Remita, animatrice du groupe TEMiC, pour son enthousiasme qu'elle a su me transmettre lors de nos conversations scientifiques ou non.

Je tiens à exprimer ma reconnaissance à Alexandre Dazzi et Ariane Deniset pour leur contribution aux manips de microscopie, pour leur sympathie et leur disponibilité.

Merci également à tous les collaborateurs extérieurs au LCP qui ont participé à mes recherches. Je pense notamment à M. Goubard, M. Aubert, M. Guigner et M. Lefrançois.

Ce travail doit une contribution importante à tous les membres de l'équipe de ELYSE, sans laquelle l'essentiel de mes recherches, aux travers des manips, n'aurait pas existé. Je tiens particulièrement à remercier Jean Philippe Larbre, Nicolas Decovemaker, Alexandre Demarque et Audrey Gayral.

À l'heure du déjeuner au laboratoire, j'ai pu profiter de l'exceptionnelle compagnie de Fabien Cailliez, Pascal Pernot, Jacqueline Ridard, Bernard Lévy, Jérémy Verdier, Isabelle Demachy et Aurélien de la Lande, merci pour ces bons moments que nous avons passé ensemble, pour le chocolat et pour le soutien de ces derniers jours.

Je voudrais profiter de l'occasion de ces quelques lignes pour remercier Mireille Benoit pour le sourire avec lequel tu m'as accueilli chaque jour dans ton bureau. Je n'oublierai pas ton soutien, ton aide au laboratoire et toutes tes solutions à mes problèmes, les rires ensemble, les cafés et la zumba.

Je remercie aussi Anne Morel et Séverine Bourguignon qui ont toujours su m'aider à résoudre mes difficultés bureaucratiques. Ainsi que Joel François et Merciano Deazevedo pour leur aide et leur gentillesse lors de l'organisation des journées des doctorants, et l'organisation de ma thèse.

Je voudrais enfin exprimer ma gratitude à l'ensemble des doctorants et post-doc du LCP pour avoir été de très bons compagnons de voyage dans cette aventure.

Je pense en particulier à Aurélie avec qui, depuis mon stage en 2012, j'ai partagé de très bons moments. De bonne collègue tu es devenue une vraie amie. Merci à Jérémy avec qui j'ai partagé les repas et l'inscription !!!! Sans toi cette dernière année aurait été difficile, merci pour ton soutien moral de tous les jours.

Merci à Iyad qui n'a jamais cessé de me faire rire et sourire, dans les bons et les mauvais moments. Et merci à mon collègue Zhengpeng, toujours disponible et prêt à m'aider en toute occasion dès les premiers jours. Et aussi merci Claire, Xiaoching, Aurelie la rose, Charyle, Rolando, Germain, Guadeloupe, Alexandre, Marie, Tiago et Luis.

Et entre les amis, je ne peux pas oublier les encouragements précieux de Josiane, Sophie et Lise. Merci pour votre constante attention et préoccupation.

Je souhaite également remercier Claudine et Gilles pour m'avoir accueilli dans leur famille, pour être toujours prêts à m'aider et pour m'avoir toujours soutenu tout au long de ces trois années.

Enfin, je voudrais remercier Carmen et Mario d'être ici aujourd'hui et toute la famille de Strasbourg pour m'avoir accueilli depuis mon premier jour en France, grâce à vous je me suis senti à la maison.

Ed eccomi a scrivere di voi, i miei amici di sempre: Flavia, Giulio, Ernesto e Andrea. Ogni volta che raggiungo un traguardo, voi siete li. Siete il mio punto di riferimento, gli amici fidati. Un grazie particolare va a Flavia, l'amica di sempre. Sai quanto il tuo sostegno sia essenziale per me. E ti sono infinitamente grata per esserci sempre.

Queste righe sono per voi Mamma, Papà, Claudia e Gianni, le persone che ho più care e che oggi sono venute qui ad ascoltarmi parlare in un'altra lingua pur di non perdersi l'evento. Vi ringrazio sinceramente, perché nessuno quanto voi può capire quanto mi sia costato tutto questo. Il vostro amore e il vostro continuo sostegno, sono le fondamenta di ogni mio traguardo.

Non posso concludere questi ringraziamenti senza dichiarare ma gratitude à toi Camille. Grazie per il cuore della mattina, il sorriso con cui mi accogli ogni giorno da cinque anni, la gentillesse avec laquelle tu me parles même quand tu n'es pas d'accord. Je n'aurais jamais pu arriver au bout de ce travail sans tes encouragements, sans ton soutien quotidien. Merci d'avoir trouvé le bon, là où je n'y voyais que du noir.

Acronyms

AFM	Atomic Force Microscopy
AFM-IR	Atomic Force Microscopy InfraRed
ATR-FTIR	Attenuated total Reflectance-Fourier Transform InfraRed spectroscopy
Cryo-TEM	Cryo-transmission-electron microscopy
DFT	Density functional theory
EDOT	3,4-Ethylenedioxythiophene
MC	Monte Carlo
MCR-ALS	Multivariate Curve Resolution Alternating Least Squares
PEDOT	poly-3,4-Ethylenedioxythiophene
Py	Pyrrole
PPy	poly-Pyrrole
SEM	Scanning electron microscopy
SVD	Singular Value Decomposition
TDDFT	Time-dependent density functional theory

Contents

Résumé	1
Introduction	5
Bibliography	17
1 Materials and Methods	23
1.1 Materials	24
1.1.1 Monomers	24
1.1.2 Oxidants	27
1.2 Methods	28
1.2.1 Water radiolysis principle	28
1.2.2 Oxidative environment	31
1.2.3 Reducing environment	34
1.2.4 Pulse radiolysis	36
1.3 Theoretical Methods of analysis	44
1.3.1 COPASI	45
1.3.2 MonteCarlo-TDDFT	45
1.3.3 SVD	45
1.4 Experimental Methods of investigation	46
1.4.1 UV-Vis	46
1.4.2 Cryo-TEM	47
1.4.3 ATR-FTIR	47
1.4.4 SEM	48
1.4.5 AFM and AFM-IR	48
1.4.6 Conductivity test	49
Bibliography	51

2	HO[•]-induced EDOT polymerization	57
2.1	EDOT oxidation	59
2.1.1	Hydroxyl radical reactivity	59
2.1.2	pH effect	75
2.2	EDOT Reduction	78
2.3	PEDOT synthesis	83
2.4	Conclusion	86
	Bibliography	89
3	Alternative radicals as oxidizing species	93
3.1	Carbonate Radicals	93
3.2	Azide radicals	98
3.3	Sulfate Radicals	100
3.3.1	Thermal reactivity of S ₂ O ₈ ²⁻ and SO ₄ ^{•-}	100
3.3.2	Reactivity of SO ₄ ^{•-} formed by radiolysis	102
3.3.3	Spectrokinetic investigation	110
3.3.4	Absorption spectra simulation	113
3.3.5	Species identification	116
3.3.6	PEDOT-SO ₄ synthesis	119
3.4	Conclusion	126
	Bibliography	129
4	Pyrrole oxidation and polypyrrole synthesis	133
4.1	Introduction	133
4.2	HO [•] -induced Py oxidation	136
4.2.1	Nanosecond time scale investigation	136
4.2.2	Microsecond time scale investigation	142
4.3	Simulation	143
4.4	Theoretical study	148
4.5	pH effect	151
4.5.1	Acidic solution	151
4.5.2	Alkaline solution	159
4.6	Carbonate	168
4.7	Polypyrrole synthesis	174

<i>CONTENTS</i>	iii
4.8 Conclusion	178
Bibliography	179
5 Conclusion and Perspective	183
A Computational study	187
B Simulation COPASI	195
Bibliography	195

Résumé

Étude du mécanisme de croissance de polymères conducteurs par radiolyse impulsionnelle

Les polymères conducteurs (PC) sont des matériaux organiques semi-conducteurs très utilisés dans diverses applications technologiques. Les propriétés optiques et conductrices de ces matériaux organiques conjugués résultent de la délocalisation électronique le long des chaînes polymères et dépendent, de ce fait, de la longueur de conjugaison. Les différentes méthodologies de synthèse des PC ont pour finalité la fabrication de nouvelles structures polymères, de stabilité contrôlée, et aux propriétés optiques et conductrices ajustables. Néanmoins, les PC qui sont actuellement fabriqués présentent encore un certain nombre de défauts, du fait d'un manque de compréhension et de contrôle du processus de polymérisation.

Parmi tous les polymères conducteurs, le poly (3, 4-éthylènedioxythiophène) (PEDOT, un dérivé de polythiophène) et le polypyrrole (PPy) ont été utilisés dans plusieurs applications pour leurs propriétés physico-chimiques particulièrement intéressantes. Les PC, comme le PEDOT et le PPy, sont habituellement synthétisés par voie chimique ou électrochimique, la polymérisation étant alors systématiquement initiée par une étape d'oxydation des monomères. Cependant, les propriétés complexes des polymères ne peuvent être optimisées que si une bonne connaissance du mécanisme de polymérisation est acquise. La bonne compréhension de ce mécanisme permettrait en effet de contrôler la synthèse des PC (fonctionnalisation adéquate, caractère plus ou moins hydrophile, contrôle de la longueur de chaîne et du niveau de dopage) afin d'en améliorer les propriétés optiques et conductrices.

La radiolyse, méthodologie basée sur l'interaction rayonnement-matière, est

connue pour être une méthode simple et efficace de synthèse de nanomatériaux dans des conditions douces de température et de pression. Au sein de notre laboratoire, la radiolyse à récemment été utilisée avec succès, comme méthodologie alternative, pour la synthèse de PC nanostructurés en solution aqueuse. Le présent travail est plus spécifiquement consacré à la synthèse de PEDOT et de PPy en solution aqueuse et à l'étude de leur mécanisme de croissance par radiolyse impulsionnelle. Grâce à l'accélérateur d'électrons ELYSE, l'utilisation de la radiolyse pulsée, couplée à la spectroscopie d'absorption résolue dans le temps, a permis d'étudier la cinétique de croissance des PC à l'échelle de la nanoseconde jusqu'à la milliseconde et d'en identifier les premières étapes réactionnelles.

Tout d'abord, l'action du radical hydroxyle sur les monomères EDOT a été étudiée. Une analyse spectro-cinétique a permis d'identifier le nombre d'espèces transitoires dont les spectres d'absorption ont été identifiés à l'aide de calculs de chimie quantique. Les résultats obtenus nous ont permis de déterminer les constantes de vitesse des premières étapes et les spectres d'absorption des premiers intermédiaires réactionnels. De plus, la réduction du monomère EDOT a été étudiée en utilisant les électrons hydratés produits lors de la radiolyse de l'eau. Cette étude a permis d'identifier le spectre d'absorption du radical anion de l'EDOT et sa constante de vitesse de formation. L'étude par radiolyse impulsionnelle a mis en évidence que la croissance des PC résultait d'un mécanisme par stades, et non d'un mécanisme en chaîne : la synthèse du PEDOT ne peut résulter que d'oxydations successives des monomères, puis des dimères et enfin des oligomères. De manière originale, le faisceau d'électrons a été utilisé comme source d'irradiation (accumulation de pulses) afin de synthétiser in situ les polymères de PEDOT dont les caractéristiques spectrales, morphologiques et conductrices ont été étudiées selon différentes techniques de caractérisation.

La deuxième partie de la thèse concerne l'oxydation de l'EDOT par d'autres types de radicaux oxydants tels que $\text{CO}_3^{\cdot-}$, N_3^{\cdot} et $\text{SO}_4^{\cdot-}$ à différents pH. Cette approche a permis de mettre en évidence l'influence des espèces oxydantes sur les premières étapes du mécanisme réactionnel et sur la nature des espèces transitoires issues de l'oxydation des monomères (radical cation, produit d'addition ou radical neutre). Il a été possible de montrer que les radicaux $\text{CO}_3^{\cdot-}$ et N_3^{\cdot} sont de mauvais candidats à l'oxydation du monomère. Au contraire, le radical $\text{SO}_4^{\cdot-}$ peut oxyder l'EDOT. L'étude cinétique couplée à une analyse spectro-cinétique

et à des calculs de chimie théorique ont permis de décrire les premières étapes de polymérisation et d'identifier les espèces transitoires produites. Comme dans le cas de l'oxydation par le radical hydroxyle, il a été montré que la croissance du PEDOT résulte d'un mécanisme par stades. L'irradiation aux électrons a été enfin utilisée pour synthétiser in situ le polymère PEDOT en présence de $\text{SO}_4^{\cdot-}$. Les propriétés spectrales et morphologiques des polymères obtenus ont été également étudiées.

La dernière partie de la thèse concerne l'étude du mécanisme de croissance du Pyrrole. Comme dans le cas de l'EDOT, les premières espèces transitoires produites lors de l'irradiation ont été identifiées. En faisant varier la dose et la concentration en monomères dans la solution, il a été possible de déterminer le coefficient d'extinction molaire et la constante de vitesse de formation de la première espèce transitoire. L'identification des espèces a été possible grâce à des calculs de chimie quantique. L'influence de la nature des espèces oxydantes sur les premières étapes réactionnelles a été étudiée en utilisant le radical carbonate $\text{CO}_3^{\cdot-}$. De manière complémentaire, il a été démontré que la valeur du pH avait une influence déterminante sur la nature même des espèces transitoires formées. Enfin, l'utilisation du faisceau d'électrons comme source d'irradiation (accumulation de pulses) a permis de synthétiser du PPy, dont les caractéristiques spectrales et morphologiques ont été déterminées.

En résumé, les résultats marquants obtenus dans cette thèse concernent la mise en évidence d'un mécanisme de croissance par stades des polymères conducteurs. La plus belle démonstration en est l'utilisation originale de pulses d'électrons successifs issus de l'accélérateur d'électrons ELYSE pour la synthèse de PEDOT et de PPy.

Introduction

In 2000 Hideki Shirakawa, Alan MacDiarmid, and Alan Heeger received the Nobel prize to "have changed this view (plastic as insulator) with their discovery that a polymer, polyacetylene, can be made conductive almost like a metal" [1]. They showed that it is possible to increase the conductivity of polymers of several order of magnitude (from 10^{-5} to 10^3 S·cm⁻¹). Although the scientific community recognizes them the discovery of conducting polymers, the first studies date back to 19th century when Fritzsche described the synthesis of polyaniline [2, 3].

In 1862, Letheby synthesized polyaniline by anodic oxidation in sulfuric acid and described as existing in four different states, each of which was an octamer [4]. Around 1950 Natta et al. [5] synthesized for the first time the polyacetylene as a linear, high molecular weight and regular structure polyconjugated polymers in hexane using Al(Et)₃/Ti(OP)₄ as initiator system. However the results, a dark insoluble powder, infusible and instable at air, did not interest the science. In 1963 Bolto and Weiss, Australian scientists, described the conduction properties of polypyrrole. Finally at the end of 70s the discovery of polyacetylene launched the research in conducting polymers.

Despite its historical role and theoretical importance, polyacetylene has not been commercialized. In fact, it is easily oxidized by the oxygen in air and is also sensitive to humidity. Since then, a number of techniques have been developed to overcome these problems [6]. Due to several studies on fundamental as well as in applied research, the attractiveness for conducting polymers increased considerably. And the scientific community interested to the polyaromatics system. Among them polypyrrole (PPy), polyaniline (PANI), polythiophene (PT), and poly (3, 4-ethylenedioxythiophene) (PEDOT) are most promising conducting polymers (CPs) (Table1).

Much work in this field has been focused on PEDOT and PPy. Indeed, PE-

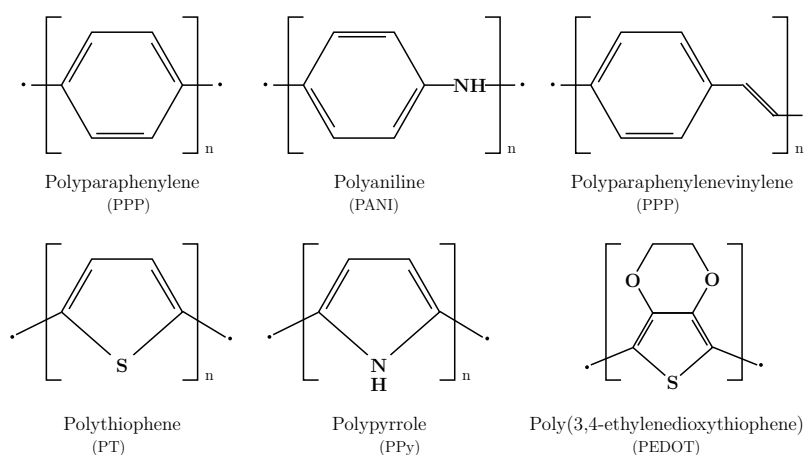


Table 1: Chemical structures of some conjugated polymers.

DOT is one of the most versatile π -conjugated conducting polymers. Today it is one of the most important conjugated polymers used in industry in different devices including light-emitting diodes (OLEDs) [7], photovoltaic cells (OPVs) [8, 9] or field-effect transistors (OFETs) [10]. On the other hand polypyrrole presents several interesting characteristics as well as good environmental stability [11], facile synthesis [12], thermal stability [13, 14] and higher conductivity [15]. The intrinsic properties of PPy are highly dependent on polymerization conditions [16]. From literature it is known that the rate of polymerization influences the conductivity of the resulting polymer and a controlled synthesis induces higher conductivities [17, 18].

The interest for conductive polymers can be attributed to their exceptional electrical and optical characteristics. First studies, through the early 1980s, focused to high electrical conductivity. Diaz *et al.* initiated the research on polyaniline and polypyrrole conductivity [19]. Successively, they have been intensively studied for electronic materials. Considered as potential substitutes of conventional conductors, technologies developed first polymer diode [20] and OFET [21]. Then, the attention shifted on optical properties. Indeed, conducting polymers are often colored and fluorescent and then research addressed to the development of LED [22] or OLED [23], optical switching, organic solar cells [24, 25], electrochromic devices [16, 26]. More recently, conducting polymers and electroactive polymers have received the attention of researchers to explore their potential in biomedical applications due to their biocompatibility [27, 28, 29].

Today the interest is turned to the synthesis of new and processable polymers. In fact the broad range of physical and chemical properties of these materials opens up for new technological applications.

Band theory

To introduce the concept of conduction in polymers, it is useful to recall the band theory which allows to explain, at least at the beginning, the electrical properties of polymers. Interaction of electrons of neighboring atoms constituting a molecule, induces the formation of molecular orbitals. The overlapping of multiple molecular orbitals can be considered as a continuum called ‘band’. In the band theory it is possible to identify two bands. The valence band (VB) corresponds to the *Highest Occupied Molecular Orbital* (HUMO). The conduction band (CB) corresponds to the *Lowest Unoccupied Molecular Orbital* (LUMO)(Figure 1).

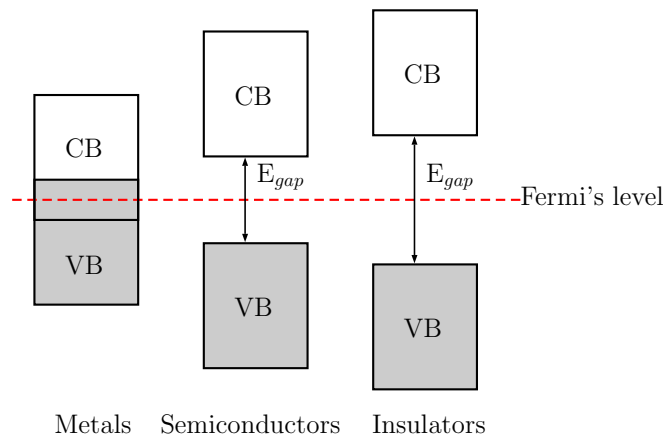


Figure 1: Scheme of conduction and valence bands in metals, semiconductors and insulators materials. The energy gap represents the distance between the two bands and the Fermi’s level indicates the energy necessary to pass the VB to CB.

The energy difference between these two bands is called *band gap*. The electrical conductivity of a material depends on its capability to flow electrons from valence band to conduction band. So, all materials can be divided into three groups: metals, insulators and semiconductors. Fermi’s level (in Figure1) indicates the work required to move an electron between different electronic states (from VB to CB). In metal, VB and CB are overlapped so the Fermi’s level is inside the overlapping and electrons can flow from VB to CB freely. In insulator

and semiconductor materials Fermi's level is exactly at the mid of the band gap. What makes a semiconductor different from insulator is the significantly smaller energy of the band gap ($E < 1.5$ eV), which allows the excitation of an electron from VB to CB.

Usually, in polymers, the high delocalization of π -electrons, all along the chain, does not allow to obtain high conductivity. The band gap is larger than 1.5 eV so they are intrinsically insulating.

Conducting polymer structure

Conducting polymers can be classified according to their structures in two systems:

- Polymer with fundamental degenerate state: it is typical of linear polymers, e.g. trans-polyacetylene. In this case two isomeric structures have the same energy, state A and state B are resonant (Figure 2).
- Polymer with fundamental non-degenerate state: it is typical of aromatics molecule. Here the resonance is between two structures with different energy, aromatic structure, more stable, and quinoid structures, less stable (Figure 2).

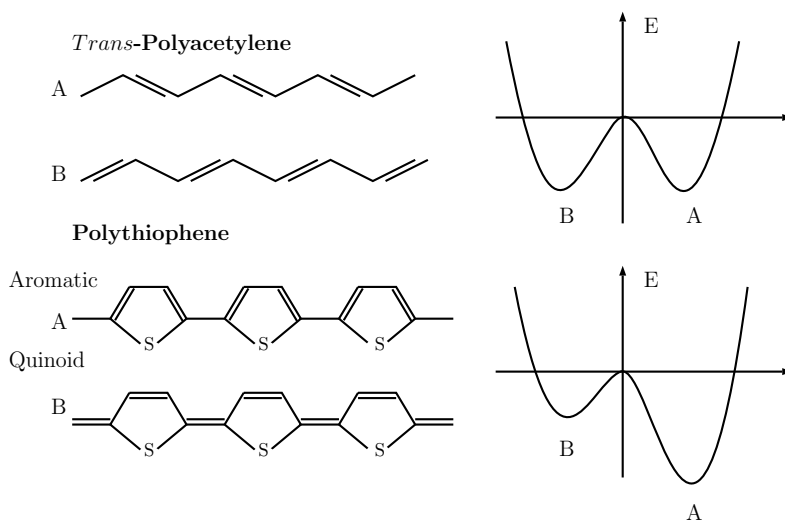


Figure 2: Scheme of degenerate state of poly-acetylene and non-degenerate states of poly-thiophene resonances

The conjugated structure with alternating single and double bonds seems to

be necessary for the polymers to become intrinsically conducting [6]. In fact it induces the formation of orbital systems that allows the charge carriers to move all along the polymer backbone. Conjugated conducting polymers have narrowed band gaps due to the overlapping of p_z atomic orbitals which decrease with the number of monomer units as shown in Figure 3.

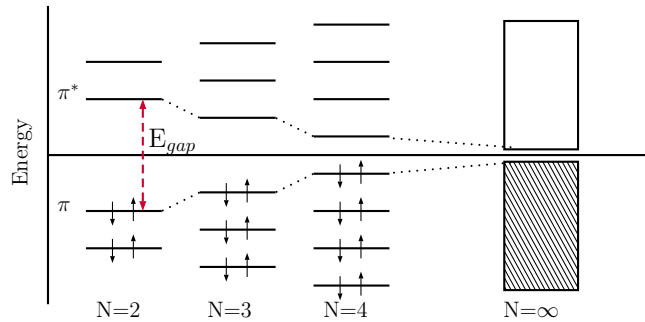


Figure 3: Schema showing the band gap decrease with increasing of the number of monomer units.

Conductive mechanism

Conduction properties of polymers result from the electronic structure of the molecule. In linear polymers the conduction is due to the formation of a soliton (Figure 4) which is a quasi-particle created by excitation in the middle of the band gap, able to generate one of the two forms of isomers of polymers (Figure 2). It represents a boundary between two segments which have opposite alternation of single and double bonds [30, 31].

In cyclic polymers the introduction of charge particle (positive or negative) in the system induces a local deformation of chain called polaron. In other words it is a radical ion (spin $1/2$) associated with a lattice distortion and the presence of localized electronic states in the gap. If a second charge particle is introduced in the system, a bipolaron is formed. It is defined as a pair of like charges which induce a strong deformation of the lattice. The formation of bipolaron is favorable and it is thermodynamically more stable than two polarons (Figure 4). The presence of bipolaron in the chain results in the possibility of two optical transitions below the band gap transition: from the VB to the lower bipolaron level and from the VB to the upper bipolaron level [30].

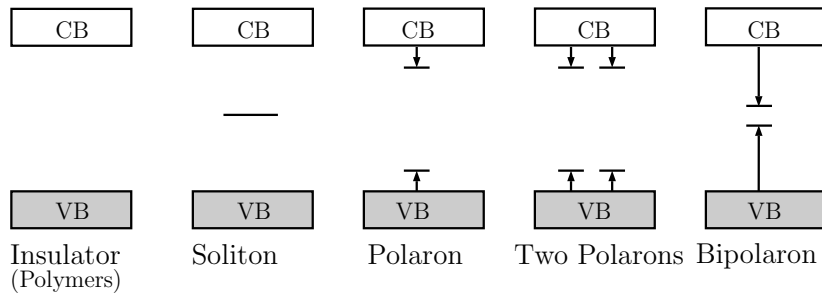


Figure 4: Scheme representing the bands in an insulator and the creation of soliton, polaron, two polarons and bipolaron in a polymer.

The population of bipolarons increases with doping level, and a high level of doping leads to new energy bands between the valence and the conduction bands, through which the electrons can flow. In the scale of conductivities (Figure 5), the conjugated polymers cover a wide range of conductivity from 10^{-7} to 10^3 $\text{S}\cdot\text{cm}^{-1}$. Nevertheless the transporting process is still not fully understood. Today it is accepted the theory that the doping process is the most obvious factor of conduction. However, others factors, as well as orientation, crystallinity and purity of conjugated polymers influence the conductivity properties [6].

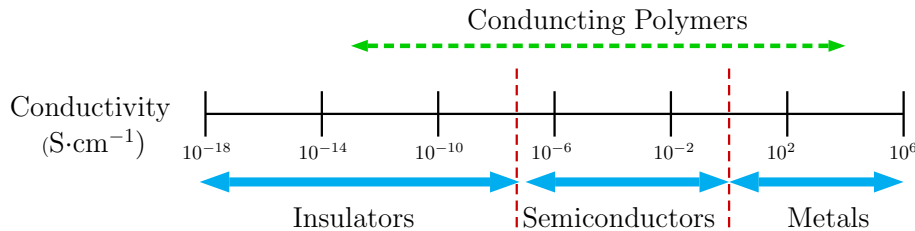


Figure 5: Scheme of conductivities range covered by polymers along conductivity scale.

State of the art

Nowadays, the research efforts focuses on understanding the mechanisms of conduction and on developing new synthesis strategies to increase conductivity. The polymerization growth plays a fundamental role in their optical and electrical properties, so many efforts are done in engineering of synthesis. Today the main methods to synthesize are chemical oxidation or electro-polymerization. The re-

action is usually an oxidative polymerization, although reductive polymerization is also possible.

The chemical route is the most useful method, it is usually recommended to produce large amounts of polymers. In simple redox reaction, conjugated monomers react with an excess amount of an oxidant in a suitable solvent and the polymerization takes place spontaneously in the bulk. In this method the further deposition of polymers onto substrates is needed. All class of polymers may be synthesized by this methodology [32, 33, 34].

The electrochemical synthesis is useful to produce polymer thin films, controlling the thickness, which is an important parameter in fabrication of optoelectronic devices. The technique involves placing both counter and reference electrodes (such as platinum), into the solution containing diluted monomers and electrolyte (the dopant) in a solvent. After applying a suitable voltage, the polymer film, which results from monomers oxidation (and diffusion), immediately starts to produce onto the working electrolyte. In this second methodology, polymers are necessary synthesized onto conductive substrates and in presence of a dopant. By the electrochemical method, it is possible to synthesized conducting polymers being simultaneously doped [35]. Moreover and contrarily to chemical synthesis, the doping level can be controlled by monitoring the amount of current. Also doping-undoping process is highly reversible with no addition of chemical products.

Even if these two methodologies are the most used for conducting polymers synthesis, some others alternative ways have been proposed. In photochemical polymerization [36], photons are used in presence of photosensitizers to initiate the reaction. The plasma polymerization technique has been explored to produce polymer films that are not easily produced *in situ* as films by other techniques [37]. The advantage of this technique is that the film begins to form from reactions in the gas phase, then it propagates and is completed at the nearest surface [38]. Another alternative way of synthesis proposed in literature is the sonochemistry [39] where the propagation of ultrasound waves through a fluid causes water homolysis and the formation of oxidizing species.

Moreover with the aim to improve the conductivity properties also the modification of polymers has received much attention. A promising method of substitution is the grafting, used to modify polymers [40].

Although the synthesis of conductive polymers has been largely studied, today the optimization of an easy preparation remains the object of many researches and the control of the polymerization mechanism remains a challenge for the scientific community.

Mechanism of polymerization

Polymerization process occurs via several reactions which, starting from monomer molecules, leads to the formation of polymer chains. The main growth mechanisms of polymerization are two:

- chain growth polymerization
- step growth polymerization

In *chain mechanism*, monomers react with each others on a large scale to generate a long polymeric chain. Usually the mechanism involves unsaturated monomers containing a carbon-carbon double bonds which participate actively to chain reaction. Polymerization consists of three stages : initiation step, propagation step and termination step. During the initiation, an active species (free radical, anion or cation) is created by a chemical process. The second step is the propagation, most of the time of growth is spent to propagate the active species in the reaction with other monomer units. The chain will grow by repeated additions of monomers with simultaneous creation of a new active site on the double bond of the annex monomer. Polymer growth is terminated by deactivation of the reactive center by an appropriate reaction depending on the type of the reactive center and the particular reaction conditions. Termination step can occur by several mechanisms as well as by combination of two active chain ends, by radical disproportion, by reaction with inhibitors or another species in polymerization mixture.

In *step polymerization* the polymer growth builds up step-by-step [37]. In this case two bi-functional molecules (monomers, dimers, etc...) react with each others. The polymerization reactions proceed by individual reactions of the functional groups in the monomers. Two monomers react to generate dimer, two dimers react to generate tetramers, and so on.

Radiolysis: an alternative method of synthesis

Radiolysis synthesis is already known as an interesting method for the synthesis of non-conducting polymers [41, 42], however it is not really used in the field of conducting polymers. In the Laboratoire de Chimie Physique d'Orsay the presence of two ionizing radiation equipments (^{60}Co source and ELYSE, electron linear accelerator) allowed to develop the synthesis of conducting polymers by using radiolysis. This method, based on the interaction of high energy radiation with matter, exhibits several advantages over other conventional methods. Indeed, it is possible to work at ambient temperature and pressure in the absence of any external chemical initiator or any dopant. Moreover, the radiolysis should lead to conducting polymers in the bulk of an aqueous or non-aqueous solution as well as directly onto substrates even if this latter are not conducting. By using pulse radiolysis the kinetics of reactions can also be followed at different timescales.

In the radiolytical synthesis compared with chemical method no external oxidant are required to initiate the polymerization and so it is free from any contamination. The reactive species come from the solvent used for the synthesis. The quantity of free radicals depends only on the energy of radiation. Also, polymerization can be switched on and off by starting or stopping the irradiation, instead of using initiator or stopper molecules such as in chemical methods.

By referring to electrochemical method, in radiolysis the preparation of sample is very easy, the use of electrolyte is not necessary. Radio-synthesis leads to the formation of polymers dispersed in water and several depositions can be envisaged onto conducting or non conducting surfaces.

In previous works, Remita *et al.* [43, 44] synthesized PEDOT polymers by using γ -irradiation. Starting from an aqueous solution of EDOT monomers, it was possible to synthesize polymers under soft conditions: at air and at room temperature without introduction of any external chemical initiators. The oxidation of EDOT monomers by hydroxyl radicals, produced by water radiolysis, led to globular nanoparticles observed by cryo-microscopy in aqueous solution. After their deposition, radiosynthesized-PEDOT were characterized by optical and electrical properties close to those of electrosynthesized PEDOT [45, 46, 47]. Successively, this study was extended to other oxidants [44] and the influence of these radicals on the polymerization was highlighted. Without any prefunc-

tionalization of EDOT monomers, differently functionalized PEDOT polymers, more or less hydrophilic, were obtained by using different oxidizing radiolytic species. Also, the morphology of polymer nanoparticles was found dependent on the nature of oxidizing radical. Due to the presence of -OH functionalities, the polymers formed by HO \cdot radicals are hydrophilic and self-assemble into globular nanostructures, while the polymers formed by using N $_3\cdot$ radicals are amphiphilic and self-assemble by π -stacking interactions into fibrillar nanostructures.

These encouraging results concerning the synthesis of conductive polymers by using ionizing radiations, led to the work presented in this thesis.

Aim of the work: Radiolysis as a tool for growth mechanism study

The complex properties of polymers can be controlled only if a good knowledge of polymerization process is acquired. In this case, it is possible to control the process during the synthesis (functionalization, hydrophilicity, chain length, doping level), and consequently to improve the conductive properties of the synthesized polymers.

Thanks to the electron accelerator ELYSE, the use of pulsed radiolysis coupled with time-resolved absorption spectroscopy allows to study the kinetics of polymerization. In fact, by real-time absorption spectroscopy, the appearance and disappearance of transient species is studied and the rate constants of the initial steps can be determined. This pulse radiolysis technique shows all advantages of radiolytical method coupled with a real-time resolution of kinetics of transient species playing a role in the polymerization. This method is also quantitative. Indeed, the use of electrons, as well as the dosimetry employed, allow to estimate the concentration of oxidizing species produced in the medium during a pulse irradiation and eventually change this concentration to study its effect.

The study of the kinetic mechanism of conducting polymers growth is the main subject of this work. Two systems will be approached. The first chapter includes the study on EDOT (ethylenedioxythiophene) molecule. Even if it is largely used and studied, its mechanism of polymerization is poorly known. In literature, few studies were focused on thiophene molecules, which looks like EDOT ones

[48, 49]. In these studies, pulse radiolysis was used to identify the first reaction between thiophene molecule and the radiolytically produced radicals showing the addition of hydroxyl radicals onto thiophene molecules [49, 48, 50]. In the present work, the reaction between EDOT and hydroxyl radicals was also investigated to identify the first steps of polymerization. The mechanism of polymerization which we proposed has successively been compared with theoretical calculations with the aim to define the transient species involved in the polymerization.

In order to synthesize conducting polymers thanks to a new alternative method based on electron beam irradiation, we also used the electron accelerator as a simple electron irradiator. Consecutive accumulated pulses were used in order to produce a high concentration in oxidative species for ensuring a quantitative polymerization of PEDOT. The resulting polymers were finally characterized by different physicochemical techniques in aqueous solution or after deposition onto substrates.

The second chapter is developed onto the study of kinetics of PEDOT growth by using other oxidizing radicals such as carbonate, azide radicals and sulfate with the aim to understand the influence of oxidizing species on polymerization. Indeed carbonate and azide radicals are less powerful than hydroxyl ones, but more selective. On the other hand, sulfate radical, having redox properties similar to hydroxyl radical, can oxidize the EDOT monomer very easily. The mechanism proposed was compared to the results found for hydroxyl oxidation. Also in this study, the electron beam was used as irradiator. By using a series of accumulated electron pulses it was possible to achieve a quantitative *in situ* PEDOT polymerization.

The third chapter concerns the study of Pyrrole. In literature wide studies focus on polymerization mechanism of Pyrrole. Electrochemical method was usually used to study the PPy growth [51]. Also radiolytical method was used to study the first step of polymerization, but the results available in literature are not complete and do not allow to identify the growth mechanism [50, 52]. Here, in this work, the mechanism of pyrrole polymerization is investigated. The oxidation of monomers by hydroxyl radicals or carbonate radicals are examined. Some theoretical simulations of the growth mechanism are proposed. Also, in the case of Py, the synthesis by electrons was investigated and the polymers were analyzed by spectroscopic and microscopic examinations.

This presentation is closed with a general conclusion about the results ob-

tained during these tree years of work on conducting polymers, showing the advantages and problems presented by our methodology. Some perspective are finally presented opening the way to new synthesis strategies based on radiation chemistry and to potential application of conducting polymers synthesized by electron irradiation.

Bibliography

- [1] B Nordén and E Krutmeijer. The nobel prize in chemistry, 2000: Conductive polymers, kungl. *Vetenskapsakademien (The Royal Swedish Academy of Sciences)*, page 1, 2000.
- [2] J Fritsche. Ueber das anilin, ein neues zersetzungsproduct des indigo. *Journal für Praktische Chemie*, 20(1):453–459, 1840.
- [3] F Wudl, RO Angus Jr, FL Lu, PM Allemand, D Vachon, M Nowak, ZX Liu, H Schaffer, and AJ Heeger. Poly-p-phenyleneamineimine: synthesis and comparison to polyaniline. *Journal of the American Chemical Society*, 109(12):3677–3684, 1987.
- [4] H Letheby. Xxix.on the production of a blue substance by the electrolysis of sulphate of aniline. *Journal of the Chemical Society*, 15:161–163, 1862.
- [5] Giulio Natta, G Mazzanti, and P Corradini. Atti accad. naz. lincci, cl. *Sci. Fis. Mat. Nat., Rend.*, 25(3), 1958.
- [6] Liming Dai. *Intelligent macromolecules for smart devices: from materials synthesis to device applications*. Springer Science & Business Media, 2004.
- [7] Y Cao, G Yu, C Zhang, Reghu Menon, and AJ Heeger. Polymer light-emitting diodes with polyethylene dioxythiophene–polystyrene sulfonate as the transparent anode. *Synthetic Metals*, 87(2):171–174, 1997.
- [8] Jean Roncali, Pierre Frère, Philippe Blanchard, Rémi de Bettignies, Mathieu Turbiez, Sophie Roquet, Philippe Leriche, and Yohan Nicolas. Molecular and supramolecular engineering of π -conjugated systems for photovoltaic conversion. *Thin solid films*, 511:567–575, 2006.
- [9] Seung Joo Lee, Hyeong Pil Kim, Abd Rashid bin Mohd Yusoff, and Jin Jang. Organic photovoltaic with pedot: Pss and v 2 o 5 mixture as hole transport layer. *Solar Energy Materials and Solar Cells*, 120:238–243, 2014.
- [10] Hu Yan, Tsubasa Kagata, and Hidenori Okuzaki. Micrometer-scaled ofet channel patterns fabricated by using pedot/pss microfibers. *Synthetic Metals*, 159(21):2229–2232, 2009.
- [11] Helmut Muenstedt and Herbert Naarmann. Long-term stability of the electrical conductivity of pyrrole polymers, March 25 1986. US Patent 4,578,433.

- [12] Chen Shen, Yupeng Sun, Wei Yao, and Yun Lu. Facile synthesis of polypyrrole nanospheres and their carbonized products for potential application in high-performance supercapacitors. *Polymer*, 55(12):2817–2824, 2014.
- [13] Andrew D Child and Hans H Kuhn. Enhancement of the thermal stability of chemically synthesized polypyrrole. *Synthetic metals*, 84(1):141–142, 1997.
- [14] M Arca, E Arca, A Yildiz, and O Güven. Thermal stability of poly (pyrrole). *Journal of materials science letters*, 6(9):1013–1015, 1987.
- [15] Yu-Chuan Liu and Chenh-Jung Tsai. Enhancements in conductivity and thermal and conductive stabilities of electropolymerized polypyrrole with caprolactam-modified clay. *Chemistry of materials*, 15(1):320–326, 2003.
- [16] Murat Ates, Tolga Karazehir, and A Sezai Sarac. Conducting polymers and their applications. *Current Physical Chemistry*, 2(3):224–240, 2012.
- [17] Alexander Kros, Nico AJM Sommerdijk, and Roeland JM Nolte. Poly (pyrrole) versus poly (3, 4-ethylenedioxythiophene): implications for biosensor applications. *Sensors and Actuators B: Chemical*, 106(1):289–295, 2005.
- [18] A Bhattacharya, A De, and S Das. Electrochemical preparation and study of transport properties of polypyrrole doped with unsaturated organic sulfonates. *Polymer*, 37(19):4375–4382, 1996.
- [19] AF Diaz and JA Logan. Electroactive polyaniline films. *Journal of Electroanalytical Chemistry and Interfacial Electrochemistry*, 111(1):111–114, 1980.
- [20] JH Burroughes, CA Jones, and RH Friend. New semiconductor device physics in polymer diodes and transistors. 1988.
- [21] Hi Koezuka, A Tsumura, and T Ando. Field-effect transistor with polythiophene thin film. *Synthetic Metals*, 18(1):699–704, 1987.
- [22] Richard Friend, Jeremy Burroughes, and Tatsuya Shimoda. Polymer diodes. *Physics world*, 12(6):35–40, 1999.
- [23] Arno Kraft, Andrew C Grimsdale, and Andrew B Holmes. Electroluminescent conjugated polymers-seeing polymers in a new light. *Angew. Chem. Int. End Engl*, 37:402–428, 1998.

- [24] Antonio Facchetti. π -conjugated polymers for organic electronics and photovoltaic cell applications. *Chemistry of Materials*, 23(3):733–758, 2010.
- [25] Holger Spanggaard and Frederik C Krebs. A brief history of the development of organic and polymeric photovoltaics. *Solar Energy Materials and Solar Cells*, 83(2):125–146, 2004.
- [26] Caixia Xu, Jinsheng Zhao, Junsheng Yu, and Chuansheng Cui. Ethylenedioxythiophene derivatized polynaphthalenes as active materials for electrochromic devices. *Electrochimica Acta*, 96:82–89, 2013.
- [27] Shyh-Chyang Luo, Emril Mohamed Ali, Natalia C Tansil, Hsiao-hua Yu, Shujun Gao, Eric AB Kantchev, and Jackie Y Ying. Poly (3, 4-ethylenedioxythiophene)(pedot) nanobiointerfaces: thin, ultrasmooth, and functionalized pedot films with in vitro and in vivo biocompatibility. *Langmuir*, 24(15):8071–8077, 2008.
- [28] Manju Gerard, Asha Chaubey, and BD Malhotra. Application of conducting polymers to biosensors. *Biosensors and Bioelectronics*, 17(5):345–359, 2002.
- [29] Gagan Kaur, Raju Adhikari, Peter Cass, Mark Bown, and Pathiraja Gunatillake. Electrically conductive polymers and composites for biomedical applications. *RSC Advances*, 5(47):37553–37567, 2015.
- [30] Jean Luc Bredas and G Bryan Street. Polarons, bipolarons, and solitons in conducting polymers. *Accounts of Chemical Research*, 18(10):309–315, 1985.
- [31] André-Jean Attias. *Polymères conjugués et polymères conducteurs électroniques*. Ed. Techniques Ingénieur, 1862.
- [32] R Corradi and SP Armes. Chemical synthesis of poly (3, 4-ethylenedioxythiophene). *Synthetic metals*, 84(1):453–454, 1997.
- [33] S Rapi, V Bocchi, and GP Gardini. Conducting polypyrrole by chemical synthesis in water. *Synthetic Metals*, 24(3):217–221, 1988.
- [34] TLA Campos, DF Kersting, and CA Ferreira. Chemical synthesis of polyaniline using sulphanilic acid as dopant agent into the reactional medium. *Surface and coatings Technology*, 122(1):3–5, 1999.
- [35] D Kumar and RC Sharma. Advances in conductive polymers. *European Polymer Journal*, 34(8):1053–1060, 1998.

- [36] S Annapoorni, NS Sundaresan, SS Pandey, and BD Malhotra. Photocarrier mobility in processable polyaniline. *Journal of applied physics*, 74(3):2109–2111, 1993.
- [37] JK Stille. Step-growth polymerization. *Journal of Chemical Education*, 58(11):862, 1981.
- [38] GJ Cruz, J Morales, and R Olayo. Films obtained by plasma polymerization of pyrrole. *Thin solid films*, 342(1):119–126, 1999.
- [39] WM De Azevedo, RA De Barros, and EF da Silva Jr. Conductive polymer preparation under extreme or non-classical conditions. *Journal of Materials Science*, 43(4):1400–1405, 2008.
- [40] A Bhattacharya and BN Misra. Grafting: a versatile means to modify polymers: techniques, factors and applications. *Progress in polymer science*, 29(8):767–814, 2004.
- [41] Adolphe Chapiro. Radiation induced polymerization. *Radiation Physics and Chemistry (1977)*, 14(1):101–116, 1979.
- [42] Yoneho Tabata. Radiation induced polymerization. *Radiation Physics and Chemistry (1977)*, 9(1):31–53, 1977.
- [43] Youssef Lattach, Ariane Deniset-Besseau, Jean-Michel Guigner, and Samy Remita. Radiation chemistry as an alternative way for the synthesis of PEDOT conducting polymers under soft conditions. *Radiation Physics and Chemistry*, 82:44–53, 2013.
- [44] Youssef Lattach, Cecilia Coletta, Srabanti Ghosh, and Samy Remita. Radiation-induced synthesis of nanostructured conjugated polymers in aqueous solution: Fundamental effect of oxidizing species. *ChemPhysChem*, 15(1):208–218, 2014.
- [45] Elodie Pardieu, Helene Cheap, Christophe Vadrine, Mathieu Lazerges, Youssef Lattach, Francis Garnier, Samy Remita, and Christine Pernelle. Molecularly imprinted conducting polymer based electrochemical sensor for detection of atrazine. *Analytica Chimica Acta*, 649(2):236–245, 2009.
- [46] Y Lattach, N Fourati, C Zerrouki, JM Fournion, F Garnier, and S Remita. Surface acoustic wave sensor combining gravimetric and electrochemical transductions: application for atrazine detection. *Sensor Letters*, 9(6):2249–2252, 2011.

- [47] Youssef Lattach, Pierre Archirel, and Samy Remita. Influence of the chemical functionalities of a molecularly imprinted conducting polymer on its sensing properties: Electrochemical measurements and semiempirical dft calculations. *The Journal of Physical Chemistry B*, 116(5):1467–1481, 2012.
- [48] Barbara B Saunders, Priscilla C Kaufman, and Max S Matheson. Reactions of thiophene with radiolytically produced radicals. 1. the hydroxyl radical. *The Journal of Physical Chemistry*, 82(2):142–150, 1978.
- [49] Barbara B Saunders. Reactions of thiophene with radiolytically produced radicals. 2. the solvated electron and the hydrogen atom. *The Journal of Physical Chemistry*, 82(2):151–154, 1978.
- [50] J Lilie. Pulsradiolytische untersuchung der oxydativen ringöffnung von furan, thiophen und pyrrol/pulsradiolytic investigations of the oxydativ ring scission of furan, thiophen and pyrrol. *Zeitschrift für Naturforschung B*, 26(3):197–202, 1971.
- [51] Said Sadki, Philippe Schottland, Nancy Brodie, and Guillaume Sabouraud. The mechanisms of pyrrole electropolymerization. *Chemical Society Reviews*, 29(5):283–293, 2000.
- [52] Claude P Andrieux, Pierre Audebert, Philippe Hapiot, and Jean Michel Saveant. Identification of the first steps of the electrochemical polymerization of pyrroles by means of fast potential step techniques. *The Journal of Physical Chemistry*, 95(24):10158–10164, 1991.

Chapter 1

Materials and Methods

This chapter introduces the methods of synthesis and investigation techniques used in this study to give the reader all the tools necessary for the understanding and interpretation of the results that will follow.

The aim of this work was to develop a new method of synthesis of conductive polymers which is easy and efficient comparing to chemical and electrochemical polymerization routes. In this context, the use of radiolysis seems to be a good approach to understand the mechanism of polymerization and eventually to improve the synthesis procedure. The use of radiation to initiate the polymerization was already developed in 20's by Lind (USA). It followed the first patent in 1940 by F. Joliot. However the foundation of radiation-induced polymerization is attributed to French researchers Magat and Chapiro [1], which were interested to the effect of radiation on initiation of polymerization by neutron, α particles and X- and γ -rays [2].

Successively the interest increased in all scientific world. Studies turned on grafting, polymers degradation, polymerization mechanism by radiation appeared in literature. Today, the ionizing radiation remains a powerful method to synthesize polymers. Nevertheless, although used for synthetic plastics preparation, it remains unemployed or almost for conductive polymers.

The polymerization by irradiation is based on the interaction of ionizing radiation with solvent molecules which produces active species, like radicals, which can initiate the polymerization.

In our study we used in particular pulsed radiolysis. This technique also allows to follow the kinetics of the reaction of transient species produced in the solution during the irradiation onto organic monomers.

1.1 Materials

In the following section all chemical products used during preparation of solution are described. The choice of products will be explain and discussed. Finally the procedure of solution preparation is detailed.

1.1.1 Monomers

EDOT

The 3,4-Ethylenedioxythiophene ($C_6H_6O_2S$) monomer (molecular weight of $142.18 \text{ g} \cdot \text{mol}^{-1}$) in Figure 1.1 was purchased from Sigma-Aldrich with purity 97% and used as received. This monomer was synthesized by Bayer in 1988. It is a derivative of thiophene molecule, characterized by the fact that the β - β' position of the thiophene ring is blocked. This prevents the α - β linkages and assures the formation of linear chain with bonds in high reactive free α - α' position [3].

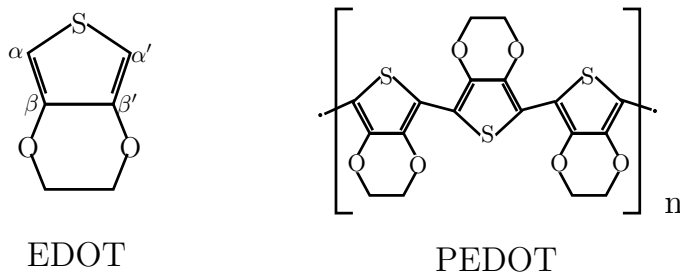


Figure 1.1: Structure of EDOT and PEDOT polymer

This characteristic induce the conjugation in molecules and allows the conduction. The derived polymer (PEDOT) in Figure 1.1 is known for its high conductivity and good optical trasparency in the visible spectral region [4]. Moreover the monomer is easily oxidized due to its low band gap (1.6-1.7 eV) [5]. EDOT is not very soluble in water (2.1 g L^{-1} at 20°C).

Due to its low solubility in water only relatively low concentrations in EDOT were used. So three different aqueous solutions were investigated: 1 mM, 5 mM and 10 mM. The monomers concentration of prepared aqueous solution was always checked by recording UV-Vis absorption spectra before and after irradiation. In Figure 1.2, it is shown typical EDOT monomer spectrum in aqueous solution at a concentration of 1 mM before irradiation.

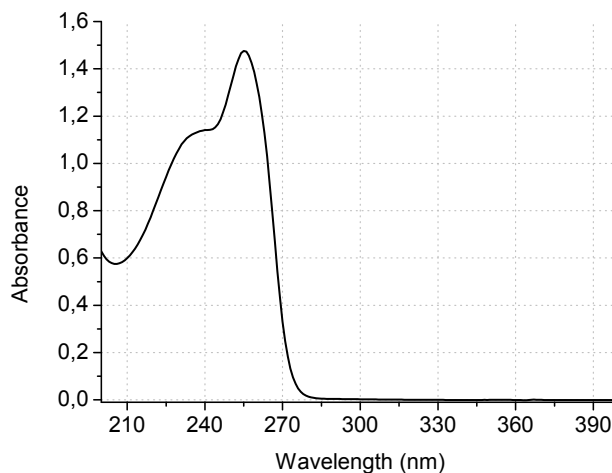


Figure 1.2: UV-Vis absorption spectrum of aqueous solution containing 1 mM in EDOT before irradiation. The length path is 0.2 cm and the reference is distilled water.

Two characteristic bands are observed at 235 and 255 nm. The extinction coefficients were estimated in the laboratory in a previous work [6].

$$\epsilon_{235} = 5650 \pm 10 \text{ L mol}^{-1} \text{ cm}^{-1}$$

$$\epsilon_{255} = 7048 \pm 200 \text{ L mol}^{-1} \text{ cm}^{-1}$$

The solution is prepared at room temperature, using distilled water (Millipore system 18.2 M Ω) as the solvent. The monomer is dissolved in water during one night on a magnetic stirrer. The solution is protected from light with aluminum foil to prevent the activation of possible photo-reactions. The pH was measured before and after irradiation. The pure EDOT solution is usually slightly alkaline with pH around 8. After irradiation no important pH changes were observed. The adjustment of pH for the study of pH effect was achieved by using sodium hydroxide (NaOH) or perchloric acid (HClO₄).

When temperature test was studied the solution were prepared in a thermostatic bath and the temperature was fixed at 25°C or 60°C. On the other hand, a cooling bath was used to prepare the solution at 0°C.

Pyrrole

The second system studied was Pyrrole. It is a monomer with formula C₄H₅N and molecular weight 67.09 g mol⁻¹ (Figure 1.3). It was purchased from Sigma Aldrich

and used as received. It is soluble in water ($45 \text{ g}\cdot\text{L}^{-1}$). Due to its relatively high solubility, the solutions were prepared only few hours before the experiments. Also in this case different concentrations were studied: 10 mM, 20 mM, 50 mM and 100 mM. The solution was usually prepared at room temperature and the solvent was distilled water.

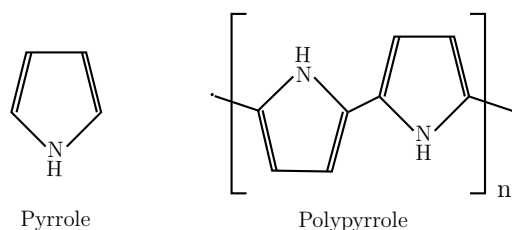


Figure 1.3: Pyrrole and Polypyrrole polymer structure.

The concentration of Pyrrole, was always checked by UV-Vis absorption spectroscopy. The Py monomer shows a band at 205 nm (Figure 1.4) with an extinction coefficient of $6730 \text{ Lmol}^{-1}\text{cm}^{-1}$ [7]. The pH of Py solutions was measured before and after irradiation. Pyrrole aqueous solution is neutral with a pH around 6. Also in this case in order to check the pH effect, pH was varied by addition of sodium hydroxide (NaOH) or perchloric acid (HClO_4).

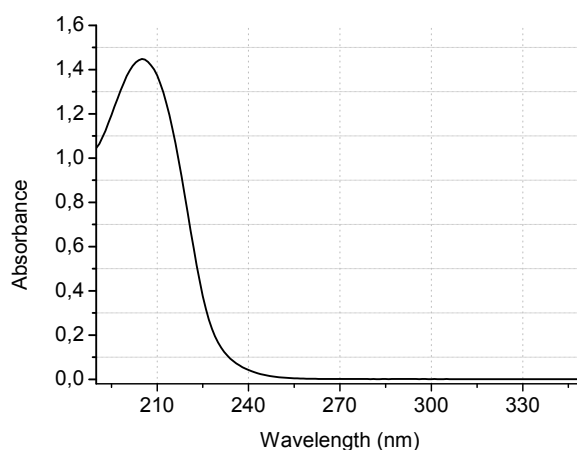


Figure 1.4: UV-Vis absorption spectrum of aqueous solution containing 1 mM in Pyrrole monomers. The length path was 0.2 cm and the reference was distilled water.

1.1.2 Oxidants

The polymerization of EDOT and Py organic monomers takes place if an active species oxidize the molecule. In this study we performed the oxidation by using several oxidants with the aim to understand the effect of each of them on polymerization.

Carbonate radical

Sodium carbonate (Na_2CO_3 , $\geq 99.5\%$, $\text{m.w.}=105,99 \text{ g}\cdot\text{mol}^{-1}$) used to scavenge hydroxyl radicals and to produce carbonate radicals in N_2O -saturated irradiated solution was from Sigma Aldrich. It is very soluble in water ($300 \text{ g}\cdot\text{L}^{-1}$), so it was possible to vary the concentration from 10 mM to 1 M. In presence of Na_2CO_3 , the aqueous solution becomes alkaline with a pH value depending in carbonate concentration.

Azide radical

Sodium azide (NaN_3 , $\geq 99\%$, $\text{m.w.}=65 \text{ g}\cdot\text{mol}^{-1}$) was purchased from Sigma-Aldrich. It was used to produce azide radicals N_3^\cdot as oxidants to initiate the polymerization of EDOT.

Sulfate radical

Potassium persulfate ($\text{K}_2\text{S}_2\text{O}_8$, $\geq 99\%$ $\text{m.w.}=270,322 \text{ g}\cdot\text{mol}^{-1}$), was purchased from Sigma Aldrich. Soluble in water 4,49 g/100 mL, it dissociates in persulfate ions. Note that potassium persulfate is totally soluble whatever the used temperatures, so different concentration were studied from 5 to 50 mM. Indeed, its solubility is 65 mM at 0°C , 222 mM at 25°C and higher than 620 mM at 60°C [8].

Nitrous Oxide and Argon

The N_2O and Ar inert gases were purchased from Air liquid. They were usually dissolved by bubbling in the solution, before and during the irradiation. The N_2O solubility expressed in mole fraction is $5.948 \cdot 10^{-4}$ at 25°C [9].

tert-Butyl Alcohol

The *tert*-Butyl Alcohol ($74.12 \text{ g}\cdot\text{mol}^{-1}$) was purchased from Sigma Aldrich. It was used as a scavenger of hydroxyl radical. Its good characteristic as well as the high vapor pressure, high miscibility in water and low melting solvent make it an excellent

freeze-drying medium [10]. This ensures the absence of this alcohol in the dried sample which are investigated by microscopies techniques.

1.2 Methods

In the *Laboratoire de Chimie Physique d'Orsay*, there are two sources of ionizing radiations: ^{60}Co source and ELYSE electron accelerator. These two facilities allow the study of the polymerization by steady state radiolysis and by pulsed radiolysis respectively.

1.2.1 Water radiolysis principle

Water radiolysis is the degradation of water molecules by ionizing radiations. This physico-chemical phenomenon has been studied since the discovery of ionizing radiations in 1895 when Röntgen identified the X-rays [11, 12, 13].

The interaction of ionizing radiations with water is usually described as the succession of two phases: the non-homogeneous and the homogeneous one, by referring to the spatial distribution of the species produced by ionizing radiation. Initially the water molecules are excited and ionized. The spatial distribution of the species produced in this first excitation and ionization is non-homogeneous. The spurs along the track of irradiation are formed with high concentrations in primary species. The heterogeneous phases is described by three steps:

- physical stage (achieved in 10^{-15} s)
- physico-chemical stage (10^{-15} to 10^{-12} s)
- chemical stage (10^{-12} to 10^{-6} s)

In the physical step, the initial event is the transfer of a sufficient energy in order to excite and ionize water molecules:



Successively, in the physico-chemical step, these first three initial species ($\text{H}_2\text{O}^{\cdot+}$, e^- , H_2O^*) begin to diffuse in the medium and eventually react with each others.

The excited molecules relax by dissociative relaxation:



or according to an ion-molecule reaction:



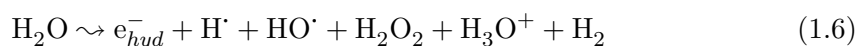
After H_2O ionization, two events can take place: the recombination of electron-hole or the electron thermalization:



The electron loses its energy by reacting with the surrounding molecules.

Finally, in chemical stage, the species, produced in the spurs, begin to diffuse randomly by reacting with each others in the regions of high local concentrations. However, some of these species escape from the reactions in the tracks and become homogeneously distributed in the medium. The escaped species can react with each others or alternatively with the solute.

Then few hundred nanoseconds after, the water radiolysis can be described by the reaction:



The process described here is summarized in Figure 1.5. All possible reactions are depicted as function of the time.

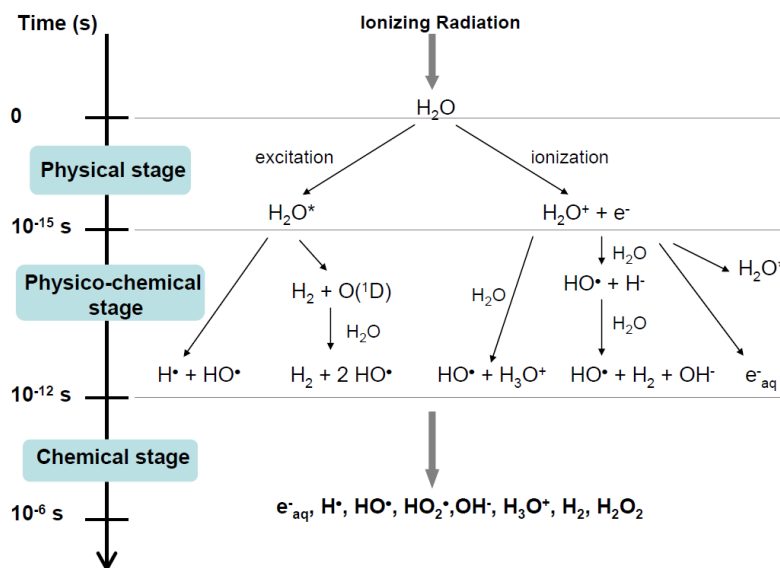


Figure 1.5: Main reactions occurring during the three stages of water radiolysis. Image from [13].

Radiolytical yield

In radiation chemistry, the yield of species produced in a medium due to exposure to high-energy radiation is defined as the number of events formed per unit of absorbed energy:

$$g = N/E \quad (1.7)$$

where g is the yield, N the number of events and E the absorbed energy. In the past, this value was expressed in number of species per 100 eV absorbed. Today the common unit is $\text{mol}\cdot\text{J}^{-1}$:

$$G(\text{mol}/\text{J}) = g(\text{events}/100\text{eV}) \times 1.036 \cdot 10^{-7} \quad (1.8)$$

The dose in a medium is expressed as the absorbed energy per unit of mass of the irradiated medium:

$$D = E/m \quad (1.9)$$

where D is the dose, E the energy absorbed in the mass m . It is expressed in Grays (Gy), so $1 \text{ Gy} = 1 \text{ J kg}^{-1}$. Since $g = N/E$ and $D = E/m$ and taking into account the volume V of the mass in which the energy E is absorbed:

$$\frac{N}{V} = \frac{G D m}{V} = G D \rho \quad (1.10)$$

In water radiolysis, ρ is approximately $1 \text{ kg}/\text{dm}^3$, so the concentration of species produced by ionizing radiation in aqueous solution, can be estimated by using the relation:

$$C = \frac{N}{V} = D G \quad (1.11)$$

Where D is expressed in J kg^{-1} (or J L^{-1}) and G in mol J^{-1} . The G value depends on the LET (linear energy transfer), so on the nature of the radiation and on time.

In Table 1.1, the radiolytical yield of water radiolysis under N_2 at neutral pH at 3 ns after the pulse are listed.

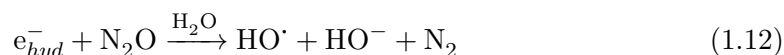
	e_{hyd}^-	$\text{H}\cdot$	$\text{HO}\cdot$	H_2O_2	H_3O^+	H_2
G ($\mu\text{mol J}^{-1}$)	0.28	0.06	0.28	0.073	0.28	0.047

Table 1.1: Radiolytic yields of water radiolysis species at homogenous stage.

1.2.2 Oxidative environment

It is always possible to choose an oxidative or reductive environment, which means to induce a reduction by hydrated electron or oxidation by hydroxyl radicals.

When the system needs the use of hydroxyl radical (oxidant environment), we take advantage of using nitrous oxide gas dissolved by bubbling in the solution. This gas reacts rapidly with hydrated electrons to give HO \cdot radicals via reaction:



By fitting with a first order reaction the decrease of hydrated electron during 100 ns, the apparent constant rate k' is determined. The rate constant of N $_2$ O with hydrated electron is $k=9.1 \cdot 10^9 \text{ M}^{-1}\text{s}^{-1}$. So the exact concentration of N $_2$ O dissolved is calculated and the concentration of hydrated electron effectively transformed is quantified.

Oxidation by hydroxyl radical

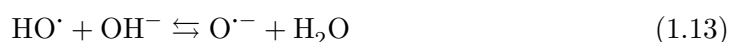
The hydroxyl radical, HO \cdot , is one of the principal reactive species produced in water radiolysis. It is a powerful oxidant with redox potential of 1.8 V $_{SHE}$ in neutral solution and 2.7 V $_{SHE}$ in acidic solutions [14] (where the potentials are given with Standard Hydrogen Electrode as reference). The HO \cdot can act on the organic molecule as an oxidant by electron abstraction leading to radical cations, by hydrogen abstraction leading to neutral radicals or by addition onto double bonds [15].

The choice of this radical is due to its powerful oxidative potential and its easily formation in water radiolysis. With the aim to develop a very simple system, it represents the best oxidant which does not induce contamination in solution. The absorption spectrum of this species in the UV ranges under 300 nm with a very weak molar absorption coefficient, so our system is not affected by its absorption.

As previously detailed, in presence of N $_2$ O, all electrons are transformed in hydroxyl radical by reaction 1.12. Then, the radiolytical yield of hydroxyl radical can be estimated as: $G(HO\cdot) = G(e_{hyd}^-) + G(HO^-) = 0.56 \mu\text{mol J}^{-1}$.

Oxidation by oxide radical

On the other hand, in strong alkaline solution hydroxyl radical is rapidly converted into oxide radical O \cdot^- , $pK_a = 11.9$ [14]. The equilibrium is described by reaction:



with rate constants: $k_f = 1.25 \cdot 10^{10} \text{ L mol}^{-1} \text{ s}^{-1}$ and $k_b = 1.7 \cdot 10^6 \text{ L mol}^{-1} \text{ s}^{-1}$ [16]. $\text{O}^{\cdot -}$ is also a powerful oxidant even if it reacts more slowly than hydroxyl radical.

Oxidation by others oxidants

In order to change the oxidant species in the system, a scavenger (S^-) of hydroxyl radical, HO^\cdot , is usually introduced. The reaction with ions S^- can be generally considered as an electron transfer:



producing the reactive oxidant radical S^\cdot .

Carbonate radical

Carbonate radical ($\text{CO}_3^{\cdot -}$) coming from CO_3^{2-} ion was used as selective secondary oxidant to oxidize EDOT and Pyrrole monomers. This radical acts predominantly as an electron acceptor. It oxidizes organic molecules [17] even if the oxidation is generally slower than that initiated by hydroxyl radical. It is a mild oxidant with a redox potential $E^0 = 1.59 \text{ V}_{SHE}$ [18].

In presence of carbonate or sodium hydroxide the solubility decreases [19, 20], so the concentration of N_2O dissolved in water was estimated from the kinetics decrease of hydrated electron.

This radical $\text{CO}_3^{\cdot -}$ can be generated radiolytically in aqueous solution by reaction with hydroxyl radical:



with a rate constant of $k = 4.2 \cdot 10^8 \text{ M}^{-1} \text{ s}^{-1}$. In highly alkaline solutions, $\text{O}^{\cdot -}$ reacts with carbonate to give the same $\text{CO}_3^{\cdot -}$ radical as with HO^\cdot radical via reaction:



but the rate constant of formation is slower than in neutral solution: $k < 10^7 \text{ M}^{-1} \text{ s}^{-1}$ [21].

This transient radical $\text{CO}_3^{\cdot -}$ produced during water radiolysis exhibits a broad optical absorption in the visible range with a maximum at 600 nm (Figure 1.6) and an extinction coefficient of $\epsilon = 1860 \pm 160 \text{ M}^{-1} \text{ cm}^{-1}$ [21].

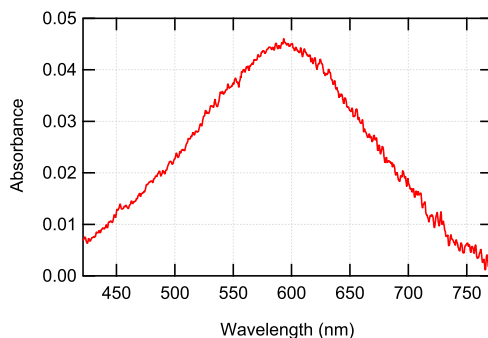
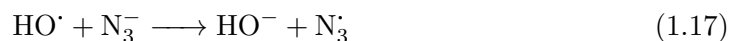


Figure 1.6: Transient spectrum of $\text{CO}_3^{\cdot-}$ radical obtained by pulse radiolysis of an aqueous solution of 100 mM of Na_2CO_3 at pH=12.6. The spectrum was taken at 5 μs after the electron pulse (Dose = 39 Gy/pulse, optical path = 1 cm).

The absorption spectrum was recorded by pulse-radiolysis, Figure 1.6 and its formation was systematically checked when irradiations were performed in the presence of Na_2CO_3 .

Azide radical

In the pH range of 4-13 the azide radical, N_3^{\cdot} , can be prepared by HO^{\cdot} oxidation of azide anions by pulse radiolysis of aqueous solution of NaN_3 saturated with N_2O via reaction [22]:



with the rate constant $k = 1.2 \cdot 10^{10} \text{ M}^{-1}\text{s}^{-1}$.

The absorption spectrum of azide radical shown in Figure 1.7 depicts a tight band at 274 nm with an extinction coefficient of $\epsilon = 2025 \pm 50 \text{ M}^{-1}\text{cm}^{-1}$ [22].

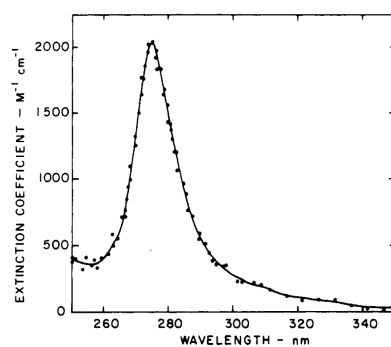


Figure 1.7: Absorption spectrum of N_3^{\cdot} as determined 1 μs after the pulse irradiating a N_2O -saturated 0.0077 M NaN_3 solution at pH 11 from reference [22]

In our experiments it was not possible to identify this species because of the intense absorption of EDOT and Pyrrole molecules at this wavelength.

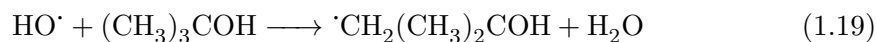
In literature several values [18, 23, 24] of the redox potential of azide radicals are reported, nevertheless a study in 2006 [25] demonstrated that the redox potential is $E^\circ_{N_3^\cdot/N_3^-} = 1.7 V_{SHE}$ and the self-exchange rate constant of N_3^\cdot/N_3^- couple is $k_{N_3^\cdot/N_3^-} = 2.7 \cdot 10^6 M^{-1}s^{-1}$. Indeed several studies [26] have suggested the recombination of azide radical with its parent ions to form N_6^- species in the equilibrium:



The absorption spectrum of N_6^- displays a peak in the visible range at 700 nm with an extinction coefficient $\epsilon = 8140 M^{-1}s^{-1}$ [27].

1.2.3 Reducing environment

When the system needs the use of hydrated electron, we need a scavenger of hydroxyl radical. For this purpose the aqueous solution is prepared in presence of *tert*-Butyl Alcohol (2-methylpropan-2-ol) which is a hydroxyl scavenger via reaction:



The *tert*-Butyl Alcohol was chosen because its radical, produced in reaction 1.19, is relatively inert and it does not react with monomer in the solution [28].

In our study the use of *tert*-Butyl Alcohol is usually coupled with the Argon degassing. It is used to remove oxygen which is an efficient e_{hyd}^- scavenger. The solution are bubbled with Argon before and during irradiation. In this way a reductive environment is obtained.

Sulfate radical

In literature, persulfate ion, $S_2O_8^{2-}$ is considered as one of the best candidates as initiator in the process of polymerization [29, 30]. It is a powerful oxidant, with a strong redox potential of $E^\circ = 2.01 V_{SHE}$ [31, 32], for this reason it is often used in chemical polymerization [30, 33]. However the interest for persulfate is due to the dissociation in sulfate radical which is a stronger oxidant with higher redox potential of $2.6 V_{SHE}$ [34].

The sulfate radical can be produced by water radiolysis:



with a rate constant of $k = 1.1 \cdot 10^{10} \text{ M}^{-1}\text{s}^{-1}$ [35]. Like hydroxyl radical, the sulfate radical is a very reactive species, it can react by electron transfer, addition or hydrogen abstraction. It is known to absorb at 455 nm, with extinction coefficient $\epsilon = 1100 \text{ L mol}^{-1}\text{cm}^{-1}$ [17] (Figure 1.8).

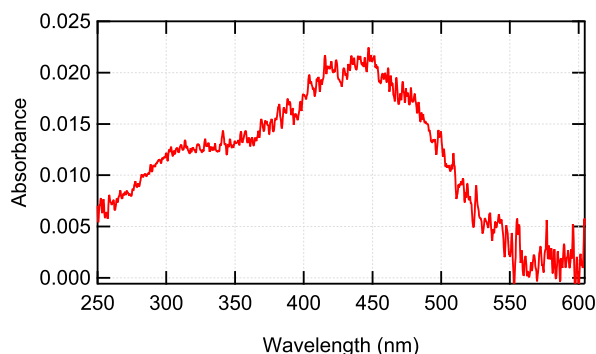


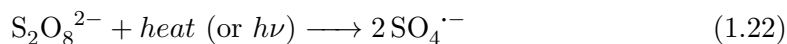
Figure 1.8: Absorption spectrum at $1\mu\text{s}$ of sulfate radical obtained by pulse radiolysis of an aqueous solution containing 20 mM of $\text{K}_2\text{S}_2\text{O}_8$ and 0.5 M *tert*-Buthyl alcohol at $\text{pH} = 3.5$ (Dose=42 Gy/pulse, optical path = 1 cm).

Note that in absence of other molecules the sulfate radical reacts with itself by reaction:



with a rate constant $k = 4 \cdot 10^8 \text{ M}^{-1}\text{s}^{-1}$ [35].

Sulfate radical can also be produced by thermolysis (or photolysis) via reaction [32, 36, 37, 38]:



In order to study the reactivity of persulfate ions on EDOT monomer, a study as function of temperature was done. Indeed persulfate is commonly used at high temperature in order to enhance its radical oxidation mechanism [32]. With the aim to prevent the action of persulfate on monomers, we proceed to study the effect of temperature in reactivity of the persulfate anions. Then, the solutions containing persulfate were prepared at 0° , to prevent the reaction of persulfate ions with monomers; at 25° to study the room temperature kinetics and at 60°C to accelerate the kinetics.

At 0°C a cooling bath was used, at 25°C and 60°C a thermostatically-controlled water bath was employed.

1.2.4 Pulse radiolysis

In order to study the mechanism of the oxidation of organic monomers which leads to the formation of polymers, the identification of the first steps and their kinetics have been studied by pulsed radiolysis technique coupled with time-resolved spectroscopy. Pulse radiolysis allows to study the reactions of short-live transient species produced by a very short pulse of high energy irradiation, [39, 40].

The experiments were carried out on the picosecond laser-triggered electron accelerator ELYSE at University Paris-Sud (Orsay). The platform uses a femtoseconds laser pulses triggering a photo-cathode to produce the initial electron bunch. The combination of laser and electron beam allows to perform pulse radiolysis as well as ultra-fast photochemistry.

Laser

In Figure 1.9, the laser scheme is shown. An optical fiber generates a laser beam with frequency 78.9 MHz inside the oscillator MENLO. After crossing a doubler crystal, the laser pulse is at 780 nm of 80 fs at around 1 nJ of energy for each pulse, not enough for experimental need. So the pulse is amplified by chirped pulse amplification. Then it is stretched to 150 ps and successively divided into two beams: one for radiolysis experiments and second for photolysis experiment.

The laser beam for radiolysis is amplified two more times by a regenerative amplifier and multi-pass amplifier. At the output of the two amplifications, the laser beam have an energy of 3,2 mJ per pulse and duration of 150 ps. At this point, the beam will be compressed to 100 fs, with an energy of 2.1 mJ at a frequency between 0 and 100 Hz and centered at 780 nm. It is then transferred to the accelerator room where its frequency is tripled to 263 nm because UV pulses are needed to generate to excite the photo-cathode for the generation of the electrons. The laser beam then enters into the accelerator through a silica window and is transported to the photo-cathode by means of a mirror inside the accelerator [39, 40].

Elyse: electrons accelerator

The ELYSE accelerator is shown in Figure 1.10. The electron bunch is generated by photoelectric effect obtained by impact of the laser pulse on the Cs₂Te photo-cathode.

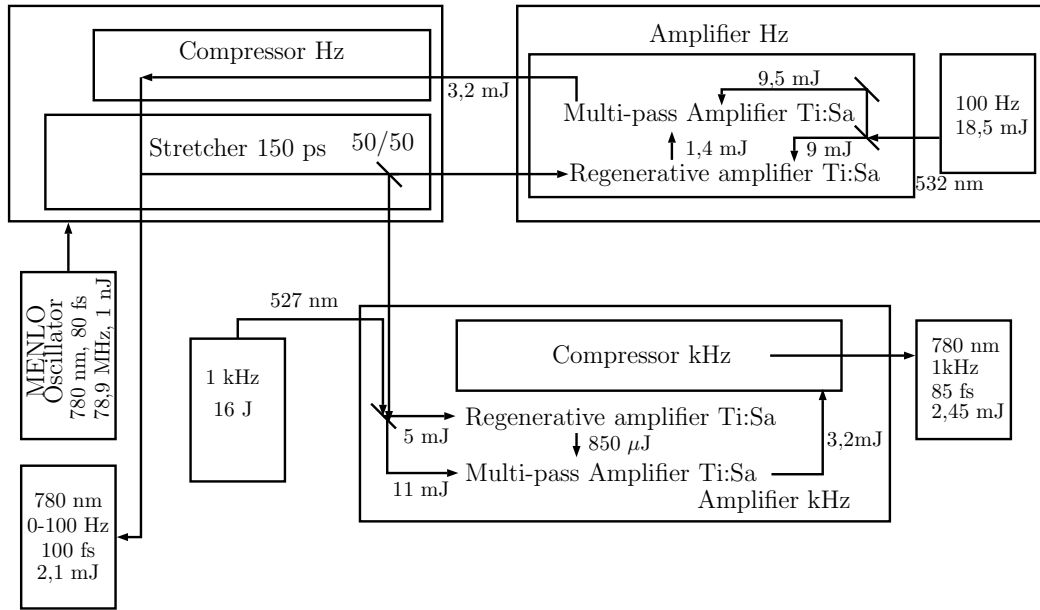


Figure 1.9: Laser scheme

The photo-cathode is prepared *in-situ* by co-evaporation of Cs and Te under extremely low pressure conditions in a vacuum chamber because of its sensitivity to oxidation by air. This chamber is directly connected to the accelerator. The photo-cathode is excited by the laser pulses at 263 nm which diameter of the laser spot on photo-cathode is about 5 mm and the charge extracted is up to 5 nC, [40]. The laser and electron gun are synchronized. Using a 80 MHz quartz oscillator controlling both the pump laser beam and the klystron RF of the laser-triggered electron beam provides a precise synchronization of both laser and electron beams.



Figure 1.10: ELYSE: electrons accelerator at LCP (Laboratoire Chimie Physique) at Orsay.

The electron bunch is emitted in a RF gun. This gun provides a beam of 4 MeV.

The additional acceleration to reach 9 MeV is provided by a four-cell booster cavity. The RF power for the gun and booster is provided by a TH2130 klystron (Thomson-CSF, 20 MW, 4 ms) and a purpose built modulator. After acceleration to the desired energy, a series of dipoles and quadrupoles ensure the transport of electrons pulses to the experiment area across the accelerator line [39].

Time-resolved spectroscopy detection

The time resolved absorption spectroscopy consists in applying a flash of analyzing light synchronized with the pulse of electrons and in sending it on a rapid detector able to measure the variation of light intensity with time. At ELYSE, the light is focused through the sample collinearly with the electron beam. This analyzing light beam is then transported by means of lenses and mirrors to the detection room, 15 m far from the sample where it is directed onto the entrance slit of a spectrograph connected to the entrance optics of a streak-camera.

Analyzing light: Two different systems allow to perform time resolved spectroscopy measurements. A pulse analyzing light is produced by a flash xenon lamp, constructed at the Laboratoire de Chimie Physique. It delivers intense and constant pulses with rise time of $2 \mu\text{s}$, which enables measurements of the evolution of the time-resolved spectrum with repetition rates up to 10 Hz. The diameter of light beam, controlled by an iris, is generally of 0.2 cm. A mirror with thickness of $200 \mu\text{m}$ is placed at 45° in front of the output window of the electrons and in front of the cell (Figure 1.11).

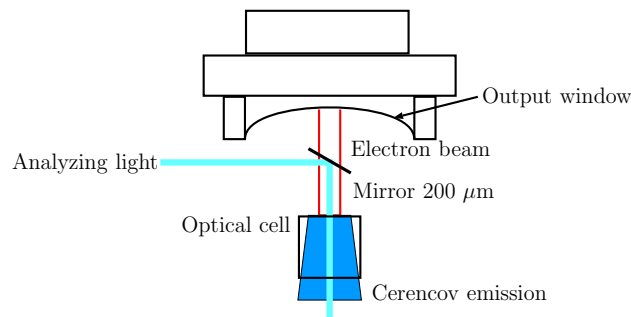


Figure 1.11: Scheme illustrating the collinearity of analyzing light and electrons beam.

In this way the light beam is reflected exactly collinear with the electron beam. In general the size of the light beam is smaller than that of electrons, the analyzing light beam cross-section in the cell is less than 0.5 mm. The spectrograph used (Chromex

250IS) is equipped with three 150 grooves/ mm grating blazed at 300, 500 and 800 nm which disperse the light on the entrance optics of a streak-camera (model C-7700 from Hamamatsu). The three grooves allow to range from UV-Vis to IR wavelength. The full spectra are obtained by two or three series of absorption measurements using the different optical filters (UG5 and GG325) to optimize the light intensity on a specific spectral domain.

Irradiation cell and pump system: The irradiated solution is renewed between two pulses. The suprasil quartz optical cells are placed at the exit of beamline and they are connected by tubes with a reservoir where the solution to be studied is stored and deaerated by flushing with an inert gas. The optical path of the cell is 1 cm. Tubes containing solution are fitted inside a circular pump mechanism which allows the solution flow.

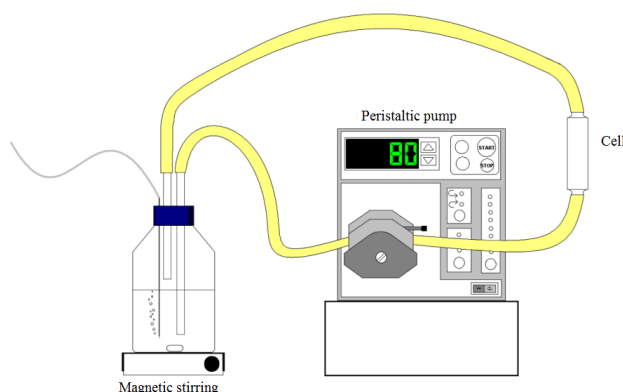


Figure 1.12: Scheme of pump system uses to circulate the solution during irradiation.

Streak-camera: For time resolved absorbance detection in the UV-Vis range, a streak camera Hamamatsu C7700-01 connected to spectrograph Chromex 250IS was used. The sweep time/full screen ranges from 500 ps to 1 ms and the characteristic spectral response is from 250 to 800 nm [40]. Absorption measurements up to 5 μ s are performed using the white light beam of the homemade Xenon flash lamp. For time range greater than 5 μ s, a continuous 300 W Xe lamp is used.

The use of streak camera allows to record the time-resolved spectrum of transient species produced after one electron pulse what is very useful for the identification of radical species involved in a polymerization mechanism. In fact by streak camera

image, it is possible to simultaneously identify the kinetics of produced species and to determine the absorption spectra.

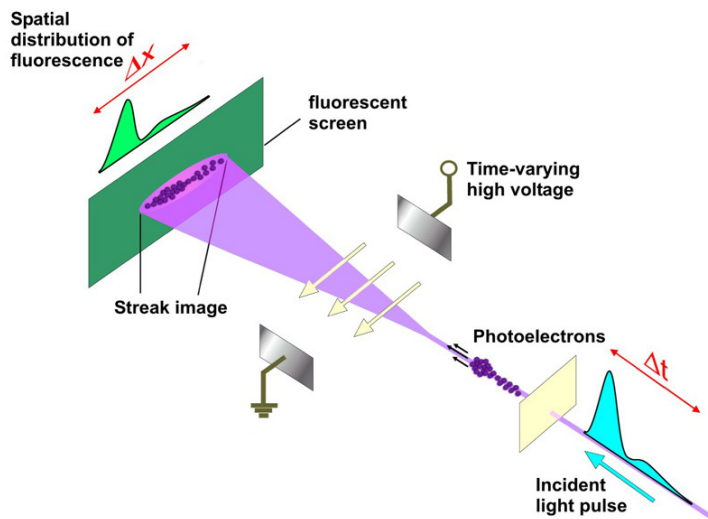


Figure 1.13: Streak camera operating principle. ©MPI for Quantum Optics / Vienna University of Technology

The spectrograph associated with the Streak-camera, has three networks different light sensitivity. The first that we used for measurements carried out in the near infrared from 500 nm to 1000 nm is blazed at 800 nm, the second blazed at 500 nm is intended to be used in the visible range, it goes from 300 nm to 1000 nm; while the last grating (blazed at 300 nm) is much sensitive in the ultraviolet in a range of 230 nm to 1000 nm. During the measurements, we place on the course of the analysis light before entering the spectrograph color filters, avoiding the generation of second order in the networks of the spectrograph.

Operating Principle: The streak camera allows to convert changes in temporal and spatial absorption into an image which shows the brightness distribution. The input light is focused on a photo-cathode and converted into a number of electrons. These latter are accelerated by electrical field and simultaneously they cross between a pair of sweep electrodes which sweep the electrons in the vertical direction from the top to the bottom. Then the photoelectrons are multiplied by a MCP (Multi Channel Plate) and directed to a phosphor screen where they are converted again into light. The intensity of the light emitted by the phosphor is proportional to the intensity of the incident light received at the entrance of the streak tube.

The image produced on the phosphorescent screen is filmed permanently by a CCD camera with a defined frequency; the images are subsequently transferred to a processing computer. The output image corresponds to the evolution of absorption as a function of time into vertical axes and the spectral resolution in horizontal axes. For each record of the streak-camera synchronized with the electron pulse, an image (1024 x 1344 pixels) resolved in time and wavelength (340 nm full screen) is acquired.

Streak camera images analysis

The results of streak camera detection is 2D images with a resolution 1023x1344 pixels (CCD resolution). Each image represents the time evolution of absorption spectrum of species produced during the irradiation.

The final image (Figure 1.14.d) is the composition of four different measurements:

- BASE (or reference): measurements of the intensity of the analyzing light without any irradiation (Figure 1.14.a);
- ABS (absorption): measurements of the intensity of the light during the irradiation of the sample by electron pulses (Figure 1.14.b);
- NOISE: noise of streak-camera is recorded in the absence of any other light signal without electron beam nor analysis light (Figure 1.14.c);
- CERC (Čerenkov): measurement of light of Čerenkov emission, recorded by irradiating the sample without analyzing light (usually it is recorded at short time, this emission causes a deformation of the absorption signal just after the electron pulse).

The optical density is then calculated by equation:

$$OD = \log \frac{BASE - NOISE}{ABS - CER} \quad (1.23a)$$

When it is not necessary to remove the intensity of the Čerenkov light the equation becomes :

$$OD = \log \frac{BASE - NOISE}{ABS - NOISE} \quad (1.23b)$$

In order to get a good signal-to-noise ratio, each acquisition consists of a series of 400 images successively averaged in a unique image. In figure 1.14.d it is shown a typical image resulting from the calculation using the images of Figure 1.14.a,b,c in the equation 1.23b. In this final image each pixels has the value of the absorbance at the corresponding time and wavelength.

After being averaged with Hamamatsu program, all images are exploited by IGOR

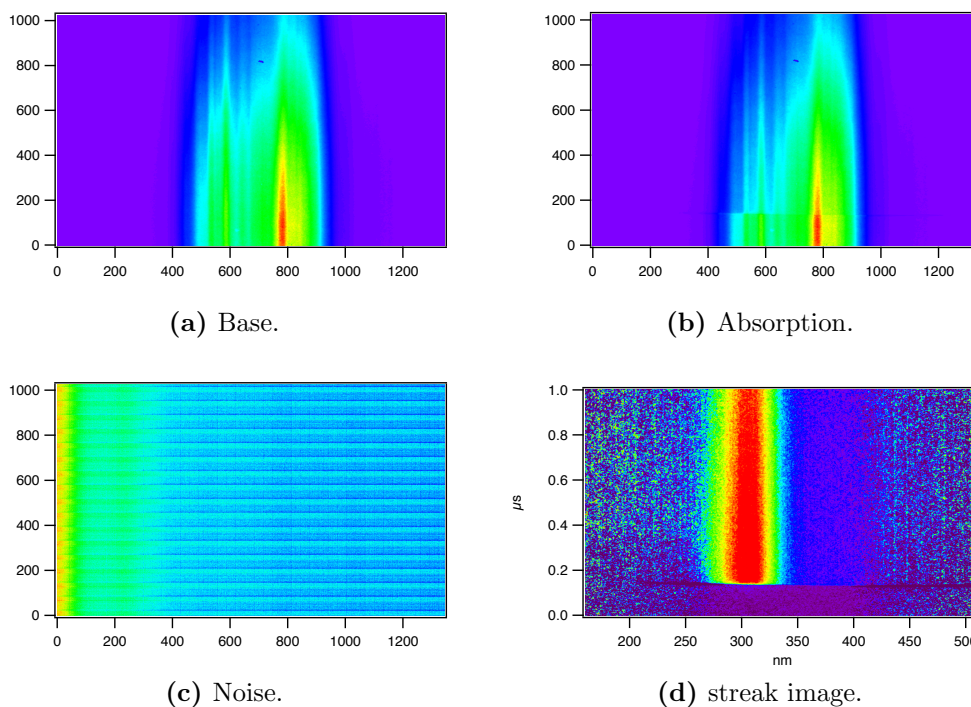


Figure 1.14: Streak images obtained by averaging 400 images: a) Base: analyzing light; b) Absorption: analyzing light during irradiation with electrons; c) Noise of streak camera without irradiation and analyzing light; d) Optical density.

Pro program [41]. IGOR program was improved and adapted by J.L. Marignier for the calculations and treatments of absorption with the streak images (calculation of absorbance, correction of noise, of the variation in the intensity of the analyzing light, of the variation of the position and amplitude of the Cerenkov emission etc...). With the optical density images it is possible to obtain kinetic profiles as well as spectra (Figure 1.15).

By selecting a wavelength, it is possible to follow the kinetics of the species absorbing in this selected wavelength after the irradiation time, (Figure 1.15.a). On the other hand by selecting a given time including in the irradiation time it is possible to obtain the transient absorption spectrum on the whole range of the wavelength recorded at a given time, (Figure 1.15.b).

The reproducibility and the good stability of the measurement is ensured by checking the overlapping of the spectra recorded at the same time with different networks of streak camera, previously introduced.

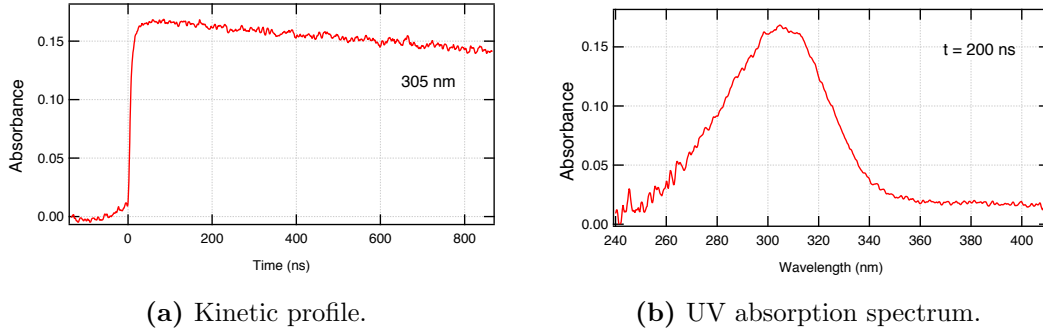


Figure 1.15: Examples of signals obtained from streak camera images by selecting vertical profile (a) or horizontal profile (b).

Dosimetry in pulse radiolysis

In order to calculate the delivered dose at each pulse of irradiation, the measurements of the dose are performed at the beginning of each experiments. Then the absorption of hydrated electron is usually recorded at 5 ns. Indeed, its concentration is directly related to the delivered dose. The Figure 1.16 shows the decreasing profile of hydrated electron over 5 ns at 660 nm obtained by a streak image of water solution irradiated. The dose per pulse was derived from the absorbance of the hydrated electron, e_{hyd}^- , in distilled water at 660 nm at 3 ns using the equation:

$$Dose[eV \cdot mL^{-1}] = \text{Log} \frac{N_a \cdot OD_{660nm,3ns}}{10 \cdot G_{e_{hyd}^-,3ns} \cdot \epsilon_{660nm} \cdot l} \quad (1.24)$$

where:

- N_a is Avogadro's number: $6.023 \cdot 10^{23} \text{ mol}^{-1}$
- $G_{e_{hyd}^-,3ns}$ is radiolytical yield of hydrated electrons at 3 ns: $34 \mu\text{mol J}^{-1}$
- ϵ is the extinction coefficient of e_{hyd}^- at 3 ns and at 660 nm: $18000 \text{ L mol}^{-1} \text{ cm}^{-1}$
- $OD_{660nm,3ns}$ is optical density measured at 660 nm and 3 ns.

If one refers to the example in Figure 1.16, the absorbance at 3 ns is 0.36 so the delivered dose at each pulse is $3.65 \cdot 10^{20} \text{ eV L}^{-1}$. Then $\text{Dose}(\text{Gy}) = 58.5 \text{ Gy}$. From the dose, it is possible to estimate the electron concentration by using the relation:

$$C(\text{mol} \cdot L^{-1}) = D(\text{J} \cdot L^{-1}) \cdot G(\text{mol} \cdot J^{-1}) \quad (1.25)$$

For example, the electron concentration produced at each pulse for the dose of 58,5 Gy

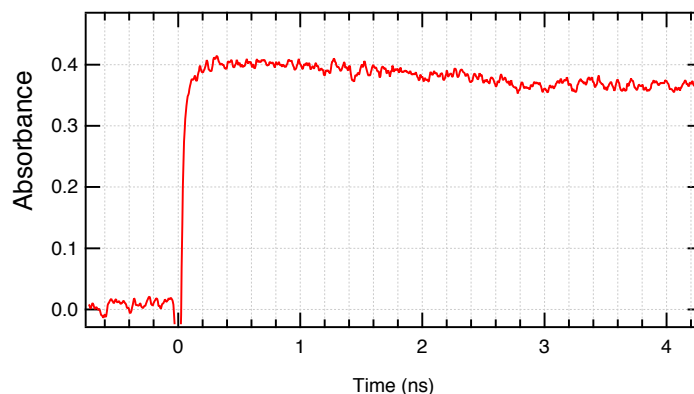


Figure 1.16: Typical kinetic profile of hydrated electron decreasing on 5 ns at 660 nm.

previously calculated :

$$C(M) = 58.5 \text{ J} \cdot \text{L}^{-1} \cdot 34 \text{ } \mu\text{mol} \cdot \text{J}^{-1} = 19.9 \text{ } \mu\text{M} \quad (1.26)$$

this value is then used to estimate the concentration of oxidizing or reducing species produced in a pulse of irradiation.

1.3 Theoretical Methods of analysis

The work presented here was coupled with theoretical studies. Simulations with an open source program, COPASI, was used to study the kinetics of the reaction mechanism.

Other studies more complexe were performed by the theoretical group of the laboratory. The simulations of the absorption spectra of molecules were performed by P. Archirel using DFT (Density Functional Theory) and TD-DFT (Time-dependent Density Functional Theory) methods or quantum chemistry. On the other hand, P. Pernot simulated and analyzed the experimental data by SVD technique. The following sections have the purpose to introduce in a very elementary way the supporting work

1.3.1 COPASI

COPASI [42] is a free software developed by three groups at the Biocomplexity Institute of Virginia Tech, the University of Heidelberg, and the University of Manchester devoted for various applications in biochemistry. We used it for the simulation and analysis of reactions kinetic. It allows to solve mathematical model describing a complex system (differential equation systems). In our study the program was used to simulate the reaction in water radiolysis and describe the oxidation reaction. By setting the growth mechanism equations in homogeneous kinetics conditions, the program describes the variation in the concentration of each species as a function of time. The initial concentration and rate constants are set considering experimental conditions (dose, concentration of monomers, time irradiation) and literature data.

1.3.2 MonteCarlo-TDDFT

Monte-Carlo simulations were first performed to depict the nuclear conformation of the studied molecules. DFT calculation are used to calculate the electronic energies. This approach was already developed in the laboratory to simulate radiolytic species in other systems [43]. Monte-Carlo simulations were done with the Gibbs program [44], electronic quantum 78 calculations with the Gaussian 09 program [45]. The solvent was modeled with the SMD method [46]. No explicit solvent molecules were added to the bare solute. The number of MC steps was currently set to 10000.

Secondly, the absorption spectra were calculated by a convolution of the first 20 TDDFT lines of a short list of configurations, according to the 15 formula of the literature [47]. This short list was built with one configuration out of fifty in the full MC list, after discard of the equilibration period. The convolution was made with gaussians with $fwhm = 0.1$ eV (full width at half maximum).

1.3.3 SVD

Spectrokinetic analysis of the streak camera images was used to identify the number of distinguishable species and candidate reaction mechanisms. The methods and algorithms used had been presented in detail in a review paper by Ruckebusch et al. [48]. The number of species is first estimated by Singular Value Decomposition (SVD) of the image matrix, retaining only the components standing out of the noise. Then, a parsimonious mechanism is proposed accordingly, and a hybrid soft-hard MCR-ALS algorithm is run to obtain the rate constants of the proposed mechanism and the spec-

tra of the candidate species. In this procedure, the kinetics of the transient species are obtained by numerical or analytical integration of the differential equations of the reaction mechanism, while the spectra are obtained as numerical vectors subject only to positivity constraints. This results in smooth kinetics and noisy spectra. Weighted least-squares are used to optimize the kinetic parameters and the spectra. The weight of each data point is the inverse of the local variance of the data, which is estimated on 5x5 image cells as the variance of the residuals of a bi-linear fit of the data. All points in a 5x5 cell get the same weight. The quality of the fit is assessed on the SVD decomposition of the matrix of residuals. The mechanism is updated if necessary. In order to perform a global analysis on the full range of times and wavelengths, streak camera images collected at different time scales and wavelength scales were assembled into a single image. The intensity of individual images was slightly scaled to ensure the continuity of the kinetic traces within each wavelength scale. No wavelength-wise matching was done. All the calculations were made with codes developed in-house in the R environment. Our hybrid MCR-ALS code is adapted from the ALS package , with the solnp constrained least-squares procedure from the Rsolnp package.

1.4 Experimental Methods of investigation

With the aim to check the polymers synthesis and to study the polymers morphology and properties, several microscopies or spectroscopies analysis were done. In this section the used experimental techniques will be presented and the procedures employed to investigate the polymers characteristics will be detailed.

1.4.1 UV-Vis

Ultraviolet-Visible (UV-Vis) spectroscopy was used to spectroscopic investigation of synthesized polymers. The absorption spectra were rerecorded with HP 8543 spectrophotometer in the spectral range from 200 to 1200 nm in the LCP laboratory before and after each experiment. Quartz cells with optical path lengths of 0.2 or 0.1 cm were used. The reference was always distilled water. This technique enables the measurements of the absorbancy, A , of sample which is directly proportional to the concentration, C , of the absorbing species in the solution and the path length, l (in cm), described by Beer-Lambert law :

$$A = \log_{10} \frac{I}{I_0} = \epsilon \ell C \quad (1.27)$$

where I and I_0 are respectively the transmitted and the incident radiation, ϵ is the extinction coefficient, at a given wavelength λ , C is the concentration of the sample and l is the path length (thickness of the sample).

1.4.2 Cryo-TEM

Cryo-transmission-electron microscopy (cryo-TEM) is a type of transmission electron microscopy (TEM) where the sample is studied at cryogenic temperatures. This technique is used to characterize the structure of synthesized polymers directly in solution. The cryo-TEM observations were carried out by J.M. Guignier in Institut de minéralogie, de physique des matériaux et de cosmochimie, University Pierre et Marie Curie (UPMC). The model used is a LaB6 JEOL JEM 2100 (JEOL, Japan) cryo microscope operating at 200 kV with a low dose system (Minimum Dose System, MDS) to protect the thin ice film from any irradiation before imaging and to reduce the irradiation during images capture. This technique ensures the observations of polymers in equilibrium in solution. Thanks to the immediate freezing of the solution. In fact, a drop of each solution is deposited on quantifoils (Quantifoil Micro Tools GmbH, Germany) 200 mesh holey-carbon-coated grids which was immediately plunged into liquid ethane in order to form a thin ice film avoiding water crystallization. The grid is successively transfer in the cryomicroscope and the images are recorded with an Ultrascan 2K CCD camera (Gatan, Pleasanton, CA).

1.4.3 ATR-FTIR

Chemical structures of synthesized polymers were investigated by Attenuated total Reflectance-Fourier transform infrared spectroscopy, ATR-FTIR, spectroscopy. Measurements were performed by Vertex 70 Bruker spectrophotometer. ATR-FTIR spectra were obtained by depositing a drop of solution containing polymers on ZeSe prism and dried at air naturally. The prism is cleaned between each acquisitions by ethanol-water-ethanol. Scanning was conducted from 4000 to 400 cm^{-1} and nominal spectral resolution was 4 cm^{-1} . Each spectrum results from 100 averaged repetitious scans. The reference spectrum was air.

All experiments were performed at Laboratoire de Chimie Physique at Orsay.

1.4.4 SEM

Scanning electron microscopy was used to check the morphology of polymers synthesized by chemical or radiolytical method. The powders obtained after lyophilization were sprinkled onto carbon tape adhered to aluminum mounts and imaged. Magnification, accelerating voltage and scale bar were 5 K X, 150 kV and 1 μm . The SEM observations were carried out using EVO MA 10 ZEISS microscope at Conservatoire National des Arts et M \acute{e} tiers (CNAM, Paris) supplied with SMRT SEM as piloting program. Functioning pressure was 10^{-5} Torr.

1.4.5 AFM and AFM-IR

Topography of different samples was imaged using Atomic Force Microscopy (AFM) operating in tapping mode. AFM is a very powerful technique of microscopy useful to provide information on structure with nanoscale resolution. The AFM has a visible laser focusing on the cantilever and a four quadrants detector measuring its deflection. It is used for the superficial morphology characterization in contact mode. The AFM images were carried out in air at atmospheric pressure. Usually a drop of solution of sample was deposited on ZnSe prism and dried naturally at air.

In the laboratory AFM technique was improved by Alexandre Dazzi by coupling it with nano InfraRed (IR) spectroscopy. The AFM-IR system combines the AFM with a pulsed infrared OPO laser to perform spectro-microscopy. This technique can be used to acquire IR absorption spectra and absorption images with spatial resolution on the 50 to 100 nm scale, versus the scale of many micrometers or more for conventional IR spectroscopy [49].

In AFM-IR measurements, the sample, in our case a drop of solution, is placed onto the upper surface of ZnSe prism (transparent in the mid-IR) and dried naturally at air. Then it is observed by nanoIRTM (@Anasys Instruments). The AFM images are recorded in contact mode as usually. To obtain relevant infrared spectra, the pulsed infrared laser setup covers the wavenumber from 3600 cm^{-1} to 1000 cm^{-1} . During the measurement, the tip of the AFM remained in contact with the object. When the sample absorbs IR laser pulse, the absorbing region warms via the photo-thermal effect and a rapid thermal expansion occurs which then impacts the tip of the AFM cantilever and causes its oscillation. As the amplitude of oscillations is proportional to the absorption, scanning the surface with a given wavenumber enables the drawing of chemical map of the sample, while changing the wavelength on a fixed position of the tip gives a local infrared spectrum [49],[50].

1.4.6 Conductivity test

The radiosynthesized polymers are also characterized by conductivity test in order to compare these materials with chemical or electrochemical synthesized polymers. Generally the powder obtained by lyophilization is dissolved in an acetonitrile solution containing NOBF_4 ($10^{-2} \text{ mol L}^{-1}$) as chemical oxidant. Then, a small drop of acetonitrile solution containing dissolved polymers is deposited on a glass slide and spined at 800 rpm for 60 s. This process is repeated for three times and a spin-coated film is obtained on the glass substrate. The thickness of the spin-coated film is then measured on a 3 Veeco Dektak 150 surface profiler. Finally, the electrical conductivity of the doped polymers film is conducted with a Kelvin four-point probe technique implemented with a Keithley 2420 system. All the measurements of thickness and conductivity were repeated for three times and an average value was calculated. The conductivity, ρ (S cm^{-1}) was then determined using the equation:

$$\rho = \left(\frac{\pi}{\ln(2)} \cdot \frac{V}{I} \cdot t \right)^{-1} \quad (1.28)$$

where V is the voltage difference (V), I is the applied current (A) and t is the thickness (cm).

Bibliography

- [1] Viacheslav Sergeevich Ivanov. *Radiation chemistry of polymers*, volume 5. Vsp, 1992.
- [2] A Chapiro, CH Cousin, Y Landler, and M Magat. Contribution à l'étude des polymérisations amorcées par des rayonnements nucléaires. *Recueil des Travaux Chimiques des Pays-Bas*, 68(11):1037–1068, 1949.
- [3] Francois Tran-Van, Sébastien Garreau, Guy Louarn, Gérard Froyer, and Claude Chevrot. Fully undoped and soluble oligo (3, 4-ethylenedioxythiophene) s: spectroscopic study and electrochemical characterization. *Journal of Materials Chemistry*, 11(5):1378–1382, 2001.
- [4] Jean Roncali, Philippe Blanchard, and Pierre Frère. 3, 4-ethylenedioxythiophene (edot) as a versatile building block for advanced functional π -conjugated systems. *Journal of Materials Chemistry*, 15(16):1589–1610, 2005.
- [5] Qibing Pei, Guido Zuccarello, Markus Ahlskog, and Olle Inganäs. Electrochromic and highly stable poly (3, 4-ethylenedioxythiophene) switches between opaque blue-black and transparent sky blue. *Polymer*, 35(7):1347–1351, 1994.
- [6] Youssef Lattach, Ariane Deniset-Besseau, Jean-Michel Guigner, and Samy Remita. Radiation chemistry as an alternative way for the synthesis of pedot conducting polymers under soft conditions. *Radiation Physics and Chemistry*, 82:44–53, 2013.
- [7] Robert M Silverstein, Francis X Webster, David J Kiemle, and David L Bryce. *Spectrometric identification of organic compounds*. John Wiley & Sons, 2014.
- [8] FMC Corporation.
- [9] LH Gevantman. Solubility of selected gases in water. *Nitric oxide (NO)*, 308(3.348):10–4, 2000.
- [10] Nina Ni, Marc Tesconi, S Esmail Tabibi, Shanker Gupta, and Samuel H Yalkowsky. Use of pure t-butanol as a solvent for freeze-drying: a case study. *International journal of pharmaceuticals*, 226(1):39–46, 2001.
- [11] WC Röntgen. Sur une nouvelle sorte de rayons. *trad. de Über eine neue Art von Strahlen*). *Comptes-rendus des réunions de la Société physico-médicale de Würzburg*, page 4, 1895.

- [12] GV Buxton. The radiation chemistry of liquid water: Principles and applications. *Charged Particle and Photon Interactions with Matter. Chemical, Physicochemical, and Biological Consequences with Applications*, pages 331–363, 2004.
- [13] Sophie Le Caer. Water radiolysis: influence of oxide surfaces on h₂ production under ionizing radiation. *Water*, 3(1):235–253, 2011.
- [14] George V Buxton, Clive L Greenstock, W Phillips Helman, and Alberta B Ross. Critical review of rate constants for reactions of hydrated electrons, hydrogen atoms and hydroxyl radicals (OH· / O·⁻ in aqueous solution. *Journal of physical and chemical reference data*, 17(2):513–886, 1988.
- [15] Leon M Dorfman and Gerald E Adams. Reactivity of the hydroxyl radical in aqueous solutions. Technical report, DTIC Document, 1973.
- [16] MS Alam and E Janata. UV absorption spectrum, formation and disappearance of the oxide radical ion O⁻ in aqueous solution: A pulse radiolysis study. *Chemical physics letters*, 417(4):363–366, 2006.
- [17] Pedatsur Neta, Robert E Huie, and Alberta B Ross. Rate constants for reactions of inorganic radicals in aqueous solution. *Journal of Physical and Chemical Reference Data*, 17(3):1027–1284, 1988.
- [18] Robert E Huie, Carol L Clifton, and Pedatsur Neta. Electron transfer reaction rates and equilibria of the carbonate and sulfate radical anions. *International Journal of Radiation Applications and Instrumentation. Part C. Radiation Physics and Chemistry*, 38(5):477–481, 1991.
- [19] Shahla Gondal, Naveed Asif, Hallvard F Svendsen, and Hanna Knuutila. Density and N₂O solubility of aqueous hydroxide and carbonate solutions in the temperature range from 25 to 80 °C. *Chemical Engineering Science*, 122:307–320, 2015.
- [20] Haruo Hikita, Satoru Asai, Haruo Ishikawa, and Naoki Esaka. Solubility of nitrous oxide in sodium carbonate-sodium bicarbonate solutions at 25. deg. and 1 atm. *Journal of Chemical and Engineering Data*, 19(1):89–92, 1974.
- [21] James L Weeks and Joseph Rabani. The pulse radiolysis of deaerated aqueous carbonate solutions. *I. Transient Optical Spectrum and Mechanism. II pk for OH radicals.* *The Journal of Physical Chemistry*, 70(7):2100–2106, 1966.

- [22] Zeev B Alfassi and Robert H Schuler. Reaction of azide radicals with aromatic compounds. Azide as a selective oxidant. *The Journal of Physical Chemistry*, 89(15):3359–3363, 1985.
- [23] Wayne K Wilmarth, David M Stanbury, James E Byrd, Henry N Po, and Chee-Peng Chua. Electron-transfer reactions involving simple free radicals. *Coordination Chemistry Reviews*, 51(2):155–179, 1983.
- [24] MS Ram and David M Stanbury. Reduction potential of the trinitrogen radical as determined by chemical kinetics: novel application of spin trapping. *Inorganic chemistry*, 24(25):4233–4234, 1985.
- [25] GT Ruiz, MP Juliarena, E Wolcan, and G Ferraudi. Kinetic and spectroscopic observations on the azidyl, N_3 radical oxidation of fac-($L_{spectator}$) $Re^I(CO)_3(L_{acceptor})$ to fac-($L_{spectator}$) $Re^{II}(CO)_3(L_{acceptor})$, $L_{spectator} = 4, 4$ -bpy; $L_{acceptor} =$ dipyridyl [3,2-a: 2'3'-c] phenazine or $L_{spectator} = Cl^-$; $L_{acceptor} =$ bathocuproindisulfonate: A revisit to the self-exchange rate constants of the N_3 / N_3^- and $Re(II)/Re(I)$ couples and to the redox potential of the N_3 radical. *Inorganica Chimica Acta*, 360(12):3681–3687, 2007.
- [26] John Butler, Edward J Land, A John Swallow, and Walter Prutz. The azide radical and its reaction with tryptophan and tyrosine. *Radiation Physics and Chemistry (1977)*, 23(1-2):265–270, 1984.
- [27] Mark S Workentin, Brian D Wagner, Janusz Luszyk, and Danial DM Wayner. Azidyl radical reactivity. N_3^- as a kinetic probe for the addition reactions of azidyl radicals with olefins. *Journal of the American Chemical Society*, 117(1):119–126, 1995.
- [28] Magnus Von Piechowski, Marie-Anne Thelen, JüRg Hoigné, and Rolf E Bühler. tert-Butanol as an OH-scavenger in the pulse radiolysis of oxygenated aqueous systems. *Berichte der Bunsengesellschaft für physikalische Chemie*, 96(10):1448–1454, 1992.
- [29] IM Kolthoff, EJ Meehan, and EM Carr. Mechanism of initiation of emulsion polymerization by persulfate. *Journal of the American Chemical Society*, 75(6):1439–1441, 1953.
- [30] Nophawan Paradee and Anuvat Sirivat. Synthesis of poly (3, 4-ethylenedioxythiophene) nanoparticles via chemical oxidation polymerization. *Polymer International*, 63(1):106–113, 2014.

- [31] Shewei Yang, Jianhua Cheng, Jian Sun, Yongyou Hu, and Xiaoyan Liang. Defluorination of aqueous perfluorooctanesulfonate by activated persulfate oxidation. *PloS one*, 8(10):e74877, 2013.
- [32] Kun-Chang Huang, Richard A Couttenye, and George E Hoag. Kinetics of heat-assisted persulfate oxidation of methyl tert-butyl ether (mtbe). *Chemosphere*, 49(4):413–420, 2002.
- [33] Olga Pyshkina, Aleksejs Kubarkov, and Vladimir Sergeyev. Poly (3, 4-ethylenedioxythiophene): synthesis and properties. *Materials Sciences and Applied Chemistry*, pages 51–54, 2010.
- [34] Yang Deng and Casey M Ezyske. Sulfate radical-advanced oxidation process (SR-AOP) for simultaneous removal of refractory organic contaminants and ammonia in landfill leachate. *Water research*, 45(18):6189–6194, 2011.
- [35] Justine Criquet and Nathalie Karpel Vel Leitner. Electron beam irradiation of aqueous solution of persulfate ions. *Chemical Engineering Journal*, 169(1):258–262, 2011.
- [36] Gertraud Mark, Man Nien Schuchmann, Heinz-Peter Schuchmann, and Clemens von Sonntag. The photolysis of potassium peroxodisulphate in aqueous solution in the presence of tert-butanol: a simple actinometer for 254 nm radiation. *Journal of Photochemistry and Photobiology A: Chemistry*, 55(2):157–168, 1990.
- [37] KI Seo and IJ Chung. Reaction analysis of 3, 4-ethylenedioxythiophene with potassium persulfate in aqueous solution by using a calorimeter. *Polymer*, 41(12):4491–4499, 2000.
- [38] Y Tang, RP Thorn, RL Mauldin, and PH Wine. Kinetics and spectroscopy of the SO_4^- radical in aqueous solution. *Journal of Photochemistry and Photobiology A: Chemistry*, 44(3):243–258, 1988.
- [39] Jacqueline Belloni, Hugues Monard, Fabrice Gobert, J-P Larbre, Alexandre Demarque, Vincent De Waele, Isabelle Lampre, J-L Marignier, Mehran Mostafavi, Jean-Claude Bourdon, et al. Elysea picosecond electron accelerator for pulse radiolysis research. *Nuclear Instruments and Methods in Physics Research Section A: Accelerators, Spectrometers, Detectors and Associated Equipment*, 539(3):527–539, 2005.

- [40] J-L Marignier, V De Waele, H Monard, F Gobert, J-P Larbre, A Demarque, M Mostafavi, and J Belloni. Time-resolved spectroscopy at the picosecond laser-triggered electron accelerator elyse. *Radiation Physics and Chemistry*, 75(9):1024–1033, 2006.
- [41] <https://www.wavemetrics.com>.
- [42] <http://copasi.org/>.
- [43] Jun Ma, Pierre Archirel, Uli Schmidhammer, Jean-Marie Teuler, Pascal Pernot, and Mehran Mostafavi. Reduction of earth alkaline metal salts in thf solution studied by picosecond pulse radiolysis. *The Journal of Physical Chemistry A*, 117(51):14048–14055, 2013.
- [44] Philippe Ungerer, Bernard Tavitian, and Anne Boutin. *Applications of molecular simulation in the oil and gas industry: Monte Carlo methods*. Editions Technip, 2005.
- [45] MJ Frisch, GW Trucks, HB Schlegel, GE Scuseria, MA Robb, JR Cheeseman, JA Montgomery Jr, TKKN Vreven, KN Kudin, JC Burant, et al. Gaussian 03, revision c. 02; gaussian, inc.: Wallingford, ct, 2004. *There is no corresponding record for this reference*, 2013.
- [46] Aleksandr V Marenich, Christopher J Cramer, and Donald G Truhlar. Universal solvation model based on solute electron density and on a continuum model of the solvent defined by the bulk dielectric constant and atomic surface tensions. *The Journal of Physical Chemistry B*, 113(18):6378–6396, 2009.
- [47] ABP Lever and SI Gorelsky. Ruthenium complexes of non-innocent ligands: Aspects of charge transfer spectroscopy. In *Optical Spectra and Chemical Bonding in Transition Metal Complexes*, pages 77–114. Springer, 2004.
- [48] C Ruckebusch, M Sliwa, P Pernot, A De Juan, and R Tauler. Comprehensive data analysis of femtosecond transient absorption spectra: A review. *Journal of Photochemistry and Photobiology C: Photochemistry Reviews*, 13(1):1–27, 2012.
- [49] Alexandre Dazzi, Craig B Prater, Qichi Hu, D Bruce Chase, John F Rabolt, and Curtis Marcott. AFM-IR: combining atomic force microscopy and infrared spectroscopy for nanoscale chemical characterization. *Applied spectroscopy*, 66(12):1365–1384, 2012.

- [50] A Dazzi, R Prazeres, F Glotin, and JM Ortega. Local infrared microspectroscopy with subwavelength spatial resolution with an atomic force microscope tip used as a photothermal sensor. *Optics letters*, 30(18):2388–2390, 2005.

Chapter 2

HO \cdot -induced EDOT polymerization

Firstly we were interesting to study the polymerization of ethylenedioxythiophene, EDOT, into PEDOT, poly (3,4- ethylenedioxythiophene). In literature two mechanisms of polymerization are usually proposed: chain mechanism [1, 2], evoked to describe EDOT polymerization mainly in the chemical synthesis and the step-by-step mechanism [3, 4], currently proposed in electrochemical synthesis. This last involves the formation of cation radical EDOT \cdot^+ which reacts with itself to form dimer following to a deprotonation, and again a new oxydation of dimers which leads to a chain length increase following to a deprotonation, as so on.

In previous studies [5, 6], our group depicted a new strategy to synthesize PEDOT in aqueous solutions by using γ -ionizing radiation either under air or N₂O atmosphere. It was indirectly demonstrated that a step-by-step mechanism is involved during PEDOT radiolytical polymerization. Moreover by using two different oxidant radicals (HO \cdot and N₃ \cdot), it was possible to oxidize EDOT monomers into PEDOT polymers of two different morphologies (PEDOT–OH) and (PEDOT–N₃). The SEM images in Figure 2.1 indicate the presence of very close-packed spheroid polymeric particles in the case of hydroxyl oxidation (PEDOT–OH) or lamellar (platelike) structures in the case of azide oxidation (PEDOT–N₃). This remarkable difference between these two kinds of polymers was explained by the difference that exists between the oxidizing behaviors of HO \cdot and N₃ \cdot radicals.

In this study here presented, the pulse radiolysis was used to investigate the oxidation mechanism of EDOT by following the time evolution of absorption spectra of transient species formed in the UV-Vis range from ns to ms. The first oxidant used

to initiate the polymerization was the hydroxyl radical, HO[•], produced directly from water radiolysis. The reactivity of this radical has already been studied by pulsed ra-

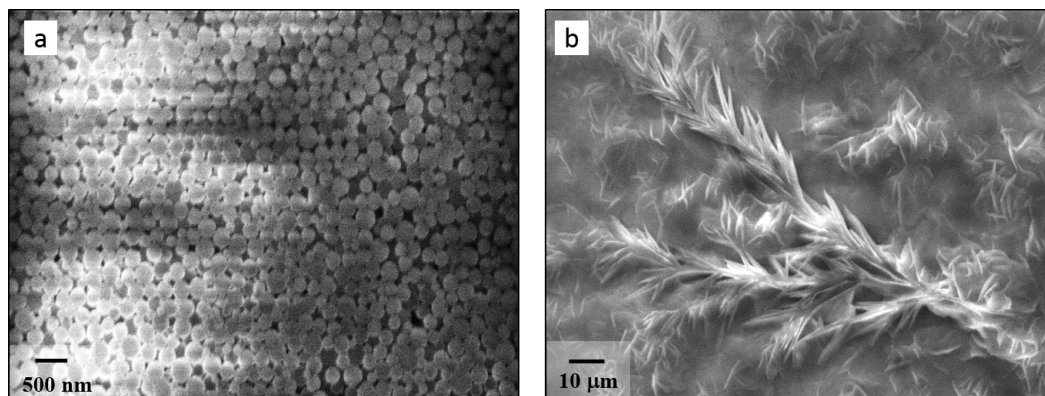


Figure 2.1: SEM images of PEDOT polymers after deposition onto gold substrates obtained by irradiation at 70 kGy: **a** (PEDOT–OH); **b** (PEDOT–N₃).

diolysis of thiophene (Th) molecules (from which EDOT derives) [7, 8, 9]. It has been found that HO[•] radical adds preferentially to the α position in Th molecule, leading to a short-lived hydroxythienyl (Th–OH)[•] radical. This latter, subsequently, undergoes a second order radical reaction with itself to produce α - α' -bithiophene. In this first section, we will study the reaction of hydroxyl radical onto EDOT monomer and compare it with literature Th molecule. With the aim to understand the pH effect on the first steps of polymerization and to check the reactivity of oxide radical (O^{•-}) predominant at high pH ($\text{pK}_a(\text{HO}^\bullet/\text{O}^{\bullet-}) = 11.9$), alkaline solutions were also investigated. Indeed in the previous mentioned Saunders's studies [8, 9], the products of the reaction between the thiophene molecule and oxide radical was also investigated in alkaline solution. It was found that the action of oxide radicals onto thiophene induces the opening of the thiohene ring. This effect inhibits the polymerization. So it is clear that the action of pH can play a fundamental role in the mechanism of the growth of the polymer.

Successively a first study on reduction of EDOT was also approached by using hydrated electron produced in water radiolysis.

The last part of this chapter will introduce a new method to synthesize PEDOT by using the electron beam, previously used in pulse radiolysis study, as a simple electron irradiation, showing the advantages implicated in the use of this methodology.

2.1 EDOT oxidation

2.1.1 Hydroxyl radical reactivity

The EDOT oxidation was firstly investigated in the simplest system. The reaction between hydroxyl radical and EDOT monomer was examined. In literature hydroxyl radical is well known to form HO-adduct radicals onto C=C double bonds [8, 9, 10, 11] but it is also known to abstract either hydrogen atoms or electrons leading to neutral radicals or to cation radicals respectively.

Generally starting from EDOT monomer, the formation of three kinds of radicals is possible: EDOT–OH \cdot adduct, EDOT \cdot radical and EDOT \cdot^+ cation radical. The last one is often proposed in literature as the first radical involved in electrochemical synthesis of PEDOT [1, 12] but no experimental evidence is given. The aim of this part of the work is to identify which radical takes place in the radiolytical mechanism of the PEDOT polymerization. A N $_2$ O-saturated aqueous solution at different concentrations (1, 5 and 10 mM) of EDOT was irradiated in the time range from 100 ns to 1 ms. We will present here the results which concern the solution containing 1 mM in EDOT saturated with N $_2$ O at pH = 8. Some remarks about the effect of concentration will be discussed at the end of the section. A volume of 200 mL of EDOT solution was placed in the reservoir connected to the flow cell. The solution circulated with a flow rate of 100 mL/min and was irradiated by the pulsed electron beam with a dose of 37 Gy per pulse. In this system the oxidants species is the hydroxyl radical produced directly from water radiolysis and the hydroxyl radical produced efficiently by reaction of hydrated electron with the scavenger N $_2$ O (see chapter 1). In Figure 2.2 the absorption spectrum and the decay of electron are depicted.

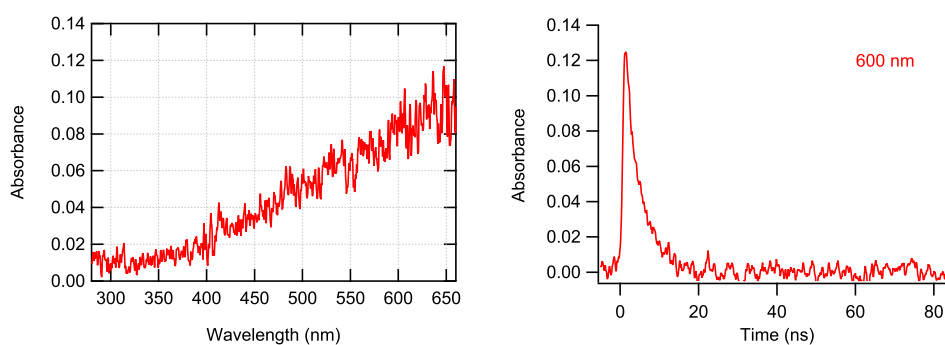


Figure 2.2: Absorption spectrum of electron on the first 20 ns (on the left) and electron decay on 100 ns (on the right) recorded in an aqueous solution containing 1 mM in EDOT under N $_2$ O atmosphere (Dose = 37 Gy/pulse, optical path = 1 cm).

It is possible to observe that it reacts very fast and in 20 ns it is completely converted in hydroxyl radical which absorbs in the UV region, (then not visible in our experiment). The streak-camera image in the Figure 2.3.a depicts the evolution with time of the transient absorption spectrum recorded in the solution during the first 800 ns after the electron pulse.

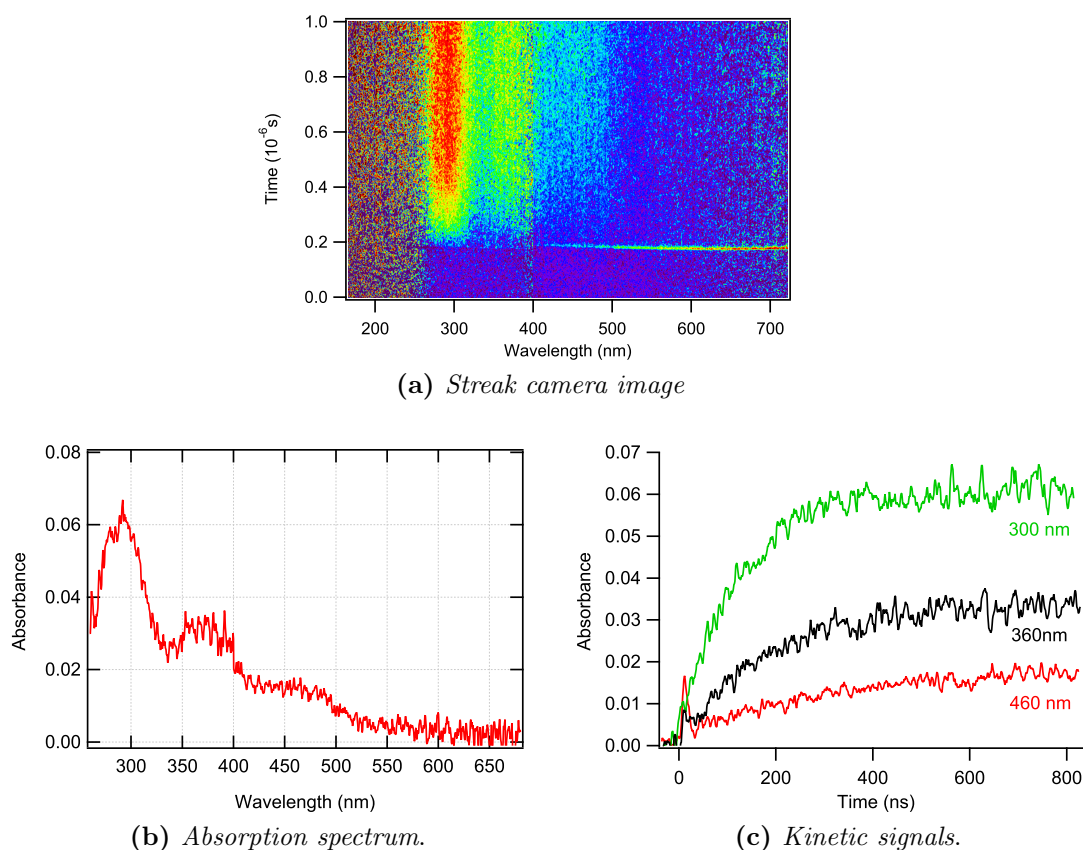


Figure 2.3: a) Streak-camera image in the first 1 μ s after the pulse obtained by pulse radiolysis of an aqueous solution containing 1 mM in EDOT under N₂O atmosphere; b) transient absorption spectrum at 800 ns after the electron pulse and c) time evolution of the absorbances at 300, 360 and 460 nm (Dose 37 Gy/pulse, Optical path = 1 cm).

The horizontal profile at 800 ns on this image shows the first absorption spectrum characterized by three peaks absorbing at 300, 360 and 460 nm, in Figure 2.3.b. This spectrum should correspond to the first transient species produced through oxidation of EDOT by hydroxyl radical. The time evolution of the three absorption maxima is displayed on Figure 2.3.c, where the kinetic profiles are recorded up to 800 ns.

Each of these kinetic profiles is fitted well by a pseudo-first order kinetics but

with different values of the rate constants. In fact, the increase at 300 nm is the fastest, showing a quite rapid formation during 400 ns, then it remains constant around its maximum till 800 ns. Differently, the two other bands at 360 nm and 460 nm demonstrate a continuous growth which is not over after 1 μ s. Moreover these signals are affected by the presence of fast electron decay on the first 20 ns.

At this stage of the study, it is not possible to distinguish how many species are really involved in the absorption spectrum. However a test of pseudo-first order describes well all kinetics and it allows to estimate the order of magnitude of the rate constants $k \simeq 10^9 \text{ M}^{-1}\text{s}^{-1}$.

When longer time ranges, as well as at 5 μ s, are investigated, a substantial difference between kinetic signals is observed. In Figure 2.4 the three kinetics profiles at 300, 360 and 460 nm are shown, depicting the difference in the evolution of absorptions. This suggests that there are almost two transient species involved on μ s time range.

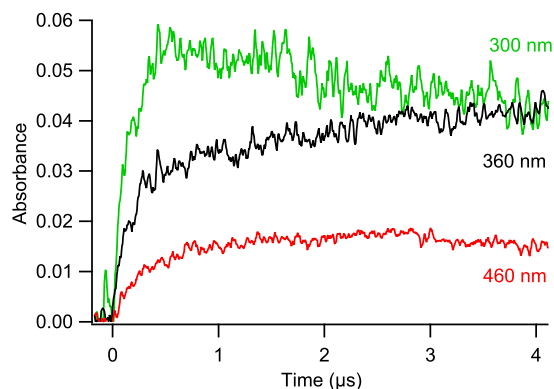


Figure 2.4: Kinetic evolution of the three absorbances at 300, 360 and 460 nm on 5 μ s after the pulse obtained by pulse radiolysis of an aqueous solution containing 1 mM in EDOT under N_2O atmosphere (Dose 37 Gy/pulse, Optical path = 1 cm).

At 50 μ s and 200 μ s the peak at 460 nm is decreasing and it is completely disappeared on 1 ms (profile not shown). On the contrary the bands at 300 nm and 360 nm decay on 200 μ s but this decrease is followed by the increase of two peaks at the same, or very near, wavelengths. Figure 2.5 shows the kinetic signal of the peak absorbing at 300 nm on 200 μ s.

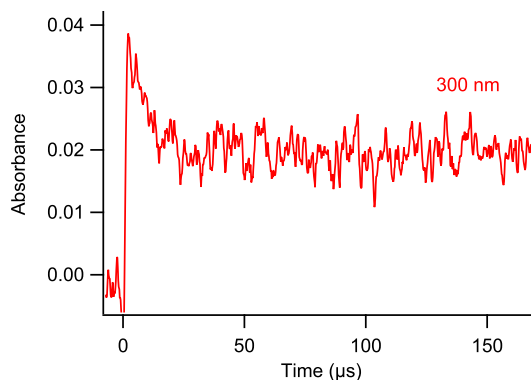


Figure 2.5: Kinetic evolution of the three absorbances at 300 nm showing the existence of two different kinetics at the same wavelength

This signal is a combination of two components: a decay on 30 μs and a growth on around the same time scale. The decomposition of the two signals is not so obvious without knowing at least one of the two rate constants of consumption or formation of the species absorbing in this wavelength.

Finally the transient spectrum recorded at 800 μs after the pulse (Figure 2.6) shows the formation of species characterized by two stable peaks at 290 and 360 nm.

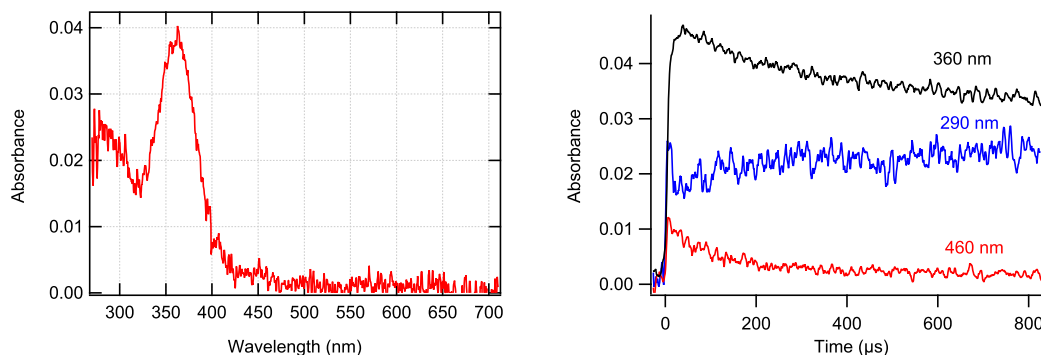


Figure 2.6: Absorption spectrum (on the left) at 800 μs after the pulse and time evolution of the absorbances at 290, 360 and 460 nm (on the right) of an aqueous solution containing 1 mM in EDOT saturated with N₂O. (Dose=37 Gy/pulse Optical path =1 cm)

This species is a stable product formed after a one-pulse irradiation. Indeed, in static UV-Vis absorption spectroscopy, the spectrum, recorded some hours after the pulse radiolysis experiments shows two bands at 290 and 360 nm, (Figure 2.7).

One can note that the absorption intensity of the two peaks intensity appears inverted compared with the transient spectrum of Figure 2.7. This is probably due to the evolution of solution after the experiment. It can be supposed that some agglomeration of dimers or small oligomers are formed in the solution at longer timescale.

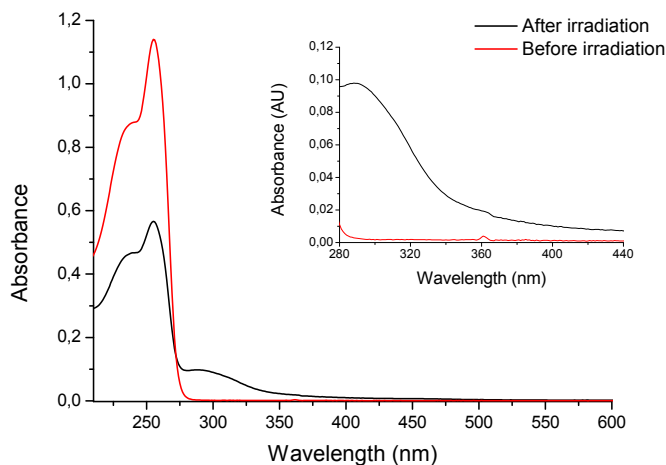


Figure 2.7: Stable absorption spectrum of an aqueous solution containing 1 mM in EDOT saturated with N_2O at $pH = 8$ before (—) and after pulse radiolysis (—) (Optical path= 0.2 cm; reference = water). Inset: zoom of spectrum between 280 and 440 nm.

At wavelength under 275 nm in Figure 2.7, the absorbance after irradiation is mainly due to the absorption of EDOT monomers which have not been consumed during the pulse radiolysis experiments. In fact it is important to remark that even if 200 mL of solution were used during experiment, only around 100 μL are really irradiated by each electron pulse before being diluted in the stock solution due to the close circuit circulation of the solution. This implies that the irradiation products are very diluted by a factor of around 2000 in the solution. Then the spectrum of the Figure 2.7 corresponds to the results solution after pulse radiolysis experiment.

Theoretical investigation

In order to determine the mechanism of EDOT oxidation by hydroxyl radical, HO^\bullet , and to identify the species involved in the mechanism, a collaboration with theoretical group (Theosim) of the Laboratoire de Chimie Physique was initiated.

Identification of plausible mechanism schemes

Spectrokinetic analysis of the streak camera images has been done to identify the number of distinguishable species and a candidate reaction mechanism. In order to perform a global analysis on the full range of times and wavelengths, streak camera images collected at different time scales (from 100 ns to 1 ms) and wavelength scales (280-398 and 400-500 nm) of the same solution previously detailed (see section 2.1) have been assembled into a single image (Figure 2.8.a).

The intensity of individual images has been slightly scaled to ensure the continuity of the kinetic traces within each wavelength scale. No wavelength-wise matching has been done. The data analysis methods used here have been presented in detail in a review paper by Ruckebusch et al. [13].

This obtained image was used for global analysis. The SVD analysis of this image shows that the spectrokinetic matrix can be factored into three components. The best fit of the image obtained by three components model is shown in Figure 2.8.b. Two different mechanisms both involving, in addition to EDOT, three supplementary (X, Y and Z) species can provide similar best fit images. The spectra of the unknown X, Y and Z species involved in both mechanisms (Figure 2.8.c and Figure 2.8.e) are strongly overlapping, and their kinetics are presented in Figure 2.8.d and Figure 2.8.f. The strong overlap found here, which we also already observed and evoked in the previous experimental section, makes necessary the use of a spectrokinetic analysis method to untangle the experimental data. Note that the shapes of the spectra of X, Y and Z species recovered for both mechanisms differ mostly by the relative peak intensities; the peak positions remain identical for all species.

The first mechanism (Scheme 1) involves the following reactions:



The first reaction follows a pseudo-first order kinetics since the amount of EDOT molecules is in excess in comparison with that of hydroxyl radicals. Note that in this mechanistic scheme, the second reaction follows a second order kinetics, while the third one is a first or a pseudo-first order reaction.

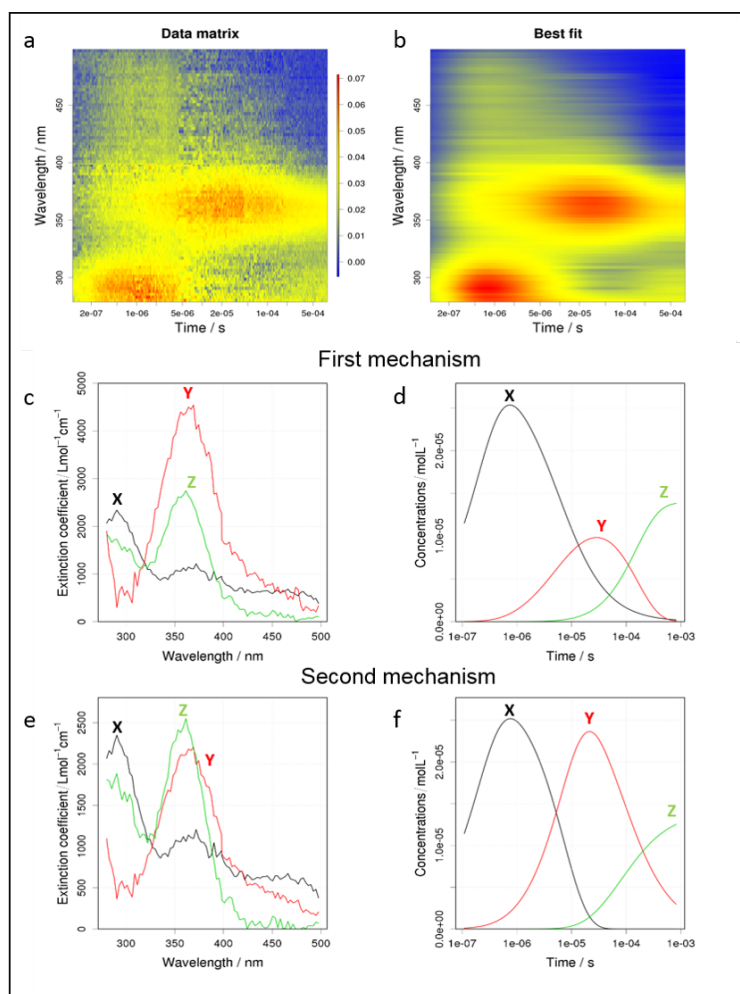


Figure 2.8: Kinetic analysis of the experimental spectrokinetic matrix (a) with a three-species model (see text): (b) image of the best-fit model; (c) best-fit spectra of the first model scheme; (d) best fit concentrations for the first model scheme. (e) best-fit spectra of the second model scheme; (f) best fit concentrations for the second model scheme. Each spectrum is associated with a concentration profile according to the color code.

In the second mechanism (Scheme 2), the successive reactions are as follows:



First reaction is the same into the two schemes. Nevertheless here, the second reaction

follows a first or a pseudo-first order kinetics, while the third one is a second order reaction.

From this analysis, we can conclude that in pulsed radiolysis of EDOT, two mechanistic schemes are plausible. In both schemes, the first and second species (X and Y respectively) are transient species which disappear within 1 ms. The first species, X, which absorbs at 300, 360 and 460 nm is formed in the μs timescale. Then, in less than 100 μs , X leads to the second species, Y, which absorbs at 360 nm. Finally, Y disappears at the ms timescale to form the third stable species, Z, which absorbs at 290 and 360 nm. This last species is the one we detected by pulsed radiolysis 1 ms after the pulse and which remains observable over a relatively long time after the end of the experiments by static UV-Vis absorption spectroscopy.

Computational study of the relevant species

The next step was to identify, thanks to computational chemistry, the unknown X, Y and Z species involved in the mechanism of EDOT oxidation and obtained by spectral deconvolution. In both schemes (Scheme 1 and 2), the first reaction involves the reaction of EDOT with hydroxyl radical. So the first transient species, X, should be one of the following species: EDOT-OH[•] adduct, EDOT[•] neutral radical or EDOT^{•+} cation radical. Then, taking into account that the disappearance of X leads to Y according to a monomolecular or bimolecular reaction and taking into account that Z is obtained from the first or second-order decay of Y, we considered all species which could be potentially produced according to Schemes 1 and 2. The structures, formula and current names of the species investigated are reported in Table 2.1.

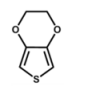
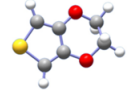

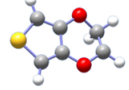
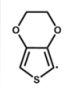
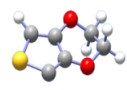
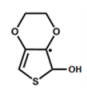
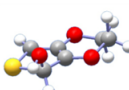
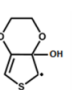
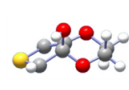
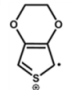
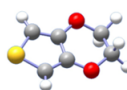
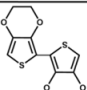
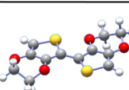
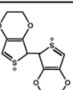
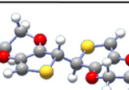
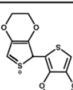
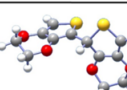
EDOT			EDOT _o			EDOT _s		
(EDOT-OH) [•] _s			(EDOT-OH) [•] _o			EDOT ^{•+}		
EDOT ₂			EDOT ₂ ²⁺			EDOT ₂ ^{•+}		

Table 2.1: Names, formula and chemical structures of all molecules of interest.

The usual notation found in literature is used in the text. However it should be noted that it suffers from some ambiguities: in particular EDOT monomer and its cation radical EDOT^+ differ by one electron, whereas EDOT_2 dimer and its radical cations EDOT_2^+ and EDOT_2^{2+} differ by one and two protons respectively. We checked that ionization of EDOT molecule removes an electron from the HOMO, which is a π orbital, mainly localized on both the carbon atoms in α -position of the S atom. Consequently, in EDOT^+ , the S atom bears a positive charge (+0,74) as can be seen in Table 2.1. On another hand, we considered two EDOT^\cdot radicals, noted $\text{EDOT}_\text{O}^\cdot$ and $\text{EDOT}_\text{S}^\cdot$, since two different H atoms, differently located in the EDOT molecule (in α -position of O atom or in α -position of S atom), can be abstracted by an hydroxyl radical. In the same way, we took into account the possible formation of two different adduct radicals: $(\text{EDOT-OH})_\text{S}^\cdot$ and $(\text{EDOT-OH})_\text{O}^\cdot$.

To identify the unknown X, Y and Z species, we decided to simulate the absorption spectra of the species displayed in Table 2.1 and then to compare them to the absorption spectra of X, Y and Z found by spectrokinetic analysis. Before the extensive application of our simulation method, we established its relevancy in the following way: we first compared our simulation possibilities for the EDOT molecule, for which the experimental spectrum is well known. We then investigated the issue of the EDOT^+ cation radical for which ordinary DFT calculations are doubtful.

Absorption spectrum of EDOT molecule

The absorption spectrum of EDOT is well known [5]. It is characterized by two absorption maxima at 235 and 255 nm with the following extinction coefficients: $\epsilon_{235} = 5650 \text{ L mol}^{-1} \text{ cm}^{-1}$ and $\epsilon_{255} = 7048 \text{ L mol}^{-1} \text{ cm}^{-1}$. We compared several simulation methods on the case of EDOT molecule (see Table A.1 in Annex A) and the best Monte-Carlo spectrum is shown in Figure 2.9.

For an easier comparison we made a fit of the recorded spectrum with three gaussians: the corresponding absorption wavelengths and molar extinction coefficients are given in Table A.1. The overestimation of the extinction coefficient is due to the used simulation method and it is detailed in the annex A.

Considering these issues, we adopted the following simulation method: we chose the Monte Carlo method at the B3LYP/cc-pvdz level with 10000 MC steps, and the spectra at the B3LYP/aug-cc-pvdz level. We calculated in this way the spectra of all the closed shell species of Table 2.1, namely EDOT monomer and all dimers: EDOT_2 , EDOT_2^+ and EDOT_2^{2+} . These spectra are gathered in Figure 2.10.

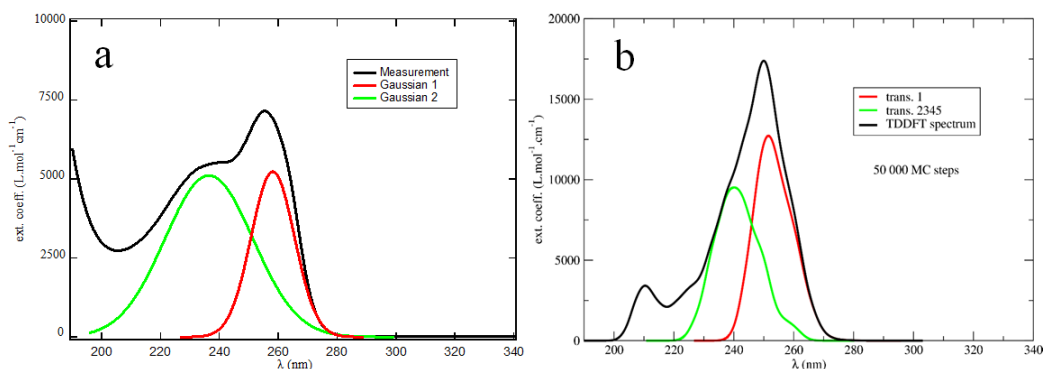


Figure 2.9: Absorption spectra of EDOT molecule: (a) experimental spectrum in aqueous solution (with a Gaussian fit) and (b) calculated spectrum with a MC simulation at the B3LYP/cc-pvdz level.

Absorption spectra of open shell radicals

Many of the radiolytic species of interest in the present work are doublet open shells, like EDOT^{•+} radical cations, EDOT–OH[•] adducts and EDOT[•] neutral radicals, with an H atom removed. In Figure 2.10 we gathered the spectra of five open shell species of present interest. It can be seen that:

1. for EDOT^{•+} cation radical, the spin screening dramatically modifies the crude TDDFT spectrum
2. this is also the case for the two neutral radicals EDOT_O[•] and EDOT_S[•], and for the (EDOT–OH)_O[•] adduct
3. on the other hand, the spin screening leaves the spectrum of the (EDOT–OH)_S[•] adduct almost invariant, at least in the low energy zone.

The results of the spin screening procedure obviously depends on the value of the threshold. In Figure 2.10 we used the value 0.9 because the extinction coefficients are larger and the absorption spectra more visible.

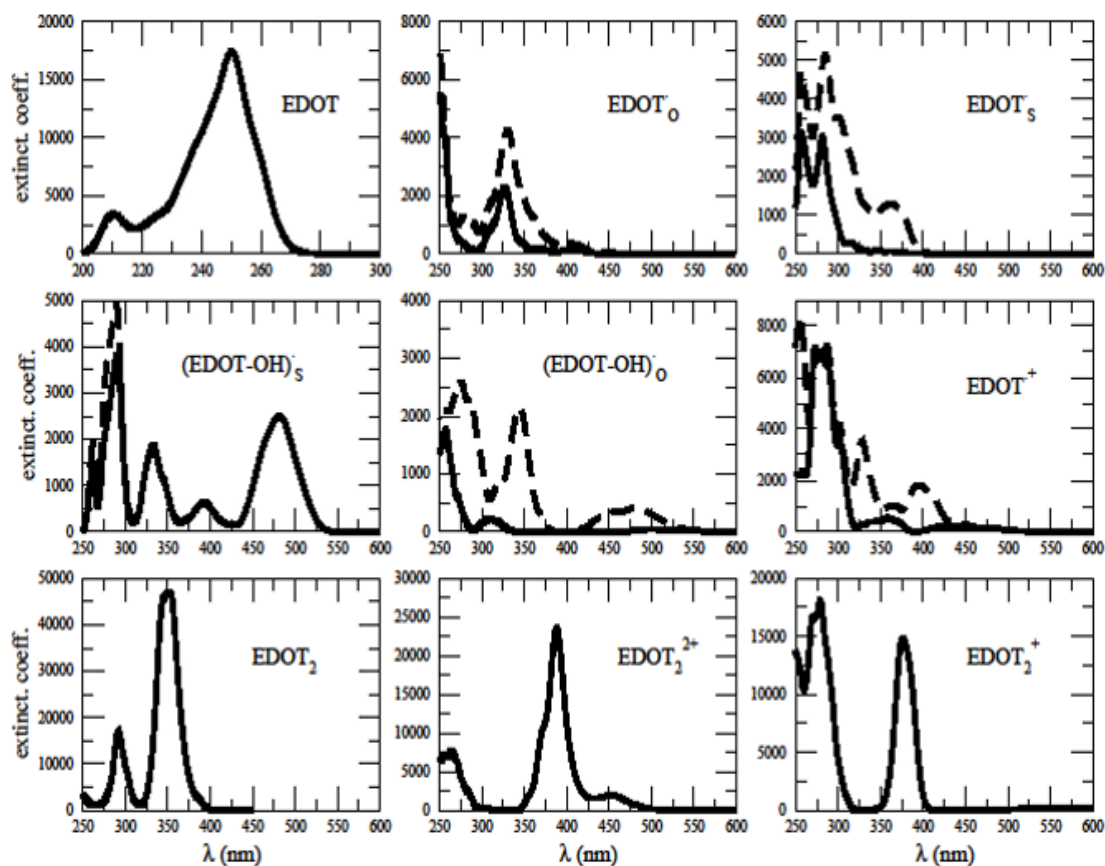


Figure 2.10: Absorption spectra of all molecules of Table 1. Absorption spectra of open shell radicals are displayed without (dotted line) and with (full line) spin screening with parameter 0.9.

Thermochemistry of the candidate reactions

Simulated absorption spectra suffer from the DFT inaccuracies and moreover these spectra often overlap, so that thermo-chemical data are most welcome in the further discussion with the aim to identify X, Y and Z species and also the effective mechanism scheme.

In table 2.2 we give the *molar* free energy change $\Delta_r G^m$ of a list of chemical reactions, relevant to the present study. All the calculations were done with B3LYP and the pSDD basis set. The molar values of the free energy change and the corresponding values at $\text{pH} = 7$, with all species (other than H^+) molar.

	Reaction step	Comment	$\Delta_r G^m$	$\Delta_r G^m$ (pH=7)	Enviroment
R1	$\text{EDOT} + \text{HO}\cdot \rightarrow \text{EDOT}\dots\text{HO}\cdot$	Transition State	+0,179		vacuum
R2	$\text{EDOT} + \text{HO}\cdot \rightarrow \text{EDOT}\dots\text{HO}\cdot$	S...O VdW complex	+0,115		vacuum
R3	$\text{EDOT} + \text{HO}\cdot \rightarrow \text{EDOT}\dots\text{HO}\cdot$	O...H H-bond	+0,136		vacuum
R4	$\text{EDOT} + \text{HO}\cdot \rightarrow (\text{EDOT}-\text{HO})_{\text{S}}$	Adduct	-0,874		vacuum
R5	$\text{EDOT} + \text{HO}\cdot \rightarrow (\text{EDOT}-\text{HO})_{\text{O}}$	Adduct	-0,370		vacuum
R6	$\text{EDOT} + \text{HO}\cdot \rightarrow \text{EDOT}^{\cdot+} + \text{HO}^-$	Charge transfer	+0,301	-0,13	water
R7	$\text{EDOT} + \text{HO}\cdot \rightarrow \text{EDOT}_{\text{S}} + \text{H}_2\text{O}$	H abstraction	+0,042		water
R8	$\text{EDOT} + \text{HO}\cdot \rightarrow \text{EDOT}_{\text{O}} + \text{H}_2\text{O}$	H abstraction	-0,917		water
R9	$\text{EDOT}^{\cdot+} \rightarrow \text{EDOT}_{\text{S}} + \text{H}^+$	Deprotonation	+1,266	+0,86	water
R10	$\text{EDOT}^{\cdot+} \rightarrow \text{EDOT}_{\text{O}} + \text{H}^+$	Deprotonation	+0,306	-0,10	water
R11	$\text{EDOT}^{\cdot+} + \text{EDOT} \rightarrow \text{EDOT}_2^{\cdot+} + \text{H}_2$	Dimerization	-0,331		water
R12	$\text{EDOT}_2^{\cdot+} + \text{EDOT} \rightarrow \text{EDOT}_2 + \text{EDOT}^{\cdot+}$	Charge transfer	+0,803		water
R13	$\text{EDOT}^{\cdot+} + \text{EDOT} \rightarrow \text{EDOT}_2^{\cdot+}, \text{H}$	Dimerization	-0,404		water
R14	$\text{EDOT}^{\cdot+} + \text{EDOT}^{\cdot+} \rightarrow \text{EDOT}_2^{2+}$	Dimerization	-0,743		water
R15	$\text{EDOT}_2^{2+} + \rightarrow \text{EDOT}_2^{\cdot+} + \text{H}^+$	Deprotonation	-0,676	-1,09	water
R16	$\text{EDOT}_2^{\cdot+} \rightarrow \text{EDOT}_2 + \text{H}^+$	Deprotonation	-0,521	-0,93	water
R17	$\text{EDOT}^{\cdot+} + \text{EDOT}_{\text{S}} \rightarrow \text{EDOT}_2^{\cdot+}$	Dimerization	-1,712		water
R18	$\text{EDOT} + \text{O}^{\cdot-} \rightarrow \text{EDOT}_{\text{S}} + \text{HO}^-$	H abstraction	+0,375		water
R19	$\text{EDOT} + \text{O}^{\cdot-} \rightarrow \text{EDOT}_{\text{O}} + \text{HO}^-$	H abstraction	-0,584		water
R20	$\text{EDOT} + \text{O}^{\cdot-} \rightarrow \text{EDOT}-\text{O}^{\cdot-}$ (open cycle)	Adduct	-1,852		vacuum

Table 2.2: Thermochemistry of some chemical reactions relevant to the present work. The $\Delta_r G^m$ are molar reaction free energies (in eV), calculated with the B3LYP functional and the pSDD basis set.

The first three reactions R1 to R3 of Table 2.2 are simple association reactions between EDOT and hydroxyl radical. The reactions R4 to R8 correspond to all candidate reactions of HO' radical with EDOT molecule. Thus, one of these reactions (R4 to R8) necessarily corresponds to the reaction 2.1 involved in both Schemes 1 and 2, reaction which yields the first transient species X. The reactions R9 to R17 of table 2.2 are the monomolecular and bimolecular reactions which could happen if the first transient species X was identified as EDOT^{·+} radical cation. Since X is indeed shown to be EDOT^{·+} (as demonstrated in next section), all the reactions which describe

the disappearance of all the other candidates for X species, namely $\text{EDOT}_{\text{O}}^{\cdot}$, $\text{EDOT}_{\text{S}}^{\cdot}$, $(\text{EDOT}-\text{OH})_{\text{S}}^{\cdot}$ and $(\text{EDOT}-\text{OH})_{\text{O}}^{\cdot}$ have been omitted from Table 2.2 for clarity. Then, among the reactions R9 to R17, one can find the reactions (2.2) and (2.3) or (2.4) and (2.5) which follow reaction (2.1) in Scheme 1 and Scheme 2 respectively.

Mechanism determination and species identification

The last step of the present investigation was to definitely identify the species and consequently to describe the EDOT oxidation mechanism. Figure 2.9 shows that the spectrum of EDOT [5] is well reproduced by the simulation. Otherwise, the absorption spectrum of the first species X produced by the reaction between EDOT monomer and hydroxyl radical, as deduced by spectrokinetic analysis (Figure 2.8), displays three peaks at 300, 360 and 460 nm. As it was already explained, X is one of the following species: $(\text{EDOT}-\text{OH})_{\text{S}}^{\cdot}$, $(\text{EDOT}-\text{OH})_{\text{O}}^{\cdot}$, $\text{EDOT}^{\cdot+}$, $\text{EDOT}_{\text{S}}^{\cdot}$ or $\text{EDOT}_{\text{O}}^{\cdot}$ which could be respectively formed by the reactions R4, R5, R6, R7 or R8 of Table 2.2.

According to the molar free energies values corresponding to these reactions (Table 2.2), except reaction R7 which is not favored due to a positive $\Delta_r G^m$, all the reactions are thermodynamically possible at neutral pH. Then, except $\text{EDOT}_{\text{S}}^{\cdot}$, all the other radical species could be formed. By comparing the simulated spectra of all these species displayed in Figure 2.10 with that of X found by spectrokinetic analysis (Figure 2.8) and with the crude experimental spectrum at 800 ns (Figure 2.3.b), one can conclude that only $\text{EDOT}^{\cdot+}$ and $(\text{EDOT}-\text{OH})_{\text{S}}^{\cdot}$ are plausible candidates. In fact, the neutral radical $\text{EDOT}_{\text{O}}^{\cdot}$ has only one peak at 325 nm while the $(\text{EDOT}-\text{OH})_{\text{O}}^{\cdot}$ radical absorbs significantly at about 300 nm.

For the first species X, we have only two plausible candidates: the $\text{EDOT}^{\cdot+}$ cation radical and the $(\text{EDOT}-\text{OH})_{\text{S}}^{\cdot}$ radical adduct since their spectra present three absorption maxima around 300, 360 and 460 nm (Figure 2.10) such as X species (Figure 2.8).

Nevertheless, one can observe that the spectrum of X fits better with that of $\text{EDOT}^{\cdot+}$. In particular the third absorption band located at around 460 nm is less intense than the other absorption bands. On the contrary, the peak at 460 nm is more intense than the other ones in the case of $(\text{EDOT}-\text{OH})_{\text{S}}^{\cdot}$. This suggests that the first X species is $\text{EDOT}^{\cdot+}$ radical cation, formed according to reaction R6 of Table 2.2 which has a negative value of $\Delta_r G^m$ (-0.13 eV at pH = 7). This is in good agreement with literature reports where the presence of $\text{EDOT}^{\cdot+}$ is often suggested [1, 3, 14, 12].

The absence of $(\text{EDOT}-\text{OH})_{\text{S}}^{\cdot}$ adduct may still be explained. Indeed, it can be seen from reactions R1 to R3 of Table 2.2 that the approach of an hydroxyl radical involves the crossing of a potential barrier larger than 0.1 eV. Then, even if the adduct

formation (R4 of Table 2.2) is possible due to its negative free energy, it is certainly made very slow by this large potential barrier. On the other hand, charge transfer reactions may occur at large distances, so that potential barriers have no effect which should explain the preferential (faster) formation of EDOT^{•+} according to:

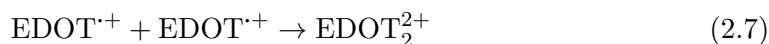


Evidently, this reaction corresponds to reaction (2.1) previously evoked in both Schemes 1 and 2. Starting from EDOT^{•+}, the reactions R9 to R17 of Table 2.2 are the monomolecular and bimolecular reactions which could further happen and lead to the unknown Y species which absorbs at 360 nm. Among all these reactions, according to Scheme 2, we can retain unimolecular reactions (R9 and R10) as well as pseudo-first order reactions (R11 and R13) as candidate steps for reaction (2.4), while according to Scheme 1, we can retain bimolecular reaction (R14) as a candidate step for reaction (2.2). Note that the other second order reactions of Table 2.2 must be excluded since, according to Scheme 1, X should react on itself in reaction (2.2) leading to the last unknown Z species.

Unimolecular reactions (R9 and R10) which should lead to the neutral radicals (EDOT_S[•] or EDOT_O[•]) must be excluded from the candidate mechanism. Indeed, EDOT_S[•] cannot be formed since the molar free energy value corresponding to reaction R9 is positive (Table 2.2), while EDOT_O[•] spectrum displays an absorption maximum at 325 nm which is far from the maximal absorption of Y species. Besides, concerning pseudo-first order reactions which could be involved in Scheme 2, reaction R13 must be excluded since the corresponding molar free energy value is positive (Table 2.2).

Contrarily to reaction R13, reaction R11 which also implies the action of EDOT^{•+} onto EDOT monomer is thermodynamically favored since the corresponding $\Delta_r G^m$ is negative. Nevertheless, a high barrier and a very low reaction rate must be expected because such a reaction needs the breaking of two C-H bonds before the formation of H₂ product. For this reason, we consider that reaction R11 is very unlikely to occur in our time window.

Thus, Scheme 2 must be excluded and X necessarily disappears according to the second order reaction R14 of Table 2.2:

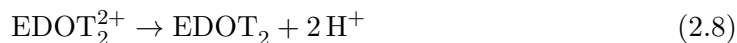


This reaction which is thermodynamically favored (very negative $\Delta_r G^m$ value, see Table 2.2) corresponds to reaction (2.2) of Scheme 1. This dimerization results from

the bond formation between two C atoms, each bearing an unpaired electron, as can be seen in Table 2.1. Thus the species Y must be identified as the EDOT_2^{2+} dimer cation. This is definitely confirmed by the fact that Y spectrum (Figure 2.8.c) is very similar to EDOT_2^{2+} simulated one (Figure 2.10).

Finally we focused on the last step of Scheme 1. This reaction (2.3) is monomolecular and leads, starting from EDOT_2^{+2} , to the Z stable species which absorbs at 290 nm and 360 nm (Figure 2.8). Note that this absorption is far from the well-known optical absorption of PEDOT polymers which has been reported around 600 nm. In literature, a pulsed radiolysis study concerning thiophene molecules [8, 9] (Th, a molecule very similar to EDOT) demonstrated that thiophene dimers (Th_2) are characterized by two absorption bands at 301 nm and 406 nm. In a previous study [6], in which PEDOT was synthesized by using γ -irradiation, our group showed that EDOT_2 dimer is a stable product and displays also two absorption bands at 290 nm and 360 nm (slightly displaced in comparison with those of Th_2).

In agreement with these results and since the absorption maxima of EDOT_2 correspond to those of Z, we supposed in the present work that EDOT_2 dimer is the last unknown stable Z species produced by pulsed radiolysis. This is confirmed by the fact that Z spectrum (Figure 2.8.c) is very similar to both simulated EDOT_2 spectrum (Figure 2.10) and experimental spectrum obtained by pulsed radiolysis 800 μs after the pulse (Figure 2.6.a). Thus, the last step involved in the experimental mechanism corresponds to the deprotonation of EDOT_2^{2+} according to:



Note that this reaction which corresponds to reaction (2.3) of Scheme 1 is thermodynamically favored at $\text{pH} = 7$. Indeed, it corresponds to the sum of two thermodynamically favored reactions (R15 and R16 of Table 4). As a conclusion, the mechanism of EDOT oxidation initiated by hydroxyl radical leads to EDOT_2 dimer according to the mechanistic Scheme 1 made up of the consecutive reactions (2.6), (2.7) and (2.8). The mechanism proposed here may neglect the formation of other minority species which could be also produced during EDOT oxidation. In particular, we could suppose the formation of small amounts of $(\text{EDOT}-\text{OH})_s^\cdot$ adduct radical, which is thermodynamically favored, and thus the potential contribution of this additional species to the spectrum which we globally attributed to $\text{EDOT}^{\cdot+}$. Unfortunately, it is not possible for us to distinguish such minority species. Spectrokinetic analysis enabled the fit of the variation of X, Y and Z concentrations over time. Thus it enabled the evaluation

of the rate constants $k_{2.6}$, $k_{2.7}$ and $k_{2.8}$ of reactions (2.6), (2.7) and (2.8) respectively. The best fit values are:

$$k_{2.6} = 4.8 \cdot 10^9 \text{ L mol}^{-1} \text{ s}^{-1} \quad (2.9)$$

$$k_{2.7} = 3.4 \cdot 10^9 \text{ L mol}^{-1} \text{ s}^{-1} \quad (2.10)$$

$$k_{2.8} = 7000 \text{ s}^{-1} \quad (2.11)$$

Due to the possible presence of minority species, not taken into account in the spectrokinetic analysis, these rate constant values could be overestimated.

Then, no products other than EDOT₂ dimers were observed, demonstrating that no polymerization takes place. This proves that PEDOT polymerization proceeds through a step-by-step mechanism made up of the following recurrent steps: (i) oxidation/ activation, (ii) growth/chain length increase, (iii) deprotonation. The amount of hydroxyl radicals generated by one pulse during the pulsed radiolysis study is then not enough to ensure polymerization. It only enables the incomplete transformation of EDOT monomers into dimers.

2.1.2 pH effect

In Table 2.2, many reactions, which could occur during EDOT oxidation, involve hydronium or hydroxide ions. Such reactions are pH-sensitive and should be thermodynamically displaced when the pH is changed. In order to check whether the pH variation affects the oxidation mechanism of EDOT, we changed the initial pH of the aqueous solution containing EDOT monomers. When the pH becomes higher than 11.9 (pKa(HO \cdot /O \cdot^-) value [15]), O \cdot^- radicals become predominant in the medium and at pH = 13, their concentration reaches 16 times that of HO \cdot hydroxyl radicals.

Then, in a pulse radiolysis experiment, a N $_2$ O-saturated aqueous solution of 1 mM in EDOT was irradiated with a dose of 37 Gy/pulse. The pH was adjusted at 13 by adding NaOH. The time resolved spectral evolution of the EDOT solution was different from that obtained at neutral pH. From first measurements at short times, three different bands (Figure 2.11) appear on the spectrum. This spectrum corresponds to the species produced through the reaction of EDOT with O \cdot^- oxide radical. Some of the possible reactions between these two reactants (R18, R19 and R20) are specified in Table 2.2.

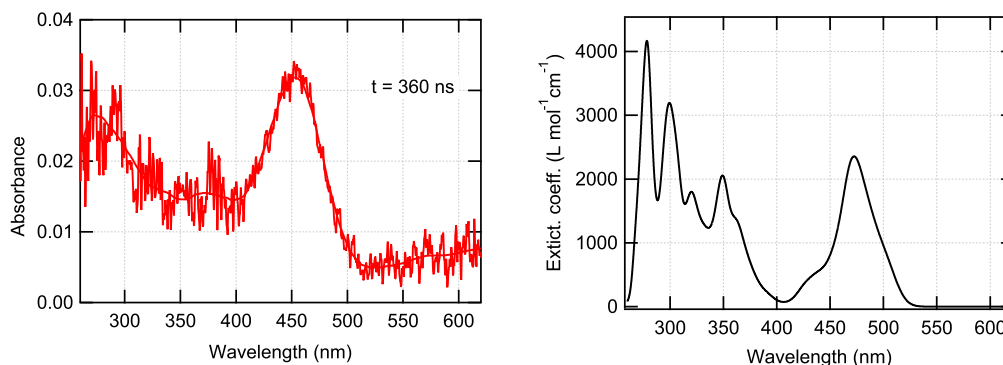
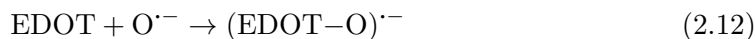


Figure 2.11: Absorption spectrum at 300 ns of a N $_2$ O-saturated aqueous solution containing 1 mM in EDOT at pH = 13 (Dose = 37 Gy, Optical Path = 1 cm), on the left. Simulated spectrum of adduct oxide radical (EDOT-O) \cdot^- , on the right.

However, the simulated spectra of the two radicals EDOT \cdot_O and EDOT \cdot_S do not show any bands at wavelength beyond 400 nm. It was so hypothesized it should be a transient species produced via reaction:



The simulated spectrum of adduct radical (EDOT-O) \cdot^- is in very good agreement with the experimental one, (Figure 2.11). Moreover thermo-chemical calculations (see

Table 2.2) demonstrated that among all the candidate reactions between EDOT and O^{•-}, the addition reaction is the more favorable since its molar free energy is very negative: $-1,85$ eV.

Then the kinetic signals (Figure 2.12) were studied by tests of pseudo-first order kinetics to highlight the same kinetics of formation. As shown in Figure 2.12, the observed rate constant were found to have the same value for all signals, as attended. It was possible to estimate a rate constant of reaction $k_{2.12} = 2 \cdot 10^9 \text{ M}^{-1}\text{s}^{-1}$. However, one can note that the kinetic profiles at 300 and 455 nm increase on $3 \mu\text{s}$ and successively the absorbance is stable at the maximum. On the contrary the signal at 350 nm shows a second increase at $3 \mu\text{s}$, explained to the overlapping of two different kinetics. This is due to the formation of a peak at 360 nm at longer time.

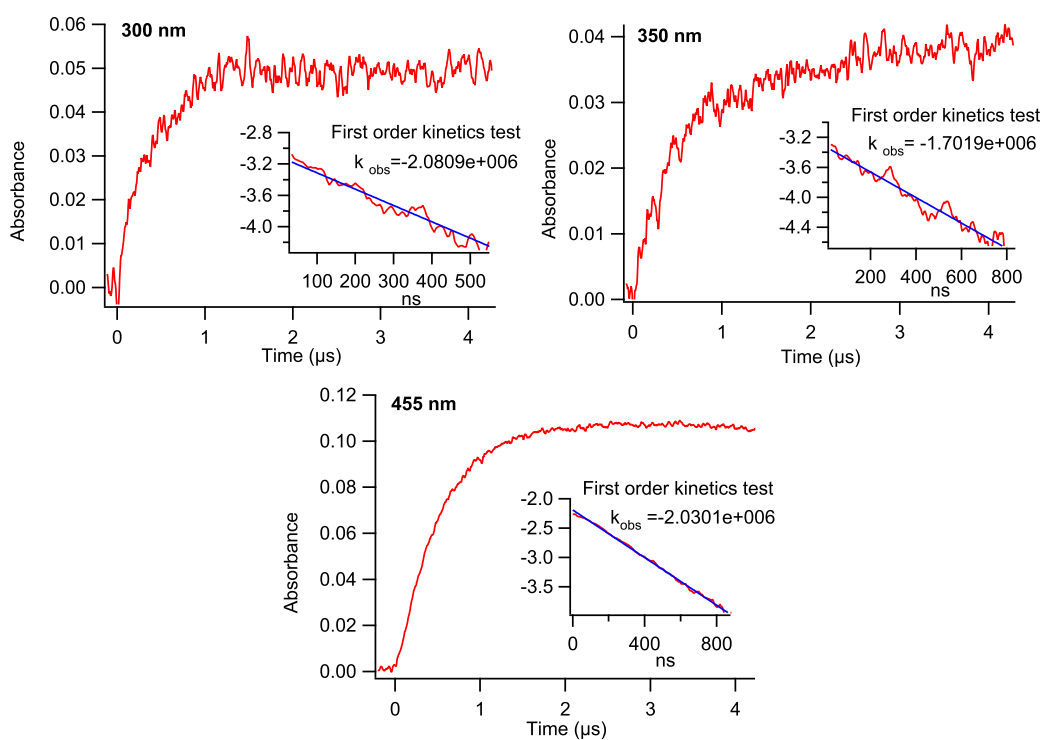


Figure 2.12: Kinetics profiles of absorption peaks of first transient species: oxyde adduct radical, $(\text{EDOT}-\text{O})^{\bullet-}$ and first kinetic order test, respectively. The constants rate observed, k_{obs} is the same for the three peaks.

Indeed in theoretical study, the geometrical optimization of the adduct, $(\text{EDOT}-\text{O})^{\bullet-}$, yielded a cycle opening. The simulated spectrum of open cycle depicts three absorption peaks at 360, 440 and 630 nm. In experimental study, a similar spectrum is observed

at 45 μs with a very good agreement with the simulated one (Figure 2.13).

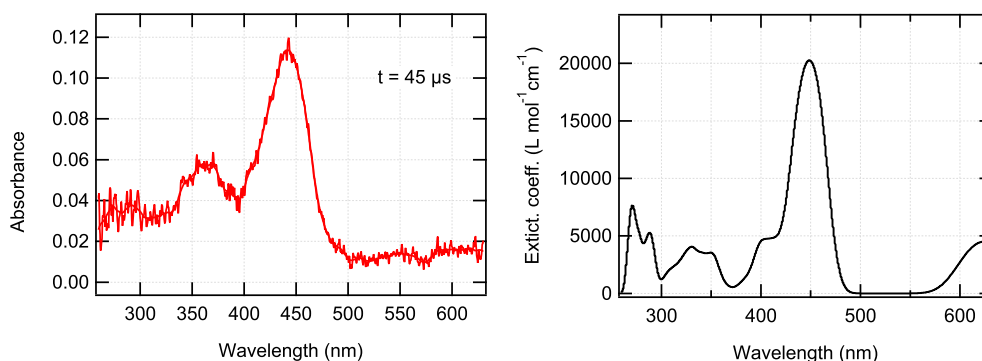


Figure 2.13: Absorption spectrum at 45 μs of a N_2O -saturated aqueous solution containing 1 mM in EDOT at $\text{pH} = 13$ (Dose = 37 Gy, Optical Path = 1 cm), on the left. Simulated spectrum of open cycle radical $\text{EDOT-O}\cdot^-$, on the right.

The opening of EDOT is not so unexpected. In a previous study on thiophene molecule the opening of cycle was also detected in alkaline solution by the action of oxide radical leading to a species which absorbs at around 430 nm with a rate constant $k = 1.4 \cdot 10^6 \text{ s}^{-1}$ [7, 8].

With the aim to estimate the rate constant of opening ring after the oxide radical addition, we studied the peak at 360 nm. We previously remarked that at this wavelength two kinetics are overlapped: the first one attributable to the formation of oxide addition on EDOT, the second one due to the formation opening ring. In order to isolate the opening ring kinetics, we subtracted the kinetic profile recorded at 300 nm. In Figure 2.14, the absorbance at 300 and 360 nm are plotted as function of time.

By normalizing the two signals and subtracting the contribution of decreasing of 300 nm in 360 nm profile, the kinetics growth of opening ring is depicted (green profile in Fig 2.14). A first kinetics order test gives a rate constant $k \simeq 7 \cdot 10^4 \text{ s}^{-1}$, that it is slightly slower than in thiophene kinetics. The same study was done on 440 and 460 nm and the same constant rate was found. A more accurate estimation of k could be evaluated by changing the irradiation dose. In this way the concentration of oxide EDOT radical changes as a function of dose and consequently also the constant rate.

The work concerning the thiophene molecule, the open cycle oxide radical disappears by mutual interaction. In our study, it was not possible to find a decreasing of second order. However at 1 ms the decay profile of the peaks characteristic of the open cycle radical is followed to the formation of peaks at 280 nm and 360 nm which were not identified. One can suppose that a stable species is produced.

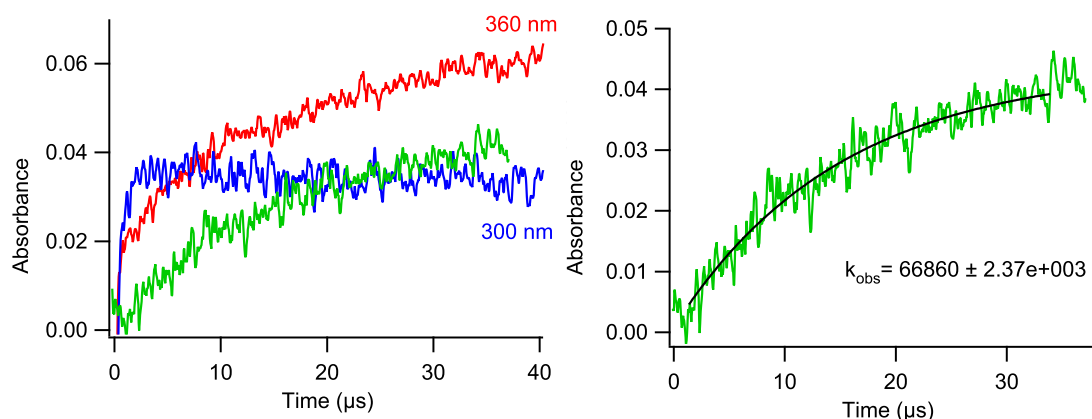


Figure 2.14: Time evolution of absorbances at – 300 nm, – 380 nm, – subtraction after normalization of 300 nm on 360 nm of a N₂O-saturated aqueous solution containing 1 mM in EDOT at pH = 13 (on the left); exponential fit of time evolution at 360 nm after correction (on the right), (Dose = 37 Gy, Optical Path = 1 cm)

Therefore, even if the addition is favorable but not stable, it is possible to detect it at time less than 10 μ s. Then, the addition is followed by the opening of the ring which is visible at longer time.

From this study it can be concluded that the action of the oxide radical produced by water radiolysis in alkaline solutions leads to the open cycle of EDOT monomer preventing any dimerization of EDOT and consequently any polymerization of PEDOT. Note that, even if some residual HO[•] radicals remain in the alkaline medium at pH = 13, their potential action onto EDOT was not distinguishable. Neither EDOT^{•+} cation radical nor (EDOT–OH)[•] adduct were observed in these alkaline conditions. Furthermore if (EDOT–OH)[•] was formed in alkaline medium, it should quickly deprotonate leading to (EDOT–O)^{•-} adduct and thus to the open cycle.

2.2 EDOT Reduction

In literature the chemical reduction of EDOT is also used to induce the formation of nanoparticles [16]. Also in the PhD thesis of Z. Cui in the LCP laboratory, e_{hyd}^- produce by γ -radiolysis was used for the synthesis of PEDOT conducting polymers. In this section we studied the reactivity of e_{hyd}^- onto EDOT molecule in order to identify the first step of polymerization.

So the reduction of EDOT was also studied by pulse radiolysis of a solution containing 1 mM in EDOT, 0.5 M in *tert*-Butanol under Argon atmosphere. The pH was

weakly acidic 5.6.

A volume of 200 mL of solution was placed in the reservoir connected to the flow cell. The solution was circulated with a flow rate of 100 mL/min and was irradiated by the electron beam with a dose of 40 Gy per pulse. *Tert*-Butanol was added to scavenge the hydroxyl radicals allowing to study the only reaction of hydrated electron onto EDOT monomers. The Argon saturation ensures the absence of oxygen in solution. Note that the reactivity of *Tert*-Butanol radicals onto EDOT molecules was investigated to ensure that no reactions take place between these two species, which was confirmed by the results.

The absorption spectrum recorded $1\mu\text{s}$ after the pulse is shown in Figure 2.15. The large band at 600 nm is the electron absorption, which has a maximum at 715 nm, not visible in this spectrum. In the UV region a weak peak at 295 nm is observed.

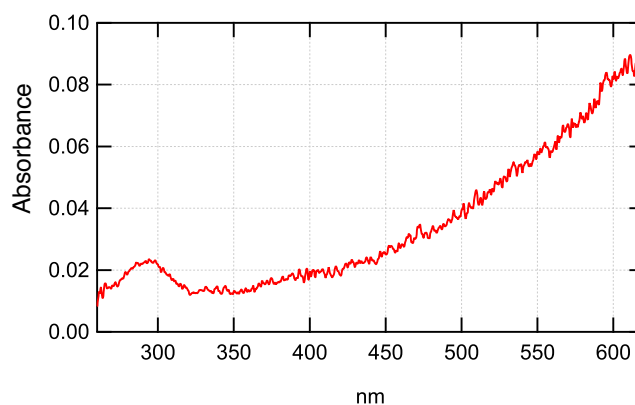


Figure 2.15: Absorption spectrum recorded $1\mu\text{s}$ after the pulse irradiation of a solution containing 1 mM in EDOT and 0.5 M in *tert*-Butanol (Dose = 40 Gy/pulse, Optical Path = 1 cm).

The kinetic profiles at these two wavelengths are shown in Figure 2.16, where the hydrated electron signal at 600 nm has been normalized to the kinetic profile at 295 nm. The decay of hydrated electron is found to be correlated with the formation of a species at 295 nm, which is supposed to be the EDOT anion radical, $\text{EDOT}^{\cdot-}$ produced by a one-electron reduction.

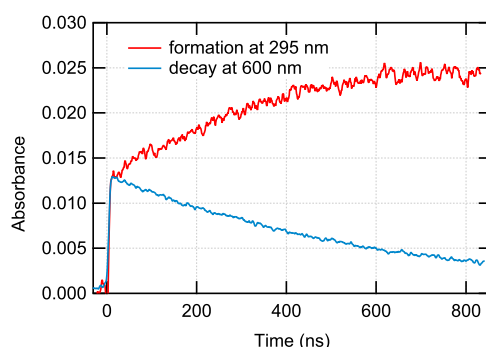


Figure 2.16: Decay of electron at 600 nm normalized at 295 nm and formation of EDOT anion radical at 295 nm in a solution containing 1 mM in EDOT and 0,5 M in *tert*-Butanol (Dose = 40 Gy/pulse, Optical path = 1 cm). (Dose = 40 Gy/pulse, optical path = 1 cm).

In order to check the correspondence between the decay at 600 nm and the formation at 295 nm, we studied the rate constants of the two kinetics. As it shown in Figure 2.17, the decay at 600 nm obeys to a pseudo-first order kinetic law with an observed rate constant $k_{obs} = 2.3 \cdot 10^6 \text{ M}^{-1}\text{s}^{-1}$.

After subtracting the hydrated electron component from the signal at 295 nm, the increase obtained obeys also to a pseudo-first order (Figure 2.17) with a similar rate constant $k_{obs} = 2.8 \cdot 10^9 \text{ M}^{-1}\text{s}^{-1}$. Consequently, we proposed that the EDOT monomer

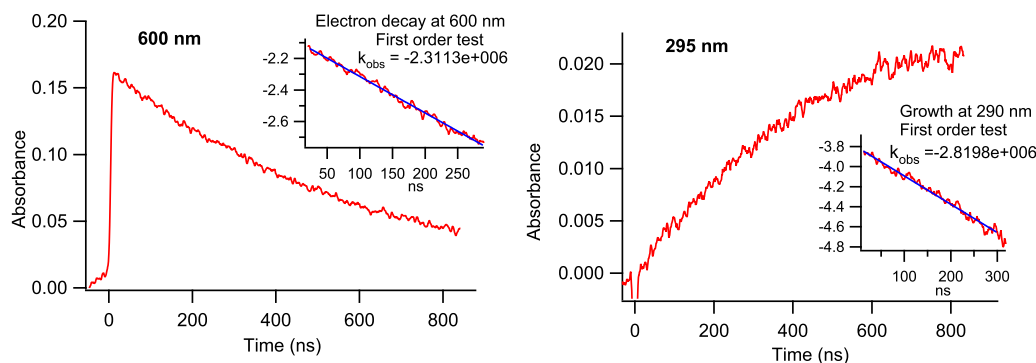


Figure 2.17: Kinetics signal at 600 (on the left) and 295 nm (on the right) showing the decay of hydrated electron and reducing EDOT radical respectively in a solution containing 1 mM in EDOT and 0,5 M in *tert*-Butanol (Dose = 40 Gy/pulse, Optical path = 1 cm). Inset: first order kinetic test.

is reduced by hydrated electron via reaction:



From these preliminary results, the reaction mechanism was simulated by COPASI program. The initial conditions were known from experimental data: EDOT concentration, deduced from absorption spectrum before irradiation, was not exactly 1 mM, but $[\text{EDOT}] = 0.91 \text{ mM}$ and $[t\text{BuOH}] = 0.5 \text{ M}$. From the dosimetry measurements, the electron and hydroxyl radical concentrations were estimated: $[e_{hyd}^-] = 1.4 \cdot 10^{-5} \text{ M}$ and $[\text{OH}^\cdot] = 1.45 \cdot 10^{-5} \text{ M}$ respectively. Some corrections on the radiolytical species concentrations were necessary in the simulation due to the variation of the dose during the experiment. The mechanism presented in Table 2.3 includes all possible reactions taking place in the system.

Reaction	Equation	Rate Constant $[\text{M}^{-1}\text{s}^{-1}]$
R1	$\text{HO}^\cdot + t\text{-BuOH} \longrightarrow \text{HO}^- + t\text{-BuOH}^\cdot$	$k = 6 \cdot 10^8 [17]$
R2	$e_{hyd}^- + \text{EDOT} \longrightarrow \text{EDOT}^{\cdot-}$	$k = 1.4 \cdot 10^9$
R3	$\text{HO}^\cdot + \text{EDOT} \longrightarrow \text{HO}^- + \text{EDOT}^{\cdot+}$	$k = 4.8 \cdot 10^9$
R4	$e_{hyd}^- + \text{H}_3\text{O}^+ \longrightarrow \text{H}^\cdot + \text{H}_2\text{O}$	$k = 2.3 \cdot 10^{10}$
R5	$2e_{hyd}^- + \text{H}_2\text{O} \longrightarrow \text{H}_2 + 2\text{OH}^-$	$k = 5.5 \cdot 10^9$

Table 2.3: Reactions involved in COPASI simulation of EDOT reduction by hydrated electron in aqueous solution

Although the reaction between EDOT and e_{hyd}^- is predominant, the formation of cation radicals and recombination of species can not to be excluded. Nevertheless in Figure 2.18 the time evolution over $1 \mu\text{s}$ of the concentrations of all species produced shows the absence of EDOT cation radical. As expected the only species produced is the EDOT anion.

According to this simulation the electron decay fits well with the growth of the EDOT anion radical formation. The rate constant found here after adjustment, was $k = 1.4 \cdot 10^9 \text{ M}^{-1}\text{s}^{-1}$.

The time evolution of the concentrations was converted into time evolution of optical density and the simulated signals were compared to the experimental ones. For electron profile, the extinction coefficient $130000 \text{ L mol}^{-1} \text{ cm}^{-1}$ at 600 nm given from literature, was used to plot the optical density as function of time. For EDOT anion radical the

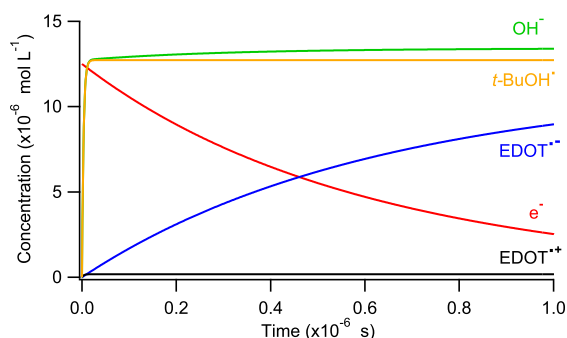


Figure 2.18: Time evolution of concentrations simulated by COPASI of a system containing 1 mM in EDOT and 0,5 M in *tert*-Butanol corrected according to the dose.

best extinction coefficient was found to be $2450 \text{ L mol}^{-1}\text{cm}^{-1}$ at 295 nm.

The good agreement between simulated signals and experimental ones is shown in Figure 2.19. The discrepancy on the last 200 ns of the kinetic profile at 295 nm can be explained by the transformation of $\text{EDOT}^{\bullet-}$ radical in a stable species not visible in the UV-Vis spectrum. Indeed at longer time the decay of anion radical can be fitted by a first order as well as second order, but no other peak appears within the spectral range we investigated.

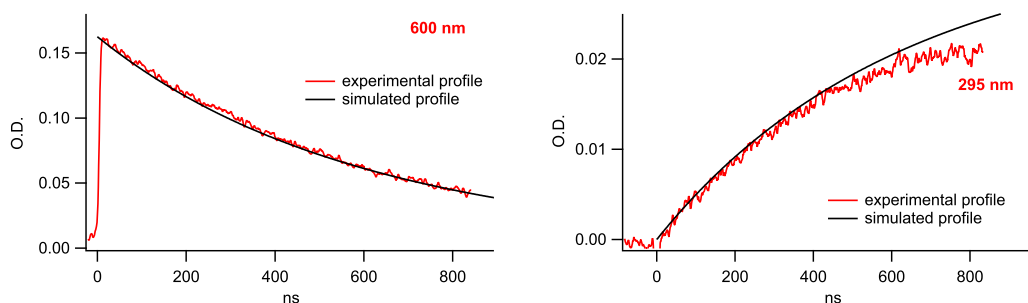


Figure 2.19: Comparison of the experimental curves with the simulated ones of time evolution of absorbance at 600 (on the left) nm and 265 nm (on the right) $1 \mu\text{s}$ of a saturated N_2O -aqueous solution containing 1 mM in EDOT (Dose = 40 Gy/pulse, optical path = 1 cm).

In this section, it was presented a first study of the reduction of EDOT by hydrated electron. A first approximately value of constant rate was deduced and the anion radical, $\text{EDOT}^{\bullet-}$, spectrum was isolated.

2.3 PEDOT synthesis

To prove that PEDOT polymerization effectively proceeds through a step-by-step oxidation process and with the aim to synthesize conducting PEDOT polymers, we used the electron beam, usually employed in fast kinetic studies, as a high energy electron irradiator. Indeed the quantitative polymerization of EDOT into PEDOT requires a very much higher concentration in hydroxyl radicals which should reach at least twice that of EDOT. As a consequence, PEDOT radioinduced synthesis could only proceed through a recurrent HO \cdot oxidation process: HO \cdot reacts with EDOT monomers, then with dimers, then with oligomers.

An aqueous solutions (4 mL) containing 10 mM in EDOT in a closed cell under N $_2$ O atmosphere was irradiated with a series of consecutive electron pulses of 40 Gy (delivered at a frequency of 10 Hz). In these conditions, a high concentration of oxidative species is produced.

Taking into account the step-by-step polymerization process described in the study of kinetics, 20 mM hydroxyl radicals are needed to ensure the quantitative polymerization of EDOT monomers into PEDOT polymers. The use of two HO \cdot radicals for one EDOT molecule is understandable since each EDOT monomer is bound to two EDOT neighbors inside the same polymer chain, which means that it has been twice oxidized.

In order to quantitatively polymerize EDOT, we irradiated the colorless and limp aqueous solution with 180 kGy which corresponds to the accumulation of 4500 pulses of 40 Gy/pulse. After such irradiation, the solution became turbid. Figure 2.20.a displays its UV-Vis absorption spectrum. No noticeable absorption band is present in the spectrum. Nevertheless, a continuous scattering appears due to the presence of a brown-yellow suspension in the bulk of the irradiated solution (photography in inset of Figure 2.20.a). This spectrum and the turbidity of the solution are in good agreement with the results we got in a previous work by γ -radiolysis [5] suggesting that polymerization effectively took place.

In order to demonstrate that the radiosynthesized products are PEDOT polymers, the turbid solution obtained after 180 kGy electron beam irradiation was centrifuged to collect the solid phase. The isolated brown powder was lyophilized to eliminate any residual water molecules which could be trapped in the polymer containing solid phase (photography in inset of Figure 2.20.b). The solid sample was then characterized by ATR-FTIR spectroscopy in order to investigate the chemical nature of the obtained polymers. The ATR-FTIR spectrum of the polymer powder is presented in the upper part of Figure 2.20.b in the wavenumber region 1600-600 cm $^{-1}$ together with the spec-

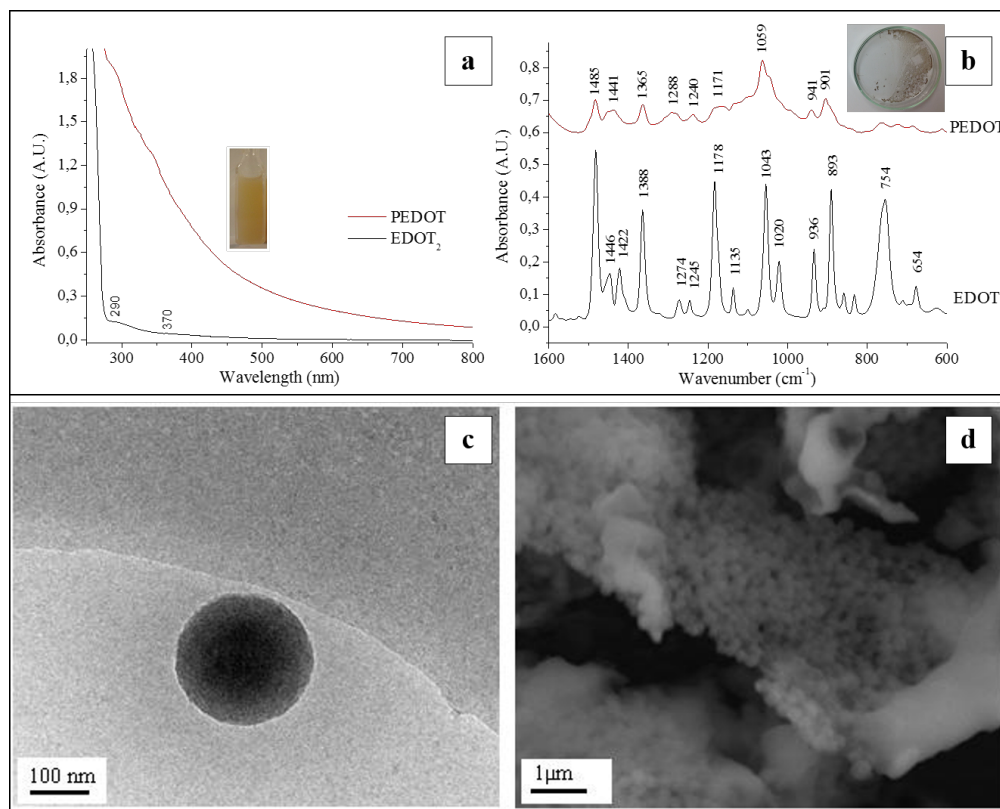


Figure 2.20: (a) Absorption spectrum of a N₂O-saturated aqueous solution of EDOT (10 mM) irradiated by an electron beam at a dose of 180 kGy (4500 pulses, 40 Gy/pulse), reference was water and pathlength was 1 mm; (inset) image of a cell containing PEDOT aqueous suspension radiosynthesized by electron beam; (b) ATR-FTIR spectra of pure EDOT (bottom spectrum) and PEDOT polymers radiosynthesized at 180 kGy (top spectrum); (inset) photograph of a cup containing the lyophilized radiosynthesized PEDOT powder; (c) Cryo-TEM image of radiosynthesized PEDOT in aqueous solution. A PEDOT nanoparticle of around 250 nm is observed; (d) SEM image of lyophilized radiosynthesized PEDOT powder. Aggregates of spherical PEDOT nanoparticles are observed.

trum of pure non irradiated EDOT (bottom of Figure 2.20.b). The two spectra are in good agreement with those our group previously reported for PEDOT and EDOT when polymerization was induced by γ -rays (instead of accelerated electrons). The IR spectrum of the polymer powder displays vibrations at 1485, 1441 and 1365 cm^{-1} which are attributable to C=C and C-C stretching modes in the thiophene ring. The vibrations observed at 1288, 1240, 1171 and 1059 cm^{-1} are assigned to the stretching modes of the ethylenedioxy groups (C-C and C-O-R-O-C). The vibration modes of C-S bond which are present in the thiophene ring can be observed at 941 and 901 cm^{-1} . Note that the intense C-H stretching band at 754 cm^{-1} , observed in the spectrum of EDOT, is clearly absent in the ATR-FTIR spectrum of polymers. This shows that EDOT polymerization quantitatively took place thanks to α,α' -coupling reactions and that the resulting solid powder obtained after lyophilisation is effectively composed of PEDOT polymers. Moreover as in γ -irradiation [6], electron beam irradiation enables the radiosynthesis of PEDOT polymers.

While one electron pulse leads to the formation of EDOT₂ dimers as stable products, the use of a series of successive pulses is necessary to generate enough hydroxyl radicals to form PEDOT polymers. We evidenced here that electron irradiation can be used as an alternative way for the synthesis of PEDOT polymers and that PEDOT growth effectively proceeds through a step by step oxidation process as expected. Aqueous solutions containing 10 mM in EDOT and irradiated by electron beam at 180 kGy were observed by cryo-transmission electron microscopy just after irradiation in order to investigate the structure and morphology of PEDOT polymers in aqueous solution. Representative images show the presence of low density globular structures forming spherical nanoparticles with a diameter ranging between 200 and 250 nm as observed on Figure 2.20.c. This result is in agreement with polymer size and shape found after γ rays-induced PEDOT synthesis. Since no other low density objects were observed during our cryo-TEM experiments, we deduce that these spherical nanoparticles are made up of PEDOT polymers. Each observed nanoparticle should be composed of polymer chains. Since no α,β' linkages could occur during polymerization, radiosynthesized PEDOT nanostructures should be composed of linear chain polymers which are no branched nor networked. Thus the globular structure observed on Figure 2.20.c should correspond to a self-assembly of independent amorphous PEDOT chain polymers. The presence of ethylenedioxy groups (H-bond acceptors) should explain not only the hydrosolubility of PEDOT polymers but also the as-observed packing and nano-structuring of the spherical supra-molecular PEDOT self-assemblies. In order to characterize the morphology of the polymers after a deposition procedure, the 180

kGy-irradiated sample was lyophilized and the black powder obtained was deposited then characterized by SEM microscopy. The images indicate the presence of very close packed polymeric particles (Figure 2.20.d). Once again PEDOT polymers appear as spherical nanoparticles. These structures should come from the globular nanostructures already observed in aqueous solution by cryo-TEM. The particles observed by SEM are almost mono-disperse in size with a mean diameter of 220 nm which is close to that observed by cryo-TEM in aqueous solution. This proves that neither phase transition nor deposition procedure affect the size and shape of PEDOT nanoparticles. This would imply the existence of very strong hydrogen-bond interactions into each polymer nanoparticle. We succeeded in the synthesis of PEDOT polymers thanks to the electrons beam irradiation of EDOT aqueous solution. The radiosynthesized PEDOT polymers form mono-disperse nanoparticles the morphology of which is kept after deposition onto substrate. Since chemically and electrochemically synthesized PEDOT polymers are very often used for their conducting properties, we wanted to check by four point probe technique whether our radiosynthesized PEDOT are also characterized by such interesting electrical properties. After irradiation and lyophilization, the obtained PEDOT powder was dissolved and treated by a chemical oxidant NOBF₄ (10⁻² M) in acetonitrile. The solution was spin-coated onto a glass substrate and a PEDOT layer was obtained. The average thickness of the doped PEDOT film was measured on a surface profiler and was found to be 105 nm. The mean value of the electrical conductivity was determined to be $9 \cdot 10^{-4}$ S cm⁻¹. This conductivity is comparable to the highest conductivities reported in literature [18, 19]. Nevertheless, we believe that the conductivity of radio-synthesized PEDOT could be further improved thanks to the control of polymerization mechanism.

2.4 Conclusion

In this first chapter, we focused on the first steps of EDOT polymerization. By means of time-resolved absorption spectroscopy available on ELYSE accelerator platform, we were able to identify the first reaction of EDOT monomer with radiolytical species.

In the simplest system studied by water radiolysis, the first transient species involved in the polymerization were investigated. The use of the SVD method for the deconvolution of spectra and the use of TD-DFT theory for the simulations of the absorption spectra of transient species, allowed to identify the first transient species, such as EDOT^{•+} cation radical, produced by the reaction between EDOT and the hydroxyl radical. The comparison of all the results, experimental and theoretical, led to the

identification of the dimerization mechanism. The rate constant of EDOT oxidation, dimerization and deprotonation were found via spectrokinetic analysis.

We also approached the reduction of EDOT by hydrated electron produced by water radiolysis. It was possible to estimate the rate constant and detect the absorption spectrum of $\text{EDOT}^{\cdot-}$ anion radical.

This study was concluded with the polymerization of EDOT by using the electron beam as a high energy electrons irradiator. Successfully, the irradiation with a series of consecutive electron pulses (180 kGy total dose) of EDOT aqueous solution enabled the synthesis of PEDOT polymers confirming that PEDOT growth follow a step-by-step oxidation mechanism.

The chemical nature of radiosynthesized PEDOT polymers was confirmed by ATR-FTIR spectroscopy while their morphology was checked in solution by cryo-TEM microscopy and after lyophilisation and deposition by SEM microscopy. Radiosynthesized PEDOT polymers were found to form monodisperse nanoparticles whose morphology was kept after deposition onto solid substrate. Finally, the electrical conductivity of radiosynthesized PEDOT was evaluated at $9 \cdot 10^{-4} \text{ S cm}^{-1}$. This conductivity is comparable to conductivities already reported in literature concerning PEDOT polymers synthesized by conventional methods.

Bibliography

- [1] Stephan Kirchmeyer and Knud Reuter. Scientific importance, properties and growing applications of poly (3, 4-ethylenedioxythiophene). *Journal of Materials Chemistry*, 15(21):2077–2088, 2005.
- [2] Igor Rocha, Emili Lucht, Izabel C Riegel-Vidotti, Marcio Vidotti, and Elisa S Orth. Kinetic approach to elucidate size controllable features in nanocomposites of gold nanoparticles and poly (3, 4-ethylenedioxythiophene) in aqueous dispersion stabilized by gum acacia. *The Journal of Physical Chemistry C*, 118(44):25756–25764, 2014.
- [3] Y-H Ha, Nikolay Nikolov, Steven K Pollack, John Mastrangelo, Brett D Martin, and Ranganathan Shashidhar. Towards a transparent, highly conductive poly (3, 4-ethylenedioxythiophene). *Advanced Functional Materials*, 14(6):615–622, 2004.
- [4] X Du and Z Wang. Effects of polymerization potential on the properties of electrosynthesized PEDOT films. *Electrochimica Acta*, 48(12):1713–1717, 2003.
- [5] Youssef Lattach, Ariane Deniset-Besseau, Jean-Michel Guigner, and Samy Remita. Radiation chemistry as an alternative way for the synthesis of PEDOT conducting polymers under soft conditions. *Radiation Physics and Chemistry*, 82:44–53, 2013.
- [6] Youssef Lattach, Cecilia Coletta, Srabanti Ghosh, and Samy Remita. Radiation-induced synthesis of nanostructured conjugated polymers in aqueous solution: Fundamental effect of oxidizing species. *ChemPhysChem*, 15(1):208–218, 2014.
- [7] J Lillie. Pulsed radiolytic investigation of oxidative ring scission of furan, thiophene and pyrrole. *Zeitschrift für Naturforschung Part B. Chemie Biochemie Biophysik Biologie und verwandten gebiete*, (3):197, 1971.
- [8] Barbara B Saunders, Priscilla C Kaufman, and Max S Matheson. Reactions of thiophene with radiolytically produced radicals. 1. the hydroxyl radical. *The Journal of Physical Chemistry*, 82(2):142–150, 1978.
- [9] Barbara B Saunders. Reactions of thiophene with radiolytically produced radicals. 2. the solvated electron and the hydrogen atom. *The Journal of Physical Chemistry*, 82(2):151–154, 1978.

- [10] P Gaikwad, KI Priyadarsini, S Naumov, and BSM Rao. Oxidation of tryptamine and 5-hydroxytryptamine: a pulse radiolysis and quantum chemical study. *The Journal of Physical Chemistry A*, 113(29):8249–8257, 2009.
- [11] Thounaojam Avinash Singh, BS Madhava Rao, and Peter O'Neill. Radical chemistry of 8-oxo-7, 8-dihydro-2-deoxyadenosine and 8-oxo-7, 8-dihydro-2-deoxyguanosine: a pulse radiolysis study. *The Journal of Physical Chemistry B*, 114(49):16611–16617, 2010.
- [12] VS Vasantha and KLN Phani. Effect of hydroxypropyl- β -cyclodextrin on the electrochemical oxidation and polymerization of 3, 4-ethylenedioxythiophene. *Journal of Electroanalytical Chemistry*, 520(1):79–88, 2002.
- [13] R Core Team. R: A language and environment for statistical computing. r foundation for statistical computing, vienna, austria. 2013, 2014.
- [14] Nophawan Paradee and Anuvat Sirivat. Synthesis of poly (3, 4-ethylenedioxythiophene) nanoparticles via chemical oxidation polymerization. *Polymer International*, 63(1):106–113, 2014.
- [15] P Neta and Robert H Schuler. Rate constants for the reaction of oxygen (1-) radicals with organic substrates in aqueous solution. *The Journal of Physical Chemistry*, 79(1):1–6, 1975.
- [16] Shanmugam Senthil Kumar, Chinnaiah Siva Kumar, Jayaraman Mathiyarasu, and Kanala Lakshminarasimha Phani. Stabilized gold nanoparticles by reduction using 3, 4-ethylenedioxythiophene-polystyrenesulfonate in aqueous solutions: nanocomposite formation, stability, and application in catalysis. *Langmuir*, 23(6):3401–3408, 2007.
- [17] George V Buxton, Clive L Greenstock, W Phillips Helman, and Alberta B Ross. Critical review of rate constants for reactions of hydrated electrons, hydrogen atoms and hydroxyl radicals (oh^{\bullet} / o^{\bullet} - in aqueous solution. *Journal of physical and chemical reference data*, 17(2):513–886, 1988.
- [18] Brad H Jones, Kai-Yuan Cheng, Russell J Holmes, and Timothy P Lodge. Nanoporous poly (3, 4-ethylenedioxythiophene) derived from polymeric bicontinuous microemulsion templates. *Macromolecules*, 45(1):599–601, 2011.

- [19] Srabanti Ghosh, Hynd Remita, Laurence Ramos, Alexandre Dazzi, Ariane Deniset-Besseau, Patricia Beaunier, Fabrice Goubard, Pierre-Henri Aubert, Francois Brisset, and Samy Remita. Pedot nanostructures synthesized in hexagonal mesophases. *New Journal of Chemistry*, 38(3):1106–1115, 2014.

Chapter 3

Alternative radicals as oxidizing species

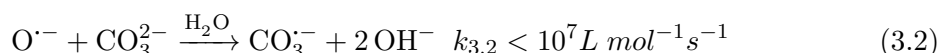
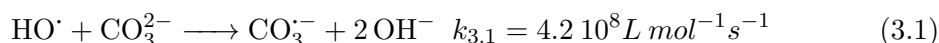
In order to study the influence of the nature of alternative radiolytical species onto the growth mechanism of PEDOT, we used other oxidants species to initiate the oxidation of EDOT monomers. Firstly we studied the action of carbonate radical, $\text{CO}_3^{\cdot-}$ and azide radical, N_3^{\cdot} . Both are produced by the reaction between an anion (CO_3^{2-} or N_3^- , respectively) with hydroxyl radical, HO^{\cdot} . These two radicals are less powerful than hydroxyl ones but more selective. The competition between these species and hydroxyl radical was also studied to explain how they operate on the growth of polymers. Then, we studied the action of sulfate radical, $\text{SO}_4^{\cdot-}$ onto EDOT monomers. With this aim, $\text{SO}_4^{\cdot-}$ was produced by the reaction between hydrated electron, e_{hyd}^- and persulfate anion, $\text{S}_2\text{O}_8^{2-}$.

3.1 Carbonate Radicals

Different from hydroxyl radical, the carbonate radical $\text{CO}_3^{\cdot-}$ is known to react selectively with aromatic compounds by direct electron transfer [1]. Moreover, it is a mild oxidant with a redox potential of 1.6 V_{SHE} which is higher than that of EDOT. In order to find the first reaction of carbonate on EDOT, we decided to produce it by pulse radiolysis by reaction of the anion CO_3^{2-} with HO^{\cdot} radicals as described in chapter 1. So we studied N_2O -saturated aqueous solution of 1 mM in EDOT containing 10 mM, 50 mM, 100, mM and 1 M in Na_2CO_3 . The pH of all solutions was around 11 for 10 mM in carbonate, around 12 for 50 and 100 mM in carbonate and around 14 for

1 M in carbonate. It was found unchanged before and after irradiation.

At short timescale, we expected the formation of carbonate radical $\text{CO}_3^{\cdot-}$ which is known to absorb at 600 nm. Note that this radical can be produced from the reaction of CO_3^{2-} with either hydroxyl radical or oxide radical, depending on the pH of solution ($\text{pK}_a(\text{HO}^{\cdot}/\text{O}^{\cdot-}) = 11.9$ [2]). However the reaction between oxide radical and carbonate ions is slower than that with hydroxyl radical. Weeks *et al.* estimated the rate constant of the two reactions [3]:



This means that oxide radical produced in water radiolysis or converted in the equilibrium between hydroxyl radical and oxide radical in alkaline solutions, can react directly with EDOT monomer as previously investigated (chapter 2, eq. 2.12).

The Figure 3.1 shows the spectra recorded 700 ns after the pulse when aqueous solutions containing 1 mM in EDOT were irradiated in the presence of different concentrations CO_3^{2-} under N_2O . The large band observed in all cases at 600 nm is the carbonate radical absorption band. The intensity of this band, and consequently the concentration of carbonate radical $\text{CO}_3^{\cdot-}$, increases linearly with the concentration of CO_3^{2-} .

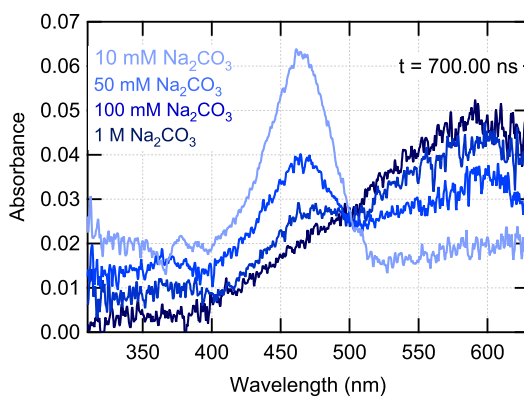


Figure 3.1: Absorption spectra recorded 700 ns after the pulse when aqueous solutions containing 1 mM in EDOT and different concentrations in carbonate: 10 mM (Dose =44 Gy/pulse), 50 mM (Dose =39 Gy/pulse), 100 mM (Dose =39 Gy/pulse) and 1 M (Dose =39 Gy/pulse) were irradiated under N_2O atmosphere. The peak at 600 nm is the carbonate radical. (Optical path = 1 cm)

On the other hand, a band at 460 nm appears when the concentration of carbonate

decreases. This band was previously detected in alkaline solutions in the absence of Na_2CO_3 , where EDOT monomers were found reacting with oxide radicals leading to an opening cycle (Chapter 2, Figure 2.11).

This is probably due to the competition between carbonate radical formation and oxide radical addition on EDOT monomers. The isosbestic point at 500 nm between the two species allows to estimate the extinction coefficient of the open cycle at 460 nm. The extinction coefficient of carbonate radical, $\text{CO}_3^{\cdot-}$, at 500 nm is $\epsilon = 890 \text{ L mol}^{-1}\text{cm}^{-1}$, as determined from the pulse radiolysis of an aqueous solution of 100 mM in carbonate. Then by comparing the absorbance at 500 nm and at 460 nm, the extinction coefficient of the open cycle at 460 nm was found $\epsilon = 2077 \text{ L mol}^{-1}\text{cm}^{-1}$. Finally, no peaks due to the reaction between EDOT and HO^\cdot are observed in the spectra.

In order to highlight the competition between the formation of the carbonate radical and of the open cycle, we studied the rate constant of the formation of two species.

By comparing the spectral evolutions at 1 μs for the four aqueous solutions of 1 mM in EDOT and containing 10 mM, 50 mM and 100 mM in Na_2CO_3 , we noticed that the absorbances at 460 nm and at 600 nm (corresponding respectively to $\text{EDOT-O}^{\cdot-}$ and $\text{CO}_3^{\cdot-}$) depend on carbonate concentration, Na_2CO_3 .

This suggests that two competitive reactions take place in this system:



The competition method is used in pulse radiolysis when neither the primary radical nor the reaction product can be observed directly. It allows to estimate the rate constant of the transient species which is not directly observed in the experiment, in our case $k_{3.3}$.

In our experiment, we can easily detect the carbonate radical at 600 nm and the yield. On the other hand the two reactions are related by:

$$\frac{G(\text{O}^{\cdot-})}{G(\text{CO}_3^{\cdot-})} = \frac{k_{3.3}[\text{EDOT}]}{k_{3.2}[\text{CO}_3^{2-}]} + 1 \quad (3.4)$$

that can be rewritten:

$$\frac{1}{G(\text{CO}_3^{\cdot-})} = f\left(\frac{1}{[\text{CO}_3^{2-}]}\right) \quad (3.5)$$

where the slope of the straight is:

$$\alpha = \frac{k_{3.3}[\text{EDOT}]}{k_{3.2}G(\text{O}^{\cdot-})} \quad (3.6)$$

The figure 3.2 shows the fit of equation 3.5. The slope value α is found $3.1 \cdot 10^4$.

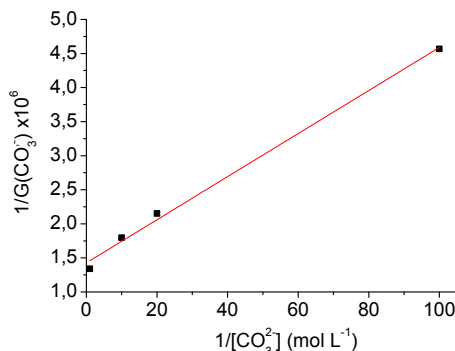


Figure 3.2: Variation of $\frac{1}{G(\text{CO}_3^{2-})}$ as a function of $\frac{1}{[\text{CO}_3^{2-}]}$. The slope of the linear fit (red line) allows to estimate the value of $k_{3.3}$.

From the equation 3.5, it is possible to estimate the rate constant $k_{3.3} = 1.7 \cdot 10^8 \text{ L mol}^{-1}\text{s}^{-1}$. Note that we assumed $G(\text{O}^{\cdot-}) = 5.6 \cdot 10^{-7} \text{ mol}\cdot\text{J}^{-1}$. Indeed in alkaline solution ($\text{pH} > \text{p}K_a(\text{HO}^{\cdot}/\text{O}^{\cdot-})$), all hydrated electrons and hydroxyl radicals are converted into oxide radicals, $\text{O}^{\cdot-}$. However at low concentrations in carbonate the presence of radiolytical hydroxyl radicals can not be completely excluded. This hypothesis was confirmed by analyzing the spectra at longer time (Figure 3.3). In presence of 10 mM of carbonate, the final spectrum appears as a combination of the species previously identified as the dimer at 300 and 370 nm and the open ring at 460 nm, with different kinetics.

The absorption of these peaks decreases with the increasing of the concentration in carbonate. At 1 M of carbonate, the spectrum at 1 ms shows less intense peaks at 300 and 370 nm, probably due to the formation of dimer induced by the hydroxyl radicals which do not react with carbonate. This means that the carbonate radical can not react with EDOT. It only controls the amount of HO^{\cdot} and $\text{O}^{\cdot-}$ radicals.

Finally the action of hydroxyl radical not converted into oxide radicals was checked by adjusting the pH below the $\text{p}K_a(\text{HO}^{\cdot}/\text{O}^{\cdot-}) = 11.9$. We studied the aqueous solution containing 100 mM of carbonate and 1 mM of EDOT at $\text{pH} = 8.6$. At low pH, in the presence of a great excess in HO^{\cdot} in comparison with $\text{O}^{\cdot-}$, one could expect the quan-

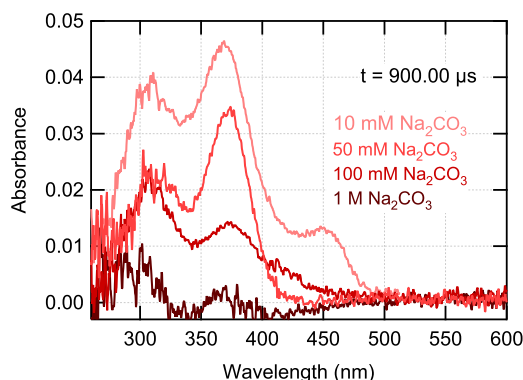


Figure 3.3: Absorption spectra at 900 μs after the pulse when aqueous solutions containing 1 mM in EDOT and 10 mM (Dose =44 Gy/pulse), 50 mM (Dose =39 Gy/pulse), 100 mM (Dose =39 Gy/pulse) and 1 M (Dose =39 Gy/pulse) in carbonate were irradiated under N_2O (Optical path = 1 cm).

titative conversion of hydroxyl radical in carbonate radical, which should successively react with EDOT monomers. Nevertheless, it was not the case. In fact, even if the carbonate radical is produced at short time, the conversion was not found total (Figure 3.4).

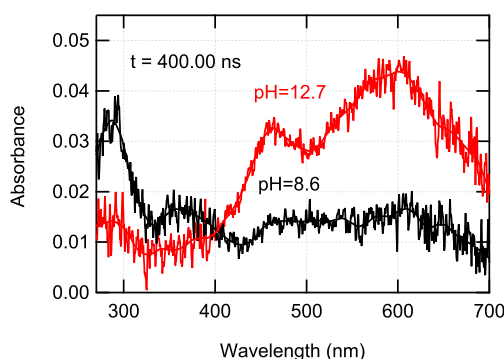


Figure 3.4: Absorption spectra recorded 400 ns after the pulse when aqueous solution containing 1 mM in EDOT and 100 mM in carbonate were irradiated at pH = 8.6 and 12.7 respectively under N_2O . (Dose = 39 Gy/ pulse; Optical path = 1 cm)

The absorption spectrum recorded at 400 ns of the solution at this pH shows a band at 600 nm corresponding to the carbonate radical and moreover it shows two bands at around 290 and 370 nm. These last peaks were found to be characteristic $\text{EDOT}^{+\cdot}$ cationic radical which was previously introduced. On the other hand, in the comparison with the alkaline solution (Figure 3.4), at pH = 12.7 the absorption spectrum shows

two bands at 450 nm and 600 nm corresponding to the open cycle and carbonate radical. Then, when the image recorded at 1 ms is observed, the intensity of dimer absorption spectrum (300 and 370 nm) is higher at pH 8.6 than at pH = 12.7 confirming the action of hydroxyl radical.

We can conclude that carbonate radical is not a good candidate to oxidize EDOT monomer. In fact even if the redox potential is higher than EDOT monomer's one, the formation of carbonate is too slow compared to the addition of oxide radical onto EDOT. Moreover, at pH around 11 as in the case of solution containing 10 mM in carbonate, the equilibrium between oxide and hydroxyl radical seems to be displaced towards the formation of hydroxyl radicals. This radical is very fast to react with monomer, then it is possible to observe the formation of dimer at longer times.

3.2 Azide radicals

The reaction of EDOT with azide radical $\text{N}_3\cdot$ was also studied. In contrast with the reaction of hydroxyl radical, where addition on aromatic ring, hydrogen or electron abstraction are possible, the $\text{N}_3\cdot$ induced oxidation is known to proceed by electron transfer [4].

Three N_2O -saturated aqueous solutions at different concentrations in NaN_3 (10, 100 mM and 1 M respectively) were studied. The azide radical $\text{N}_3\cdot$ is radiolytically prepared by $\text{HO}\cdot$ -induced oxidation of azide anions with a rate constant of $1.2 \cdot 10^{10} \text{ M}^{-1} \text{ s}^{-1}$ in the pH range of 4-13 (solution at 10 and 100 mM of NaN_3) or by oxide radical $\text{O}\cdot^-$ with a rate constant of $3.8 \cdot 10^8 \text{ M}^{-1} \text{ s}^{-1}$ in alkaline solutions (1 M NaN_3) [4]. The characteristic absorption peak of azide radical $\text{N}_3\cdot$ is at 274 nm in the UV region [4]. In our solutions the large absorption band of EDOT monomer at 255 nm avoids the observation of azide radical formation. At nanosecond timescale the absorption spectra of three solutions did not show peaks. When the microsecond was investigated the solution containing 10 mM in NaN_3 showed two peaks at 290 and 370 nm. With the increasing of NaN_3 concentration, the intensity of these peaks decreases. This first result induced the hypothesis of a competition mechanism for hydroxyl radical between a reaction with azide anion and with other species. This thesis was successively confirmed by kinetic study at longer time. The spectra recorded 1 ms after the pulse for the three solutions are displayed in Figure 3.5. The solution less concentrated in sodium azide shows the typical peaks of EDOT dimer at 290 and 370 nm. When the concentration is increased up to 1 M, these peaks disappear proving the action of hydroxyl radical on EDOT rather than azide radical.

On the other hand, when the NaN_3 concentration increases, the hydroxyl radicals are totally converted in azide radicals.

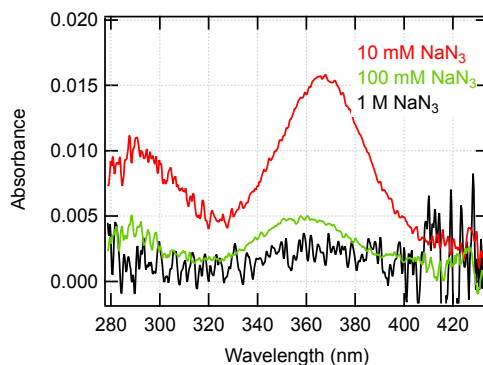


Figure 3.5: Spectra at 1 ms of the aqueous solutions containing 1mM in EDOT and respectively 10, 100 mM and 1 M of NaN_3 under N_2O (Dose = 40 Gy per pulse; Optical path = 1 cm).

But no other peaks are observed at higher concentration in UV region. On the contrary a large absorption band was found at 645 nm (Figure 3.6) at $2\ \mu\text{s}$ after the pulse in the solution containing 1 mM in EDOT and 1 M in NaN_3 .

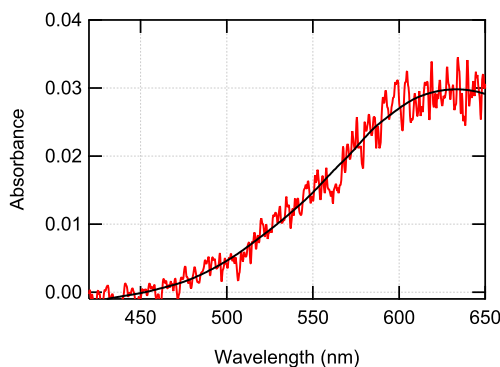


Figure 3.6: Absorption spectrum at $2\ \mu\text{s}$ after the pulse of an aqueous solution containing 1mM in EDOT and 1 M of NaN_3 displaying the characteristic peak of $\text{N}_6^{\cdot-}$ at 645 nm (Dose = 40 Gy/pulse; Optical path = 1 cm).

In literature this transient absorption band is attributed to the $\text{N}_6^{\cdot-}$ radical [5, 6, 7, 8]. The yield of this radical is dependent on the concentration of azide anions. For this reason a high concentration in N_3^- is necessary to detect it [8]. It is formed in the equilibrium reaction:



with an equilibrium constant K of 0.33 [5]. However the rate constant of this equilibrium in water are not reported in literature. So also the azide radical seems to be not a good candidate to polymerize the EDOT molecule.

As a conclusion, at low concentration in N_3^- , HO^\cdot preferentially reacts onto EDOT monomers and do not quantitatively form N_3^\cdot radicals. At high concentration, $N_6^{\cdot-}$ is formed and no EDOT oxidation is observed.

3.3 Sulfate Radicals

Continuing the study on investigation of EDOT kinetics polymerization with other oxidants than hydroxyl radicals, we used the sulfate radical, $SO_4^{\cdot-}$, produced by the reaction of the hydrated electron with persulfate anions, $S_2O_8^{2-}$.

Studies developed by Neta et al. [9] indicate that with many organic compounds, $SO_4^{\cdot-}$ reacts as a more effective oxidant than HO^\cdot because it is more selective to oxidation, [1]. The action of sulfate radical was widely studied on styrene chemical polymerization [9, 10] or radiolysis polymerization [11, 12].

The use of $SO_4^{\cdot-}$ as oxidizing radical was justified by: *i*) its easy and well known radiolytic formation through the reaction of hydrated electrons (produced by water radiolysis) with persulfate anions $S_2O_8^{2-}$ [13, 14], *ii*) its high redox potential ($E^\circ = 2.6$ V)[15] close to that of hydroxyl radical, which should enable it to oxidize EDOT monomers *iii*) its relatively well known reactivity onto organic compounds, $SO_4^{\cdot-}$ generally leads to radical cations[9, 11, 10, 12] and thus, when reacting onto EDOT monomers by the way of radiolysis, it should produce, such as hydroxyl radical, EDOT $^{\cdot+}$ radical cations. However, there are few reports on the synthesis of PEDOT with $SO_4^{\cdot-}$ by chemical methods.

Since sulfate radicals are radiolytically obtained from persulfate anions (known as efficient oxidizing species [16, 17]) which are present in excess in the aqueous medium, we also check the direct chemical reactivity of $S_2O_8^{2-}$ onto EDOT monomers and study the influence of temperature $S_2O_8^{2-}$ induced production of PEDOT.

3.3.1 Thermal reactivity of $S_2O_8^{2-}$ and $SO_4^{\cdot-}$

Aqueous solutions containing both EDOT (5 mM) and $K_2S_2O_8$ (20 mM) were prepared under air at different temperatures (0°C, 25°C and 60°C) in the presence of *tert*-butanol. Thi last is introduced with the aim to reproduce the same experimental conditions of pulse radiolysis study, where the *tert*-butanol scavenges the hydroxyl

radicals $\text{HO}\cdot$ and produced an inert radical (see chapter 1). The reaction kinetics was then followed by UV-Vis absorption spectrophotometry (Figure 3.7) during five hours, which is the time needed for pulse radiolysis experiments.

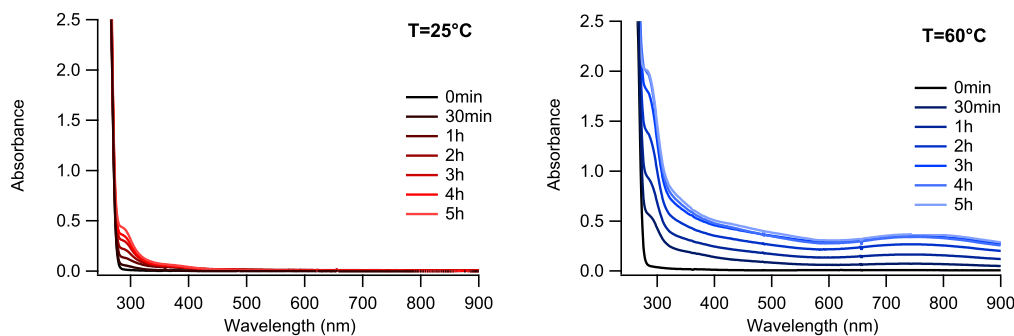


Figure 3.7: Time evolution, over five hours, of the absorption spectra of aqueous solutions containing 5 mM in EDOT, 20 mM in $\text{K}_2\text{S}_2\text{O}_8$ and 0.5 M in *tert*-butanol at $T=25^\circ\text{C}$ on the left and $T=60^\circ\text{C}$ on the right. The spectra were recorded just after solution preparation and after 0.5; 1; 2; 3; 4 and 5 h. Optical path = 0.2 cm, Reference: water.

At $T=25^\circ\text{C}$, absorption spectrum of the solution shows two bands at 290 and 350 nm which increases with time (Figure 3.7). These peaks were attributed, in our previous work, to EDOT_2 dimers [18, 19]. Moreover after more than one day, it appears a large absorption band around 750 nm. According to literature, such an absorption band is characteristic of PEDOT polymers [20]. This observation proves that a slow oxidation of EDOT by persulfate anions takes place at ambient temperature. Nevertheless, only dimers are found five hours after sample preparation.

At 60°C , the polymerization is much faster. Indeed, after only 30 minutes, the large characteristic band of PEDOT polymers can be observed around 750 nm (Figure 3.7). Also, a component appears in the spectrum due to the presence of a yellow-brown suspension in the bulk of the solution. The intensity of the absorption band at 750 nm increases quickly with time over five hours. Such a fast spectral evolution is due to the production of sulfate radicals by heat decomposition of persulfate, which should significantly enhance the oxidation kinetics of EDOT and then the resulting production of PEDOT.

In order to avoid any thermal oxidation of EDOT by both persulfate anion and sulfate radical, the solution containing EDOT (5 mM), $\text{K}_2\text{S}_2\text{O}_8$ (20 mM) and *tert*-butanol was prepared at 0°C and kept in a cooling bath. In these conditions spectral evolution shows a drastic reduction of dimerization kinetics. Indeed a slight increase

in the absorption at 290 nm is visible after 5 hours (Figure 3.8). However this amount is negligible with respect to monomer concentration. It does not affect the reaction of EDOT monomers with sulfate radicals in pulse radiolysis experiment.

Then the kinetic study by pulse radiolysis can be performed at low temperature, assuming that the sulfate radicals react predominantly with EDOT monomers, which concentration is higher than that of dimers.

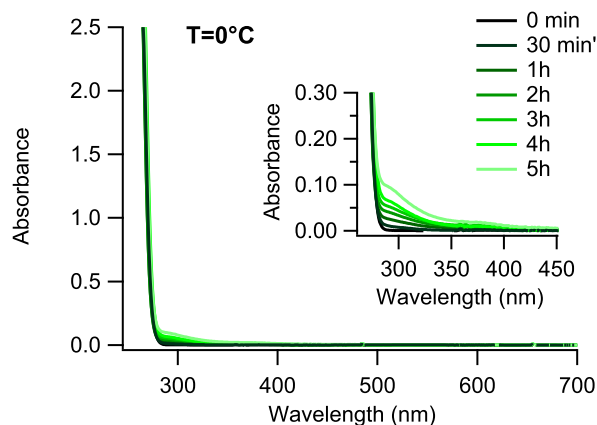


Figure 3.8: Time evolution, over five hours, of the absorption spectrum of aqueous solution containing 5 mM in EDOT, 20 mM in $K_2S_2O_8$ and 0.5 M in *tert*-butanol $T=0^\circ\text{C}$. The spectra were recorded just after solution preparation and after 0.5; 1; 2; 3; 4 and 5 h. Optical path = 0.2 cm, Reference: water. Inset: zoom of the image at 300-450 nm.

3.3.2 Reactivity of $\text{SO}_4^{\cdot-}$ formed by radiolysis

An Ar-saturated aqueous solution containing 5 mM in EDOT, 20 mM in persulfate and 0.5 M in *tert*-BuOH at $\text{pH} = 3.5$ was studied by pulse radiolysis at the temperature of 0°C .

The evolution of absorption of the irradiated solution was investigated in the timescale from 100 ns to 1 ms. As usually, a volume of 200 mL of solution was placed in the reservoir kept at 0°C and connected to the flow cell. The flow rate of the solution was of 100 mL/min and the irradiation dose delivered by the electron beam was 37 Gy/pulse.

At nanosecond timescale, we expected the formation of sulfate radical and the first transient specie produced by the reaction between the sulfate radical and EDOT monomer. In Figure 3.9 the absorption spectrum recorded at 40 ns after the electron

pulse shows three bands at 295, 380 and 455 nm. The absorption band at 455 nm is the sulfate radical which very well known spectrum is characterized by a large band centered at 455 nm and a weak band at 300 nm.

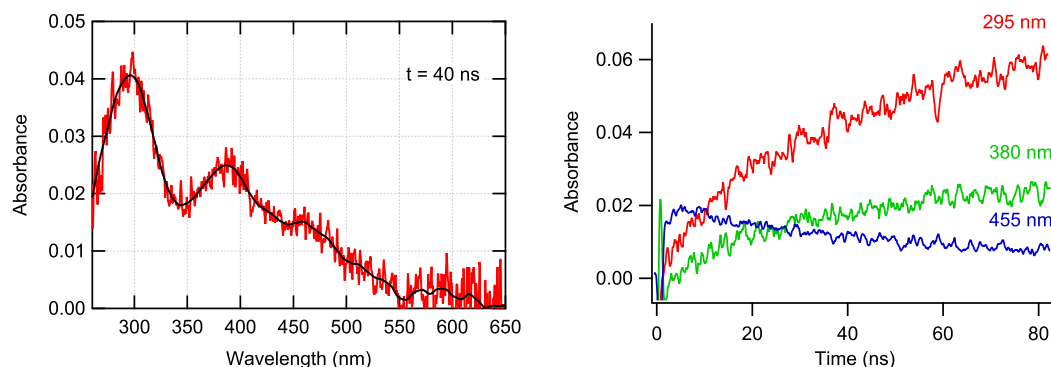


Figure 3.9: Absorption spectrum recorded 40 ns after the pulse of an aqueous solution containing 5 mM in EDOT, 20 mM in persulfate, 0.5 M in *tert*-butanol saturated with argon and irradiated with 37 Gy/pulse, on the left. Evolution of the absorbances at 295, 380 and 455 nm at 100 ns after the pulse, on the right (Optical path 1 cm).

Figure 3.9 depicts the time evolution of the absorbance at the three wavelengths. In order to estimate the rate constant of formation and decay of each peak, the kinetic profile of the electron, recorded at 600 nm, was normalized and subtracted from the three signals. Also the contribution of sulfate radical absorption at 295 and 380 nm was subtracted after normalization of the decay at 455 nm taking into account the ratio of the extinction coefficient for each wavelength.

At 455 nm the sulfate radical is formed in around 10 ns (Figure 3.9) which corresponds to the life time of hydrated electron and then decays according to a pseudo-first order which could be ascribed to the reaction of $\text{SO}_4^{\cdot-}$ with EDOT.

On the other hand, the decay of 455 nm and the formation of the two peaks at 295 and 380 nm are on the same timescale ($\simeq 100$ ns). Indeed the three signals are well fitted by a pseudo-first order reaction (Figure 3.10) and the observed rate constant is the same order with a value of around $k_{obs} = 3.3 \cdot 10^7 \text{ s}^{-1}$.

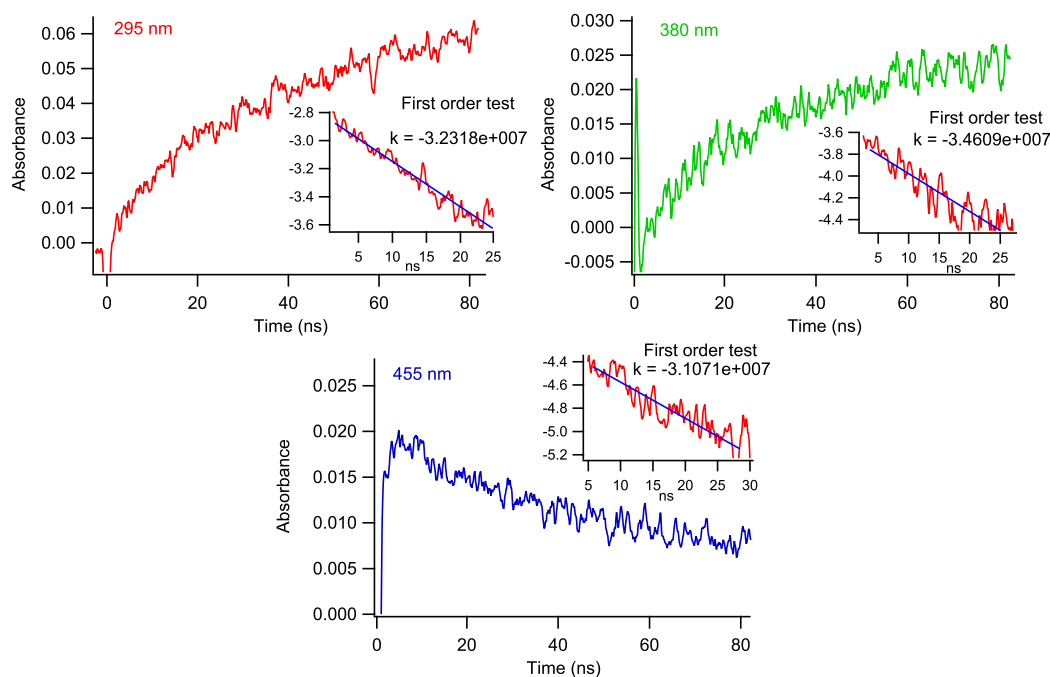


Figure 3.10: Evolution of absorbances at 295, 380 and 455 nm 100 ns after the pulse (Dose=37 Gy/pulse, Optical path =1 cm). Inset pseudo first order kinetic test.

Then, we can assume that the two peaks at 295 and 380 nm belong to the same species A which results from the reaction between EDOT and sulfate radicals. After 600 ns the absorption spectrum of the species A is visible (Figure 3.11).

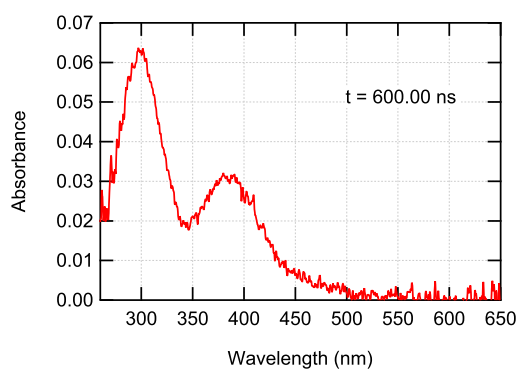


Figure 3.11: Absorption spectrum recorded 600 ns after the pulse of an aqueous solution containing 5 mM in EDOT, 20 mM in persulfate, 5 M in *tert*-butanol saturated with argon (Dose=37 Gy/pulse, Optical Path =1 cm).

At longer time the kinetic study in Figure 3.12 shows the peaks reach their maxima

at around 300 ns. Then, the peak at 295 nm begins to decay. On the other hand, the peak at 380 nm continues to increase slowly. This increase is also visible at 455 nm. Indeed the decay of the peak at 455 nm does not go to zero as expected if the sulfate radical was the only species absorbing at this wavelength.

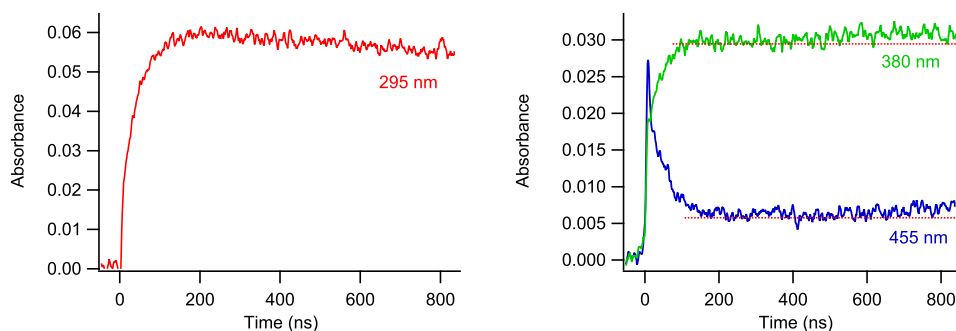


Figure 3.12: Evolution of absorbances at 295, 380 and 455 nm at 1 μ s after the electron pulse. (Dose=37 Gy/pulse, Optical path =1 cm)

This effect can be explained by supposing the formation of another species in this region of wavelengths. This hypothesis was also confirmed by the absorption spectra recorded at longer time.

Two absorption spectra recorded at 5 μ s and 18 μ s are displayed in Figure 3.13. While the spectrum at 5 μ s displays two bands characteristic of species A at 295 and 380 nm, which are nevertheless less intense than at 600 ns, the spectrum at 18 μ s highlights the presence of two new bands at 425 and 520 nm (Figure 3.13). This explains the weak increasing of the absorption at 380 and 455 nm we observed at 1 μ s.

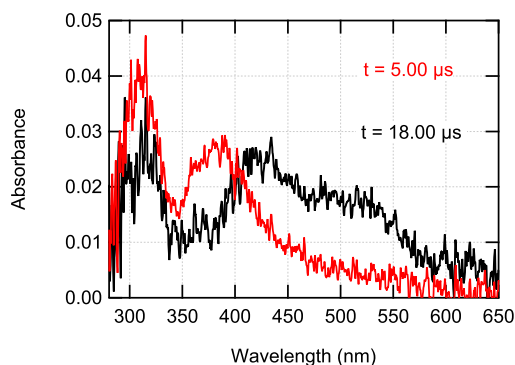


Figure 3.13: Absorption spectrum recorded at 5 and 18 μ s after the pulse of an aqueous solution containing 5 mM in EDOT, 20 mM in persulfate, 0.55 M in *tert*-butanol saturated with argon (Dose=37 Gy/pulse, Optical path =1 cm).

The kinetic investigation on 20 μs shows that the peaks at 425 and 500 nm grow up according to the same kinetics (Figure 3.14). These two peaks are thus characteristic of a second transient species, B. Moreover, an isosbestic point is found at 406 nm characterized by a constant absorbance during the evolution with time of the spectra (Figure 3.14). It is a consequence of the overlaps the absorption spectra of the two transient species, A and B and indicates the direct correlation between the two species: B being the product of the reaction of A.

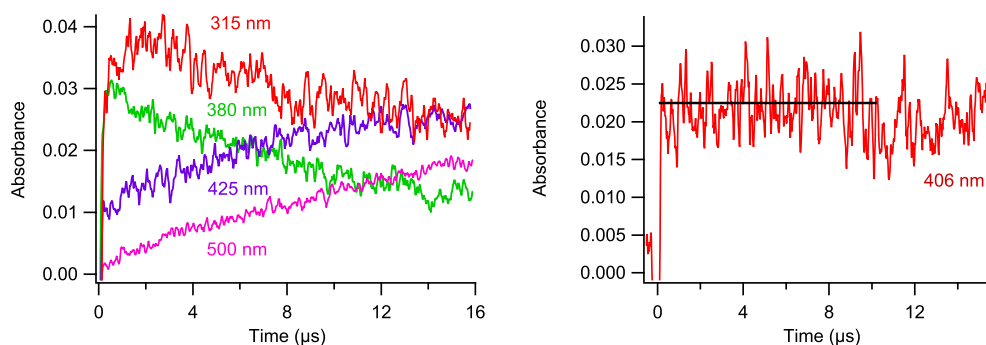


Figure 3.14: Evolution of absorbances at 315, 380, 425 and 500 nm at 20 μs after the electron pulse, on the left. Constant value of the absorbance at 406 nm indicates the presence of an isosbestic point, on the right (Dose = 37 Gy/pulse, Optical path = 1 cm).

As expected from the isosbestic point, the kinetic signals at 380 and 425 nm on each side of the isosbestic point are symmetrical, showing the direct correlation between the two kinetics.

Then, knowing that the species A absorbs at the wavelength 295 and 380 nm, we compared their two kinetics profiles, expecting the same decay.

Note that the kinetics at 295 nm was studied on 315 nm due to the noise of the signal in the UV region on the image recorded at 20 μs . Moreover the Cherenkov signal affects the signal and an increasing appears on the first microsecond.

We found that the two decays follow the same kinetics in the first 10 μs indicating the disappearance of A, then a difference between the two absorbance time evolution occurs on longer timescale. This idea was confirmed by the observation of the absorption spectrum at 40 μs which clearly depicts three bands, at 315, 425 and 500 nm (Figure. 3.15). Probably this spectrum represents the superposition of different spectra.

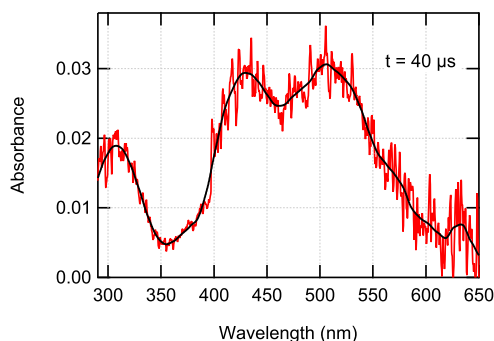


Figure 3.15: Absorption spectrum recorded $40 \mu\text{s}$ after the pulse of an aqueous solution containing 5 mM in EDOT, 20 mM in persulfate, 0.5 M in *tert*-butanol saturated with argon (Dose = 37 Gy/pulse, Optical path = 1 cm).

Indeed the time evolution of the absorbances at these three wavelengths is very different (Figure 3.16).

The peaks at 315 nm decays over $30 \mu\text{s}$ and then the absorbance remains stable. One can suppose that in addition to A species which absorbs at this wavelength and which continuously decays, a new species C is formed. So, the decay is slowed because it corresponds to the overlapping of a decay and the appearance of a new transient species. The peak at 425 nm increases over $30 \mu\text{s}$ whereas the peaks at 500 nm increases rapidly. Again this effect can be explained by the formation of another species (probably again the species C) at the same wavelength. Finally, the time evolution of absorption at 380 nm is depicted to show the disappearance of this absorbance at this timescale, which indicates the total consumption of the species A.

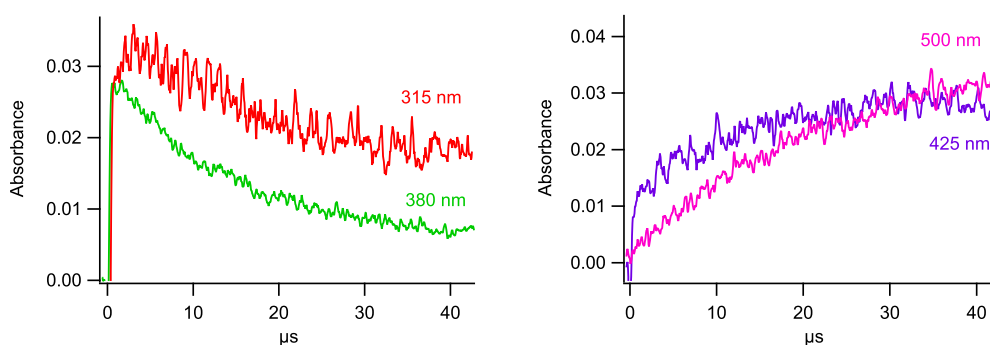


Figure 3.16: Evolution of absorbances at $50 \mu\text{s}$ after the pulse at 315 and 380 nm, on the left and at 425 and 500 nm, on the right (Dose = 37 Gy/pulse, Optical path = 1 cm).

In order to identify the species C, the image recorded 200 μs after the pulse was investigated. The Figure 3.17 displays the absorption spectrum recorded 180 μs after the pulse. It is characterized by two absorption bands, at 315 nm and 500 nm which should be characteristic absorption maxima of C. A weak shoulder at 425 nm is nevertheless still observed indicating at this time that B transient species still remains in the medium.

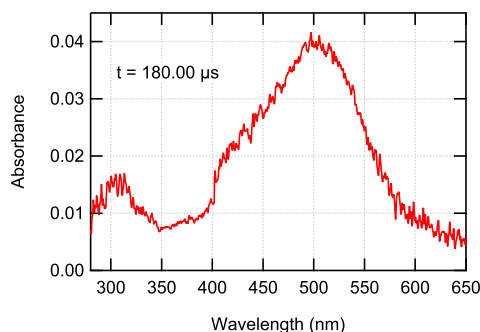


Figure 3.17: Absorption spectrum recorded 180 μs ns after the pulse of an aqueous solution containing 5 mM in EDOT, 20 mM in persulfate, 5 M in *tert*-butanol saturated with argon (Dose = 37 Gy/pulse, Optical path =1 cm).

These three peaks follow different kinetics (Figure 3.18). The peak at 425 nm decays slowly. The peak at 315 nm is stable after 100 μs . The peak at 500 nm reaches the maximum of absorbance at 130 μs and then begins to decay. However the peaks at 315 and 500 nm were previously associated to the species C. As a consequence, the difference in the kinetic evolution of the two peaks at 315 and 500 nm implies the presence of another species D formed at longer time.

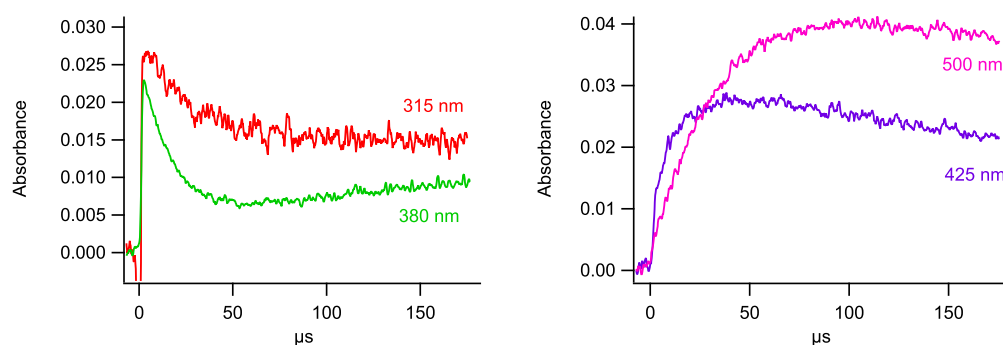


Figure 3.18: Evolution of absorbances at 200 μs after the pulse at 315 and 380 nm, on the left and at 425 and 500 nm, on the right (Dose = 37 Gy/pulse, Optical path =1 cm).

The longer time investigated, 1 ms, enables to recorded an absorption spectrum characterized by three peaks at 315, 360 and 500 nm (Figure 3.19). Even if the overlapping of the spectra does not allow to isolate precisely the species. One can note that 315 nm is the stable band already observed since 60 μ s. The band at 500 nm has decreased and a new band appears at around 360 and 380 nm, the growth of which was observed after 50 μ s (Figure 3.18).

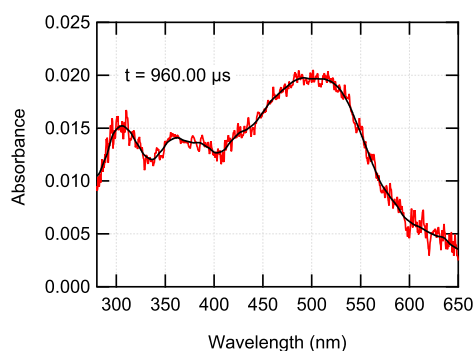


Figure 3.19: Absorption spectrum recorded 960 μ s ns after the pulse of an aqueous solution containing 5 mM in EDOT, 20 mM in sulfate, 5 M in *t*BQH saturated with argon (Dose = 37 Gy/pulse, Optical path =1 cm).

The kinetic study enables to suppose that the species D absorbs at 315 and 360 nm (Figure 3.20). Indeed the absorbance at 315 nm remains stable while the absorbance at 360 nm clearly increases. The kinetics of 425 nm is the convolution of two kinetics: the decay of the species B and the formation of D at 360 nm which affects the profile. Also the species C, which absorbs at 500 nm decreases slowly over 1 ms.

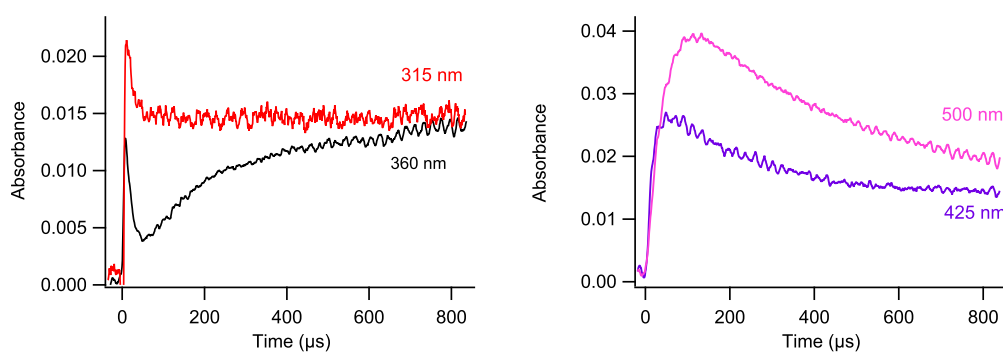


Figure 3.20: Evolution of absorbances at 1 ms after the pulse at 315 and 380 nm, on the left and at 425 and 500 nm, on the right (Dose=37 Gy/pulse, Optical path =1 cm).

So this kinetic study reveals the presence of at least four transient species (A,B,C and D). The first one, species A, is formed in 100 ns from the reaction between sulfate radical and EDOT monomer. It absorbs at 295 and 380 nm. An isosbetic point at 406 nm shows that the species A is converted into the species B absorbing at 425 and 500 nm in a few μ s. then, the kinetic evolution over 50 μ s depicts the formation of the species C at 315 and 500 nm. Finally over 1 ms the transient species D appears and is observable at 360 and probably at 315 nm. In the Table 3.1 all absorbing transient species detected during the kinetics study are listed.

Transient Species	Absorption Maxima (nm)
$\text{SO}_4^{\cdot-}$	455
A	295 380
B	425 500
C	315 500
D	315 360 500

Table 3.1: Absorption maxima of transient species identify.

The strong overlapping of the spectra of all these species and consequently of their kinetics does not allow to clearly highlight the absorption spectra and to precisely evaluate the rate constants. It was only possible in the case of the species A to determine a pseudo-first order reaction of formation and the corresponding observed rate constant, $k_{obs} = 3.5 \cdot 10^7 \text{ s}^{-1}$. In order to deconvolute and identify the absorption spectra, we proceeded again with a theoretical study.

3.3.3 Spectrokinetic investigation

As in the case of hydroxyl radical, we proceeded in the spectrokinetic analysis of the streak camera images obtained in the presence of persulfate. The investigations allowed to identify the number of species and a candidate reaction mechanism. The global analysis on the full range of times and wavelengths was performed by assembling the streak camera images at different time scales (from 100 ns to 1 ms) and wavelength scales (290 – 398 and 400 – 600 nm) the same irradiated aqueous solution (Figure 3.21).

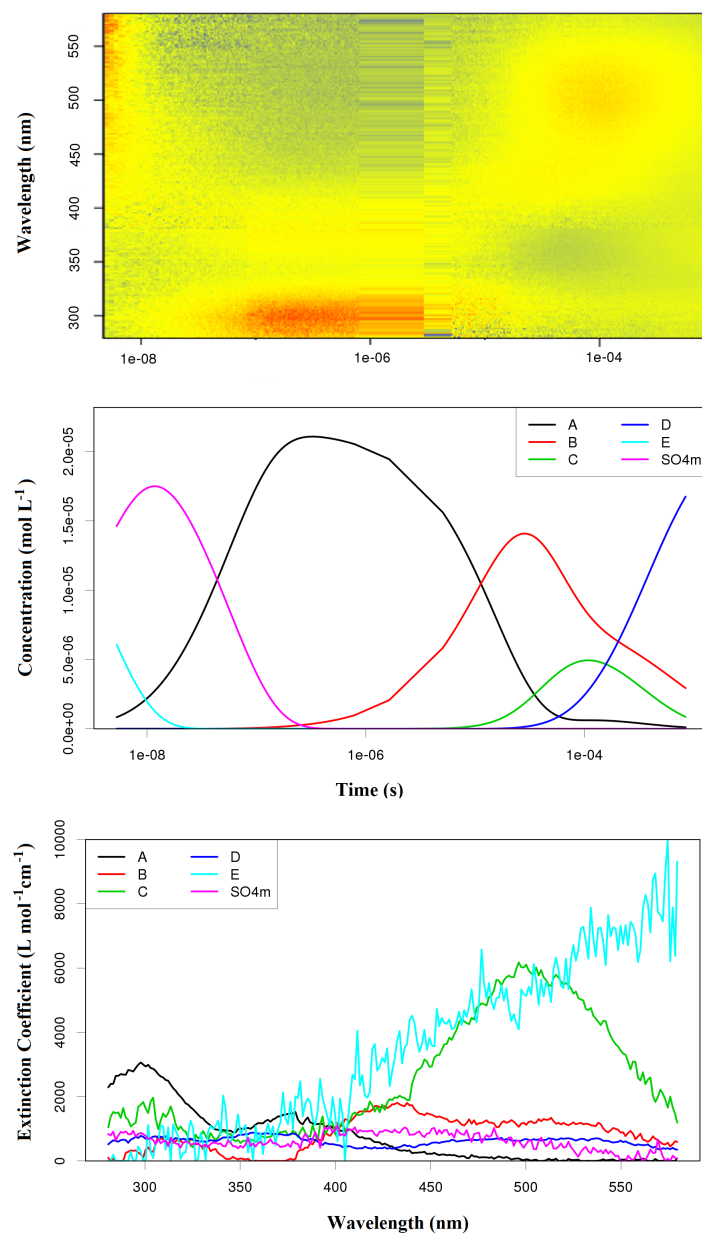
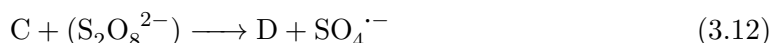
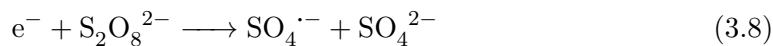


Figure 3.21: Kinetic analysis of the experimental spectrokinetic matrix with a four-species model (a); best-fit kinetics (b) and best fit spectra (c) for the model scheme. Each spectrum is associated with a concentration profile according to the color code.

As we observed on the various spectra and kinetics described above, the SVD analysis of the obtained image shows that the spectrokinetic matrix can be factored into four components (A, B, C and D) (Figure 3.21).

Moreover the deconvoluted kinetics allows to propose the following chemical mechanism:



The deconvolution of the kinetics and the spectra of the four species is depicted in Figure 3.21.b and c respectively.

The first reaction describes the well known conversion of the hydrated electrons in sulfate radical with a rate constant $k = 1.1 \cdot 10^{10} \text{ L mol}^{-1} \text{ s}^{-1}$. The sulfate radical react with EDOT monomers present in excess according to a pseudo-first order reaction to produce a species A absorbing at 300 and 360 nm. The species A is then transformed in B which absorbs at 425 and 500 nm. Successively the species B dimerizes in C. The absorption spectrum of C shows mainly a large band at 500 nm which was previously detected in the experimental analysis at 200 μs .

Finally the species C decreases according to a first order or pseudo-first order reaction giving D which absorbs at 360 and 500 nm. As it will be explain later, this reaction is due to the oxidation of C by the only species which is still present in excess at this time range: $S_2O_8^{2-}$ anions.

The mechanism proposed here may neglect the formation of other minority species which could be also produced during EDOT/ $SO_4^{\cdot-}$ interaction or in the recombination of sulfate radical. Indeed, it is not possible to distinguish such minority species. The best fit was obtained of four species (A, B, C and D). Then the rate constants, $k_{3.9}$, $k_{3.10}$, $k_{3.11}$ and $k_{3.12}$ were estimated:

$$k_{3.9} = 3.3 \cdot 10^9 \text{ L mol}^{-1} \text{ s}^{-1}$$

$$k_{3.10} = 6.8 \cdot 10^4 \text{ s}^{-1}$$

$$k_{3.11} = 2.8 \cdot 10^8 \text{ L mol}^{-1} \text{ s}^{-1}$$

$$k_{3.12} = 5.1 \cdot 10^5 \text{ L mol}^{-1} \text{ s}^{-1}$$

These values are in good agreement with rate constants deduced from experimental pulse radiolysis study. The same order of magnitude is found for the formation of the

first species A. However, due to the approximation included in the model, these values can be overestimated.

The Table 3.2 resumed the results obtained by SVD investigation.

Transient Species	Absorption Maxima (nm)	SVD Deconvolution (nm)
$\text{SO}_4^{\cdot-}$	455	455
A	295 - 380	300 - 370
B	425 - 500	425 - 500
C	315 - 500	300 - 500
D	315 - 360 - 500	300 - 360 - 500

Table 3.2: Absorption maxima of kinetic study and SVD decomposition.

3.3.4 Absorption spectra simulation

In order to identify the unknown species A, B, C and D involved in the mechanism of EDOT oxidation, the simulations were performed using MC/DFT method previously introduced. Firstly, the sulfate radical spectrum was simulated. The good agreement between the experimental spectrum recorded at 300 ns after the pulse and simulated one is shown in Figure 3.22.

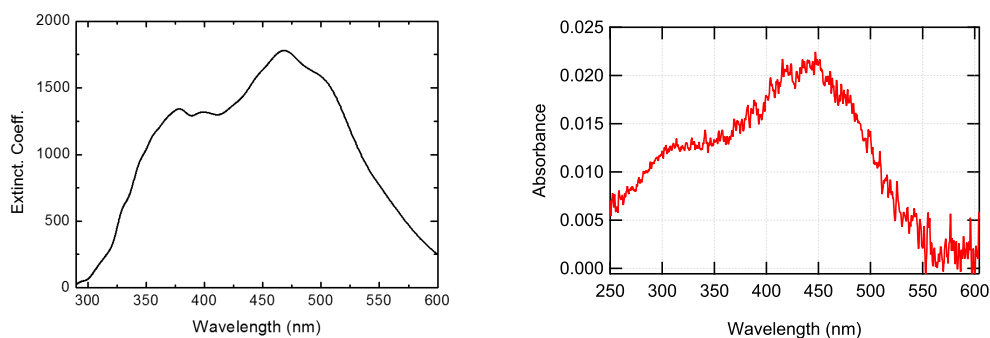
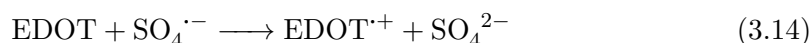
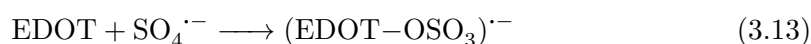


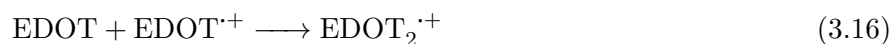
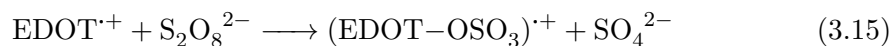
Figure 3.22: Absorption spectrum of sulfate radical simulated by MC/DFT(B3LYP) method on the left. Absorption spectrum of sulfate radical recorded at 300 ns after the pulse of an aqueous solution containing 20 mM in persulfate $\text{K}_2\text{S}_2\text{O}_8$ and 0.5 M in *tert*-butanol saturated with argon (Dose = 42 Gy/pulse, Optical path = 1 cm), on the right.

Then, we focused our study to the species produced by the reaction 3.9 between EDOT monomer and sulfate radical. For this direct reaction between these two species we considered the production of two potential species, which could corresponds to the species A:

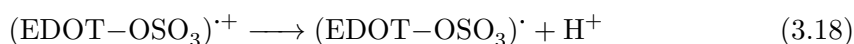
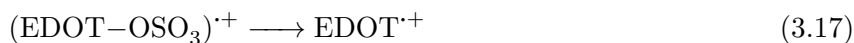
- $(\text{EDOT-OSO}_3)^{\cdot-}$ which comes from the addition of $\text{SO}_4^{\cdot-}$ onto EDOT via C-O bond, reaction 3.13
- $\text{EDOT}^{\cdot+}$ which comes from a simple electron abstraction (one-electron oxidation of EDOT), reaction 3.14:



After reaction 3.9, the species A disappears according to a first or pseudo-first order reaction (3.10). If a pseudo-first order is supposed, the species A disappears with the species in excess in the medium, $\text{S}_2\text{O}_8^{2-}$ or EDOT, by the reactions:

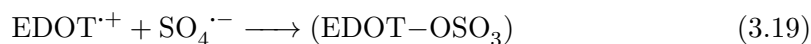


If a first order reaction takes places, the disappearing of the species B can be described by the reactions:



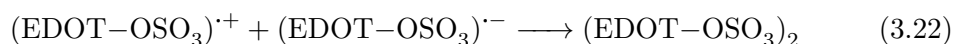
Then, the possible adduct radicals are the cation sulfate adduct radical $(\text{EDOT-OSO}_3)^{\cdot+}$, the anion sulfate adduct radical, $(\text{EDOT-OSO}_3)^{\cdot-}$ or the neutral sulfate adduct radical $(\text{EDOT-OSO}_3)^{\cdot}$.

However the second order reaction between cation radical $(\text{EDOT-OSO}_3)^{\cdot+}$ and sulfate anion radical which could produce also the neutral species $(\text{EDOT-OSO}_3)^{\cdot}$ in the reaction:



cannot take place since the reaction 3.10 is a first order. As reported by the found scheme mechanism, the species B dimerizes according to the reaction 3.11 and leads to

C. From the potential B species, several charged and uncharged dimers can be formed. We particularly considered the neutral and stable one $(\text{EDOT-OSO}_3)_2$. By starting from the previous radicals, different reactions can produce this stable species:



The same dimer is formed. Nevertheless it can be take different isomers differing by the position of H atoms that we distinguish in the text with the following notation. The *isomer1* displays the H atoms on the C. The *isomer2* shows the H atoms on the oxygen of the adduct OSO_3 . And finally the hybrid dimers non conjugated, *isomer3*, depicts an H atom on the C and another on the oxygen of the adduct OSO_3 .

The DFT calculations showed that the hybrid dimer, *isomer3* is the most stable ($E = 0$ eV), on the other hand the conjugated dimer, *isomer1* is unstable ($E=0.292$ eV) and less stable ($E = 0.737$ eV) is the *isomer2*.

In Table 3.3 the name formula and chemical structure of all molecules studied in this work are depicted.

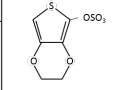
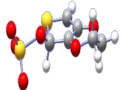
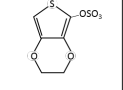
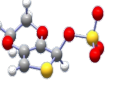
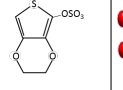
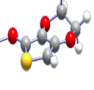
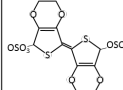
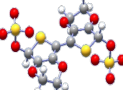
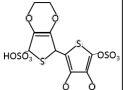
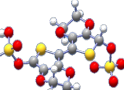
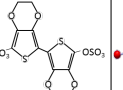
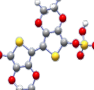
$(\text{EDOT-OSO}_3)^{\cdot+}$			$(\text{EDOT-OSO}_3)^{\cdot-}$			$(\text{EDOT-OSO}_3)^{\cdot}$		
$(\text{EDOT-OSO}_3)_2$ <i>Isomer 1</i>			$(\text{EDOT-OSO}_3)_2$ <i>Isomer 2</i>			$(\text{EDOT-OSO}_3)_2$ <i>Isomer 3</i>		

Table 3.3: Names, formula and chemical structures of all molecules potentially involved in the mechanism in the presence of sulfate radicals.

In Figure 3.23, all simulated absorption spectra of all these species at ambient temperature are shown. Note that the spectrum of hybrid dimer *isomer3* was not simulated.

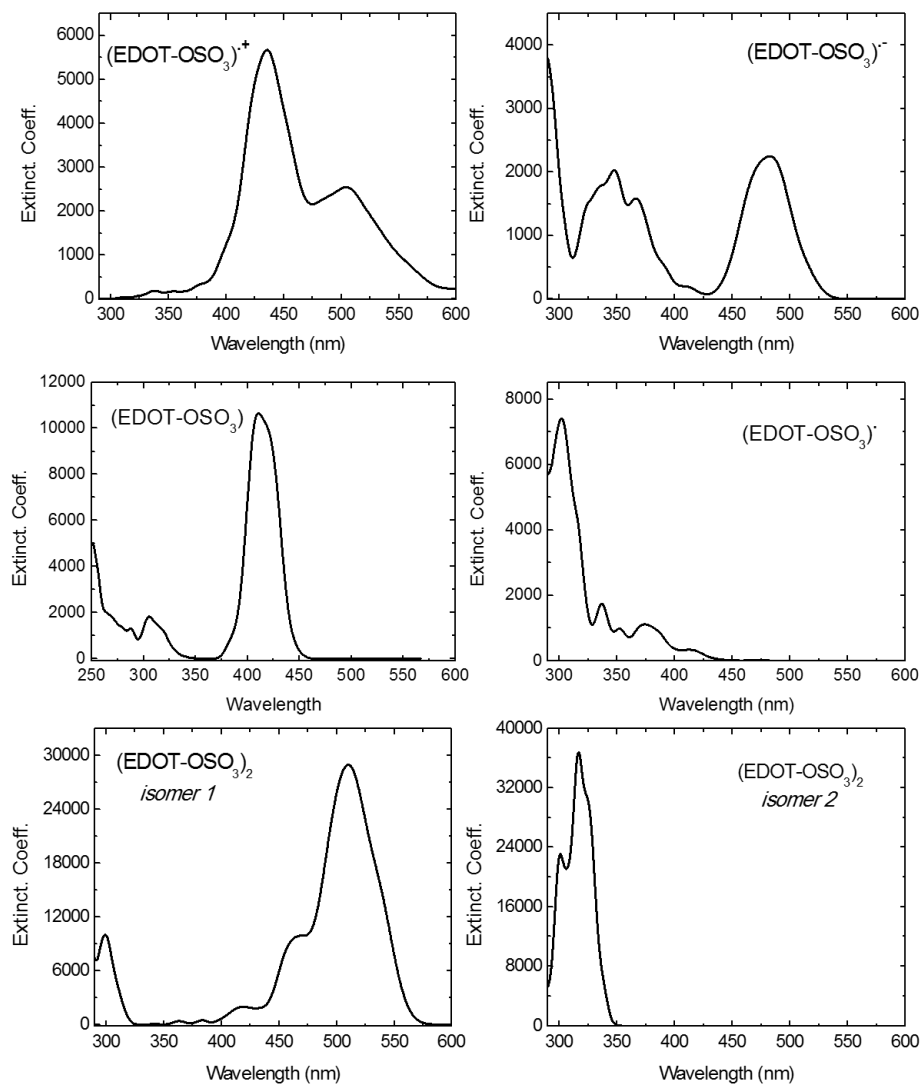


Figure 3.23: Simulated absorption spectra of all molecules of Table 3.3 at ambient temperature by using MC/DFT (B3LYP) method.

3.3.5 Species identification

In the experimental study, we showed that the first transient species, A, is produced by the reaction between EDOT monomer and sulfate radical. So, it should be one of the two radicals previously introduced: $\text{EDOT}^{\cdot+}$ or $(\text{EDOT-OSO}_3)^{\cdot-}$ produced in the reactions 3.13 or 3.14. The experimental absorption spectrum of species A shows mainly two peaks at 295 and 360 nm.

Since the simulated spectrum of $(\text{EDOT}-\text{OSO}_3)^{\cdot-}$ shows clearly absorption maxima at 350 and 500 nm, this anion radical can not be the first species. On the other hand, the simple cation radical, $\text{EDOT}^{\cdot+}$ has been shown in chapter 2 to present two bands at around 300 and 360 nm, which is in good agreement with the spectrum of the first deconvoluted species A and also with the experimental spectrum recorded at 100 ns. As a consequence one can assume that the first reaction corresponds to the formation of the cation radical $\text{EDOT}^{\cdot+}$ (eq. 3.14).

Then the species A, namely $\text{EDOT}^{\cdot+}$, is transformed in species B via first or pseudo first order reaction 3.10 depicted in the scheme mechanism deduced from spectrokinetic analysis. Starting from $\text{EDOT}^{\cdot+}$, no plausible first order mono-molecular reaction was found. On the contrary, pseudo-first order bi-molecular reactions are found possible.

Indeed, in the solution the species in excess, EDOT monomers and persulfate anions, $\text{S}_2\text{O}_8^{2-}$, are present. So the cation radical $\text{EDOT}^{\cdot+}$ can react with one of them.

In the reaction between EDOT and cation radical $\text{EDOT}^{\cdot+}$ a cation dimer could be produced. However, as demonstrated in chapter 2, its spectrum shows an intense peak at 360 nm which is not present in deconvoluted spectrum. Moreover, as previously discussed, the persulfate anion, $\text{S}_2\text{O}_8^{2-}$, is very reactive species and one can hypothesize the formation of cationic radical $(\text{EDOT}-\text{OSO}_3)^{\cdot+}$ by reaction 3.15. The strong reactivity of persulfate anions with organic molecules was widely studied in literature [10, 21, 22]. Indeed the reaction between persulfate anions and organic monomer is often proposed as one of radical chain reaction in persulfate chemistry, [21, 23, 24].

When comparing the simulated spectrum (bands at 420 and 500 nm) of cation adduct radical and the deconvoluted spectrum of the species B one can find clear a the strong similarity.

Nevertheless in its deconvoluted spectrum, the species B shows a peak at around 310 nm not present in the simulated one. In the same way the simulated absorption spectrum of neutral adduct radical, $(\text{EDOT}-\text{OSO}_3)^{\cdot}$ displays a peak in this region. Then it is possible that an equilibrium (protonation/deprotonation, reaction 3.18) takes place between the two sulfate adduct radicals which differ by one proton. Then we can suppose that the spectrum of the species B is combination of the two adduct sulfate radicals spectrum: $(\text{EDOT}-\text{OSO}_3)^{\cdot+}$ and $(\text{EDOT}-\text{OSO}_3)^{\cdot}$ formed by the reactions 3.15 and 3.18.

Note that this assumption is not in contradiction with the spectra and kinetics deconvolution. Indeed, if the two species are present in the solution, their kinetics are the same and is can not be possible to distinguish them. A study in pH can be useful to prove the presence of the two species.

As shown by the mechanism proposed in spectrokinetics analysis, the species B dimerizes and a species C is formed according to reaction 3.11. This species shows a large band of absorption at 500 nm and a weak band at around 300 nm (Figure 3.17 and 3.21). Among the simulated absorption spectra of neutral adduct dimers, only $(\text{EDOT-OSO}_3)_2$ spectrum shows the same bands. This result is not unexpected. Indeed by starting from the two adduct sulfate radicals, $(\text{EDOT-OSO}_3)^{+\cdot}$ and $(\text{EDOT-OSO}_3)^{\cdot-}$, the dimer $(\text{EDOT-OSO}_3)_2$ can be produced in the two reactions 3.20 and 3.21.

Finally, the species D is formed on the ms time scale. The deconvoluted absorption spectrum is characterized by three bands at 300, 360 and 500 nm. This spectrum can not definitely be identified. However it can be suggested that it is the overlapping of two species, the adduct dimer absorbing at 500 nm and the more stable configuration of adduct dimer absorbing at 300 and 360 nm. Moreover the static absorption spectrum recorded after the pulse radiolysis experiment shows two bands at around 300 and 360 nm (Figure 3.24).

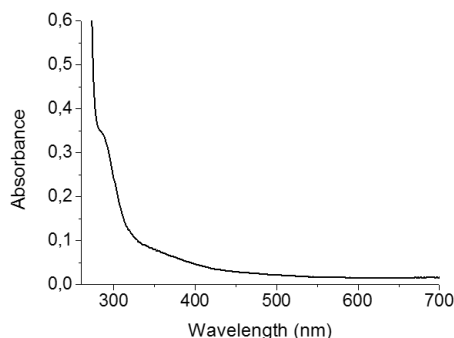
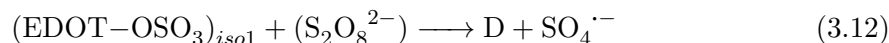
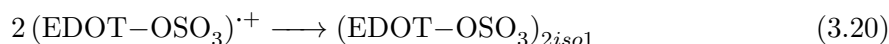
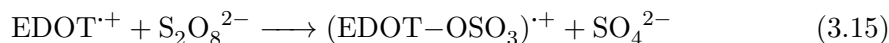


Figure 3.24: Static absorption spectrum after pulse radiolysis irradiation of an aqueous solution containing 5 mM in EDOT, 20 mM in $\text{K}_2\text{S}_2\text{O}_8$ and 0.5 M in *tert*-butanol. The path length was 0.2 cm and the reference was distilled water.

This could be explained by the totally conversion of adduct dimers into more stable adduct dimer. Note that the intensity of the two peaks is at 300 and 360 inverted due to the presence of characteristic peaks of EDOT monomers and $\text{S}_2\text{O}_8^{2-}$ anions which extend to 280 and affects the spectrum.

If the last species is the more stable dimer, absorbing at 300 and 360 nm this means that the species D observed at 1 ms is an intermediate one which probably reacts after this time to give the final dimer. It could be interesting to observe the kinetics at time longer than 1 ms, time limit of the streak camera.

We can conclude to proposed the following mechanism:



where the characteristic bands of each species are listed in table.

Transient Species	Absorption Maxima (nm)	SVD Deconvolution (nm)	Species
SO ₄ ^{·-}	455	455	SO ₄ ^{·-}
A	295 - 380	300 - 370	EDOT ^{·+}
B	425 - 500	425 - 500	(EDOT-OSO ₃) ₂ ^{·+}
C	315 - 500	300 - 500	(EDOT-OSO ₃) _{2iso1}
D	315 - 360 - 500	300 - 360 - 500	D

Table 3.4: Absorption maxima of kinetic study and SVD decomposition

3.3.6 PEDOT-SO₄ synthesis

After the successful polymerization by hydroxyl radical, we investigated the polymerization by using sulfate radical with the aim to improve the method. Indeed according to the step-by-step polymerization process, already highlighted when hydroxyl radical was used, we expected that sulfate radical should also lead to PEDOT conducting polymers. In order to avoid any thermal oxidation of EDOT by both persulfate anion and sulfate radicals, as previous mentioned, the solution containing EDOT (5 mM), K₂S₂O₈ (20 mM) and *tert*-butanol was prepared at 0°C and kept in a cooling bath under argon atmosphere. Nevertheless when installed in the accelerator room, the sample reached after few hours the temperature of the room, which was usually lower than ~ 20°C. This enables to neglect the thermal polymerization.

Then, a series of 2000 consecutive pulses (84 kGy, 42 Gy per pulse at a repetition frequency of 5 Hz) was used in order to produce a concentration of 30 mM in SO₄^{·-} radicals and to ensure complete oxidation of EDOT monomers and quantitative synthesis of PEDOT polymers. The UV-Vis absorption spectrum (Figure 3.25) of the solution drastically changed upon irradiation.

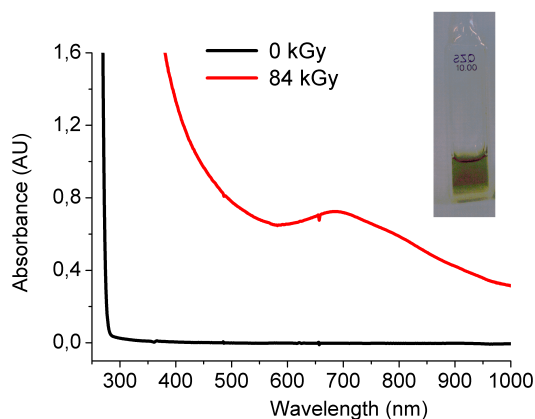


Figure 3.25: UV-Vis spectrum of solution containing 5 mM EDOT 20 mM $K_2S_2O_8$ and 0.5 M *tert*-butanol under argon irradiated by 2000 picoseconds pulses of 42 Gy at frequency of 5 Hz (Optical path = 0.2 cm). Inset: image of cell with solution after irradiation.

After irradiation, a large absorption band is observable around 690 nm together with a continuous scattering of the analyzing light. This result is in good agreement with the polymerization obtained by thermal polymerization at 60°C (Figure 3.7), suggesting that PEDOT polymers were successfully produced by electron beam irradiation.

In order to investigate the morphology of radiosynthesized polymers in liquid phase the solution obtained from radiolysis experiments was observed by cryo-TEM. Representative image (Figure 3.26) shows the presence of dispersed platelet-shaped nanoparticles with a size ranging between 50 and 400 nm. Contrarily to what we previously observed by cryo-TEM in the case of PEDOT polymers synthesized by radiolysis in the presence of hydroxyl radicals as oxidizing species, no spherical PEDOT nanoparticles (neither isolated nor aggregated) are observed, this time, by cryo-TEM in aqueous solution. In an early explanation we supposed that these nanoplates are made of or contain PEDOT polymers. However the presence of $K_2S_2O_8$ or eventually *tert*-butanol into these nano objects can not be excluded.

Nevertheless, the observation of such platelet-shaped nanoparticles is not surprising since comparable structures have already been found and described in literature in the case of PEDOT polymers synthesized by emulsion polymerization in the presence of an iron salt, namely $Fe_2(SO_4)_3$ [25].

IR spectroscopy was used in order to study the chemical nature of the obtained nanoparticles (Figure 3.27). The turbid solution obtained after electron irradiation was lyophilized in order to collect the solid phase in the absence of any residual water

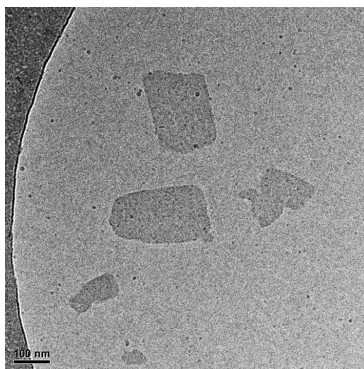


Figure 3.26: Cryo-TEM image of PEDOT synthesized by electron beam irradiation (84 kGy) in the presence of $K_2S_2O_8$. Platelet-shaped nanoparticles are observed

molecules which could be trapped in the polymer containing solid phase. The ATR-FTIR spectra were recorded in the wave number range $1800-600\text{ cm}^{-1}$. In Figure 3.27, ATR-FTIR spectrum of the obtained powder supposed to contain PEDOT was compared with those of EDOT monomer, *tert*-butanol and pure potassium persulfate salt ($K_2S_2O_8$) and PEDOT-OH.

One can note, in the spectrum of the powder obtained by electron beam irradiation, the absence of the characteristic bands of *tert*-butanol in the PEDOT spectrum. In particular, the intense peak at 912 cm^{-1} visible in alcohol spectrum has disappeared, proving the quantitative elimination of the alcohol from the sample thanks to lyophilization. However the presence of three large intense bands around 1265 , 1054 and 700 cm^{-1} demonstrate the presence of persulfate salt $K_2S_2O_8$ salt. The main conclusion here is that lyophilization, which enables *tert*-butanol extraction, does not lead to $K_2S_2O_8$ elimination. Due to the very small amount of powder which was collected after each irradiation, washing of the sample, in order to remove $K_2S_2O_8$ salt, was impossible in our experimental conditions. Nevertheless, we can note that complete elimination of inorganic salts from polymer nanoparticles is not so easy.

In the spectrum of obtained powder, in addition to intense absorption bands of $K_2S_2O_8$, one can observe the presence of many bands which fit well with those of PEDOT polymers previously synthesized by radiolysis by using hydroxyl radicals as oxidizing species, even if these bands appear slightly displaced, (Figure 3.27) may be due to the functionalization of PEDOT polymers by OSO_3 groups. The spectrum of the powder obtained after electron beam irradiation displays vibrations at 1484 , 1446 and 1363 cm^{-1} which are attributable to C=C and C-C stretching modes in the thiophene ring. The vibrations observed at 1301 , 1236 , 1168 and 1054 cm^{-1} are assigned to

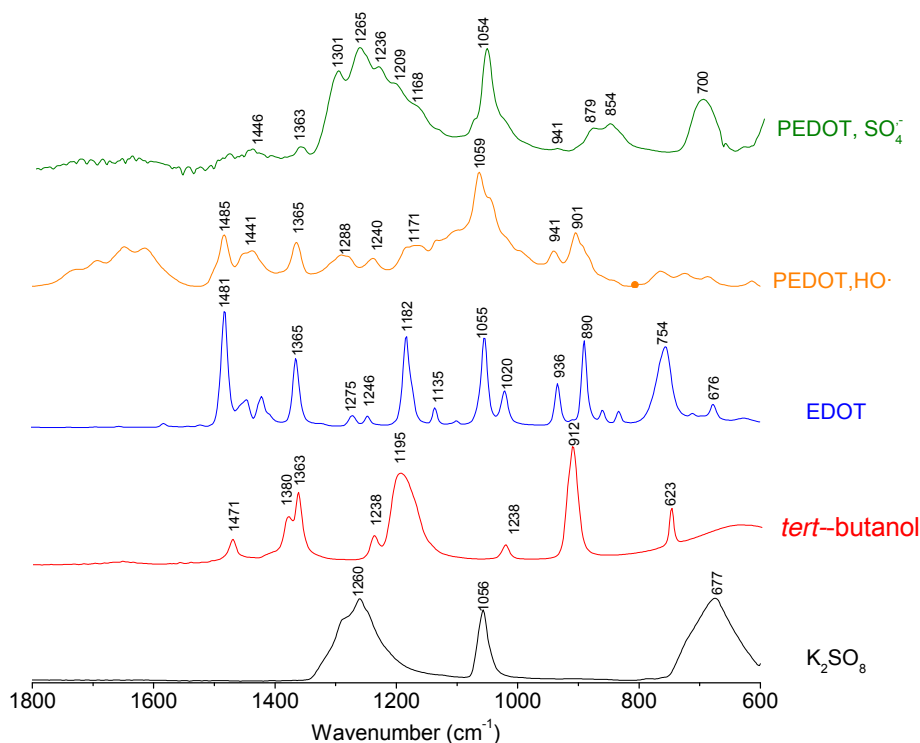


Figure 3.27: ATR-FTIR spectra of (–) PEDOT synthesized by electron beam irradiation (84 kGy) in the presence of $\text{K}_2\text{S}_2\text{O}_8$ using SO_4^- as oxidant (after lyophilization), (–) PEDOT polymers previously synthesized by radiolysis using HO^\cdot as oxidant (after lyophilization), (–) pure EDOT, (–) pure *tert*-butanol and (–) (–) pure $\text{K}_2\text{S}_2\text{O}_8$ salt.

the stretching modes of the ethylenedioxy groups (C-C and C-O-R-O-C). The vibration modes of C-S bond which are present in the thiophene ring can be observed at 941, 879 and 854 cm^{-1} .

Thus, the resulting solid powder obtained after lyophilisation contains, in addition to $\text{K}_2\text{S}_2\text{O}_8$ salt, PEDOT polymers. Note that the intense C-H stretching band at 754 cm^{-1} , observed in spectrum of EDOT monomer (Figure 3.27), is clearly absent PEDOT spectrum. This show that under electron beam irradiation, EDOT polymerization quantitatively took place thanks to α,α' -coupling reactions and that no more EDOT monomers remain present in the sample after irradiation.

In order to characterize the morphology after a deposition procedure, the dried powder, obtained by lyophilization, was dissolved in ethanol, deposited, dried and finally imaged and characterized by AFM-IR nanospectroscopy as shown in Figure 3.28.

According to the AFM images of the sample recorded in contact mode (Figure 3.28),

the bottom dark areas having no thickness correspond to the substrate. The topography of the sample, displayed as the bright areas, correspond to the thicker regions made up of more or less flat platelet-shaped nanoparticles. This AFM observation agrees well with the particles morphology previously observed in aqueous solution by Cryo-TEM (Figure 3.26). The image depicts an agglomeration of globular nanoparticles with size ranging between 50 and few hundred nm, while some plates appear huge, while some plates appear huge, with a micrometric size.

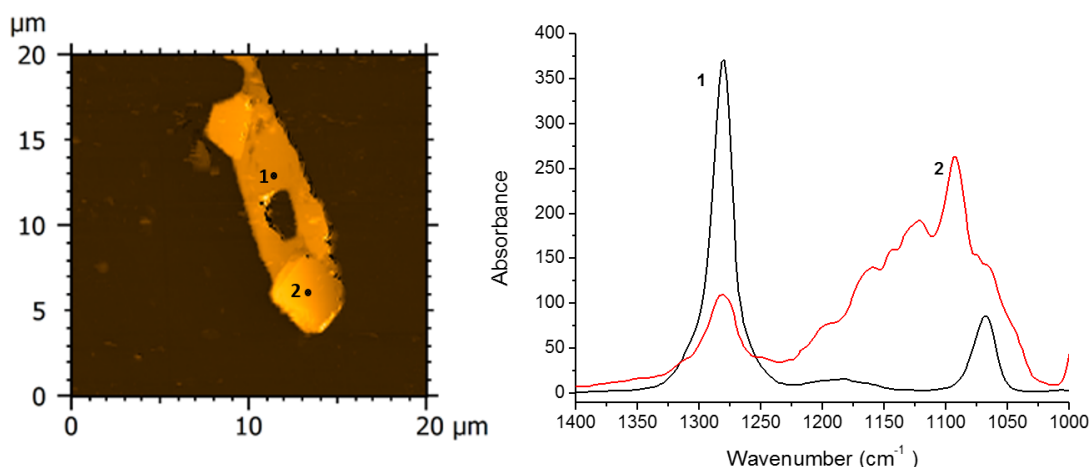


Figure 3.28: AFM-IR characterization of PEDOT polymers synthesized by electron beam irradiation (84 kGy) of the powder obtained by the irradiation of an aqueous solution containing 5 mM in EDOT, 20 mM in persulfate, 5 M in *tert*-butanol on the left and AFM topographic images in contact mode (on the left), and local AFM-IR spectra recorded when the tip is located in positions 1 and 2 of images (on the right).

Since no *tert*-butanol remains in the sample after lyophilisation, as demonstrated by ATR-FTIR spectroscopy, we conclude that the nanoplates, which were observed by cryo-TEM and which are also observed by AFM, do not contain alcohol. Also their morphology is not affected by the presence of *tert*-butanol.

In order to check the chemical nature of these plates, the sample was observed by AFM-IR from 1400 to 1000 cm^{-1} . Since changing the wavelength on a fixed position of the tip gives a local infrared spectrum, we also checked the chemical homogeneity of the platelet-shaped particles by recording infrared spectra at different positions.

The local IR-spectrum (black one) recorded in position 1, which corresponds to a thin zone, fits well with that of pure $\text{K}_2\text{S}_2\text{O}_8$ salt (Figure 3.27) since it displays two intense peak 1260 and 1056 cm^{-1} . This means that these regions are mainly made of potassium persulfate. Differently the local IR spectrum (red one) recorded in position

2 (Figure 3.28), which belongs to a thicker zone, displays a more complex structure. Indeed the two bands characteristic of $K_2S_2O_8$ are still present, but additional absorption peaks and shoulder, which are the signature of PEDOT polymers already described and in agreement with literature [26], appear at 1236, 1209, 1168 and 1054 cm^{-1} .

When we carefully observe by AFM, with a good spatial resolution, another area (Figure 3.29), it is possible to detect the presence of closely packed globular nanostructures (few hundred nm to one μm in diameter) which seem to be adsorbed at the surface of the plates. This AFM observation agrees well with the morphology of PEDOT polymers previously synthesized by radiolysis [27] even if the particle size appears larger here. We deduce that these more or less spherical nanoparticles are made up of radiosynthesized PEDOT polymers. Each globular structure should correspond to the self-assembly of independent amorphous PEDOT polymer chains which interact all together by Hydrogen-bonds ([28]).

Even if we did not remove $K_2S_2O_8$ from the irradiated sample in order to obtain PEDOT polymers, we were able to discriminate PEDOT polymers and $K_2S_2O_8$ inorganic salt and to probe the local chemical composition of PEDOT nano-structures thanks to the use of high resolution AFM microscopy, coupled with infrared nanospectroscopy.

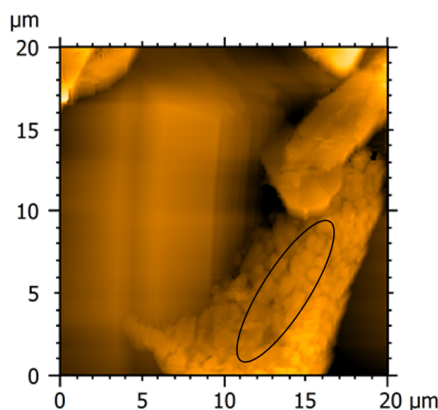


Figure 3.29: AFM-IR characterization of PEDOT polymers synthesized by electron beam irradiation (84 kGy) of the powder obtained by the irradiation of an aqueous solution containing 5 mM in EDOT, 20 mM in persulfate, 5 M in *tert*-butanol.

In order to highlight the role of persulfate in the final morphology of the observed nanoparticles, ethanolic solution of pure $K_2S_2O_8$ was also imaged. The AFM observation (Figure 3.30), after deposition and drying procedure in air, shows the presence of platet-shaped particles in the absence of any adsorbed globular structures (Figure 3.30).

The morphology of these materials is not surprising since the ionic solid particles (composed here of K^+ cations and $S_2O_8^{2-}$ anions in electrostatic interaction) are usually characterized by regular shape. This definitely demonstrates that the poly-dispersed nanoplates observed in cryo-TEM and AFM, are made of $K_2S_2O_8$. Nevertheless, the observation by cryo-TEM of $K_2S_2O_8$ particles, in aqueous solution, is rather surprising, even if their size is much smaller than that of particles imaged by AFM. Indeed, potassium persulfate salt is very soluble in water, even at low temperatures, and the concentration we used is lower than $K_2S_2O_8$ solubility. Maybe, during cryo-TEM experiments, when samples are quench-frozen by being plunged into liquid ethane, while water crystallization is avoided, $K_2S_2O_8$ ionic solid crystallization happens.

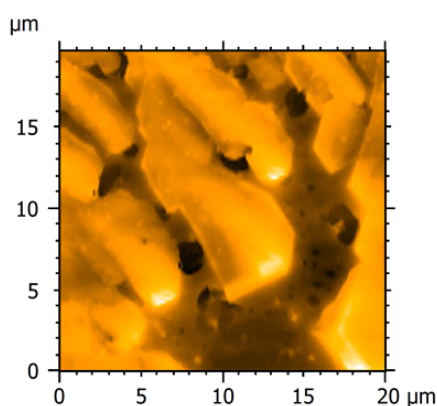


Figure 3.30: AFM-IR characterization of pure $K_2S_2O_8$ salt. AFM topographic image in contact mode.

In order to check whether the substrate nature affects the morphology of PEDOT/ $K_2S_2O_8$ particles, the lyophilized powder, obtained after a 84 kGy electron beam irradiation, was deposited onto carbon film to aluminum mounts and observed by SEM microscopy. In Figure 3.31.a representative images are shown. A polydispersed platet-shaped particles are observed, demonstrating that the nature of the substrate has no influence on the morphology of our system. In addition, as observed in Figure 3.31.a, some aggregated globular structures of PEDOT are once again found adsorbed on the $K_2S_2O_8$ ionic solid particles. Some of these particles are surrounded in the figure for clarity. Note that only the bigger PEDOT particles (1 μm in diameter) can be observed by SEM.

In order to check the morphology of PEDOT polymers in the absence of any $K_2S_2O_8$ particles which could remain in excess after irradiation, we irradiated, under argon at-

mosphere at 0°C, an aqueous solution containing 5 mM in EDOT, 20 mM in $K_2S_2O_8$ and 0.5 M in *tert*-butanol at a dose of 168 kGy (4000 pulses, 42 Gy/pulse). This irradiation dose is theoretically high enough to transform all $S_2O_8^{2-}$ anions into sulfate radicals. As a consequence, no more $K_2S_2O_8$ particles should remain present in the sample after irradiation. The lyophilized powder obtained after electron beam irradiation at 168 kGy was observed by SEM microscopy (Figure 3.31b). Contrarily to what we had foreseen, some platelet-shaped particles were still observable. But clearly, they were smaller and less numerous than those we got at 84 kGy. Due to the lower effective remaining concentration in potassium persulfate, we predominantly observed rod-shaped particles which had never been detected at lower doses. As it can be seen in Figure 3.31, the relatively low amount of $K_2S_2O_8$ in the sample enables the better observation of PEDOT polymers (some of them are surrounded in the figure for clarity). These polymers appear as aggregated globular structures, not free once again, but in the vicinity of $K_2S_2O_8$ nanorods or plates. Evidently, since the irradiation at 84 kGy was enough to ensure the quantitative polymerization of EDOT, no effect of the dose was expected, at 168 kGy, on the number and the size of PEDOT polymers.

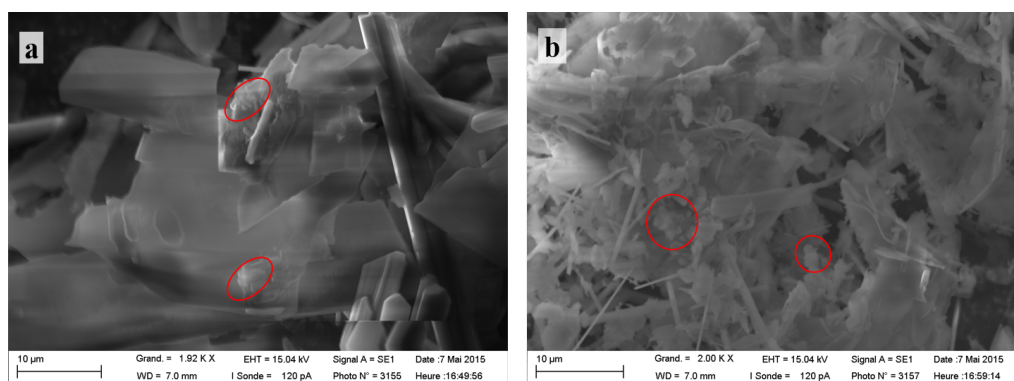


Figure 3.31: SEM images of PEDOT polymers synthesized by electron beam irradiation in the presence of $K_2S_2O_8$ at (a) 84 kGy and (b) 168 kGy

3.4 Conclusion

In this chapter we introduced the study of the growth mechanism of PEDOT by three different oxidizing radicals, such as carbonate, azide and sulfate radicals.

In the case of radicals, such as the azide or the carbonate radicals, the study showed that these radicals are not able to induce EDOT monomers oxidation and then PEDOT polymerization. Indeed at low concentrations, carbonate reacts too slowly with

EDOT while at higher concentration it was not possible to induce the reaction between carbonate and EDOT monomer. On the other hand, azide radical has a too low redox potential, so it does not react with EDOT but with itself to form $N_6^{\cdot-}$ radical.

We concluded the present study with the use of sulfate radical. The pulse radiolysis study realized at low temperature to avoid the thermal polymerization coupled with molecular simulations and spectrokinetic analysis was used to identify the mechanism of $SO_4^{\cdot-}$ -induced oxidation of EDOT in aqueous solution. We determined the mechanism of EDOT oxidation by sulfate radical and the rate constants of the first reactions involved in the growth mechanism. Moreover thanks to a comparison with the theoretical study it was possible to determine the spectra of some of the first transient species. The results showed that after one pulse only a dimer is formed. This suggest that the growth of polymer proceeds by a step-by-step mechanism. Nevertheless, note that contrarily to the case of HO^{\cdot} the EDOT dimers are here functionalized by sulfate groups.

Electron irradiation was finally used to produce PEDOT polymer. Starting from EDOT monomers dissolved in water at $0^{\circ}C$, in the presence of potassium persulfate, $K_2S_2O_8$, as sulfate radical precursor, PEDOT was synthesized in aqueous solution by using a series of accumulated electron pulses. This methodology enabled complete EDOT oxidation and quantitative *in situ* PEDOT polymerization through a step-by-step oxidation mechanism. PEDOT polymers synthesized by electron beam irradiation form a relatively stable yellow-brown suspension which was characterized by a large absorption band around 700 nm. The chemical nature of PEDOT polymers was confirmed by ATR-FTIR spectroscopy, while their morphology was checked in solution by cryo-TEM microscopy and after lyophilisation and deposition by SEM. Also, high resolution AFM microscopy, coupled with infrared nanospectroscopy, was used to probe the local chemical composition of the nanostructures generated by electron beam irradiation. The results demonstrated that PEDOT polymers form globular nanostructures which were always, and whatever the characterization technique, observed self-assembled and adsorbed at the surface of platelet-shaped $K_2S_2O_8$ particles. Nevertheless, at this stage of the work we are not able to confirm the functionalization of PEDOT polymers by sulfate group.

The present results show the versatility of our methodology based on pulsed electron beam irradiation, and highlight the efficiency of alternative oxidizing radicals, such as sulfate radicals for the preparation of nanostructured conducting polymers.

Bibliography

- [1] Pedatsur Neta, Robert E Huie, and Alberta B Ross. Rate constants for reactions of inorganic radicals in aqueous solution. *Journal of Physical and Chemical Reference Data*, 17(3):1027–1284, 1988.
- [2] George V Buxton, Clive L Greenstock, W Phillips Helman, and Alberta B Ross. Critical review of rate constants for reactions of hydrated electrons, hydrogen atoms and hydroxyl radicals $\cdot\text{OH}/\cdot\text{O}^-$ in aqueous solution. *Journal of physical and chemical reference data*, 17(2):513–886, 1988.
- [3] James L Weeks and Joseph Rabani. The pulse radiolysis of deaerated aqueous carbonate solutions. i. transient optical spectrum and mechanism. ii. pk for oh radicals1. *The Journal of Physical Chemistry*, 70(7):2100–2106, 1966.
- [4] Zeev B Alfassi and Robert H Schuler. Reaction of azide radicals with aromatic compounds. azide as a selective oxidant. *The Journal of Physical Chemistry*, 89(15):3359–3363, 1985.
- [5] John Butler, Edward J Land, A John Swallow, and Walter Prutz. The azide radical and its reaction with tryptophan and tyrosine. *Radiation Physics and Chemistry (1977)*, 23(1-2):265–270, 1984.
- [6] Mark S Workentin, Brian D Wagner, Janusz Lusztyk, and Danial DM Wayner. Azidyl radical reactivity. n_6^- . as a kinetic probe for the addition reactions of azidyl radicals with olefins. *Journal of the American Chemical Society*, 117(1):119–126, 1995.
- [7] Mark S Workentin, Brian D Wagner, Fabrizia Negri, Marek Z Zgierski, Janusz Lusztyk, Willem Siebrand, and Danial DM Wayner. N_6^- . spectroscopic and theoretical studies of an unusual pseudohalogen radical anion. *The Journal of Physical Chemistry*, 99(1):94–101, 1995.
- [8] Ajit Singh, Grant W Koroll, and Robert B Cundall. Pulse radiolysis of aqueous solutions of sodium azide: reactions of azide radical with tryptophan and tyrosine. *Radiation Physics and Chemistry (1977)*, 19(2):137–146, 1982.
- [9] P Neta, V Madhavan, Haya Zemel, and Richard W Fessenden. Rate constants and mechanism of reaction of sulfate radical anion with aromatic compounds. *Journal of the American Chemical Society*, 99(1):163–164, 1977.

- [10] NA McAskill and DF Sangster. A pulse radiolysis study of the reaction of the sulfate radical ion in aqueous solutions of styrene. *Australian Journal of Chemistry*, 32(12):2611–2615, 1979.
- [11] Qiu Dai, Yunjing Li, Lei Zhai, and Wenfang Sun. 3, 4-ethylenedioxythiophene (edot)-based π -conjugated oligomers: facile synthesis and excited-state properties. *Journal of Photochemistry and Photobiology A: Chemistry*, 206(2):164–168, 2009.
- [12] IM Kolthoff, PR O’connor, and JL Hansen. Mechanism of emulsion polymerization of styrene with persulfate as activator in the absence and presence of mercaptan and a retarder. *Journal of Polymer Science*, 15(80):459–473, 1955.
- [13] Om P Chawla and Richard W Fessenden. Electron spin resonance and pulse radiolysis studies of some reactions of peroxydisulfate (so4. 1, 2). *The Journal of Physical Chemistry*, 79(24):2693–2700, 1975.
- [14] Justine Criquet and Nathalie Karpel Vel Leitner. Electron beam irradiation of aqueous solution of persulfate ions. *Chemical Engineering Journal*, 169(1):258–262, 2011.
- [15] Yang Deng and Casey M Ezyske. Sulfate radical-advanced oxidation process (sr-aop) for simultaneous removal of refractory organic contaminants and ammonia in landfill leachate. *Water research*, 45(18):6189–6194, 2011.
- [16] D A. House. Kinetics and mechanism of oxidations by peroxydisulfate. *Chemical reviews*, 62(3):185–203, 1962.
- [17] Yusuf G Adewuyi and Nana Y Sakyi. Simultaneous absorption and oxidation of nitric oxide and sulfur dioxide by aqueous solutions of sodium persulfate activated by temperature. *Industrial & Engineering Chemistry Research*, 52(33):11702–11711, 2013.
- [18] Youssef Lattach, Ariane Deniset-Besseau, Jean-Michel Guigner, and Samy Remita. Radiation chemistry as an alternative way for the synthesis of pedot conducting polymers under soft conditions. *Radiation Physics and Chemistry*, 82:44–53, 2013.
- [19] Cecilia Coletta, Zhenpeng Cui, Pierre Archirel, Pascal Pernot, Jean-Louis Marignier, and Samy Remita. Electron-induced growth mechanism of conducting polymers: A coupled experimental and computational investigation. *The Journal of Physical Chemistry B*, 119(16):5282–5298, 2015.

- [20] HJ Ahonen, J Lukkari, T Hellström, J Mattila, and J Kankare. Characterisation of poly (3, 4-ethylenedioxythiophene) films polymerised in aqueous media. *Synthetic metals*, 119(1-3):119–120, 2001.
- [21] A Ledwith and PJ Russell. Cation radicals: The mechanism of initiation by peroxydisulphate ion in emulsion polymerization of styrene. *Journal of Polymer Science: Polymer Letters Edition*, 13(2):109–112, 1975.
- [22] KI Seo and IJ Chung. Reaction analysis of 3, 4-ethylenedioxythiophene with potassium persulfate in aqueous solution by using a calorimeter. *Polymer*, 41(12):4491–4499, 2000.
- [23] Kun-Chang Huang, Richard A Couttenye, and George E Hoag. Kinetics of heat-assisted persulfate oxidation of methyl tert-butyl ether (MTBE). *Chemosphere*, 49(4):413–420, 2002.
- [24] Ar A Berlin. Kinetics of radical-chain decomposition of persulfate in aqueous solutions of organic compounds. *Kinet. Catal.(Engl. Transl.);(United States)*, 27(1 PT 1), 1986.
- [25] Olga Pyshkina, Aleksejs Kubarkov, and Vladimir Sergeyev. Poly (3, 4-ethylenedioxythiophene): synthesis and properties. 2010.
- [26] Xinrui Zhong, Guoxia Fei, and Hesheng Xia. Synthesis and characterization of poly (3, 4-ethylenedioxythiophene) nanoparticles obtained through ultrasonic irradiation. *Journal of applied polymer science*, 118(4):2146–2152, 2010.
- [27] Zhenpeng Cui, Cecilia Coletta, Rolando Rebois, Sarah Baiz, Matthieu Gervais, Fabrice Goubard, Pierre-Henri Aubert, Alexandre Dazzi, and Samy Remita. Radiation-induced reduction–polymerization route for the synthesis of pedot conducting polymers. *Radiation Physics and Chemistry*, 119:157–166, 2016.
- [28] Youssef Lattach, Cecilia Coletta, Srabanti Ghosh, and Samy Remita. Radiation-induced synthesis of nanostructured conjugated polymers in aqueous solution: Fundamental effect of oxidizing species. *ChemPhysChem*, 15(1):208–218, 2014.

Chapter 4

Pyrrole oxidation and polypyrrole synthesis

4.1 Introduction

Polypyrrole (PPy) is one of the mostly investigated conducting polymers because of its good environmental stability, facile synthesis and high conductivity. Generally, polymerization of pyrrole monomers (Py) into PPy could be achieved by traditional chemical and electrochemical methods. Although the synthesis of PPy polymers has been widely studied for a long time, the mechanism of polymerization of pyrrole is today a controversial subject. Wide studies were focused on [1, 2, 3], but no mechanism is today universally accepted. Most of studies concern the electro-polymerization [1, 4, 5], where oxidative polymerization of pyrrole into polypyrrole proceeds via one electron oxidation of monomer into cation radical which is supposed to be the first transient species involved. Then this cation associates with another cation radical to form the 2,2-bipyrrole, and so on to polypyrrole [5, 6]. Several studies suggest the chemical polymerization of pyrrole as first order with respect to Pyrrole monomer [7, 8]. However recently Tan and Ghandi [9] proposed a mechanism which involves the formation of cation radical in the first step which further reacts with neutral monomer. This is followed by oxidation and deprotonation to yield the dimer, which again will be oxidized to dimeric radical cation which will react with neutral monomer again, and so on.

Concerning alternative radiolytical method, only few studies focused on the mechanism of Py oxidation. The most detailed studies on the use of radiolytical method are Lillie *et al.*'s [2] and Hapiot *et al.*'s works [3].

Lilie's mechanism

In the mechanism proposed by Lilie (Fig. 4.1), pyrrole monomer is oxidized by hydroxyl radical. The reaction induces the formation of an adduct radical (PyOH) \cdot which can dimerize or be protonated (PyHOH) \cdot^+ , if it is in an acidic solution. The pK_a of these two forms was found to be 4.5. Then the protonated radical (PyHOH) \cdot^+ can also dimerize or eventually undergo a ring opening. In figure 4.1 a synthesis of Lilie's results is presented.

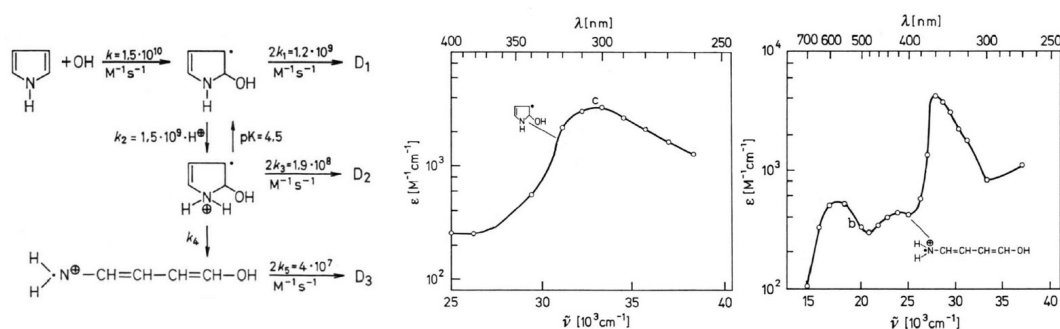


Figure 4.1: Mechanism of HO \cdot -induced pyrrole oxidation proposed by Lilie et al. (on the left). Absorption spectra of adduct radical (on center) and of the open ring (on the right). Figures from ref.[2].

Hapiot's work

Hapiot and his collaborators worked largely on pyrrole [3, 5, 6]. Generally their work concerns the electrochemically induced oxidation. However in a comparative investigation, photolysis and radiolysis techniques were used to detect the radicals involved in the mechanism of bipyrrrole oxidation. Their results showed that the chain length increase takes place by a step-by-step mechanism which involves the formation of cation radical, the dimerization and the deprotonation (Figure 4.2). Moreover the observation of pH effect demonstrated that in alkaline solution the formation of neutral bipyrrrole radical prevents the conjugation of dimers.

However, these interesting results are not sufficient to define the mechanism of polymerization. In fact, if in Lilie's study the formation of cation radical is not considered, in Hapiot's work the hydroxyl radical is not involved in the mechanism. Indeed a scavenger is used to transform the hydroxyl radical into another oxidant species ($\text{CO}_3^{\cdot -}$ or $\text{Br}_2^{\cdot -}$) and the complete conversion of hydroxyl radical is assumed.

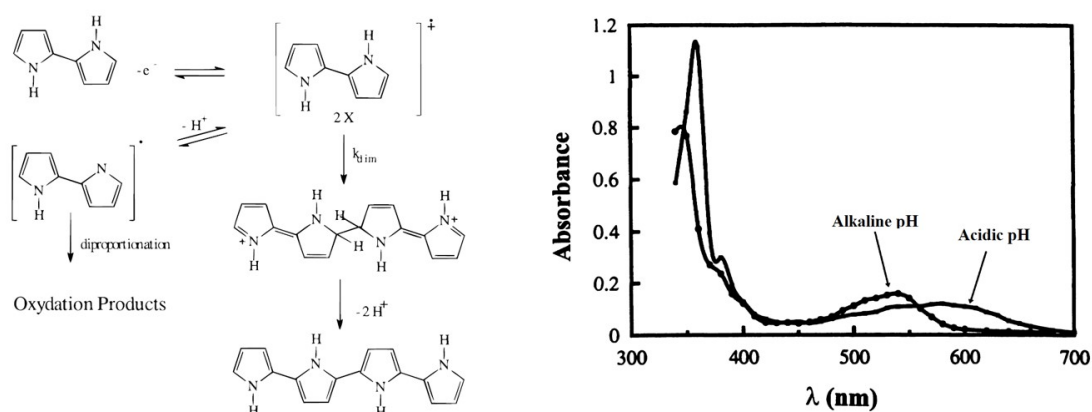


Figure 4.2: Mechanism proposed in Hapiot's work on left. The absorption spectra of neutral bipyrrole radical in alkaline solution and cation bipyrrole radical in neutral solution (on right). Figure from ref.[5].

Our aim in the present work is to identify the mechanism of polymerization by considering all the actors playing a possible role in the system. Thanks to the pulse radiolysis and time resolved absorption spectroscopy, we were able to define the first steps of PPy growth in different conditions (pH and oxidizing species).

Finally, as in EDOT study, polypyrrole synthesis by electron beam irradiation was undertaken. Note that the radiolytic synthesis of polypyrrole has already been studied in our laboratory. Indeed Cui *et al.* [10] succeeded in the synthesis of polypyrrole by using γ -radiation. In fact, the oxidation of pyrrole monomers by hydroxyl radicals, produced in the water radiolysis, led to the formation of a black suspension attributed to polypyrrole.

A detailed investigation on the morphology of these radiosynthesized polymes by using several techniques of microscopy (Figure 4.3) showed the formation of spherical nanoparticles. Moreover a comparative study on the electrical conductivity of chemical or radio-synthesized polypyrrole showed that the electrical conductivity of radio synthesized polypyrrole ($5.7 \cdot 10^{-2} \text{ S}\cdot\text{cm}^{-1}$) is nearly five time higher than that of polypyrrole synthesized by chemical route ($1.2 \cdot 10^{-2} \text{ S}\cdot\text{cm}^{-1}$).

Starting from these encouraging results, this work has been oriented to the synthesis of polypyrrole by the means of electron beam irradiation. This study will be the subject of the last section of this chapter.

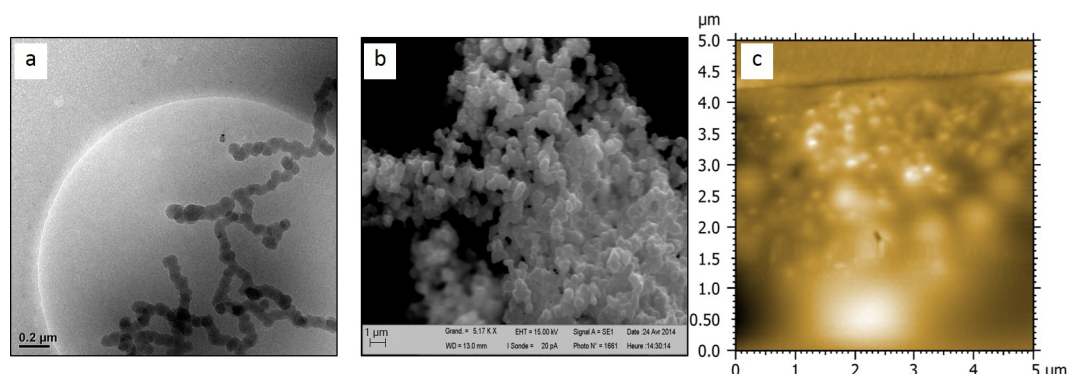


Figure 4.3: Images showing the globular nanostructures of radio-synthesized PPy at 72 kGy 4.3 starting from an aqueous solution containing 20 mM in Py under N_2O . **a:** Cryo-TEM image, **b:** SEM image after liophylization and **c:** AFM topographic image in contact mode.

4.2 HO^\bullet -induced Py oxidation

4.2.1 Nanosecond time scale investigation

The study of growth mechanism of PPy started by an investigation which concerns the HO^\bullet -induced oxidation of Pyrrole monomer. The radiolysis of N_2O -saturated aqueous solution containing Py monomers leads to the formation of the very strong oxidant hydroxyl radical (redox potential of 1.8 V_{SHE} at neutral solution [11]) which should react with Py by addition H-abstraction or e^- abstraction. The first reaction between hydroxyl radical and Pyrrole monomer was investigated on nanosecond time range. An aqueous solution containing 100 mM in pyrrole at $pH = 6$ was irradiated with a dose of 50 Gy per pulse. The solution circulated with a flow rate of 100 mL/ min.

As in the case of Lilie's study the first species obtained from Py oxidation displays an intense peak at 305 nm and a large weak band at 400 nm (Figure 4.4). When the time evolution of the absorbance was investigated, we noted that the appearance of this transient species A at 305 nm seems to fit well with the decay of the absorption at 600 nm, characteristics of the hydrated electron. However the decay of electron produces hydroxyl radical which absorbs in the UV region of the spectrum (and which is not visible with the Streak Camera), so electron decay can't be directly related to the formation of the species A at 305 nm. This fact let us investigate the kinetic equations of the two main reactions involved in these first steps. The electron decay and the production of the first transient species A are described by the following reactions:

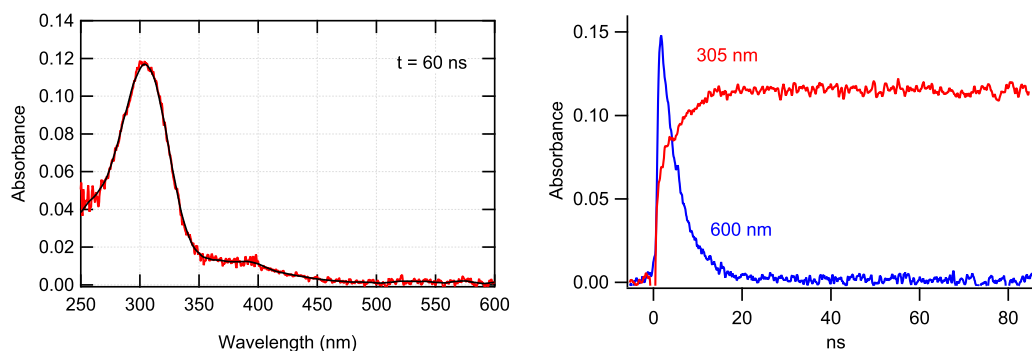
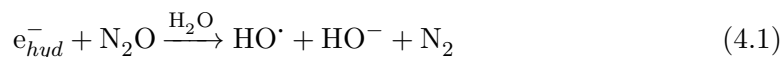


Figure 4.4: Absorption spectrum (on the left) of the first transient species produced at 60 ns after the pulse (50 Gy per pulse) in an aqueous solution containing 100 mM of Pyrrole under N₂O. Time evolution of the absorbances (on right) at 305 nm and at 600 nm over 100 ns after the pulse.



Let k_1 be the rate constant of the first equation 4.1. So the rate of hydrated electron disappearance is given by

$$\frac{d[e_{hyd}^-]}{dt} = -k_1[N_2O][e_{hyd}^-] = -\tilde{k}_1[e_{hyd}^-] \quad (4.3)$$

where $\tilde{k}_1 = k_1[N_2O]$ is k_{obs} since N₂O is considered as a constant. So time evolution of electron concentration is

$$[e_{hyd}^-]_t = [e_{hyd}^-]_0 e^{-\tilde{k}_1 t} \quad (4.4)$$

which fits well the decay observed at 600 nm on Figure 4.4. Since HO[•] radical is, at the same time, produced by the first reaction and consumed by the second one, the evolution of [HO[•]] is related to [e_{hyd}⁻] and [A] by the following identity

$$\frac{d[HO^\bullet]}{dt} = -\frac{d[e_{hyd}^-]}{dt} - \frac{d[A]}{dt} \quad (4.5)$$

which, by integrating (note $[A]_0 = 0$), gives

$$[\text{HO}\cdot]_t = [\text{HO}\cdot]_0 + [e_{hyd}^-]_0 - [e_{hyd}^-]_t - [A]_t. \quad (4.6)$$

Now, let k_2 be the rate constant of the second equation 4.2 and $\tilde{k}_2 = k_2[\text{Py}]$ the k_{obs} associated ($[\text{Py}]$ is considered as constant). The rate equation is

$$\frac{d[A]}{dt} = \tilde{k}_2[\text{HO}\cdot]. \quad (4.7)$$

So by using 4.5, one obtains finally that time evolution of $[\text{HO}\cdot]$ solves the following differential equation

$$\frac{d[\text{HO}\cdot]}{dt} + \tilde{k}_2[\text{HO}\cdot] = [e_{hyd}^-]_0 \tilde{k}_1 e^{-\tilde{k}_1 t}. \quad (4.8)$$

By integrating this equation, it comes

$$[\text{HO}\cdot]_t = \left([\text{HO}\cdot]_0 + [e_{hyd}^-]_0 \frac{\tilde{k}_1}{\tilde{k}_2 - \tilde{k}_1} \left(e^{(\tilde{k}_2 - \tilde{k}_1)t} \right) \right) e^{-\tilde{k}_2 t}. \quad (4.9)$$

So finally, by 4.6, the time evolution of $[A]$ is given by

$$[A]_t = [\text{HO}\cdot]_0 + [e_{hyd}^-]_0 - [e_{hyd}^-]_0 e^{-\tilde{k}_1 t} - \left([\text{HO}\cdot]_0 + [e_{hyd}^-]_0 \frac{\tilde{k}_1}{\tilde{k}_2 - \tilde{k}_1} \left(e^{(\tilde{k}_2 - \tilde{k}_1)t} \right) \right) e^{-\tilde{k}_2 t}. \quad (4.10)$$

In order to fit the time evolution of the absorption at 305 nm, it is necessary first to take into account all the species which absorb at this wavelength and second to convert the concentrations into absorptions:

$$\text{Abs}_{305} = \epsilon_{305,A}[A]_t + \epsilon_{305,e_{hyd}^-}[e_{hyd}^-]_t + \epsilon_{305,\text{HO}\cdot}[\text{HO}\cdot]_t$$

which is, by the expression obtained above,

$$\begin{aligned} \text{Abs}_{305}(t) &= \epsilon_{305,A}([e_{hyd}^-]_0 + [\text{HO}\cdot]_0) - (\epsilon_{305,A} - \epsilon_{305,e_{hyd}^-})[e_{hyd}^-]_0 e^{-\tilde{k}_1 t} \\ &\quad - (\epsilon_{305,A} - \epsilon_{305,\text{HO}\cdot}) \left([\text{HO}\cdot]_0 + [e_{hyd}^-]_0 \frac{\tilde{k}_1}{\tilde{k}_2 - \tilde{k}_1} \left(e^{(\tilde{k}_2 - \tilde{k}_1)t} \right) \right) e^{-\tilde{k}_2 t} \end{aligned} \quad (4.11)$$

If we assume that the first transient species A is the adduct radical PyOH, as suggested by Lilie [2], we can use the extinction coefficient $\epsilon_{305,A} = 3500 \text{ L mol}^{-1} \text{ cm}^{-1}$. For

electron and hydroxyl radical extinction coefficients at 305 nm, we referred to the values given in literature: $\epsilon_{305, e_{hyd}^-} = 1045 \text{ L mol}^{-1} \text{ cm}^{-1}$ and $\epsilon_{305, HO^\bullet} = 100 \text{ L mol}^{-1} \text{ cm}^{-1}$ [12].

Then we proceeded to the fit of the kinetic signal at 305 nm with the expression 4.11. All parameters (concentrations, k_1 rate constant and extinction coefficients) were fixed expect for the value of $\epsilon_{305, A}$ and the value of \tilde{k}_2 which were optimized by the fit.

Py concentration effect

The study on the effect of Py concentrations aimed to demonstrate that the first transient species was formed by a pseudo-first order reaction which, therefore, depends on the initial concentration of pyrrole. So, the kinetics of the first transient species A absorbing at 305 nm was studied at three different Py concentrations (20, 50 and 100 mM).

The comparison of the three kinetics shows clearly a dependency on the Pyrrole initial concentration as observed in Figure 4.5.

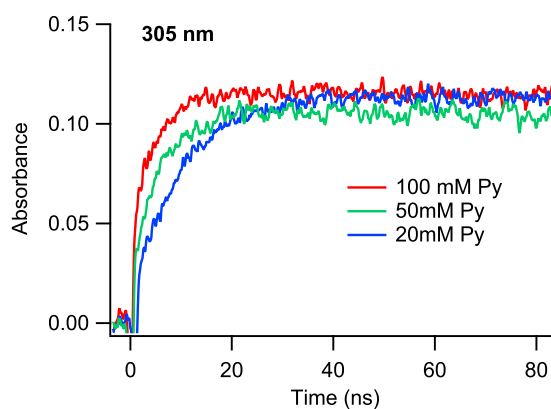


Figure 4.5: Comparison of the kinetics of A formation for three different concentrations in Py (20, 50 and 100 mM) at pH = 6. Irradiated at 50 Gy per pulse (for 20 and 100 mM Py solutions) and at 45 Gy per pulse (50 mM Py) (Optical path = 1 cm).

Then, it was possible to determine the rate constant of reaction between hydroxyl radical and Pyrrole monomer by fitting the increase of the absorbance at 305 nm with the equation 4.11 for the three different concentrations (Figure 4.6).

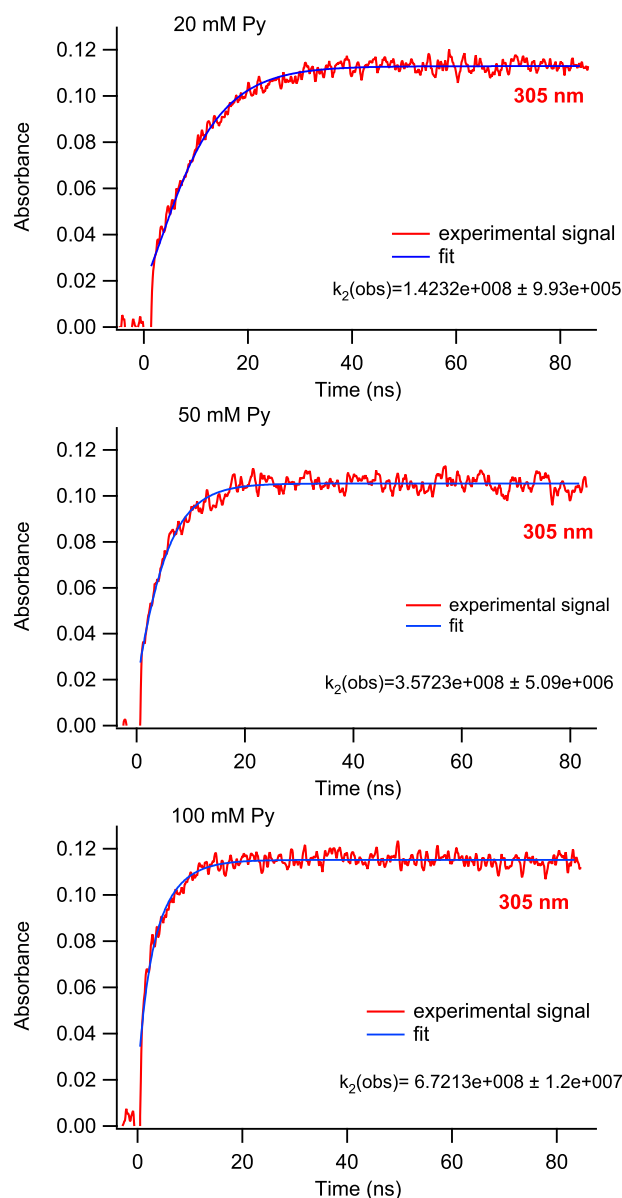


Figure 4.6: Fit of experimental signals at 305 nm of three N_2O -saturated aqueous solutions containing 20 mM, 50 mM and 100 mM in Py (Dose = 50 Gy/pulse for 20 and 100 mM in Py and 45 Gy/pulse for 50 mM in Py; Optical path = 1 cm)

The fit described well the kinetics and the values found for observed rate constants \tilde{k}_2 increase linearly with Py concentration as attended. By plotting the values of the observed rate constants, \tilde{k}_2 as function of Pyrrole concentration (Figure 4.7), we found the rate constant value: $k_2 = 6.5 \cdot 10^9 \text{ L mol}^{-1}\text{s}^{-1}$.

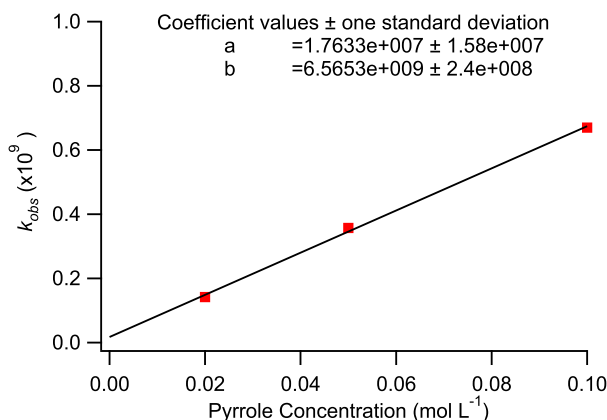


Figure 4.7: Observed rate constant, \tilde{k}_2 , deduced from the fits of Figure 4.6, as a function of pyrrole concentration.

Dose effect

Finally, in order to estimate the extinction coefficient at 305 nm, we studied the absorption of the N₂O-saturated aqueous solution containing 20 mM in Py irradiated at three different doses (37, 45 and 69 Gy/pulse). The Figure 4.8 shows the three spectra recorded 80 ns after the pulse. Then by plotting the absorption values at 305 nm as a function of the first transient species A concentration (Figure 4.8), it was possible to extrapolate the ϵ_{305nm} value. Indeed if we assume that all of the hydroxyl radicals, produced by water radiolysis, react with pyrrole to give the first transient species, the concentration of the absorbing species at 305 nm can be considered equal to that of hydroxyl radical. By fitting the data with linear equation, the slope of the curve gives the value of the extinction coefficient, (note the path length was 1 cm). It was obtained a value of $\epsilon_{305nm} = 3299 \pm 36 \text{ L mol}^{-1} \text{ cm}^{-1}$ which is in good agreement with the value proposed by Lilie, ($3500 \text{ L mol}^{-1} \text{ cm}^{-1}$) [2].

On the other hand, the dependency of the absorption on the dose suggests that the concentration of the first transient species A is due to the hydroxyl radicals, which was our assumption. Indeed, the concentration of hydroxyl radicals is linearly dependent on the dose. This allows to establish that the first transient species, the extinction coefficient of which is $\epsilon_{305nm} = 3299 \pm 36 \text{ L mol}^{-1} \text{ cm}^{-1}$, is produced by the reaction:



with a rate constant $k_2 = 6.5 \cdot 10^9 \text{ L mol}^{-1} \text{ s}^{-1}$. At this stage of the work the identification of A is not possible. The species A could be $\text{Py}^{\cdot+}$, Py^{\cdot} or PyOH .

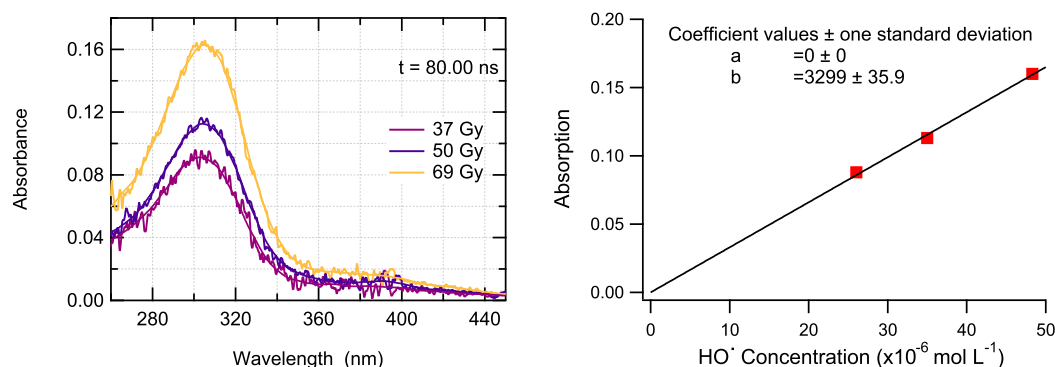


Figure 4.8: Absorption spectra recorded 80 ns after the pulse at three different doses of a solution containing 20 mM in Py at neutral pH (on the left) and the estimation of the extinction coefficient of the first transient species at 300 nm (on the left) by using the absorption values at at 305 nm. The absorptions are plotted as a function of concentration of hydroxyl radical produced by radiolysis. The extinction coefficient is extrapolated by the slope of the curve.

4.2.2 Microsecond time scale investigation

The evolution of this transient species A was followed at longer time scale up to 1 ms. The absorption at 305 nm decreases very slowly on microsecond time scale. This decrease parallels the increase of the absorbances at around 270 and 340 nm (Figure 4.9). At 1 ms it is possible to observe a change in the spectrum. The absorption at

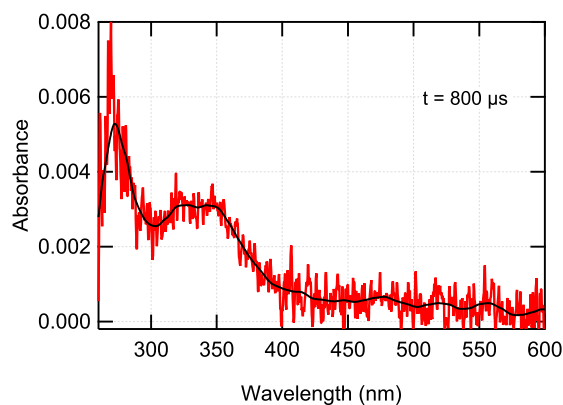


Figure 4.9: Absorption spectrum recorded 800 μs after the pulse of a N_2O -saturated aqueous solution containing 100 mM in Pyrrole (Dose = 50 Gy; Optical path = 1 cm).

340 nm is very weak and the signal to noise ratio is very bad. Also the peak at 270 nm is affected by the absorption decrease of A at 305 nm. Then, it was impossible to study

the kinetic signal at these wavelengths. However, the high intensity absorption at 305 nm allows to study the kinetics. So, in order to understand what is the second step which corresponds to the disappearing of A of polymerization, the decay at 305 nm was investigated on the microsecond time scale (Figure 4.10). A second order kinetic test

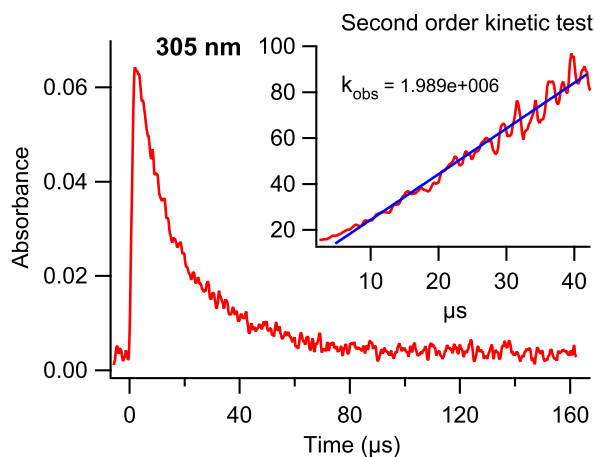


Figure 4.10: Evolution of absorbance at 305 nm over 200 μs on a solution containing 100 mM in Pyrrole under N_2O (Dose = 50 Gy/pulse; Optical path = 1 cm). Inset: second order kinetic test.

describes well the signal of the Figure 4.10, suggesting that the species A disappears according to a bimolecular reaction:



with a constant rate observed $k_{obs} = 1.9 \cdot 10^6 \text{ L mol}^{-1}\text{s}^{-1}$. At this stage of the work, either Py^\cdot , $\text{Py}^{\cdot+}$ or $(\text{PyOH})^\cdot$ dimerization remain possible. Then, in this preliminary study a simple mechanism of oxidation of Pyrrole monomer and a further dimerization were proposed.

4.3 Simulation

The kinetic mechanism of Py oxidation was simulated by using COPASI software. By setting the reactions involved in the mechanism in homogeneous kinetic conditions, the program describes the variation of concentration of each species as a function of time. The initial concentrations (Table 4.1) and the rate constants are set considering the experimental conditions (dose, concentration of Pyrrole, rate constants, pH) and

literature data (rate constants)[2].

Initial Concentration [M]	Dose [Gy/puls]	Radiolytic species initial concentration [M]
[Py] = 0.1 [N ₂ O] = 0.024	45	[e _{hyd} ⁻] = [H ₃ O ⁺] = 1.57 10 ⁻⁵ [HO [·]] = 1.66 10 ⁻⁵ [H [·]] = 2.47 10 ⁻⁶

Table 4.1: Experimental parameters values used in the simulations at pH = 6.

The Table 4.2 shows the reactions taken into account in the simulation. Even if the conversion of electron in hydroxyl radical (R1) is the main reaction, the others reactions (R2-6) involved in water radiolysis were included to estimate the concentration of hydroxyl radicals which can effectively react with Pyrrole. The reaction (R7) and (R9) were deduced from kinetic study. And finally we included the reaction (R8) representing the protonation of transient species as proposed by Lilie *et al.*

This mechanism was used to simulate the kinetics obtained by irradiating at 50 Gy per pulse in the solution containing 100 mM in Py.

Reaction	Equation	Constant Rate [L mol ⁻¹ s ⁻¹]
R1	e _{hyd} ⁻ + N ₂ O → N ₂ + HO [·]	k = 9.1 10 ⁹
R2	e _{hyd} ⁻ + HO [·] → HO ⁻	k = 3.0 10 ¹⁰
R3	2 e _{hyd} ⁻ → H ₂ + HO ⁻	k = 5.5 10 ⁹
R4	e _{hyd} ⁻ + H ₃ O ⁺ → H [·]	k = 2.3 10 ¹⁰
R5	H [·] + HO [·] → H ₂ O	k = 7.0 10 ⁹
R6	2 HO [·] → H ₂ O ₂	k = 5.5 10 ⁹
R7	Py + HO [·] → A	k = 6.5 10 ⁹
R8	A + H ₃ O ⁺ → AH ⁺ + H ₂ O	k = 1.5 10 ⁹
R9	2 A → B	k = 1.9 10 ⁹

Table 4.2: Reactions involved in Pyrrole oxidation in aqueous solution at neutral pH.

The Figure 4.11 depicts the time evolution of the concentrations of the main species produced or consumed on 100 ns after the electron pulse.

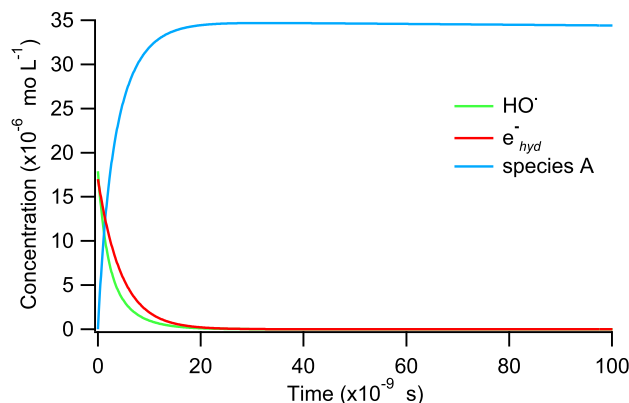


Figure 4.11: Time evolution over 100 ns of the concentrations in HO·, e_{hyd}⁻ and A of a solution containing in 100 mM in Pyrrole under N₂O on simulated by COPASI.

The decrease of electron concentration is mainly due to its conversion in hydroxyl radical by N₂O (R1). At the same time hydroxyl radical is consumed by reaction with Pyrrole, and its decrease depends on monomer concentration.

The reaction between Pyrrole and HO· (R7) induces the formation of the first transient species which is observed in experimental spectra at 305 nm. In order to compare the experimental curve (absorption vs time) with simulated one (concentration vs time) it was necessary to insert the molar extinction coefficient by using Beer-Lambert equation:

$$A = \epsilon \ell C \quad (4.14)$$

Then, the extinction coefficient represents the coefficient of normalization between the two profiles. First, the experimental kinetics profile of electron was compared with the simulated one. The used extinction coefficient, $\epsilon_{600nm} = 13000$ was taken from literature. In Figure 4.12, the good agreement between the two profiles is highlighted at 600 nm.

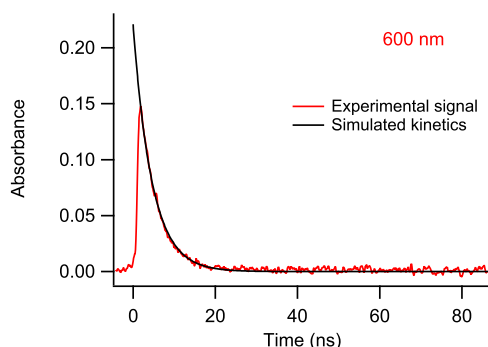


Figure 4.12: Comparison between experimental kinetic profile of electron decay (100 mM in Py, pH = 6, Dose = 50 Gy/pulse Optical path = 1 cm) and simulated one at 600 nm on 100 ns.

Then, we tested the formation of the first transient species A observed at 305 nm. As previously detailed, the signal at this wavelength is composed by the absorptions of first transient species in addition to those of hydroxyl radicals and hydrated electrons. A linear combination of the three absorbances at 305 nm allows to describe the experimental profile. As in the case of the fit, the extinction coefficient of hydrated electron and hydroxyl radical at 305 nm were $\epsilon_{305, e_{hyd}^-} = 1045 \text{ L mol}^{-1} \text{ cm}^{-1}$ and $\epsilon_{305, HO\cdot} = 100 \text{ L mol}^{-1} \text{ cm}^{-1}$ respectively. For the species A, was used the value of $\epsilon_{305, A} = 3300 \text{ L mol}^{-1} \text{ cm}^{-1}$ obtained by the study on the dose effect, (Figure 4.13).

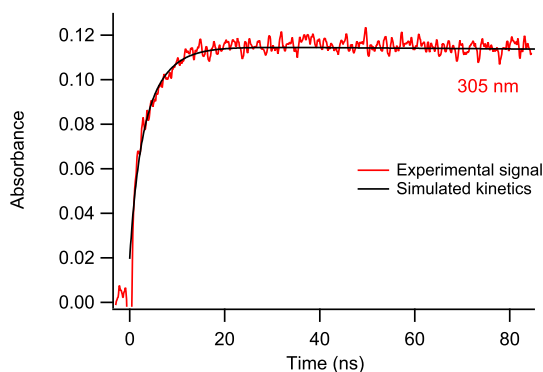


Figure 4.13: Comparison between experimental kinetic profile (100 mM in Py, pH = 6, Dose = 50 Gy/pulse, Optical path = 1 cm) and simulated one of at 305 nm over 100 ns.

The same simulation was used to study a solution containing 20 mM in Py,

also in that case there is a good agreement between simulated and experimental signals. Finally we simulated the kinetics at longer time scale in order to follow the decay of A and the potential formation of AH^+ on the one hand and of B on the other hand. On $200 \mu s$ (Figure 4.14) it is possible to observe the decay of A and the formation of the two species AH^+ and B.

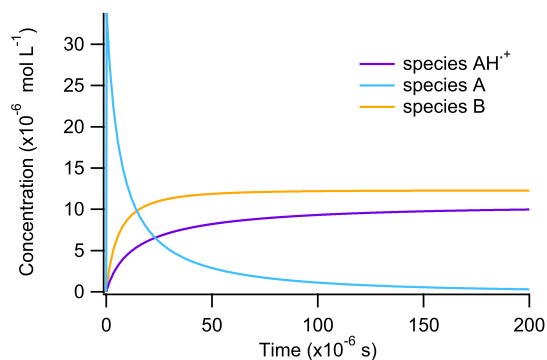


Figure 4.14: Time evolution over $200 \mu s$ of the concentrations in A, AH^+ and B in a solution containing 100 mM in Pyrrole on $200 \mu s$ as simulated by COPASI.

Then we compared the simulated decay of the first transient species A with the decay observed experimentally. Also in this case we found a very good agreement between the simulation and the experimental data (Figure 4.15).

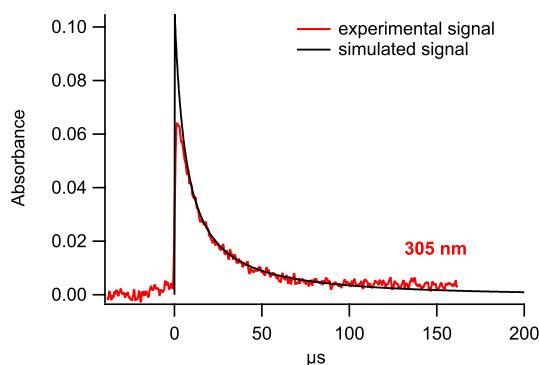


Figure 4.15: Comparison between experimental kinetic profile of A (100 mM in Py, pH = 6, Dose = 50Gy/pulse, Optical path = 1 cm) and simulated one at 305 nm over $200 \mu s$.

Note that only the extinction coefficient of A ($\epsilon_{305,A} = 3300 \text{ L mol}^{-1} \text{ cm}^{-1}$) was used to transform the concentration evolution into absorption decay. Indeed the electron and hydroxyl radical are completely consumed at this time scales

so they do not more contribute in the time evolution of absorption at 305 nm. Thanks to COPASI simulation it was possible to describe the first steps of Pyrrole oxidation. However, the step following the addition still need to be investigated. Two possible reactions have been proposed here and could be involved: the protonation (R8) or the dimerization (R9). Due to the estimate concentration of H_3O^+ and the species A, these two reaction proceed according to a second order kinetics.

4.4 Theoretical study

In the kinetic study of experimental data, two spectra were isolated. At nanosecond time scale, the spectrum characterized by an intense peak at 305 nm and a weak large band at 400 nm (Figure 4.4) which could be Py^\cdot , $Py^{\cdot+}$ or, according to Lilie [2], $(PyOH)^\cdot$, resulting from the reaction between hydroxyl radical and Pyrrole monomers. On microsecond time scale, the spectrum of the species A composed by two weak peaks at 270 and 350 nm was not identified (Figure 4.9). Does it correspond to a single species (AH^+ or B) or to a combination of the two species (AH^+ and B)? With the aim to determine the nature A and that of the species absorbing at the microsecond time scale we proceeded to DFT/ TD-DFT calculations to simulate the absorption spectra of all possible species. The structures, formula and current names of the species investigated are reported in Table 4.3.

Py			Py^\cdot			Py^+		
$(PyOH)^\cdot$			$PyHOH^{+\cdot}$			PyO^\cdot		
$BPy_{\alpha-\alpha}$			$BPyOH$			$BPyHOH^{2+}$		

Table 4.3: Names, formula and chemical structures of all Pyrrole species studied by simulation.

The simulated absorption spectra of all species of Table 4.3 are depicted in Figure 4.16. Note that the spectrum of the open cycle is not presented because the method B3LYP was not enough accurate to simulate its absorption spectrum.

Absorption spectra of Pyrrole and Bypirrole molecules

First the absorption spectrum of Pyrrole monomer was compared with the experimental spectrum shown in literature [10] and with that obtained by experiments (Chapter 1, Figure 1.4). This last is composed by a narrow band at 205 nm, with a molar extinction coefficient: $\epsilon_{205nm} = 6730 \text{ L mol}^{-1} \text{ cm}^{-1}$ [13]. As in EDOT study, the simulation method consists in the Monte Carlo method at the B3LYP/cc-pvdz level with 10000 MC steps, and the spectra at the B3LYP/cc-pvdz level. Due to the good agreement between experimental and simulated spectra, this method was adopted for all simulations.

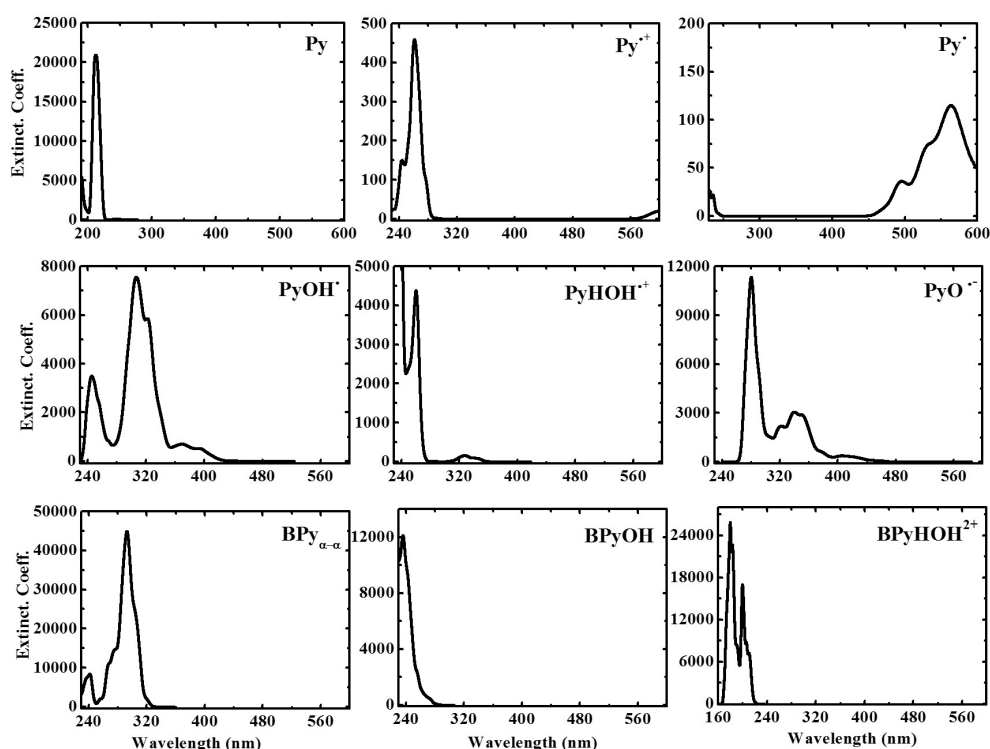


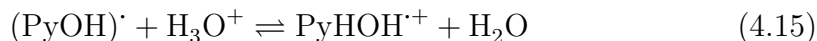
Figure 4.16: Theoretical absorption spectra of all molecules presented in Table 4.3 simulated by MC-DFT/ TD-DFT B3LYP.

The spectrum of neutral Bipyrrrole was simulated in methanol with the aim to compared with the results presented by Rapoport and Castagnoli [14]. Also in this case the simulated spectrum is in good agreement with the spectrum shown in literature.

Species identification

The absorption spectrum of the first species, A, produced by reaction between Pyrrole monomer and hydroxyl radical displays a peak at 305 nm and a large band at 400 nm. From this reaction, knowing the reactivity of HO \cdot , three Pyrrole radicals can be produced: neutral radical Py \cdot , cationic radical Py \cdot^+ , and adduct radical, (PyOH) \cdot . As observed in Figure 4.16, Py \cdot and Py \cdot^+ do not present any absorption band at 305 nm. On the contrary, the simulated absorption spectrum of (PyOH) \cdot fits very well with the experimental spectrum of the species A. Then the first transient species can be attributed to the adduct radical: (PyOH) \cdot . This result is in agreement with Lilie study [2].

In the kinetic simulation at microsecond time scale, it was suggested that the species A (the adduct radical, (PyOH) \cdot) at neutral pH decays by following a second order reaction. So the second transient species, absorbing at 270 nm and around 340 nm can be one of the species due to the protonation of adduct radical PyHOH $^{+\cdot}$ or the dimerization into BPy or BPyOH. By comparing the experimental spectra with simulated ones, it appears clearly that the spectrum which fits the best is that of the protonated adduct radical, PyHOH $^{+\cdot}$, whose spectrum presents two maxima at 260 and 330 nm. Also in this case the result is in agreement with Lilie *et al.* Moreover the pK $_a$ proposed by Lilie for the two species was given at 4.5, while in our experiment the pH = 6, was above this pK $_a$ value. We can then suppose a very low concentration in protonated species PyHOH $^{+\cdot}$ and consequently a weak absorption in the experimental spectrum due to the slow equilibrium :



At the same time, we can suppose that the adduct radical (PyOH) \cdot dimerizes into BPyOH which absorbs at around 240 nm. Knowing that in our experiments, it is not possible to follow any kinetics at this wavelength the observation of the

dimers remains impossible. Nevertheless, thanks to this study it was possible to identify the mechanism of Py oxidation. The addition of hydroxyl radical produced by water radiolysis induces the formation of a first transient species absorbing at 305 nm, identified as the adduct radical (PyOH) \cdot . The rate constant $k_2 = 6.5 \cdot 10^9 \text{ L mol}^{-1} \text{ s}^{-1}$ was determined and the extinction coefficient of (PyOH) \cdot $\epsilon = 3300 \text{ L mol}^{-1} \text{ cm}^{-1}$ at 305 nm was estimated. This radical is then slowly protonated into PyHOH $^{+}$ absorbing at 270 and around 340 nm. This transient is not stable and is probably transformed at time scale longer than 1 ms (time limit of our experimental observations).

4.5 pH effect

The previous study on Py oxidation mechanism showed the presence of (PyOH) \cdot and its protonated form to PyHOH $^{+}$, implying a pH effect on the polymerization mechanism of Py. Moreover the relevance of pH in pyrrole polymerization mechanism is often suggested in literature [1, 2, 3, 15]. A low pH favors the polymerization but induces the opening of the ring. On the other hand at alkaline solution the polymer chain can be non conjugated and undergoes a deprotonation, which induces the decreasing of conductivity.

The pH effect was here investigated by pulse radiolysis of a solution containing 20 mM in Py under N₂O at two different pH: 2.8 (acidic) and 13.5 (alkaline). The final products and the intermediate species produced during the irradiation were then studied.

4.5.1 Acidic solution

A N₂O-aqueous solution containing 20 mM in Py was studied at pH = 2.8. The pH was adjusted by adding HClO₄. In acidic solution the presence of a high concentration of proton could induce the protonation of a radical species [2, 15]. The Figure 4.17 depicts the spectrum 100 ns after the pulse. At short time scale, the first transient species is again the hydroxyl adduct radical, (PyOH) \cdot .

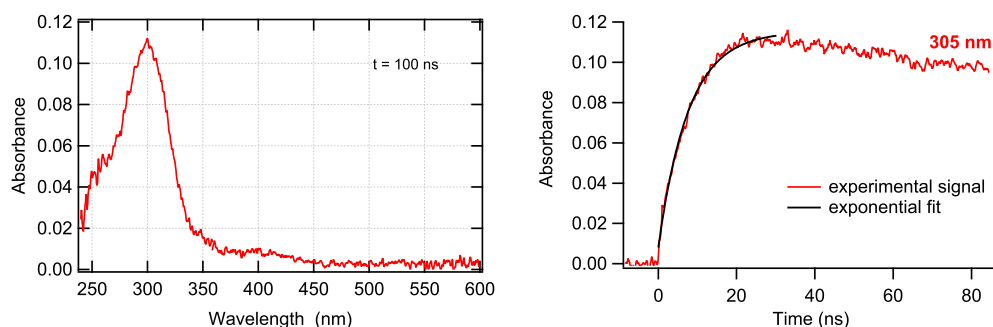


Figure 4.17: Absorption spectrum of a N_2O -saturated aqueous solution containing 20 mM in Py at $pH = 2.8$ recorded 100 ns after the pulse (on the left). Time evolution of absorbance at 305 nm over 100 ns (on the right) (Dose = 43 Gy/pulse; Optical path = 1 cm).

Indeed the absorption spectrum shows the same peak at 305 nm and a large weak band at around 400 nm. Also in this case the $(PyOH)^\cdot$ radical is produced fast over 20 ns. The observed rate constant, k_{obs} , was $1.3 \cdot 10^8$ s^{-1} , which corresponds to a rate constant $k = 6.5 \cdot 10^9$ $mol\ L^{-1}\ s^{-1}$, the same value obtained at neutral pH. At longer time, 2 μs , the absorption spectrum shows two peaks, a band at a wavelength lower than 260 nm, a weak band at 350 nm and a weak absorbance at around 600 nm (Figure 4.18).

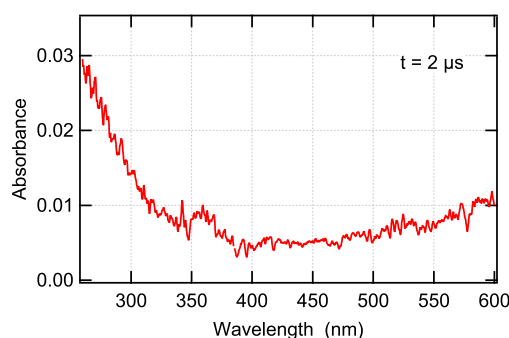


Figure 4.18: Absorption spectrum of a N_2O -saturated aqueous solution containing 20 mM in pyrrole at $pH = 2.8$ recorded over 2 μs after a pulse (Dose = 43 Gy/pulse, Optical path = 1 cm).

It is possible here to distinguish the spectrum protonated adduct radical $PyHOH^\cdot+$ previously introduced in neutral pH with bands located at 270 and around 340 nm. The absorbance is higher than in the case of neutral pH and

the decay kinetics at 305 nm of $(\text{PyOH})^\cdot$ and the increase at 260 nm of $\text{PyHOH}^{+\cdot}$, allowed to identify the rate constant.

The kinetic evolution of the absorbance at 260 nm, (Figure 4.19) is affected to the decay of the absorption peak at 305 nm, resulting in the convolution of two different kinetics.

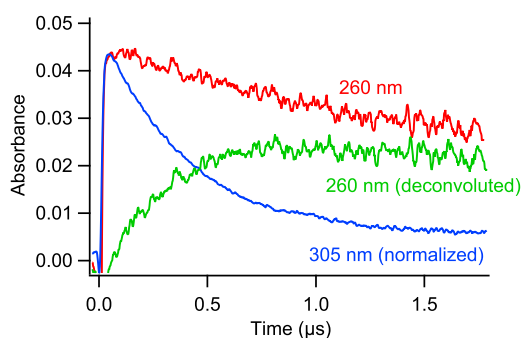


Figure 4.19: Time evolution of absorbances over 2 μs at 260 nm, 305 nm and 260 nm (after subtraction of the contribution of 305 nm) of a N_2O -saturated aqueous solution containing 20 mM in Py at pH= 2.8 (Dose = 43 Gy/pulse; Optical path = 1 cm).

With the aim to isolate the kinetics of the absorbing species at 260 nm, the signal 305 nm has been normalized on the profile at 260 nm and then it was subtracted. The green profile, in the Figure 4.19, shows the growth of the species at 260 nm. A pseudo-first order fits well this signal and no others components affect the decay. Moreover the rate constants describing the decrease at 305 nm and the increase at 260 nm are very similar, showing the direct correlation between the two species.

Then we deduced the experimental signal is the overlapping of the decay of PyOH^\cdot radical absorbing at 305 nm and the increase of $\text{PyHOH}^{+\cdot}$ absorbing at 260 nm. The observed rate constant fitting the growth at 260 nm was $k_{obs} = 3.52 \cdot 10^6 \text{ s}^{-1}$. By supposing a concentration of H_3O^+ of around $1.6 \cdot 10^{-3} \text{ M}$, we can estimate a $k = 2.2 \cdot 10^9 \text{ L mol}^{-1}\text{s}^{-1}$. This value is similar to the value calculated by Lilie, $k = 1.5 \cdot 10^9 \text{ L mol}^{-1}\text{s}^{-1}$, [2].

On the other hand a kinetic test of pseudo-first order on 305 nm profile give a $k_{obs} = 2.6 \cdot 10^6 \text{ s}^{-1}$ which corresponds to a constant rate $k = 1.66 \cdot 10^9 \text{ L mol}^{-1}\text{s}^{-1}$. This value is consistent with the value of k at 260 nm. Indeed the decay at 305 nm is affected by the increase at 260 nm which weakly contributes at this wavelength

and the decay appears slower.

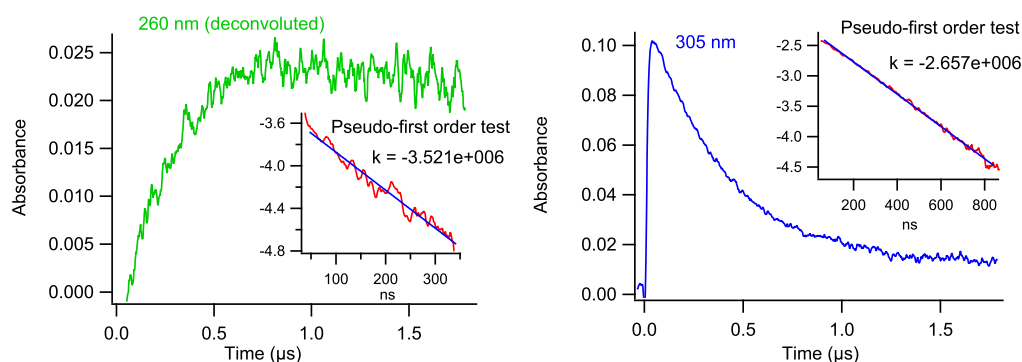


Figure 4.20: Time evolution of absorbances over 2 μs at 305 nm and 260 nm after subtraction of the contribution of 305 nm of a N_2O -saturated aqueous solution containing 20 mM in Py at pH= 2.8 (Dose = 43 Gy; Optical path = 1 cm).

However, a more accurate value of the rate constant could be estimated by comparing different concentrations of pyrrole monomer at this pH.

The spectrum in Figure 4.18 also shows a large band at 600 nm and a continuous absorption on the wavelength range from 360 to 600 nm. The kinetics in this region of the spectrum is different from to the kinetics at 260 and 340 nm while it is almost simultaneous.

Indeed, the protonated pyrrole radical, PyHOH^+ , is a very reactive species. Two reactions could be expected following the formation of this radical: the opening of the ring or a dimerization via dehydration.



Indeed, these species were already studied and detected in literature by Lilie [2]. The overlapping of absorptions of various species along the whole spectrum affects the time evolution of absorbances. So, it was not possible to identify the order of the reactions at no one of these wavelengths.

At this stage of the study, we proceeded by comparison with literature data to suggest a first interpretation. The spectrum, recorded at 50 μs , shows the absorption maxima at 350, 450 and around 600 nm (Figure 4.21) and appears

similar to a transient spectrum already observed by Lilie *et al.* [2] (Figure 4.21) which was attributed to the opening of the cycle of the protonated adduct pyrrole radical but with some differences at $\lambda > 400$ nm.

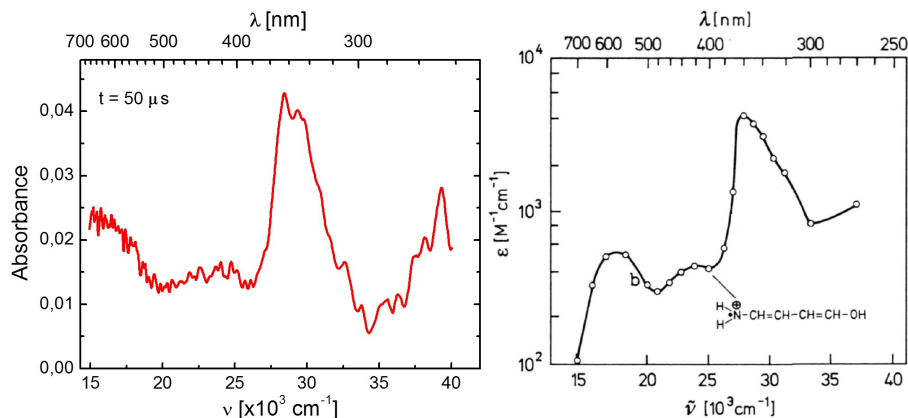


Figure 4.21: On the left the experimental spectrum of a N_2O -saturated aqueous solution containing 20 mM in Py recorded over $50 \mu\text{s}$ after the pulse (pH = 2.8, Dose = 43 Gy/pulse; Optical path = 1 cm), on the right the absorption spectrum of the opening ring protonated pyrrole radical proposed by Lilie [2].

This suggests that, also in our case, at $50 \mu\text{s}$ the spectrum is partially due to the open cycle radical formed at the first microsecond and another species produced slowly (Figure 4.22). Probably the absorption spectrum of Lilie could be the overlapping of two species which were not distinguished.

When the time evolutions of absorbances are investigated, some important differences were highlighted (Figure 4.22). The two peaks at 450 and 630 nm seem to have the same growth on $10 \mu\text{s}$ which is almost completed at the end of $50 \mu\text{s}$. The two peaks at 339 and 352 nm show the same kinetic profile (Figure 4.22) characterized by at least two components: a growth which occurs on $10 \mu\text{s}$, common with the others peaks and a slower second growth which is not completed over $50 \mu\text{s}$. At this time scale it is not possible to distinguish the evolution of each of them. We can suppose that during the first $10 \mu\text{s}$, the reaction 4.16 inducing the opening of the ring of PyHOH^+ radical takes place. Simultaneously, another species, absorbing at around 350 nm, is formed with a slower rate constant. We can suppose that this second increase is due to the dimerization of protonated Pyrrole radicals.

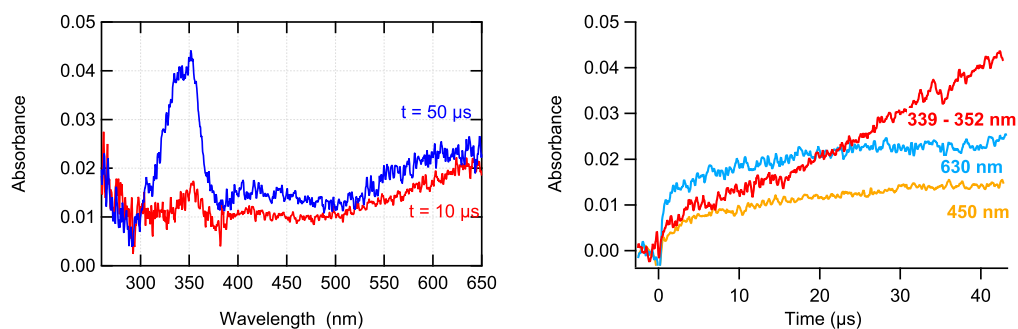


Figure 4.22: Absorption spectra of a N_2O -saturated aqueous solution containing 20 mM in Py at $\text{pH} = 2.8$ recorded at 10 and 50 μs after the pulse (on the left). Time evolution of absorbance at 339, 352, 450 and 630 nm over 50 μs (Dose = 43 Gy/pulse; Optical path = 1 cm).

This idea was confirmed when the image recorded at 200 μs was analyzed. Indeed the relative absorption intensities of the peaks change and the peak centered to 630 nm is shifted to 600 nm (Figure 4.23). This spectrum can be explained as the overlapping of the spectrum of the opening ring coming from PyHOH^+ radical previously introduced, and spectrum of a possible dimers. If we compared the simulated spectra in Figure 4.16 with the experimental one recorded at 180 μs , no one fits well. Indeed, unfortunately, the simulated species absorb in UV region, and if they are produced, we cannot observe in our spectra.

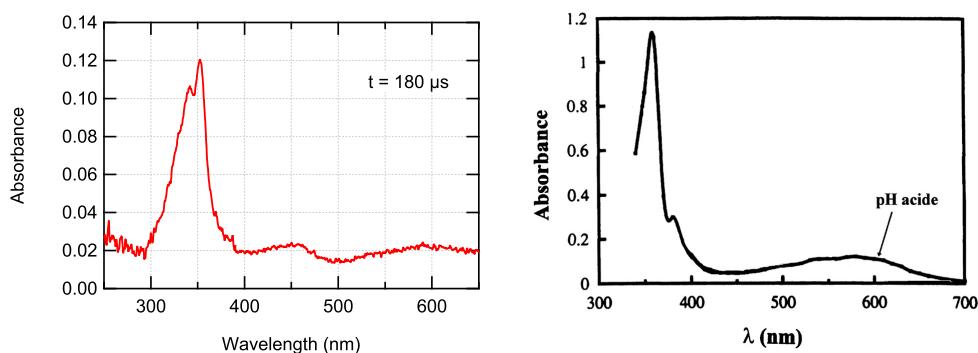


Figure 4.23: On the left the experimental spectrum of a N_2O -saturated aqueous solution containing 20 mM in Py recorded over 180 μs after the pulse ($\text{pH} = 2.8$, Dose = 43 Gy/pulse; Optical path = 1 cm), on the right the absorption spectrum of $\text{BPy}^{\cdot+}$ radical from reference [3].

On the other hand, this spectrum is close to that found in literature for $\text{BPy}^{\cdot+}$

with absorption maxima at 360 and 580 nm (Figure 4.23), [3].

This interpretation would explain the overlapping of two different kinetic profiles on the same wavelengths. When the kinetics of the four main peaks at 339, 352, 450 and 600 nm is studied over 200 μs , (Figure 4.24), the differences in kinetics evolutions appeared clearly. All signals are composed by one or two components and, evidently, one component is common to all peaks. In particular, the peaks at 352 seems to differ from that at 339 nm.

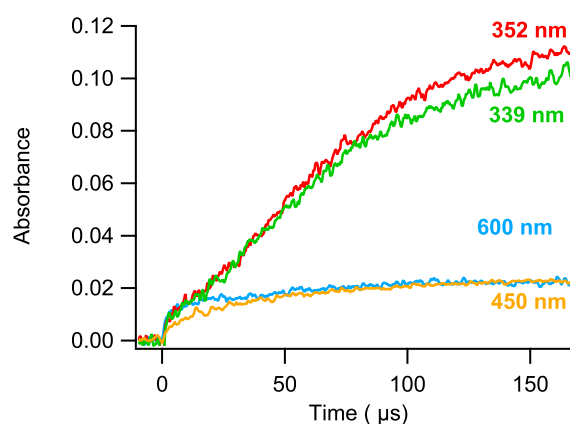


Figure 4.24: Time evolution of absorbances at 339, 352, 450 and 600 nm over 200 μs (Dose = 43 Gy/pulse; Optical path = 1 cm).

On the other hand, the absorption at 600 nm and 450 nm do not follow no more the same kinetic evolution. Unfortunately, it was not possible to identify the common signal and the deconvolution was not possible due to the number of species in the system.

Finally, 1 ms after the pulse, the absorption spectrum does not show relevant change as possible to see in Figure 4.25. However, it was always possible to highlight the difference in the kinetics of the four absorption bands. In the Figure 4.25, the two peaks at 339 and 352 nm are no longer related but their decays are affecting each other.

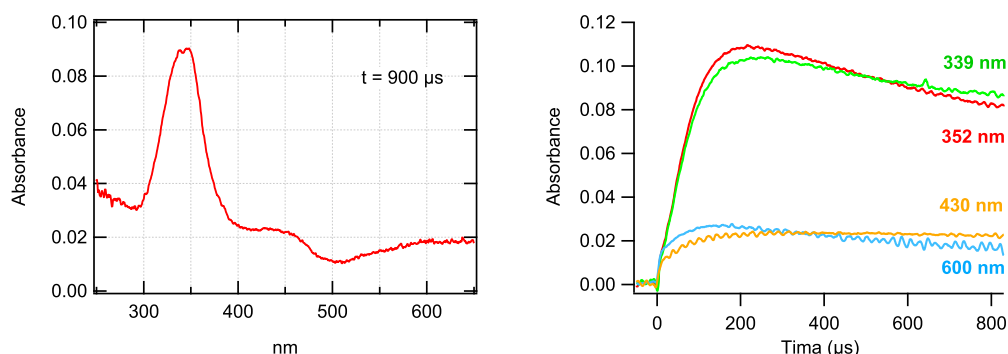


Figure 4.25: Absorption spectra of a N_2O -saturated aqueous solution containing 20 mM in Py at $\text{pH} = 2.8$ recorded at 1 ms after the pulse (on the left). Time evolution of absorbance at 339, 352, 450 and 630 nm over 50 μs (Dose = 43 Gy/pulse; Optical path = 1 cm).

Contrarily to the other experiments, in this case, the absorption spectrum recorded after the experiment shows some of the bands visible in the spectrum recorded at 900 μs . The Figure 4.26 shows the spectrum of solution recorded after the pulse radiolysis experiment. What is amazing is the increase of the absorption and the broadband at 850 nm not visible at 900 μs . This means that the solution continues to react after the pulse irradiation to induce a probable chain length increase. Indeed, after the irradiation, the solution color changes from transparent into black.

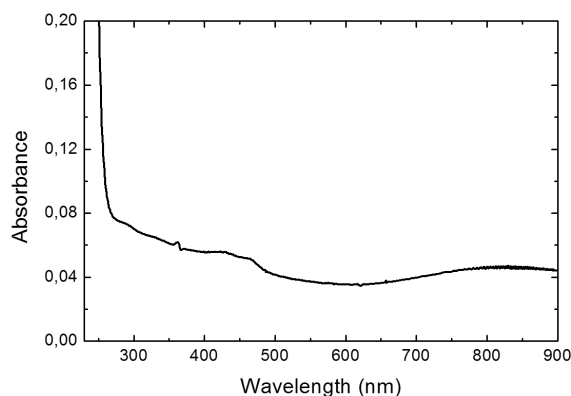


Figure 4.26: Static absorption spectrum of a solution containing 20 mM in Py at $\text{pH} = 2.8$ after the pulse radiolysis experiment (Optical path = 0.2 cm).

This spectrum is in agreement with that found in literature [16], showing an

absorption band in the range 300-350 nm which could correspond to the π - π^* transition due to the formation of polypyrrole. Also, the shoulder-like appearance observed from 400 nm to 500 nm corresponds to a bi-polaron transition, a characteristic feature for the oxidized state of polypyrrole.

4.5.2 Alkaline solution

In order to avoid the opening of the cycle and to favor the dimerization, we studied the solution in alkaline solution.

Due to the alkaline pH (13.5), the H_3O^+ are not produced in water radiolysis and the oxidant species that can react with Pyrrole is mainly the oxide radical, $\text{O}^{\cdot-}$, ($\text{pK}_a(\text{HO}^{\cdot} / \text{O}^{\cdot-}) = 11.9$) Indeed, the hydroxyl radical HO^{\cdot} , produced during the radiolysis, is transformed in oxide radical, $\text{O}^{\cdot-}$. In the next section, a kinetic simulation will show the competition between the two radicals (HO^{\cdot} and $\text{O}^{\cdot-}$), demonstrating why the contribution of hydroxyl radical can be neglected.

We studied a solution containing 20 mM in Py where the pH was adjusted 13.5 with NaOH and it was irradiated at 40 Gy per pulse. The spectrum observed 70 ns after the pulse was very similar to that observed in neutral solutions, although it is present a shift of the peak at 305 nm to 295 nm, and from 400 nm to 380 nm, (Figure 4.27). The action of hydroxyl radical can not be excluded due to its very fast rate constant previously determined at $6.5 \cdot 10^9 \text{ L mol}^{-1} \text{ s}^{-1}$. However its concentration is too low to produce an amount of adduct radicals detectable.

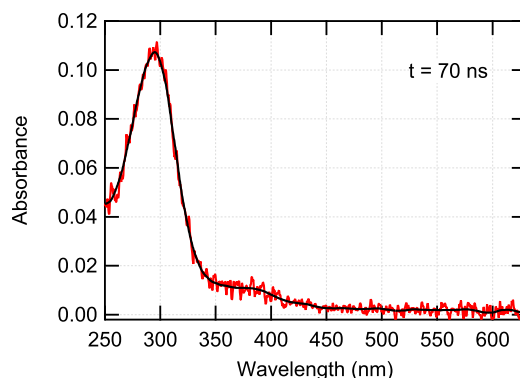


Figure 4.27: Absorption spectrum of first transient species produced at 70 ns after the pulse of 40 Gy in a solution containing 20 mM in Py at pH= 13.5 under N_2O .

So, as in the case of EDOT (chapter 2), it is possible to suppose that this absorption spectrum corresponds to that of the product of the addition of $O^{\cdot-}$ onto Py, namely the oxide adduct radical, $PyO^{\cdot-}$. Moreover the simulated spectrum, previously presented in Figure 4.16, shows two absorption peaks at 280 nm and 360 nm which fit relatively well to this experimental spectrum, and which are coherent with the shift observed by comparison with $PyOH^{\cdot-}$.

With the aim to determine the rate constant of the formation of $PyO^{\cdot-}$, the time evolution of absorbance at 295 nm was analyzed. A pseudo-first order kinetics fits well the kinetic signal (Figure 4.28).

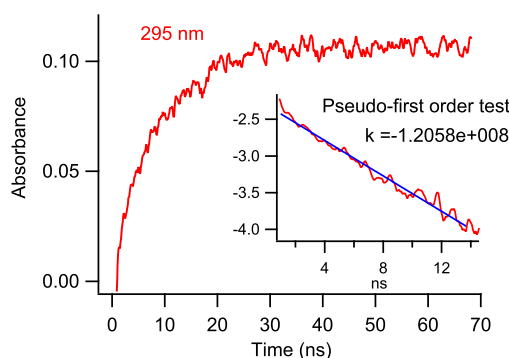


Figure 4.28: Time evolution of absorbance at 295 nm over 100 ns of a solution containing 20 mM in Py at pH= 13.5 under N_2O (Dose = 40 Gy/pulse; Optical path = 1 cm). Inset: pseudo-first order fit.

The observed rate constant is $k_{obs} = 1.2 \cdot 10^8 \text{ s}^{-1}$ which corresponds to a rate constant of $6.0 \cdot 10^9 \text{ L mol}^{-1}\text{s}^{-1}$. Unlike the kinetic signal recorded at 305 nm in acidic solution which begins to decay after 30 ns, the kinetics profile at 295 nm is stable after this same time range.

The time evolution of the absorption spectrum was followed at longer time from 1 μs to 1 ms. It does not change significantly on the microsecond time scale. Only a decrease of the absorbance at 295 nm is visible over 50 μs . Indeed, the first transient species, supposed to be the $PyO^{\cdot-}$ radical, decreases slowly on this time scale. In order to determine the rate constant of the decay, we studied the kinetics profile at 295 nm on 200 μs , where the decay is complete (Figure 4.29).

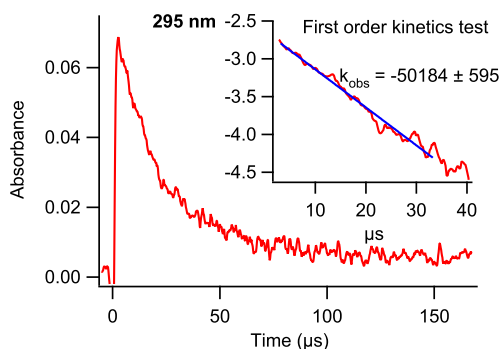


Figure 4.29: Time evolution of absorbance at 295 nm over 200 μs of a solution containing 20 mM in Py at pH= 13.5 under N_2O (Dose = 40 Gy/pulse; Optical path = 1 cm). Inset: pseudo-first order fit.

The radical absorbing at 295 nm reacts following a pseudo-first order law ($k_{obs} = 5.0 \cdot 10^4 \text{ s}^{-1}$) as shown in Figure 4.29. This is not in favor of a dimerization process, but probably in a transformation into another radical or into a stable species.

At longer time the spectrum at 800 μs is characterized by two peaks: a large band at around 320 nm with a shoulder at 340 nm and a peak at a wavelength lower than 270 nm which is difficult to identify due to the too low value of the absorbance (Figure 4.30). Moreover the high concentration used in Py monomer (20 mM) which absorbs significantly in the UV, induces a peak broadening which avoids to observe the wavelengths below 270 nm. The kinetic signal at 325 nm is also shown in Figure 4.30.

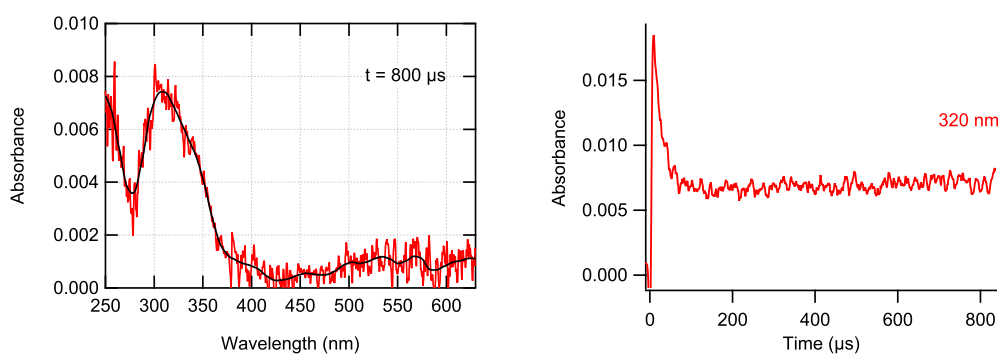


Figure 4.30: Absorption spectrum of a N_2O -saturated aqueous solution containing 20 mM in Py at pH = 13.5 recorded 800 μs after the pulse (on the left). Time evolution of absorbance at 325 nm over 800 μs (Dose = 40 Gy/pulse; Optical path = 1 cm).

The deconvolution was possible thanks to SVD analysis of the image recorded at 1 ms. The matrix was factored into two components the spectra and kinetic signals of which are depicted in Figure 4.31. The decomposition of the absorption spectrum shows the first species spectrum absorbing at 295 nm and around 400 nm which corresponds to the PyO^- radical. It decays on around $40 \mu\text{s}$ to produce the second species which absorbs at 330 nm and at around 600 nm.

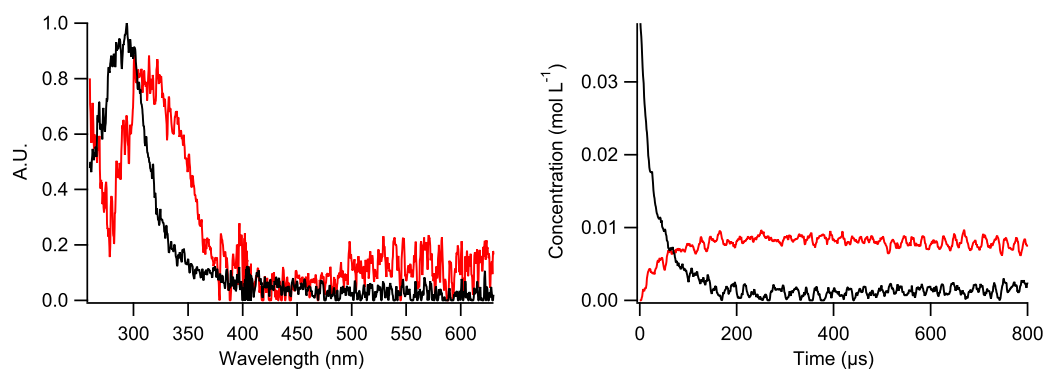


Figure 4.31: SVD deconvolution of the image recorded 1 ms after the pulse of a N_2O -saturated aqueous solution containing 20 mM in Pyrrole at pH 13.5 (Dose = 40 Gy/pulse).

This stable species was not identified but the kinetic deconvolution clearly shows that its growth corresponds to the decay at 295 nm. This means that the observed rate constant, $k_{obs} = 5.0 \cdot 10^4 \text{ s}^{-1}$, previously deduced from the decay at 295 nm, has to be of the same order of magnitude for the growth at 325 nm.

The UV-Vis spectrum recorded after the pulse radiolysis experiments is shown in Figure 4.32. The spectrum shows two bands at 270 nm and 330 nm, which were already observed during the pulse radiolysis experiment on 1 ms.

Note that also here, a large and intense band at wavelengths lower than 250 nm is present. This is certainly due to the absorption of Pyrrole at 205 nm which remains in excess in the solution (peak not visible here due to the zoom and the saturation of spectrum at this wavelength).

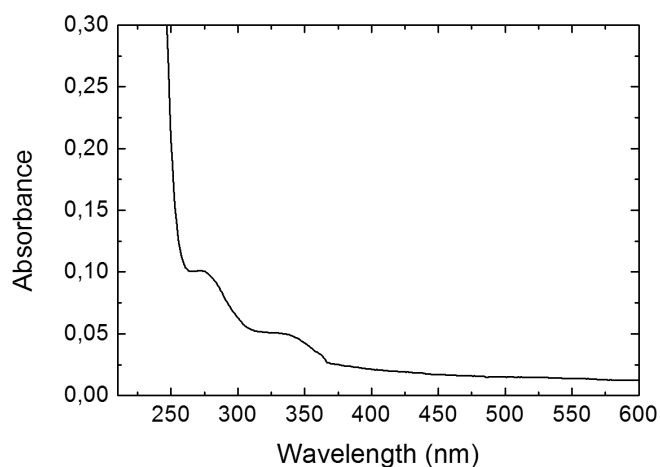


Figure 4.32: Static UV-Vis absorption spectrum of a solution containing 20 mM in Py at pH =13.5 after irradiation (Dose = 40 Gy/pulse; Optical path = 0.2 cm).

Indeed, before irradiation the solution contains 20 mM in Pyrrole. At the end of the experiment, the Py concentration is not significantly affected. Finally the absorption from 350 to 600 nm can be associated to the oligomers probably produced at longer time.

Kinetic simulation in alkaline solution

The aim of the simulation was to definitely identify the mechanism involved in the first steps of Pyrrole oxidation in alkaline solution. Indeed, the data analysis of experiments did not allow to prove completely the action of oxide radical on Pyrrole monomers on nanoscale time range. And it was not possible to determine the species involved in the reaction following the oxidation of Pyrrole.

As previously, the simulation includes all water radiolysis reactions (R1-R6), detailed in Table 4.4.

Reaction	Equation	Rate Constant (L mol ⁻¹ s ⁻¹)
R1	$e_{hyd}^- + N_2O \longrightarrow N_2 + HO\cdot$	$k = 9.1 \cdot 10^9$
R2	$e_{hyd}^- + HO\cdot \longrightarrow HO^-$	$k = 3.0 \cdot 10^{10}$
R3	$2 e_{hyd}^- \longrightarrow H_2 + HO^-$	$k = 5.5 \cdot 10^9$
R4	$e_{hyd}^- + H_3O^+ \longrightarrow H\cdot$	$k = 2.3 \cdot 10^{10}$
R5	$H\cdot + HO\cdot \longrightarrow H_2O$	$k = 7.0 \cdot 10^9$
R6	$2 HO\cdot \longrightarrow H_2O_2$	$k = 5.5 \cdot 10^9$
R7	$Py + HO\cdot \longrightarrow (PyOH)\cdot$	$k = 6.5 \cdot 10^9$
R8	$Py + O\cdot^- \longrightarrow PyO\cdot^-$	$k = 7.5 \cdot 10^9$
R9	$PyO\cdot^- \longrightarrow X$	$k = 5 \cdot 10^4 \text{ (s}^{-1}\text{)}$
R10	$HO\cdot + HO^- \rightleftharpoons O\cdot^- + H_2O$	$k_{10} = 1.25 \cdot 10^{10} ; k_{-10} = 1.7 \cdot 10^6$

Table 4.4: Reaction involve in Pyrrole oxidation in aqueous solution at alkaline pH.

Due to the alkaline environment, the equilibrium reaction of $HO\cdot/O\cdot^-$ ($pK_a = 11.9$) (R10) was also introduced to estimate the effective concentration of hydroxyl and oxide radicals. The competition between the hydroxyl and oxide radicals was involved in the system by including the two possible reactions with Pyrrole monomers (R7 and R8). The rate constants were from literature for all reactions of water radiolysis. The rate constant of reaction R7 was deduced from our study at neutral pH. The rate constants of reaction between Pyrrole monomers and oxide radicals (R8) and the dimerization of adduct oxide radical (R9) were from the estimation achieved in the previous experimental data analysis. Also in this case, the initial concentrations (Table 4.5) of radiolytical species where calculated from dosimetry measurements.

Initial Concentration [M]	Dose [Gy/pulse]	Radiolytic species concentration [M]
$[Py] = 0.02$ $[HO^-] = 0.6$ $[N_2O] = 0.022$	39	$[e_{hyd}^-] = [H_3O^+] = 1.36 \cdot 10^{-5}$ $[HO\cdot] = 1.45 \cdot 10^{-5}$ $[H\cdot] = 2.5 \cdot 10^{-6}$

Table 4.5: Experimental parameters used in the simulation in alkaline solution.

It has to be noted again that the high concentration of HO^- , estimated directly

from the value of pH (13.5), shifts the equilibrium towards the formation of oxide radicals ($pK_a = 11.9$).

First, the time evolution of concentrations over 100 ns was investigated. At this time scale, it was previously observed an absorption spectrum showing a peak at 295 nm and a weak band at around 380 nm. This absorption spectrum was identified as that of the oxide adduct radical, $\text{PyO}^{\cdot-}$. In fact, the concentration of hydroxyl radical is too low to induce the formation of hydroxyl adduct radical. As shown in Figure 4.33, 100 ns after the pulse the concentration of HO^{\cdot} is less than $1 \cdot 10^{-6} \text{ mol L}^{-1}$.

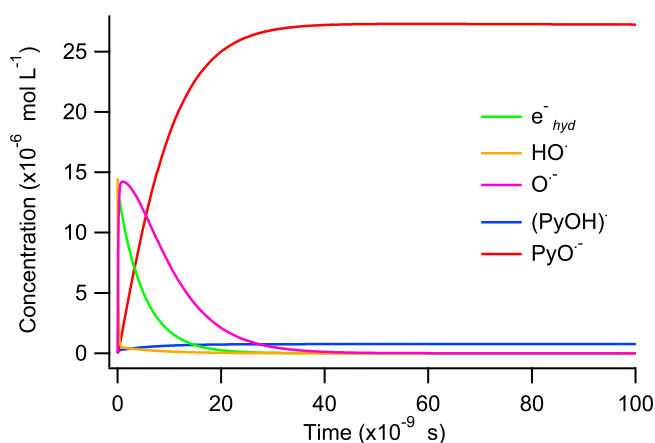


Figure 4.33: Time evolution of all species implied in the reaction mechanism of a system containing 20mM in Py in alkaline pH (pH = 13.5) under N_2O .

For this reason its contribution to the growth of the peak at 295 nm can be neglected. On the other hand, the oxide radical concentration is higher and it is rapidly converted by the reaction with Py monomer.

After this consideration on time evolution of radiolytical species concentration, we compared the experimental signals with the simulated ones. In Figure 4.34 the experimental adduct oxide radical $\text{PyO}^{\cdot-}$ growth and hydrated electron decay are compared with the simulated signals.

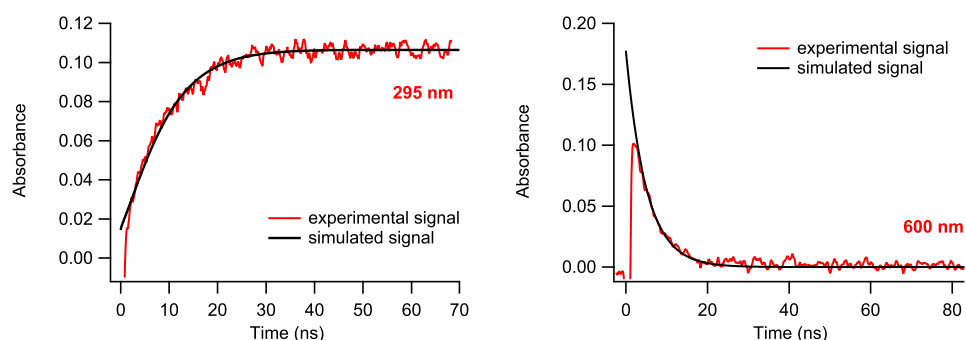


Figure 4.34: Comparison between experimental time evolution of absorbance and simulated one of the first transient species absorbing at 295 nm (on the left) and of the hydrated electron absorbing at 600 nm (on the right) over 100 ns under N_2O (Dose = 40 Gy/pulse, Optical path = 1 cm).

Again, the extinction coefficient of electron used to transform the concentration in optical density was $13000 \text{ L mol}^{-1}\text{cm}^{-1}$. On the other hand the extinction coefficient used at 295 nm was adjusted at $\epsilon = 3900 \text{ L mol}^{-1}\text{cm}^{-1}$ to reproduce the kinetic signal. The first observation is that the rate constant chosen to fit well the experimental signal is faster than that estimated from experimental data. The value of $7.5 \cdot 10^9 \text{ L mol}^{-1} \text{ s}^{-1}$ instead of $6.0 \cdot 10^9 \text{ L mol}^{-1} \text{ s}^{-1}$ covered 15% of systematic error made in the extrapolation of the rate constant value.

At longer time, the decay of the adduct oxide radical $PyO^{\cdot-}$ on $200 \mu\text{s}$ follows a first or a pseudo-first order law with an observed rate constant of $5.0 \cdot 10^4 \text{ s}^{-1}$ giving a species which grows at 325 nm. Two possibilities can be envisaged: $PyO^{\cdot-}$ transforms according to a unimolecular reaction or reacts onto a species present in excess according to a pseudo-first order reaction. These species in excess could be Py or HO^- . Nevertheless, since no reaction of EDOT radicals with EDOT monomers was observed and since a step-by-step reaction was suggested (chapter 2), we suppose that also in this case the reaction of $PyO^{\cdot-}$ on Py can be excluded. And probably $PyO^{\cdot-}$ undergoes a chain opening.

In Figure 4.35 the simulation of the reaction mechanism is shown during the first $200 \mu\text{s}$. The decay at 295 nm is plotted on the experimental signal. The time evolution concentration is again adjusted by the extinction coefficient at 295 nm $\epsilon = 3900 \text{ L mol}^{-1}\text{cm}^{-1}$.

Finally the growth of the species at 325 nm on 1 ms was compared with the simulated one (Figure 4.36). The signal is a combination of two components, the

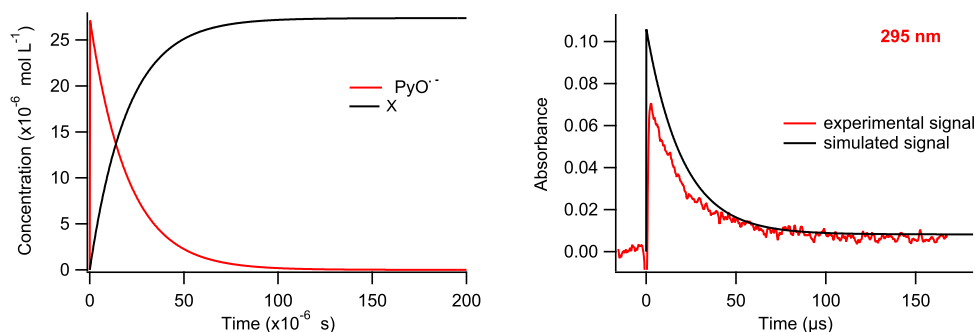


Figure 4.35: Simulation of time evolution of $\text{PyO}^{\bullet-}$ and X concentration in a solution containing 20 mM in Py at $\text{pH} = 13.5$ under N_2O (on the left); comparison simulated signal and experimental one at 295 nm over 200 μs .

decay at 295 nm which weakly affects the signal at 325 nm and the growth of the species X. At 325 nm the extinction coefficient of $\text{PyO}^{\bullet-}$ was estimated at $500 \text{ L mol}^{-1}\text{cm}^{-1}$. This value was obtained by considering the loss of signal on the first μs on the image recorded in the millisecond time scale. The ratio of absorbances at 295 and 325 nm on 100 ns was used to evaluate the ratio between the extinction coefficient values at the same wavelength. And this ratio was successively used to estimate the value of extinction coefficient at 325 nm on 1 ms. The extinction coefficient of species X was adjusted at $230 \text{ L mol}^{-1}\text{cm}^{-1}$ at 325 nm to fit well the signal.

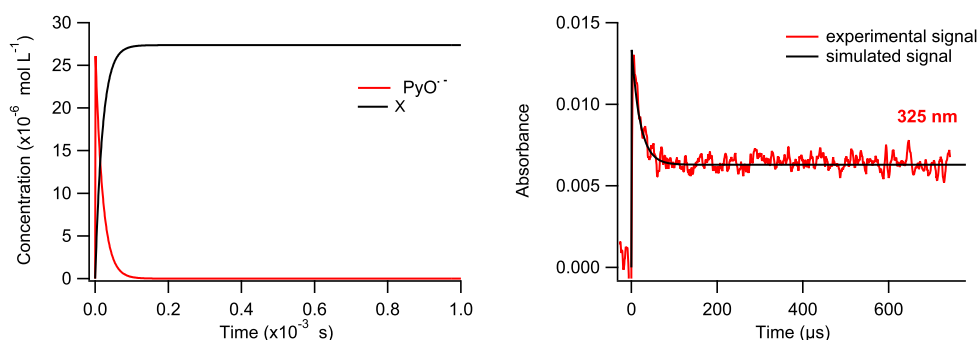


Figure 4.36: Simulation time evolution of $\text{PyO}^{\bullet-}$ and X concentration in a solution containing 20mM in Py at $\text{pH} = 13.5$ under N_2O (on the left); comparison simulated signal and experimental one at 325 nm over 800 μs .

Thanks to the COPASI simulation it was possible to describe the reaction of oxide radicals on Pyrrole monomer in alkaline medium. The oxidation of Pyrrole

by oxide radical induces the formation of adduct radical, $\text{PyO}^{\cdot-}$. This last is successively involved in a reaction of the first order giving a stable species X absorbing at 325 nm.

4.6 Carbonate

As in the case of EDOT polymerization, we were interesting to investigate Pyrrole monomers oxidation by using an alternative oxidizing radiolytic species, the carbonate radical, $\text{CO}_3^{\cdot-}$. With the aim to determine the action of carbonate radical, we studied the N_2O -saturated aqueous solutions containing 1 M in Na_2CO_3 and respectively 20 mM, 50 mM, and 100 mM in Py. The solutions at 20 and 50 mM in Py were irradiated at 45 Gy per pulse, whereas the solution containing 100 mM in Py was irradiated with 37 Gy per pulse. Therefore in order to compare the three solutions, the kinetic signals and spectra of the solution concentrated at 100 mM in Py were normalized to a dose of 45 Gy.

For the three solutions, the pH was 13.5. This means that HO^{\cdot} radicals produced by radiolysis of water as well as those issued from the reaction of hydrated electron e_{hy}^- with N_2O are in the form of oxide radicals $\text{O}^{\cdot-}$. However the carbonate radical $\text{CO}_3^{\cdot-}$ can be indifferently produced from the reaction with either hydroxyl radical or oxide radical but with different rate constants.

At short time scale, we expected the decay of electron followed by the formation of carbonate radical $\text{CO}_3^{\cdot-}$ at 600 nm. In fact, the formation of carbonate radicals was not so evident as attended. The characteristic absorption band at 600 nm was not enough intense and an unattended peak appeared at 295 nm. The figure 4.37 shows the spectra recorded at the time corresponding to the maximum of absorption at 295 nm for the three irradiated solutions (20, 50 and 100 mM in Py).

In the solution containing 100 mM in Py, the species absorbing at 295 nm is completely formed over 30 ns. On the other hand for the solution containing 50 mM in Pyrrole the maximum of absorption is reached over 40 ns, and finally 70 ns are necessary for the solution containing 20 mM in Py. This transient species absorbing at 295 nm was already observed at alkaline solution (in absence of Na_2CO_3) and its dependence on Pyrrole monomer concentration suggests that it can be due to the addition of oxide radical on Pyrrole giving $\text{PyO}^{\cdot-}$ as already de-

scribed. Moreover also the carbonate radical absorption is inversely proportional to Pyrrole monomer concentration.

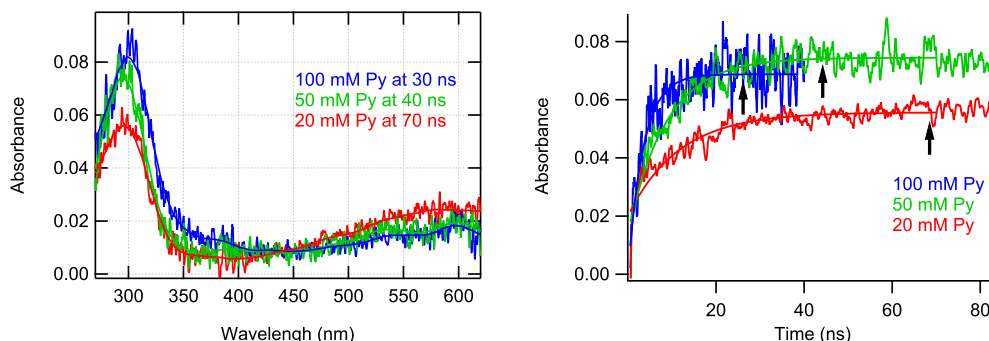


Figure 4.37: Absorption spectra recorded over 70 ns after the pulse of the solution containing 1 M in Na_2CO_3 and 20 mM in Py and at 40 ns after the pulse for the solutions containing 1 M in Na_2CO_3 and 50 and 100 mM in Py, respectively. On the right the comparison of the increase at 295 nm for three solutions. Note that the spectrum and the growth signal of the solution containing 100 mM in Py is corrected by a normalization due to the different dose of irradiation (Optical path = 1 cm).

These results can be explained by a complex system of competition reactions as described in Table 4.6. Indeed during the first 100 ns after the pulse, the radiolytical species can react either with Pyrrole monomers or with carbonate radicals. Thanks to a simulation performed with COPASI program, it was possible to estimate the concentrations of first species produced after the pulse. All the rate constants are from literature except that of Pyrrole radicals which were from this work.

This mechanism does not include the consumption of transient species produced on 100 ns. Indeed, the complexity of the system does not allow to estimate the rate constants of consumption of carbonate or Pyrrole radicals. This omission induces an error on the final concentrations, but the aim was to understand the role of each radical on the oxidation of Pyrrole monomer in the medium (presence of Na_2CO_3 at alkaline medium).

In order to show the effect of monomer concentrations on the kinetics, the simulation was performed for the three solution at 20, 50 and 100 mM in Pyrrole at the same irradiation dose of 45 Gy. The Table 4.7 shows the parameters used for the simulation. As usually, the concentrations of radiolytical species were estimated from dosimetry. The concentration of carbonate anions, CO_3^{2-}

Reaction	Equation	Constant Rate (L mol ⁻¹ s ⁻¹)
R1	$e_{hyd}^- + N_2O \longrightarrow N_2 + HO^\cdot$	$k = 9.1 \cdot 10^9$
R2	$e_{hyd}^- + HO^\cdot \longrightarrow HO^-$	$k = 3.0 \cdot 10^{10}$
R3	$2 e_{hyd}^- \longrightarrow H_2 + HO^-$	$k = 5.5 \cdot 10^9$
R4	$e_{hyd}^- + H_3O^\cdot \longrightarrow H^\cdot$	$k = 2.3 \cdot 10^{10}$
R5	$H^\cdot + HO^\cdot \longrightarrow H_2O$	$k = 7.0 \cdot 10^9$
R6	$2 HO^\cdot \longrightarrow H_2O_2$	$k = 5.5 \cdot 10^9$
R7	$Py + HO^\cdot \longrightarrow (PyOH)^\cdot$	$k = 6.5 \cdot 10^9$
R8	$Py + O^{\cdot-} \longrightarrow PyO^{\cdot-}$	$k = 8 \cdot 10^9$
R9	$CO_3^{2-} + HO^\cdot \longrightarrow CO_3^{\cdot-} + HO^-$	$k = 4 \cdot 10^8$
R10	$CO_3^{2-} + O^{\cdot-} \longrightarrow CO_3^{\cdot-}$	$k = 4.4 \cdot 10^7$
R11	$HO^\cdot + HO^- \rightleftharpoons O^{\cdot-} + H_2O$	$k_{11} = 1.25 \cdot 10^{10}$; $k_{-11} = 1.7 \cdot 10^6$

Table 4.6: Reaction taken into account to simulate the kinetic process involved in a N₂O-saturated aqueous solution containing Pyrrole monomer and carbonate anions at pH = 13.5 irradiated with electron pulse (Dose = 45 Gy/pulse).

was 1 M for each solution. Indeed, given the $pK_a(HCO_3^{\cdot-}/CO_3^{2-}) = 10.33$, the concentration of HCO_3^- , which can eventually react with hydroxyl radical to produce the same carbonate radical $CO_3^{\cdot-}$, is $6.3 \cdot 10^{-4}$ M at pH 13.5. And it can be neglected compared to the CO_3^{2-} concentration.

Initial Concentration [M]	Dose [Gy/pulse]	Radiolytic species concentration[M]
[Py] = 0.02 [Py] = 0.05 [Py] = 0.1 [HO ⁻] = 0.31 [N ₂ O] = 0.026	45	$[e^-] = [H_3O^+] = 1.53 \cdot 10^{-5}$ $[HO^\cdot] = 1.62 \cdot 10^{-5}$ $[H^\cdot] = 2.4 \cdot 10^{-6}$

Table 4.7: Experimental parameters used in the simulation in the case of a solution containing 1 M in carbonate and three different concentration of Pyrrole under N₂O at pH = 13.5.

In Figure 4.38, the three graphics depict the time evolution of the first transient species over 100 ns.

It appears clearly a competition between the reactions R7, R8 and R9 (or R10). Indeed the increase of Pyrrole decreases the carbonate radicals concentration. On the contrary, the concentrations of Pyrrole radicals, $\text{PyO}^{\cdot-}$ and PyOH^{\cdot} , increase with the concentration of Pyrrole monomers.

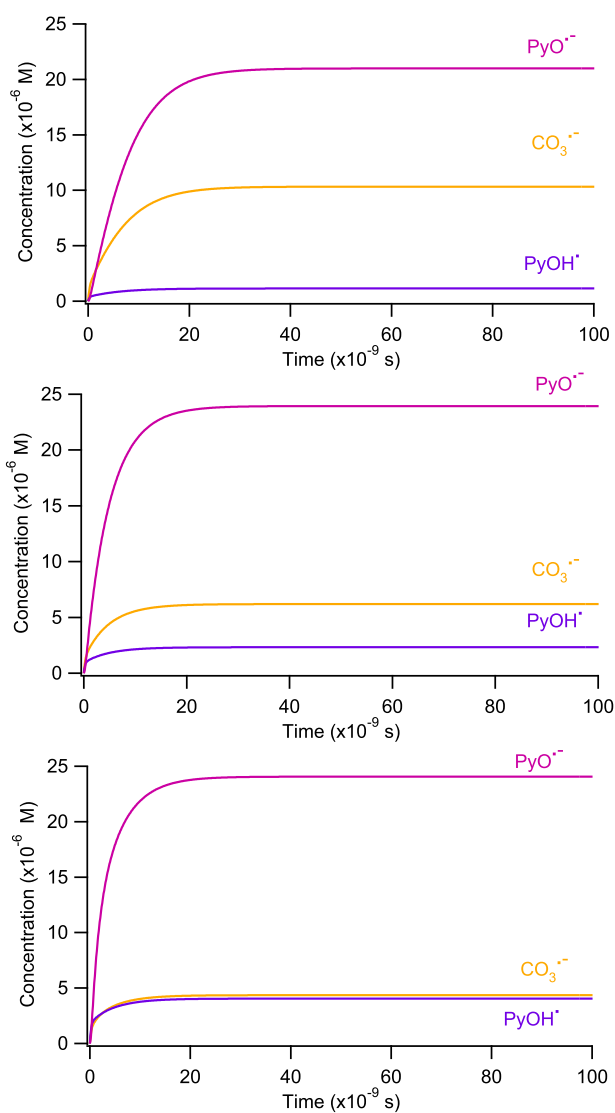


Figure 4.38: Simulation of the time evolution of the concentration of three transient species ($\text{CO}_3^{\cdot-}$, PyOH^{\cdot} and $\text{PyO}^{\cdot-}$) produce in the aqueous solutions containing 1 mM in carbonate and respectively 20, 50 and 100 mM in Py respectively (from the top to the bottom of the figure). In order to compare the effect of Py concentrations, the simulation were all realized at 45 Gy.

As observed HO^\cdot or $\text{O}^{\cdot-}$ react preferentially onto Py monomers. Only a small part of these radicals react onto CO_3^{2-} leading to $\text{CO}_3^{\cdot-}$. Then the carbonate radical can not oxidize quantitatively the monomer on the first 100 ns.

We studied the absorption spectra at longer time. Due to the action of oxide radical on Pyrrole, one expects to find the formation of the peak at 325 nm, as in the case of alkaline solution (see section 4.5.2). On the contrary, the time evolution of the absorption of the adduct oxide radical, $\text{PyO}^{\cdot-}$, produced over 100 ns, is very different from that observed in alkaline solution. On first microseconds, the decay of the peak at 295 nm is followed by the formation of three peaks at 345, 400 and 545 nm showed in Figure 4.39.

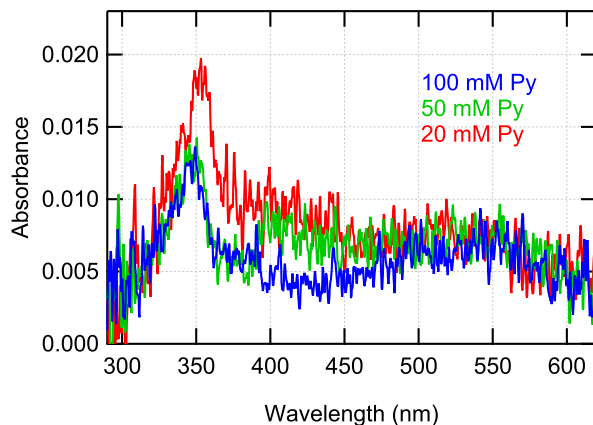


Figure 4.39: Absorption spectra recorded 190 μs after the pulse of the N_2O -saturated aqueous solutions containing 1 mM in Na_2CO_3 and 20, 50 and 100 mM in Py, respectively. Note that the spectra of the solution containing 100 mM in Py is corrected by a normalization due to the different dose of irradiation (Dose=45 Gy/pulse, Optical path = 1 cm).

The kinetics of these peaks are different. In Figure 4.40, the kinetic profiles at 345 and 545 nm are shown. Note that the wavelength 400 nm is exactly in the overlapping region of the two spectra recorded with the two different networks of the streak camera, and the signal is too noisy; so it is not presented.

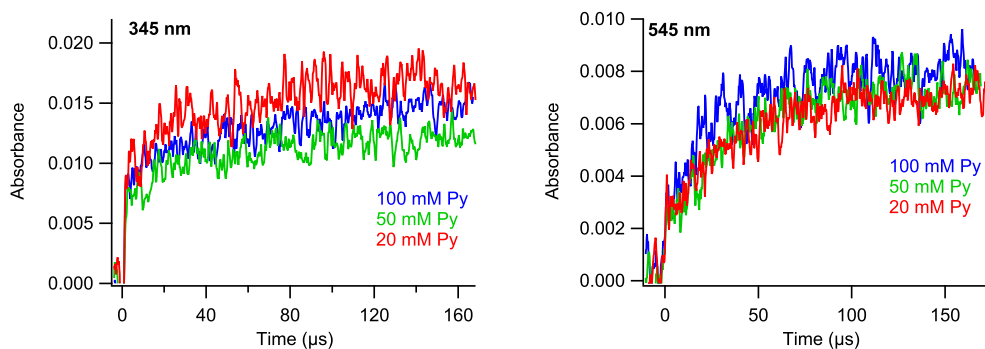


Figure 4.40: Kinetic profiles of main peaks over 190 μs after the pulse of the N_2O -saturated aqueous solutions containing 1 mM in Na_2CO_3 and 20, 50 and 100 mM in Py, respectively. Note that growth signal of the solution containing 100 mM in Py is corrected by a normalization due to the different dose of irradiation (Dose=45 Gy/pulse, Optical path = 1 cm).

Due to the overlapping of the absorptions, it was not possible to deconvolute the different transient spectra and kinetics. However these results are very interesting for several reasons. First, the adduct oxide radical, PyO^- , absorbing at 295 nm does not react as in the case of alkaline solutions. This result suggests that the carbonate is involved in the reaction mechanism, but not in the first step of growth.

Moreover, the spectrum recorded on 1 ms is very similar to that recorded at the same time in acidic solutions. In Figure 4.41, the comparison between the two spectra is depicted in the absence of carbonate. However, there are some important differences between the two spectra. First, the absorption intensity is 10 times higher at low pH in the absence of carbonate than high pH in the presence of carbonate. This is probably due to the concentration of the species produced and the extinction coefficient. Indeed, another difference not negligible is the shift of around 50 nm between the peak at 600 nm in acidic solution and at 550 nm in alkaline solution in the presence of carbonate. This difference can be interpreted as the formation of two different opening radicals depending on what chemical bond of the cycle is broken.

In acidic pH in the absence of carbonate the opening of the ring follows the protonation, so the radical is positively charged. On the other hand, in alkaline solution and in presence of carbonate the concentration of H_3O^+ is too low and probably a neutral or negatively charged open radical is produced. Besides in the

study of Hapiot [5], we can note a shift in the spectrum due to the difference in charge of the two Bypyrrole radicals, $BP^{\cdot+}$ and BP^{\cdot} .

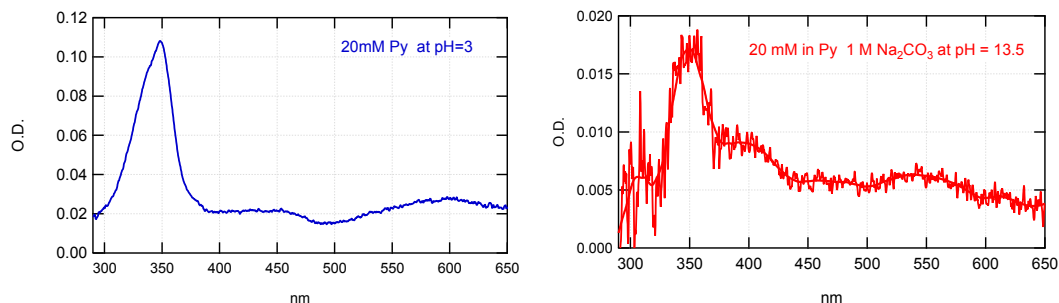


Figure 4.41: Absorption spectra over $300 \mu s$ after the pulse of a solution containing 20 mM in Pyrrole at $pH = 2.8$ on the left and a solution containing 20 mM in Py and 1 M in CO_3^{2-} at $pH = 13.5$ on the right.

We previously introduced the idea that at low pH and at high pH in the absence of carbonate the Pyrrole molecule could be open in a linear radical. Moreover, it was already demonstrated that also the EDOT ring is broken at very high pH. It is not incoherent to suppose that also at too high pH the Pyrrole can be broken.

4.7 Polypyrrole synthesis

With the aim to polymerize pyrrole into polypyrrole, as in the case of EDOT, a recurrent oxidation process seems necessary. Then, a solution containing 20 mM in Py in a closed cell under N_2O atmosphere was irradiated with a series of consecutive electron pulses.

In order to obtain sufficient concentrations in hydroxide radicals to completely oxidize red 20 mM of Py monomers, we estimated the dose to deliver at 70 kGy, which corresponds to ~ 1500 pulses of 45 Gy/pulse. This dose was chosen according to a previous work based on γ -radiolysis, where Cui *et. al.* showed that 70 kGy were sufficient to polymerize polypyrrole [10].

The Figure 4.42 displays the UV-Vis absorption spectra of Py monomer (red one) and PPy polymers (black one). After irradiation the solution color changes from transparent to yellow-black. And the UV-Vis spectrum shows a continuous diffusion on spectral range between [250-800] nm and three bands are visible at

300 , 360 and 600 nm after the irradiation. According to literature, the shoulder at 300 nm should be attributed to tertpyrrole, [17] and the band at about 360 nm could be associated with inter-band $\pi - \pi^*$ transition whose intensity is related to neutral PPy content, [18]. This spectrum is in agreement with the results previously obtained by gamma radiolysis [10], where the scattering observed on the spectrum explains the presence of PPy nanoparticles in aqueous solution.

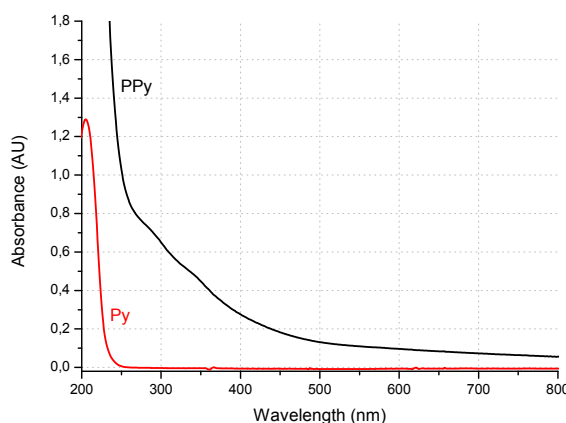


Figure 4.42: UV-Vis spectrum of 20 mM in Pyrrole, before irradiation (diluted 20 times, red line) and after irradiation at 70 kGy (black line) (irradiated with 1500 pulses of 45 Gy/pulse)

The sample was then characterized by ATR-FTIR spectroscopy in order to check its chemical composition and to prove that the solution contains PPy. A drop of the solution containing the yellow-black suspension was deposited on the prism and dried at air. Figure 4.43 shows Pyrrole monomer ATR-FTIR spectrum (red one) and Polypyrrole spectrum (black one). The two spectra presented are in agreement with those of Py and PPY found in literature [10].

In Pyrrole monomers IR-spectrum the band at 3394 cm^{-1} is attributed to the in-plane stretching of N-H, [18, 19]. The weak band at 1466 cm^{-1} originates from C-C in-ring-stretch modes, [18]. The intense band at 1047 cm^{-1} is mostly attributed to C-C out-of-plane deformation vibration, [18]. Finally the band at 725 cm^{-1} is C-H wag vibration in α, α' positions, [20, 21]. Nevertheless, this band is absent in the spectrum after irradiation suggesting the quantitative synthesis of PPy by electron-beam irradiation.

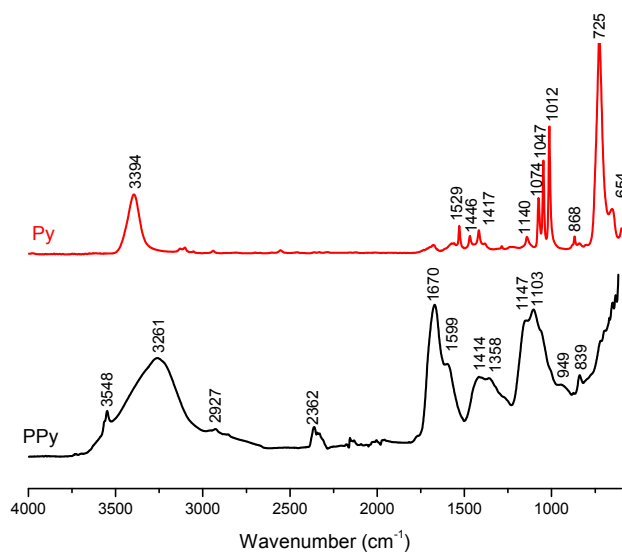


Figure 4.43: AFT-IR spectrum of Pyrrole monomer (red one) and Polypyrrole polymer (black one).

In PPy polymer IR-spectrum the band of N-H bond is displaced from 3394 to 3261 cm^{-1} . This large band should result from the N-H groups of the polymers and could also originate from -OH functionalization of the polymers by hydroxyl radical. Indeed, this has already been established in the case of PEDOT and it is in good agreement with literature, [18, 10]. The band at 1670 cm^{-1} is the C=O vibration, [19]. According to Vetter *et al.*, the presence of this peak demonstrates that the PPy synthesized by electron beam is overoxidized [17]. The band at 949 cm^{-1} corresponds to the C-H out of plane bending [22]. The peaks at 2927 cm^{-1} and 2860 cm^{-1} originate from C-H symmetric and antisymmetric deformation in CH_2 and CH_3 aliphatic, [21].

This result proves the success of electron beam induced synthesis of PPy suggesting that the growth proceeds via step-by-step mechanism.

In order to characterize the morphology of electron beam induced PPy, we proceeded with AFM-IR nanospectroscopy. A drop of solution containing the PPy black suspension was deposited on ZeSe prism and dried naturally at air. Then, it was imaged by AFM-IR. As shown in Figure 4.44, the topographic image depicts the formation of some globular structures which are agglomerated.

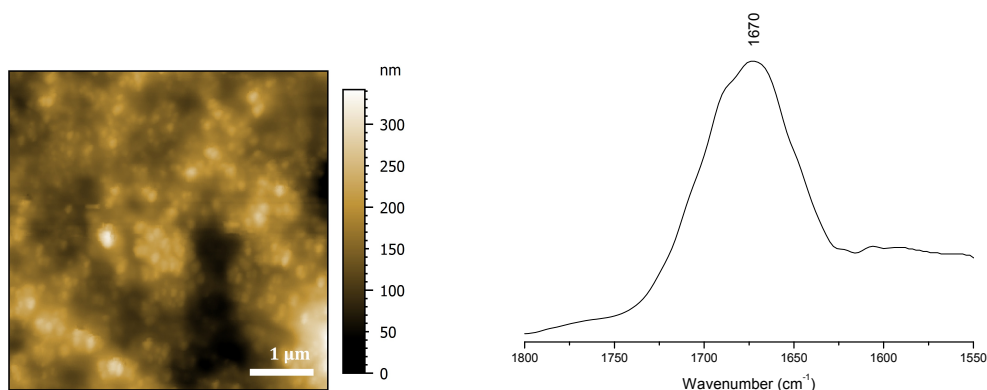


Figure 4.44: AFM topographic image (on the left) and local IR spectrum (on the right) of Polypyrrole synthesized by electron beam irradiation of an aqueous solution containing 20 mM in Py with a dose of 70 kGy.

This morphology could be explained as a complex structure composed by polymeric chains. Since the AFM-IR technique combines atomic force microscopy and infrared nanospectroscopy, it was possible to characterize the chemical composition of PPy by infrared spectroscopy.

According to the AFM image of PPy recorded in contact mode (Figure 4.44), the dark areas having no thickness correspond to the substrate. On the other hand the bright areas correspond to the thicker regions made up of PPy nanoparticles closely packed smaller ones (200-300 nm in average).

In order to confirm that the nanoparticles observed in contact mode are made up of PPy polymers, the sample was observed by AFM-IR in the range of 1600-1800 cm^{-1} . The spectrum of (Figure 4.44) displays a peak at 1670 cm^{-1} , which is characteristic of C=O bonds. The same band has been previously detected by ATR-FTIR spectroscopy in PPy polymers (black spectrum, Figure 4.43) and not in Py monomers (red spectrum, Figure 4.43). Then the globular structures observed in Figure 4.44 contains close-packed PPy polymers.

These results are in good agreement with the size and the shape found for PPy nanoparticles synthesized by γ -radiolysis, [10].

4.8 Conclusion

In this work, we presented the study of the first steps of Pyrrole oxidation and polymerization. The kinetic study at neutral pH allowed to identify the first transient species involved in the mechanism and to determine the rate constants thanks to a comparative study with the simulated spectra. The action of HO^\cdot onto Py leads to the formation of hydroxyl adduct radical $(\text{PyOH})^\cdot$, the spectrum of which shows an intense peak at 305 nm and a weak band at around 400 nm.

By changing the concentration of Pyrrole monomers, the rate constant of oxidation was determined: $k = 6.5 \cdot 10^9 \text{ L mol}^{-1} \text{ s}^{-1}$. On the other hand the effect of dose allowed to estimate the extinction coefficient $\epsilon_{305\text{nm}} = 3299 \pm 36 \text{ L mol}^{-1} \text{ cm}^{-1}$. Thanks to the investigation on pH effect, it was possible to demonstrate that in acidic solution the adduct Pyrrole radical, $(\text{PyOH})^\cdot$, is protonated into PyHOH^+ which absorbs at 260 and around 340 nm and successively it can dimerize or undergo to opening the ring. At alkaline solutions, due to the action of $\text{O}^{\cdot-}$, the first transient species was the anion adduct radical, $\text{PyO}^{\cdot-}$, which absorbs at 295 nm and around 380 nm. This species decays by a first (or pseudo-first) order, may be into an open cycle.

Then, carbonate radicals were used to oxidize Py but due to the competitive reactions with $\text{O}^{\cdot-}$, these radicals were found to poorly react onto Py.

Finally, we succeeded in polymerization by electron beam irradiation. As revealed by ATR-FTIR spectroscopy, the probable presence along the polymeric chains of O-H and C=O functionalities, which should come from the addition of hydroxyl radicals during the polymer growth.

Morphological study by AFM revealed the formation of globular PPy nanostructures comparable to the results obtained in literature. This success, by using repetitive electron pulses suggest first the dimer formation, then polymer growth through a recurrent step-by-step mechanism which involves a recurrent oxidation process by hydroxyl radicals formed during water radiolysis.

Bibliography

- [1] Said Sadki, Philippe Schottland, Nancy Brodie, and Guillaume Sabouraud. The mechanisms of pyrrole electropolymerization. *Chemical Society Reviews*, 29(5):283–293, 2000.
- [2] J Lilie. Pulsradiolytische untersuchung der oxydativen ringöffnung von furan, thiophen und pyrrol/pulsradiolytic investigations of the oxydativ ring scission of furan, thiophen and pyrrol. *Zeitschrift für Naturforschung B*, 26(3):197–202, 1971.
- [3] Laurent Guyard, Philippe Hapiot, and Pedatsur Neta. Redox chemistry of bipyrrroles: further insights into the oxidative polymerization mechanism of pyrrole and oligopyrrroles. *The Journal of Physical Chemistry B*, 101(29):5698–5706, 1997.
- [4] Reza Ansari. Polypyrrole conducting electroactive polymers: synthesis and stability studies. *Journal of Chemistry*, 3(4):186–201, 2006.
- [5] Claude P Andrieux, Pierre Audebert, Philippe Hapiot, and Jean Michel Saveant. Identification of the first steps of the electrochemical polymerization of pyrroles by means of fast potential step techniques. *The Journal of Physical Chemistry*, 95(24):10158–10164, 1991.
- [6] Claude P Andrieux, Pierre Audebert, Phillippe Hapiot, and Jean Michel Saveant. Observation of the cation radicals of pyrrole and of some substituted pyrroles in fast-scan cyclic voltammetry. standard potentials and lifetimes. *Journal of the American Chemical Society*, 112(6):2439–2440, 1990.
- [7] MF Planche, JC Thieblemont, N Mazars, and G Bidan. Kinetic study of pyrrole polymerization with iron (iii) chloride in water. *Journal of applied polymer science*, 52(13):1867–1877, 1994.
- [8] Robert B Bjorklund. Kinetics of pyrrole polymerisation in aqueous iron chloride solution. *Journal of the Chemical Society, Faraday Transactions 1: Physical Chemistry in Condensed Phases*, 83(5):1507–1514, 1987.
- [9] Yang Tan and Khashayar Ghandi. Kinetics and mechanism of pyrrole chemical polymerization. *Synthetic Metals*, 175:183–191, 2013.
- [10] Zhenpeng Cui, Cecilia Coletta, Alexandre Dazzi, Patrice Lefrancois, Matthieu Gervais, Stéphane Néron, and Samy Remita. Radiolytic method as a novel ap-

- proach for the synthesis of nanostructured conducting polypyrrole. *Langmuir*, 30(46):14086–14094, 2014.
- [11] George V Buxton, Clive L Greenstock, W Phillips Helman, and Alberta B Ross. Critical review of rate constants for reactions of hydrated electrons, hydrogen atoms and hydroxyl radicals (oh/ o- in aqueous solution. *Journal of physical and chemical reference data*, 17(2):513–886, 1988.
- [12] Leon M Dorfman and Gerald E Adams. Reactivity of the hydroxyl radical in aqueous solutions. Technical report, DTIC Document, 1973.
- [13] Robert M Silverstein, Francis X Webster, David J Kiemle, and David L Bryce. *Spectrometric identification of organic compounds*. John Wiley & Sons, 2014.
- [14] Henry Rapoport and Neal Castagnoli. 2, 2'-bipyrrole. *Journal of the American Chemical Society*, 84(11):2178–2181, 1962.
- [15] Qibing Pei and Renyuan Qian. Protonation and deprotonation of polypyrrole chain in aqueous solutions. *Synthetic metals*, 45(1):35–48, 1991.
- [16] Meenakshi Choudhary, Rafique Ul Islam, Michael J Witcomb, and Kaushik Mallick. In situ generation of a high-performance pd-polypyrrole composite with multi-functional catalytic properties. *Dalton Transactions*, 43(17):6396–6405, 2014.
- [17] Christopher A Vetter, Abhijit Suryawanshi, Jessica R Lamb, Benedict Law, and Victoria J Gelling. Novel synthesis of stable polypyrrole nanospheres using ozone. *Langmuir*, 27(22):13719–13728, 2011.
- [18] Xin-Gui Li, Ang Li, Mei-Rong Huang, Yaozu Liao, and Yong-Gen Lu. Efficient and scalable synthesis of pure polypyrrole nanoparticles applicable for advanced nanocomposites and carbon nanoparticles. *The Journal of Physical Chemistry C*, 114(45):19244–19255, 2010.
- [19] RN Singh, Poonam Rawat, Sangeeta Sahu, and Yashvinder Kumar. Antimicrobial activity, structural evaluation and vibrational (ft-ir and ft-raman) study of pyrrole containing vinyl derivatives. *Spectrochimica Acta Part A: Molecular and Biomolecular Spectroscopy*, 154:47–57, 2016.
- [20] Jude O Iroh and Wencheng Su. Effect of process parameters on the electropolymerization potential and rate of formation of polypyrrole on stainless steel. *Journal of applied polymer science*, 66(13):2433–2440, 1997.

- [21] Lisete C Scienza and George E Thompson. Preparation and surface analysis of ppy/sdbs films on aluminum substrates. *Polimeros*, 11(3):142–148, 2001.
- [22] Jullieth Suárez-Guevara, Omar Ayyad, and Pedro Gómez-Romero. Copper@ polypyrrole nanocables. *Nanoscale research letters*, 7(1):1–6, 2012.

Chapter 5

Conclusion and Perspective

Current research aims to develop new synthesis strategies and new conducting polymers with the aim to control and improve the optical and electrical properties of conducting polymers.

Usually chemical and electrochemical routes are the most useful method to synthesize conducting polymers. Recently a new method has been proposed in our laboratory which use the oxidizing species induced by radiolysis of water as initiator of conducting polymers synthesis. This method, already used for non-conducting polymers, shows several advantages. The polymerization is performed at ambient temperature and pressure. The oxidation takes places thanks to the water radiolysis products, and no external chemical initiators are necessary. In this work we used pulse radiolysis technique to study the growth mechanism and to synthesize the PEDOT and PPy.

Firstly the reactivity of hydroxyl radical onto EDOT molecules at neutral pH was detailed. The mechanistic scheme of EDOT oxidation by hydroxyl radical was established, the rate constants were determined and the transient species involved in the oxidation process were identified thanks to the comparison of their experimental and simulated UV-Vis absorption spectra. We used a mixed simulation method, using the Monte-Carlo sampling of the molecular geometries, the DFT calculation of the electron structures and the PCM modeling of the solvent. In neutral aqueous solutions, after one pulse irradiation (40 Gy), no other products than EDOT₂ dimers were observed, demonstrating that no polymerization takes place. This results prove that a recurrent oxidation is necessary to polymerize the molecule. Then we concluded that the PEDOT polymerization proceeds through a step by step mechanism made up of the following recurrent steps: (i) oxidation/activation, (ii) growth/chain length increase, (iii) deprotonation.

On the other hand in alkaline medium, the mechanism is mostly different since HO^\bullet deprotonates into its alkaline form, oxide radical, which adds onto EDOT monomer. This addition leads to an open cycle and prevents any dimerization of EDOT and consequently any polymerization to PEDOT.

In order to synthesize conducting PEDOT polymers, we used the pulse electron beam of the accelerator ELYSE, usually employed in fast kinetic studies, as a high energy electrons irradiator. Successfully, the irradiation with a series of consecutive electron pulses on EDOT aqueous solution enabled the production of a very high concentration of hydroxyl radicals and thus the quantitative synthesis of PEDOT polymers. The chemical nature of radiosynthesized PEDOT polymers was confirmed by ATR-FTIR spectroscopy while their morphology was observed in solution by cryo-TEM microscopy and after lyophilisation and deposition by SEM microscopy. Radiosynthesized PEDOT polymers were found to form monodisperse nanoparticles whose morphology was kept after deposition onto solid substrate. The success of PEDOT polymers synthesis by using accumulated electron pulses, is also in favor of conducting polymers growth proceeding through a step-by-step oxidation mechanism. Also, it highlights the promising potentiality of pulsed electron accelerators in the field of conducting polymers synthesis.

Successively, the action of other radicals, such as the carbonate or the azide radicals, have been investigated. The study showed that these radicals are not enough strong oxidant to induce the monomer oxidation and then the polymerization. Indeed, carbonate appears inefficient to react with EDOT. Moreover at low concentration of carbonate a competition between $\text{O}^{\bullet-}$ oxidation of EDOT and $\text{CO}_3^{\bullet-}$ formation prevents the reaction between EDOT monomers and carbonate radical, $\text{CO}_3^{\bullet-}$.

On the other hand, azide radical has a too low redox potential, so it does not react with EDOT. And at high concentration it reacts with itself to form $\text{N}_6^{\bullet-}$ radical.

Finally the reactivity of sulfate radical was investigated. Indeed this radical has a very high redox potential close to that of hydroxyl radical, which should enable it to oxidize EDOT monomers. The first step of oxidation by sulfate radical was determined and thanks to simulation the transient species spectra were identified. Also in this case we used the electron beam as a source of ionizing radiation to produce PEDOT polymers. The polymerization produced a relatively stable yellow-brown suspension which was characterized by a large absorption band around 700 nm corresponding to the characteristic absorption band of PEDOT polymer. The success of PEDOT polymers synthesis by using accumulated electron pulses, highlight the versatility of our methodology based on the use of ionizing radiation. Also it shows the promising potentiality of pulsed electron accelerators in the field of conducting polymers synthesis.

These encouraging results on EDOT suggested to investigate the polymerization of other conducting polymers, such as polypyrrole.

The kinetics investigation shows again that the polymerization takes place by a step-by-step mechanism. In this case, by coupling the experimental study with theoretical simulation, it was possible to prove the formation of adduct hydroxy radical, $(\text{PyOH})\cdot$ as the primary step. Moreover, a study on the dose effect allows to determine the extinction coefficient of this first radical.

The investigation on pH effect enabled us to demonstrate that in acidic solution the adduct pyrrole radical, $\text{PyOH}\cdot$, is protonated and then it can dimerize or undergo to the ring opening. On the other hand, in alkaline solutions, the first transient species was the oxide adduct radical, $\text{PyO}\cdot^-$. The action of oxide radical onto Py monomer instead of hydroxyl radical was demonstrated by a kinetic simulation of the reaction mechanism.

Moreover, using another oxidant, the carbonate radical, it was demonstrated its inefficacy to oxidize the pyrrole but contrary to the case of EDOT it induces the ring opening of the neutral pyrrole radical.

Finally, we succeeded in polymerization of pyrrole by electrons beam. Morphological study by AFM revealed the formation of globular aggregation comparable to the results in literature. We demonstrated that radiation induced pyrrole polymerization proceeds through a recurrent step-by-step mechanism which involves a recurrent oxidation process by hydroxyl radicals formed during water radiolysis.

The present study bears witness to the potential of such a new electrons-based methodology and gives us a glimpse of future promising industrial applications in the field of conducting polymers synthesis. Indeed, thanks to the accelerated electrons-based nano-beams which are nowadays available, it should appear possible to synthesize conducting polymers onto conducting or even non conducting substrates with a high spatial resolution in order to produce conductive patterns at a nanometric scale. The fact that conducting polymer growth proceeds through a step by step mechanism, and not according to a chain reaction, should enable the control of the chain length thanks to the adjustment of the irradiation dose.

Appendix A

Computational study

The computational study of the system was developed by P. Archirel in Theos group of LCP laboratory. The approach used for the investigation and the choose of the simulations methods are here detailed. Before the extensive application of our simulation method, we established its relevancy in the following way: we first compared our simulation possibilities for the EDOT molecule, for which the experimental spectrum is well known. We then investigated the issue of the EDOT^{•+} cation radical for which ordinary DFT calculations are doubtful.

Absorption spectrum of EDOT molecule

Several simulation methods (Table A.1) were tested to choose the better simulation method. We compared the Monte-Carlo (MC) and Molecular Dynamic (MD) [1] simulations, different numbers of simulation steps, and the use of different functionals and basis sets. The results are given in Table A.1 and the best Monte-Carlo spectrum is shown in Figure A.2.b. For comparison with experimental spectrum (Figure A.2.a), we extracted two bands from our calculated spectrum. We could easily attribute the first transition to a first band, but we had to gather the next four transitions (2 to 5) in the unique second band. We performed the B3LYP simulations with two basis sets:

1. the small pSDD basis set [2]. In this case the spectrum was calculated with the pSDD basis enriched with two shells of diffuse s and p gaussians on every atom
2. the larger cc-pvdz basis. In this case the spectrum was calculated with the aug-cc-pvdz basis.

The results of Table A.1 call for the following comments:

1. the results obtained with 10000 and 50000 MC steps show that the smaller number of MC steps (10000) is sufficient. This results in reasonable simulation times for EDOT molecule and radicals (a few days each) and for the dimers (2-3 weeks

Method		exp.	MC	MC	MC	MD	MC
Functional			B ₃ LYP	B ₃ LYP	B ₃ LYP	B ₃ LYP	BLYP
basis (simulation)			pSDD	cc-pvdz	cc-pvdz	cc-pvdz	cc-pvdz
basis (spectrum)			pSDD + diff	aug-cc-pvdz	aug-cc-pvdz	aug-cc-pvdz	aug-cc-pvdz
nbr of steps			10000	10000	50000	10 μ s	10000
spectrum	λ_{\max}	255	243	250	250	253	282
	E	7048	19434	17454	17868	15604	11954
first band	λ_{\max}	258	250	252	251	255	284
	E	5652	12535	14045	12505	12952	10601
	Width	20	14	14	16	14	18
second band	λ_{\max}	235	242	240	240	240	263
	E	5135	13586	9838	10149	10137	8347
	$\Delta\lambda_{\max}$	23	8	12	11	15	21

Figure A.1: Absorption spectrum of EDOT molecule: measured and calculated values of the absorption maximum wavelength (in nm), extinction coefficient (in $\text{L mol}^{-1} \text{cm}^{-1}$) and band width (in nm)

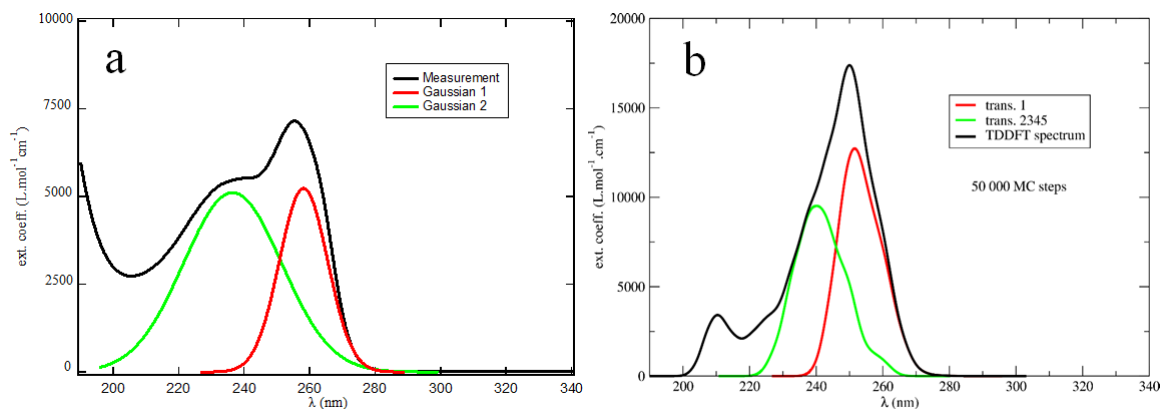


Figure A.2: Absorption spectra of EDOT molecule: (a) experimental spectrum in aqueous solution (with a Gaussian fit) and (b) calculated spectrum with a MC simulation at the B₃LYP/cc-pvdz level.

each) on our 8 cores machines.

2. B3LYP yields acceptable values of the global λ_{max} and the cc-pvdz basis yields the best values, 250 nm (with MC, error: 0,10 eV) and 253 nm (with MD, error: 0,04 eV)
3. the MC and MD results are very close to each other, though MD results are slightly better. This suggests that our MC sampling is correct. Note that the use of molecular dynamics doubles computation times for the EDOT molecule.
4. B3LYP clearly overestimates the value of the extinction coefficient, by a factor 2,5 (with MC) and 2,2 (with MD).
5. we tested a few other functionals and found that only BLYP yields a smaller value of ϵ : 12000 L mol⁻¹ cm⁻¹. This value is still overestimated, and moreover the BLYP λ_{max} is poor (282 nm).

An overestimated ϵ may be due to at least the following issues:

1. the DFT transition dipole is inaccurate. We checked that the "velocity" and "position" values of the transition dipoles are very close to each other. According to the hypervirial theorem [3] this shows that no numerical error interferes
2. the DFT overestimates the transition dipole. Our group already published the case of an (inorganic) molecule for which B3LYP yields an oscillator strength larger than the (more correct) PBE value by a factor 2[2]. This discrepancy was due to an inaccurate B3LYP geometry. In the present case, we found that B3LYP overestimates the SC bond lengths: the B3LYP optimized value (1,74 Å) is larger than the measured value (in the solid state, for a substituted molecule: 1,69-1,71 Å). We found no noticeable influence of this bond length on the transition dipole, nevertheless.
3. the DFT potential surface is too rigid. A good measure of this rigidness is the value of the band width: it can be seen that the value increases in the order B3LYP/pSDD < B3LYP/cc-pvdz < BLYP/cc-pvdz < measured value. We found that the value of the ZPE (zero point energy) of the molecule follows the same law: 0,111632 H (B3LYP/pSDD) < 0,111078 H (B3LYP/cc-pvdz) < 0,107345 H (BLYP/cc-pvdz). This shows that the potential surface is less and less rigid. We have no accurate value of this quantity, unfortunately.
4. the ϵ value of the total spectrum depends on the overlap of the bands. It can be seen that the methods which give the best value of this quantity (MD/B3LYP and MC/BLYP) also give the largest separation of the two bands. It remains that the value of the first band is overestimated in all cases.

Absorption spectrum of open shell

We here face the issue that DFT and TDDFT methods usually use the UHF (Unrestricted Hartree-Fock) formalism, which ensures that the projection M_S of the total spin can be monitored, but that its modulus S cannot. As a consequence the DFT wavefunctions of such systems display the right value $|M_S| = 0,5$, but the mean value of the S^2 operator is not equal to $S(S+1) = 0,75$. Since it is due to the interference of quartet states, this feature has been called spin contamination. In Table A.1 we give the values of the $\langle S^2 \rangle$ quantities for EDOT⁺ cation radical. It can be seen that:

- (a) for the ground state, it amounts to 0,754, showing a weak spin contamination
- (b) for excited states it is much larger, and values as large as 1,6 can be found, showing a strong contamination by quartet states. Note that for a pure quartet this value would be 3,75.

In order to analyse the TDDFT results we used the SACCI method [4], which handles true spin eigenfunctions and gives acceptable computation times. The SACCI results are joined to the TDDFT results in table A.1, as well as TDDFT results for the transitions between quartet states. In order to make the SACCI calculations feasible we had to work in the vacuum and to drop diffuse gaussians from the basis sets, so that the results cannot be expected to be realistic. We only aimed at a comparison between two methods, free and not free from spin contamination.

The results of Table A.1 call for the following comments:

- (a) the SACCI method only yields two weak transitions, before the intense one at 309 nm.
- (b) the TDDFT method yields a wealth of six weak transitions before the intense one (at 264 nm), with $\langle S^2 \rangle$ values lying between 0,77 and 1,6.
- (c) a great number of quartet states exist in the zone of spin contamination, and may interfere.

The TDDFT spectra for $|M_S| = 0,5$ and $1,5$ are shown on figure A.3. The TDDFT results can be made closer to the SACCI results if the transitions with a $\langle S^2 \rangle$ value larger than some value, say 0,82, are dropped from the list. These discarded lines are bracketed in table A.1. Doing so, we obtain the "screened" spectrum of figure A.3.

method basis	Doublet			Quartet		
	Δ (eV)	λ (nm)	f	$\langle S^2 \rangle$	ΔE (eV)	λ (nm)
SACCI cc-pvtz	0,84	1477	0,0005	0,75	-	-
	3,27	380	0,0002	0,75	-	-
	4,01	309	0,1502	0,75	-	-
	4,63	268	0,0032	0,75	-	-
	4,82	257	0,0343	0,75	-	-
DFT	0	-	-	0,754	-	-
TDDFT cc-pvtz	0,55	2228	0,0004	0,767	-	-
	-	-	-	-	2,04	606
	-	-	-	-	2,38	519
	2,79	444	0,0008	0,791	2,84	436
	(3,19	389	0,0177	1,598)	3,21	386
	-	-	-	-	3,29	376
	(3,68	337	0,0034	1,045)	3,68	337
	-	-	-	-	3,72	333
	(3,85	322	0,02224	1,468)	377	329
	4,12	300	0,0014	0,779	4,00	309
4,68	264	0,1466	0,829	4,35	285	

Table A.1: Comparison of the first calculated transitions of the open shell EDOT⁺ cation radical with SACCI (free from spin contamination) and TDDFT (not free). These transitions are calculated at the optimized geometry in the vacuum. Bracketed transitions are discarded in the present work

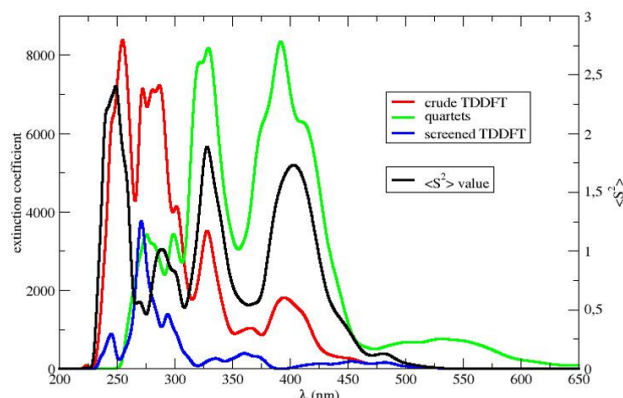


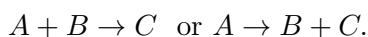
Figure A.3: Absorption spectra of EDOT^{•+} radical cation: TDDFT results for $|M_S| = 0,5$ ("crude" spectrum) and 1,5 ("quartet" spectrum), and screened TDDFT spectrum with the value 0,82 of the screening parameter. The "spectrum" of the $\langle S^2 \rangle$ mean value for the crude TDDFT spectrum is also shown

On this figure we join the "spectrum" of the $\langle S^2 \rangle$ values, namely the equivalent of the absorption spectrum, with the oscillator strength replaced by the $\langle S^2 \rangle$ value. This $\langle S^2 \rangle$ spectrum was normalized, so as to give the value 0,75 to the low energy band (2228 nm, see Table A.1). It can be seen that:

- (a) the band at 400 nm in the crude spectrum can be attributed to quartet states, as shown by the large value of $\langle S^2 \rangle$ in this zone (1,72) and by a band in the quartet spectrum. As a consequence this band is completely dropped by the spin screening.
- (b) the same holds for the band at 330 nm, also displaying a large value of $\langle S^2 \rangle$ (1,88) and clearly present in the quartet spectrum.

In Figure A.3 we displayed the spectrum of EDOT^{•+} cation radical obtained with the value 0,82 which ensures the best comparison with the experimental spectrum.

Thermochemistry In a previous work, our group had shown that PCM (Polarized Continuum) methods, like SMD, can be very unreliable and hazardous when used for chemical reactions of the type [5]



This is due to the poor treatment of the translation rotation entropy, which is

given an electrostatic additivity in PCM methods. Consequently, we used the following methods:

- (a) for all $A + B \rightarrow C + D$ reactions we used the SMD method, the free energy change for such a reaction is therefore:

$$\Delta_r G^m = E_{smd}(C) + E_{smd}(D) - E_{smd}(A) - E_{smd}(B) \quad (\text{A.1})$$

where E_{smd} is the energy in the dielectric cavity. Using full free energies G_{smd} in equation A.1 yields only tiny differences.

- (b) for $A + B \rightarrow C$ reactions, where all species are neutral, we calculated the free energy changes in the vacuum:

$$\Delta_r G^m = G_{vac}(C) - G_{vac}(A) - G_{vac}(B) \quad (\text{A.2})$$

where the G_{vac} are the full free energies in the vacuum, including in particular the vibration, rotation and translation entropies. We think that using vacuum quantities is less hazardous than using PCM quantities in this case.

- (c) for $A + B \rightarrow C$ reactions, where some species bear an electrostatic charge, we calculated the free energy changes in the vacuum and added a solvation contribution given by the Born formula and the sphere radius deduced from the electron density [6].

$$\Delta_r G^m = G_{vac}(C) - G_{vac}(A) - G_{vac}(B) + \Delta_{solv}(C) - \Delta_{solv}(A) - \Delta_{solv}(B) \quad (\text{A.3})$$

- (d) for reactions involving a proton, we used the published value of the proton solvation free energy: -1144 eV [7].

Appendix B

Simulation COPASI

The simulation of kinetics mechanism of a solution containing 20 mM in Pyrrole was simulated with COPASI program. The conditions of simulation are reported in table B.1. The concentration of radiolytical species were estimated from the dose.

Pyrrole Concentration [M]	Dose [Gy/pls]	Radiolytic species concentration[M]
$20 \cdot 10^{-03}$	45	$[e^-] = [H_3O^+] = 1.57 \cdot 10^{-05}$ $[HO^\cdot] = 1.66 \cdot 10^{-05}$ $[H^\cdot] = 2.47 \cdot 10^{-06}$

Table B.1: Experimental parameters insert in simulations

As in the case of 100 mM in Pyrrole, the evolution of electron hydroxyl radical and first transient species A concentrations were simulated by COPASI program on 100 ns as shown in figure B.1. Also in this case the electron and hydroxyl radical kinetics profiles decrease. On the other hand the first transient species increase slower than in the case of a solution containing 100 mM in Py. Successively the experimental signals were compared with simulated ones. Again the extinction coefficients of electron were from literature, $\epsilon=13000$ at 600 nm and $\epsilon=900$ at 300 nm.

Bibliography

- [1] J Cuby Řezáč. 4, software framework for computational chemistry.

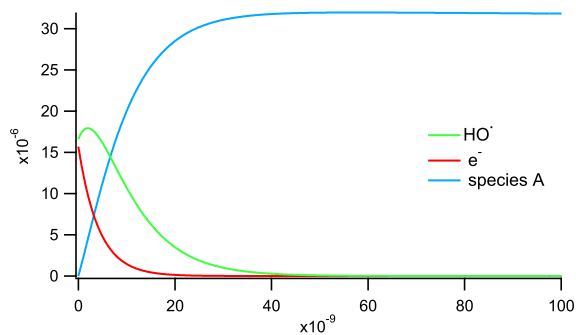


Figure B.1: Time evolution of concentration all species contained in a solution of 100mM in Pyrrole on 100 ns simulated by COPASI.

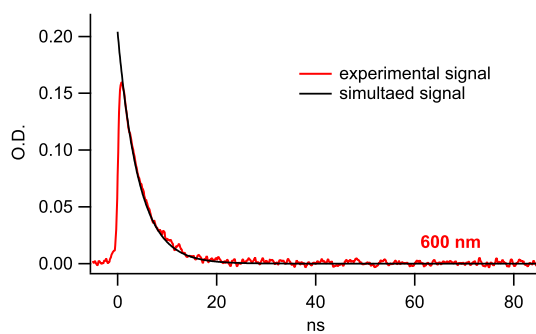


Figure B.2: Comparison between experimental kinetic profile and simulated one of the electron decay at 600 nm on 100 ns.

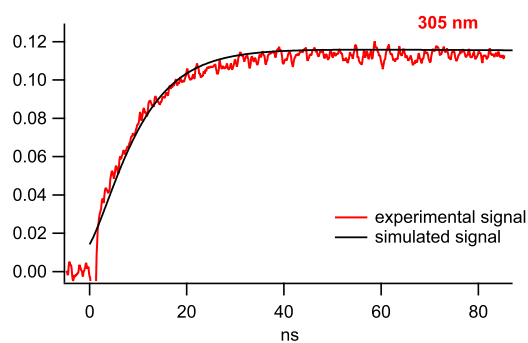


Figure B.3: Comparison between experimental kinetic profile and simulated one of growth of first transient species at 305 nm on 100 ns.

- [2] Franck Rabilloud, Moussab Harb, Hameth Ndome, and Pierre Archirel. Uv- visible absorption spectra of small platinum carbonyl complexes and particles: A density functional theory study. *The Journal of Physical Chemistry A*, 114(23):6451–6462, 2010.
- [3] Joseph O Hirschfelder. Classical and quantum mechanical hypervirial theorems. *The Journal of Chemical Physics*, 33(5):1462–1466, 1960.
- [4] Ryoichi Fukuda and Hiroshi Nakatsuji. Formulation and implementation of direct algorithm for the symmetry-adapted cluster and symmetry-adapted cluster–configuration interaction method. *The Journal of chemical physics*, 128(9):094105, 2008.
- [5] Youssef Lattach, Pierre Archirel, and Samy Remita. Influence of the chemical functionalities of a molecularly imprinted conducting polymer on its sensing properties: Electrochemical measurements and semiempirical dft calculations. *The Journal of Physical Chemistry B*, 116(5):1467–1481, 2012.
- [6] Max Born. Volumen und hydrationswärme der ionen. *Zeitschrift für Physik A Hadrons and Nuclei*, 1(1):45–48, 1920.
- [7] Michael D Tissandier, Kenneth A Cowen, Wan Yong Feng, Ellen Gundlach, Michael H Cohen, Alan D Earhart, James V Coe, and Thomas R Tuttle. The proton’s absolute aqueous enthalpy and gibbs free energy of solvation from cluster-ion solvation data. *The Journal of Physical Chemistry A*, 102(40):7787–7794, 1998.

Titre : Etude du mécanisme de croissance de polymères conducteurs par radiolyse

Mots clés : radiolyse impulsienne, polymères conducteurs, spectroscopie

Les polymères conducteurs (PC) sont des matériaux organiques semi-conducteurs très utilisés dans diverses applications technologiques. Les différentes méthodologies de synthèse des PC ont toujours pour finalité la fabrication de nouvelles structures polymères stables dans différents environnements, et dont les propriétés optiques et conductrices seraient ajustables.

Parmi tous les polymères conducteurs, le poly(3, 4-éthylènedioxythiophène) (PEDOT) et le polypyrrole (PPy) sont déjà utilisés dans plusieurs applications pour leurs propriétés chimiques et physiques. Les PC, comme le PEDOT et le PPy, sont habituellement synthétisés par voie chimique ou électrochimique, la polymérisation étant systématiquement initiée par une étape d'oxydation des monomères. La radiolyse de l'eau représente une méthode simple et efficace qui permet la polymérisation à température et pression ambiantes, sans aucun dopant externe, mais qui à notre connaissance n'avait jamais été utilisée seule pour la synthèse de PC.

Au sein de notre laboratoire, une méthodologie alternative basée sur l'interaction rayonnement-matière a récemment été utilisée avec succès

pour la synthèse de PC nanostructurés en solution aqueuse. Le présent travail est plus spécifiquement consacré à la synthèse de PEDOT et PPy en solution aqueuse et à l'étude de leur mécanisme de croissance par radiolyse pulsée. Grâce à l'accélérateur d'électrons ELYSE, l'utilisation de la radiolyse pulsée couplée à la spectroscopie d'absorption résolue dans le temps a permis d'étudier la cinétique des réactions à l'échelle de la nanoseconde et de la milliseconde. Les spectres d'absorption des espèces transitoires impliquées dans le mécanisme réactionnel ont été identifiés grâce à des calculs de chimie quantique. Tout d'abord, la réaction du radical hydroxyle avec les monomères EDOT et Py a été étudiée, ainsi que la polymérisation induite par le rayonnement. Ensuite, l'étude a été transposée à d'autres radicaux oxydants tels que $\text{CO}_3^{\cdot-}$, N_3^{\cdot} et $\text{SO}_4^{\cdot-}$ à différents pH. Enfin, le faisceau d'électrons a été utilisé comme source de rayonnement ionisant (accumulation de pulses) afin de synthétiser in situ les polymères conducteurs PEDOT et PPy. Ces résultats démontrent que le mécanisme de croissance des PC n'est pas un mécanisme en chaîne, mais un mécanisme par stades.

Title : Study of growth mechanism of conducting polymers by pulse radiolysis

Keywords : Pulse Radiolysis, Conducting Polymers, Spectroscopy

Today conductive polymers have many applications in several devices. For these reasons they have received much attention in recent years. The methods of polymerization are limited to two principal ways: chemical and electrochemical synthesis. On the other hand, the complex properties of polymers can be controlled only if a good knowledge of polymerization process is acquired. Water radiolysis represents an easy and efficient method of synthesis comparing to chemical and electrochemical polymerization routes. It enables the polymerization under soft conditions: ambient temperature and pressure, without any external dopant.

Among all conductive polymers, poly(3,4-ethylenedioxythiophene) (PEDOT, a derivate of polythiophene) and polyPyrrole (PPy) have gained some large scale applications for their

chemical and physical properties. The aim of the present work was the synthesis of PEDOT and PPy in aqueous solution and the study of their growth mechanism by pulsed radiolysis. Thanks to the electron accelerator ELYSE, the use of pulsed radiolysis coupled with time-resolved absorption spectroscopy allowed to study the kinetics of polymerization. The first transient species involved in the mechanism were identified by time resolved spectroscopy and the rate constants were determined. First, the reaction of hydroxyl radicals onto EDOT and Py monomers was studied, as well as the corresponding radiation induced polymerization. Then, the study was transposed to others oxidizing radicals such as $\text{CO}_3^{\cdot-}$, N_3^{\cdot} and $\text{SO}_4^{\cdot-}$ at different pHs. Finally, the electron beam was originally used as a simple electron irradiator in order to in situ synthesize PEDOT and PPy.



250IS) is equipped with three 150 grooves/mm grating blazed at 300, 500 and 800 nm which disperse the light on the entrance optics of a streak-camera (model C-7700 from Hamamatsu). The three grooves allow to range from UV-Vis to IR wavelength. The full spectra are obtained by two or three series of absorption measurements using the different optical filters (UG5 and GG325) to optimize the light intensity on a specific spectral domain.

Irradiation cell and pump system: The irradiated solution is renewed between two pulses. The suprasil quartz optical cells are placed at the exit of beamline and they are connected by tubes with a reservoir where the solution to be studied is stored and deaerated by flushing with an inert gas. The optical path of the cell is 1 cm. Tubes containing solution are fitted inside a circular pump mechanism which allows the solution flow.

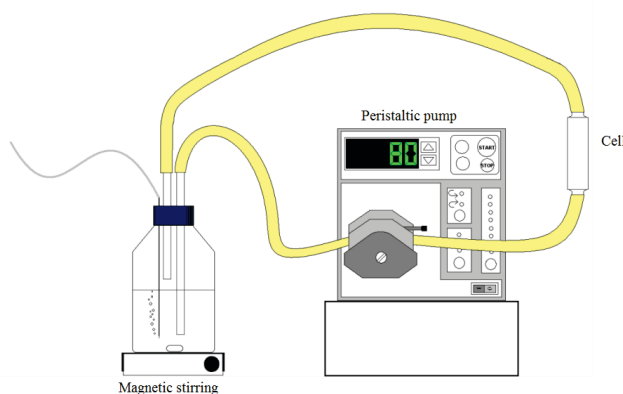


Figure 1.12: Scheme of pump system uses to circulate the solution during irradiation.

Streak-camera: For time resolved absorbance detection in the UV-Vis range, a streak camera Hamamatsu C7700-01 connected to spectrograph Chromex 250IS was used. The sweep time/full screen ranges from 500 ps to 1 ms and the characteristic spectral response is from 250 to 800 nm [40]. Absorption measurements up to 5 μ s are performed using the white light beam of the homemade Xenon flash lamp. For time range greater than 5 μ s, a continuous 300 W Xe lamp is used.

The use of streak camera allows to record the time-resolved spectrum of transient species produced after one electron pulse what is very useful for the identification of radical species involved in a polymerization mechanism. In fact by streak camera

to initiate the polymerization was the hydroxyl radical, HO[•], produced directly from water radiolysis. The reactivity of this radical has already been studied by pulsed ra-

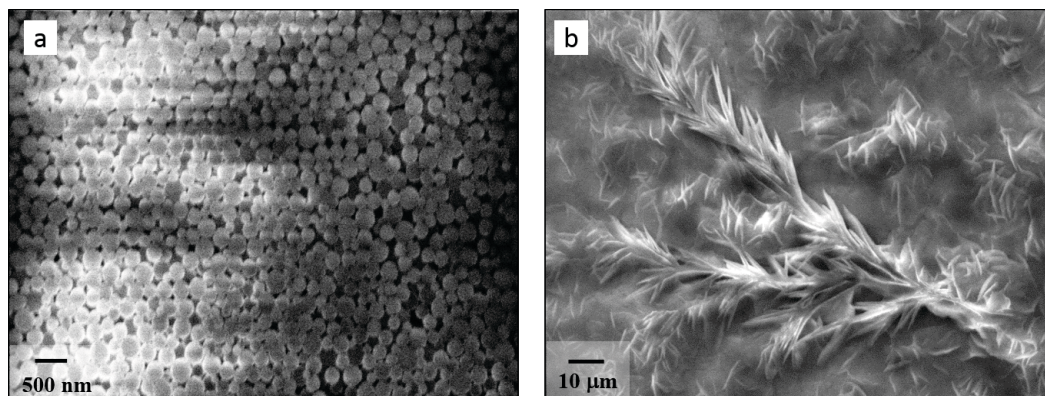


Figure 2.1: SEM images of PEDOT polymers after deposition onto gold substrates obtained by irradiation at 70 kGy: **a** (PEDOT–OH); **b** (PEDOT–N₃).

diolysis of thiophene (Th) molecules (from which EDOT derives) [7, 8, 9]. It has been found that HO[•] radical adds preferentially to the α position in Th molecule, leading to a short-lived hydroxythienyl (Th–OH)[•] radical. This latter, subsequently, undergoes a second order radical reaction with itself to produce α - α -bithiophene. In this first section, we will study the reaction of hydroxyl radical onto EDOT monomer and compare it with literature Th molecule. With the aim to understand the pH effect on the first steps of polymerization and to check the reactivity of oxide radical (O^{•-}) predominant at high pH ($\text{pK}_a(\text{HO}^\bullet/\text{O}^{\bullet-}) = 11.9$), alkaline solutions were also investigated. Indeed in the previous mentioned Saunders's studies [8, 9], the products of the reaction between the thiophene molecule and oxide radical was also investigated in alkaline solution. It was found that the action of oxide radicals onto thiophene induces the opening of the thiohene ring. This effect inhibits the polymerization. So it is clear that the action of pH can play a fundamental role in the mechanism of the growth of the polymer.

Successively a first study on reduction of EDOT was also approached by using hydrated electron produced in water radiolysis.

The last part of this chapter will introduce a new method to synthesize PEDOT by using the electron beam, previously used in pulse radiolysis study, as a simple electron irradiation, showing the advantages implicated in the use of this methodology.

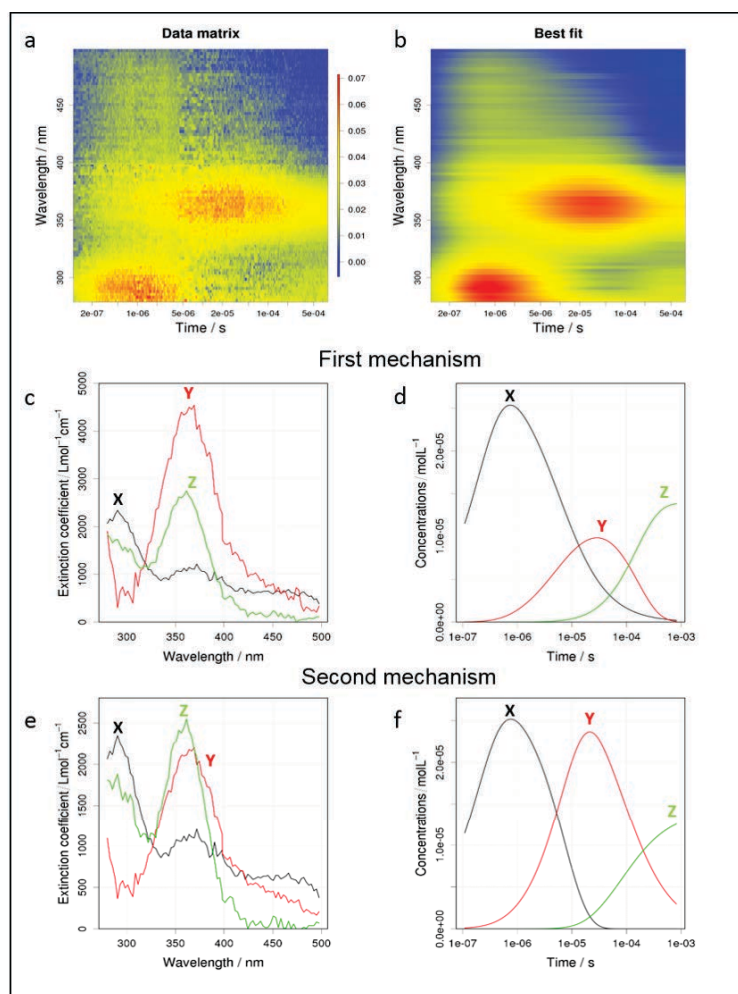


Figure 2.8: Kinetic analysis of the experimental spectrokinetic matrix (a) with a three-species model (see text): (b) image of the best-fit model; (c) best-fit spectra of the first model scheme; (d) best fit concentrations for the first model scheme. (e) best-fit spectra of the second model scheme; (f) best fit concentrations for the second model scheme. Each spectrum is associated with a concentration profile according to the color code.

In the second mechanism (Scheme 2), the successive reactions are as follows:



First reaction is the same into the two schemes. Nevertheless here, the second reaction

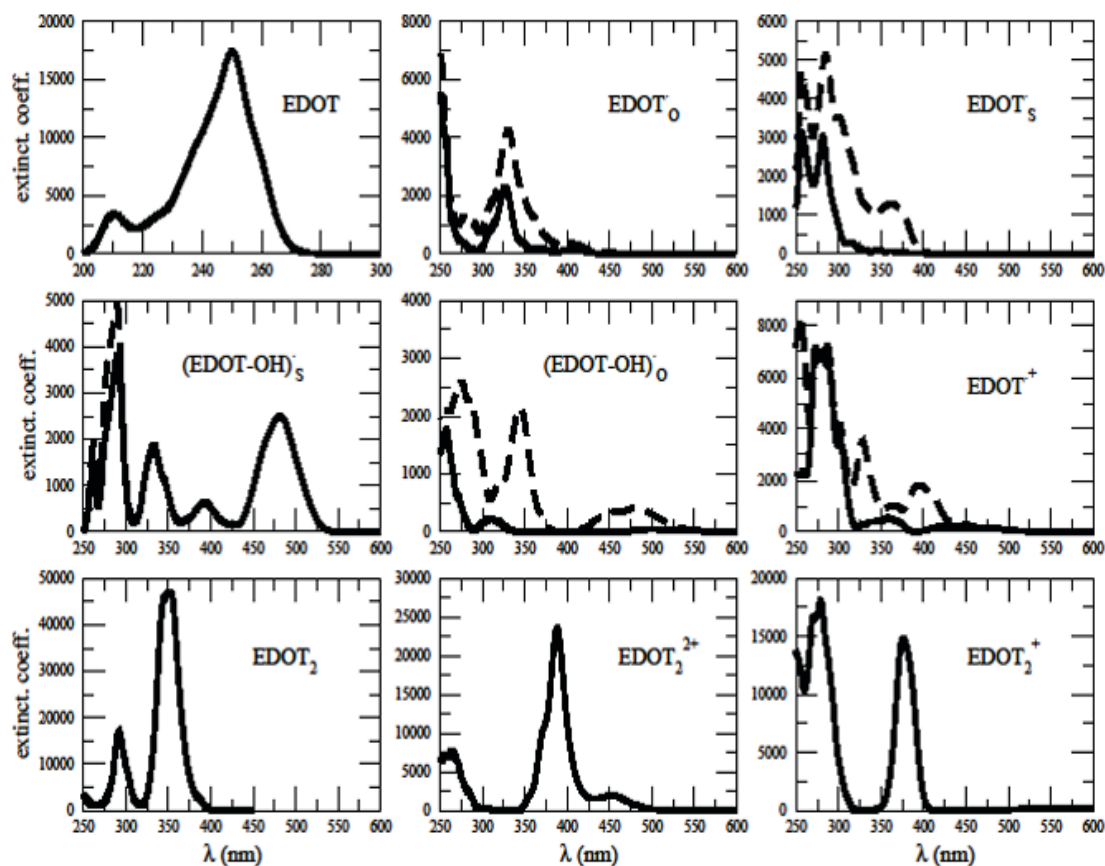


Figure 2.10: Absorption spectra of all molecules of Table 1. Absorption spectra of open shell radicals are displayed without (dotted line) and with (full line) spin screening with parameter 0.9.

Thermochemistry of the candidate reactions

Simulated absorption spectra suffer from the DFT inaccuracies and moreover these spectra often overlap, so that thermo-chemical data are most welcome in the further discussion with the aim to identify X, Y and Z species and also the effective mechanism scheme.

In table 2.2 we give the *molar* free energy change $\Delta_r G^m$ of a list of chemical reactions, relevant to the present study. All the calculations were done with B3LYP and the pSDD basis set. The molar values of the free energy change and the corresponding values at $\text{pH} = 7$, with all species (other than H^+) molar.

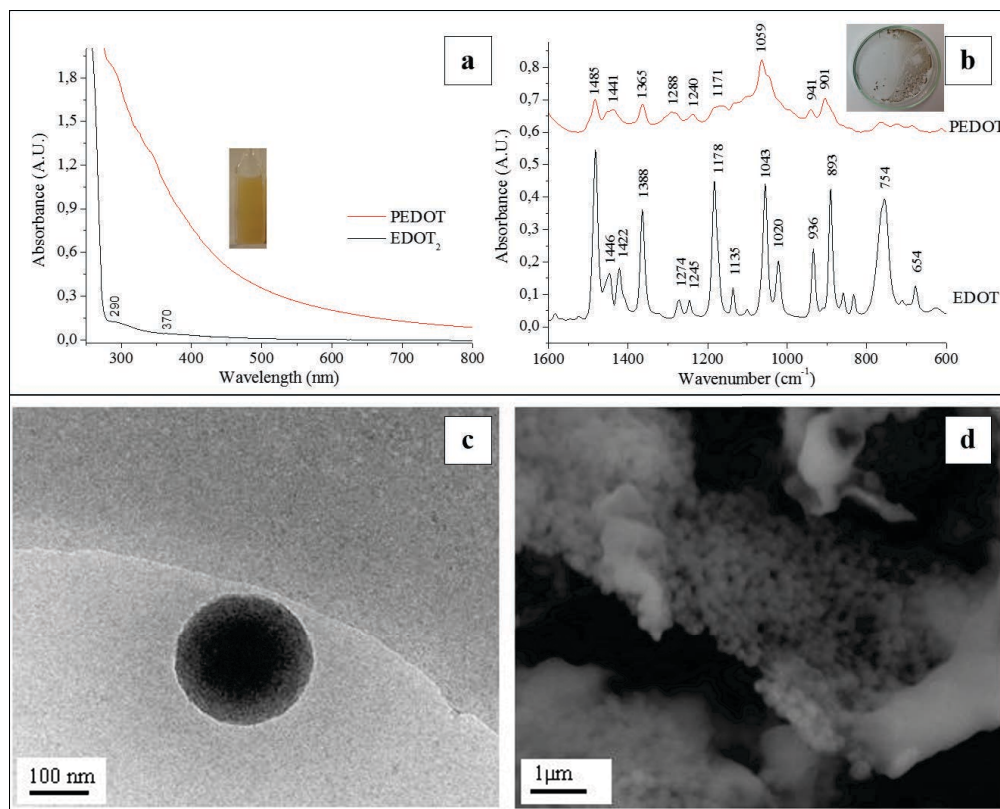


Figure 2.20: (a) Absorption spectrum of a N₂O-saturated aqueous solution of EDOT (10 mM) irradiated by an electron beam at a dose of 180 kGy (4500 pulses, 40 Gy/pulse), reference was water and pathlength was 1 mm; (inset) image of a cell containing PEDOT aqueous suspension radiosynthesized by electron beam; (b) ATR-FTIR spectra of pure EDOT (bottom spectrum) and PEDOT polymers radiosynthesized at 180 kGy (top spectrum); (inset) photograph of a cup containing the lyophilized radiosynthesized PEDOT powder; (c) Cryo-TEM image of radiosynthesized PEDOT in aqueous solution. A PEDOT nanoparticle of around 250 nm is observed; (d) SEM image of lyophilized radiosynthesized PEDOT powder. Aggregates of spherical PEDOT nanoparticles are observed.

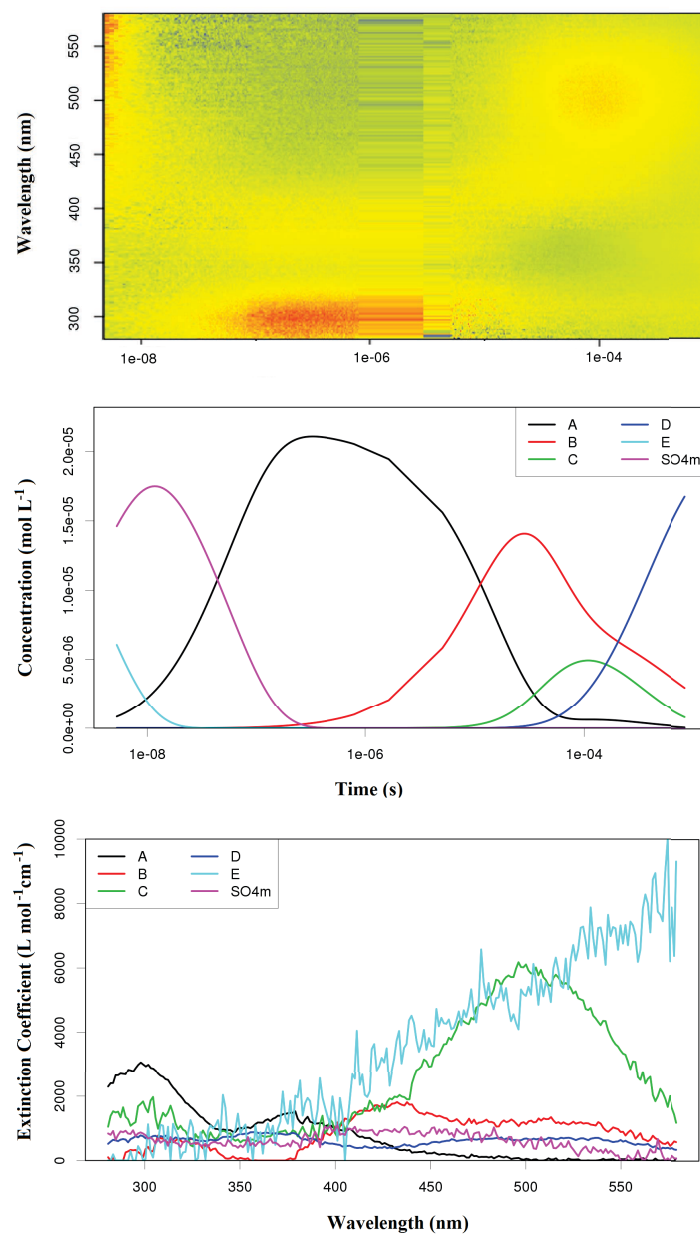


Figure 3.21: Kinetic analysis of the experimental spectrokinetic matrix with a four-species model (a); best-fit kinetics (b) and best fit spectra (c) for the model scheme. Each spectrum is associated with a concentration profile according to the color code.

As we observed on the various spectra and kinetics described above, the SVD analysis of the obtained image shows that the spectrokinetic matrix can be factored into four components (A, B, C and D) (Figure 3.21).

first species A. However, due to the approximation included in the model, these values can be overestimated.

The Table 3.2 resumed the results obtained by SVD investigation.

Transient Species	Absorption Maxima (nm)	SVD Deconvolution (nm)
$\text{SO}_4^{\cdot-}$	455	455
A	295 - 380	300 - 370
B	425 - 500	425 - 500
C	315 - 500	300 - 500
D	315 - 360 - 500	300 - 360 - 500

Table 3.2: Absorption maxima of kinetic study and SVD decomposition.

3.3.4 Absorption spectra simulation

In order to identify the unknown species A, B, C and D involved in the mechanism of EDOT oxidation, the simulations were performed using MC/DFT method previously introduced. Firstly, the sulfate radical spectrum was simulated. The good agreement between the experimental spectrum recorded at 300 ns after the pulse and simulated one is shown in Figure 3.22.

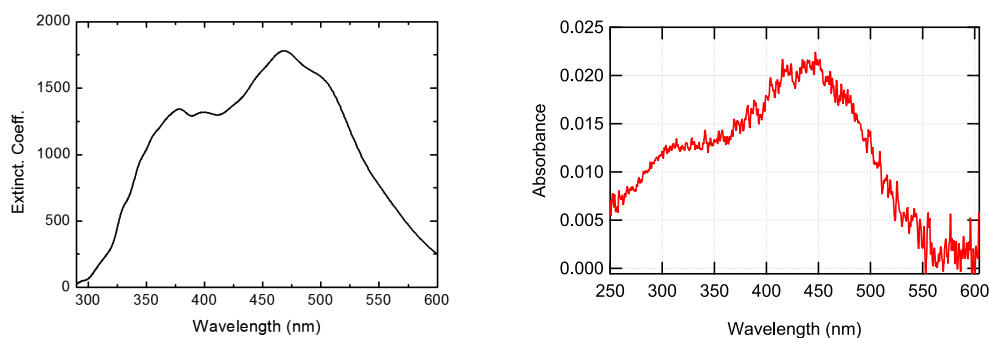
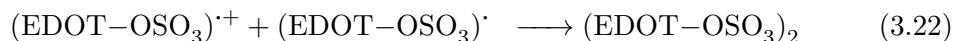


Figure 3.22: Absorption spectrum of sulfate radical simulated by MC/DFT(B3LYP) method on the left. Absorption spectrum of sulfate radical recorded at 300 ns after the pulse of an aqueous solution containing 20 mM in persulfate $\text{K}_2\text{S}_2\text{O}_8$ and 0.5 M in *tert*-butanol saturated with argon (Dose = 42 Gy/pulse, Optical path = 1 cm), on the right.

C. From the potential B species, several charged and uncharged dimers can be formed. We particularly considered the neutral and stable one $(\text{EDOT-OSO}_3)_2$. By starting from the previous radicals, different reactions can produce this stable species:



The same dimer is formed. Nevertheless it can be take different isomers differing by the position of H atoms that we distinguish in the text with the following notation. The *isomer1* displays the H atoms on the C. The *isomer2* shows the H atoms on the oxygen of the adduct OSO_3 . And finally the hybrid dimers non conjugated, *isomer3*, depicts an H atom on the C and another on the oxygen of the adduct OSO_3 .

The DFT calculations showed that the hybrid dimer, *isomer3* is the most stable ($E = 0$ eV), on the other hand the conjugated dimer, *isomer1* is unstable ($E=0.292$ eV) and less stable ($E = 0.737$ eV) is the *isomer2*.

In Table 3.3 the name formula and chemical structure of all molecules studied in this work are depicted.

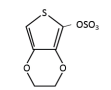
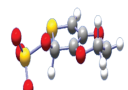
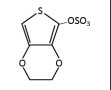
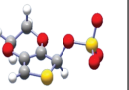
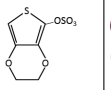
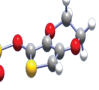
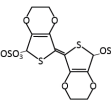
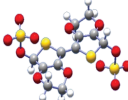
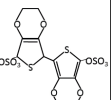
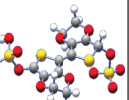
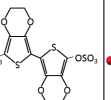
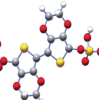
$(\text{EDOT-OSO}_3)^{\cdot+}$			$(\text{EDOT-OSO}_3)^{\cdot-}$			$(\text{EDOT-OSO}_3)^{\cdot}$		
$(\text{EDOT-OSO}_3)_2$ <i>Isomer 1</i>			$(\text{EDOT-OSO}_3)_2$ <i>Isomer 2</i>			$(\text{EDOT-OSO}_3)_2$ <i>Isomer 3</i>		

Table 3.3: Names, formula and chemical structures of all molecules potentially involved in the mechanism in the presence of sulfate radicals.

In Figure 3.23, all simulated absorption spectra of all these species at ambient temperature are shown. Note that the spectrum of hybrid dimer *isomer3* was not simulated.

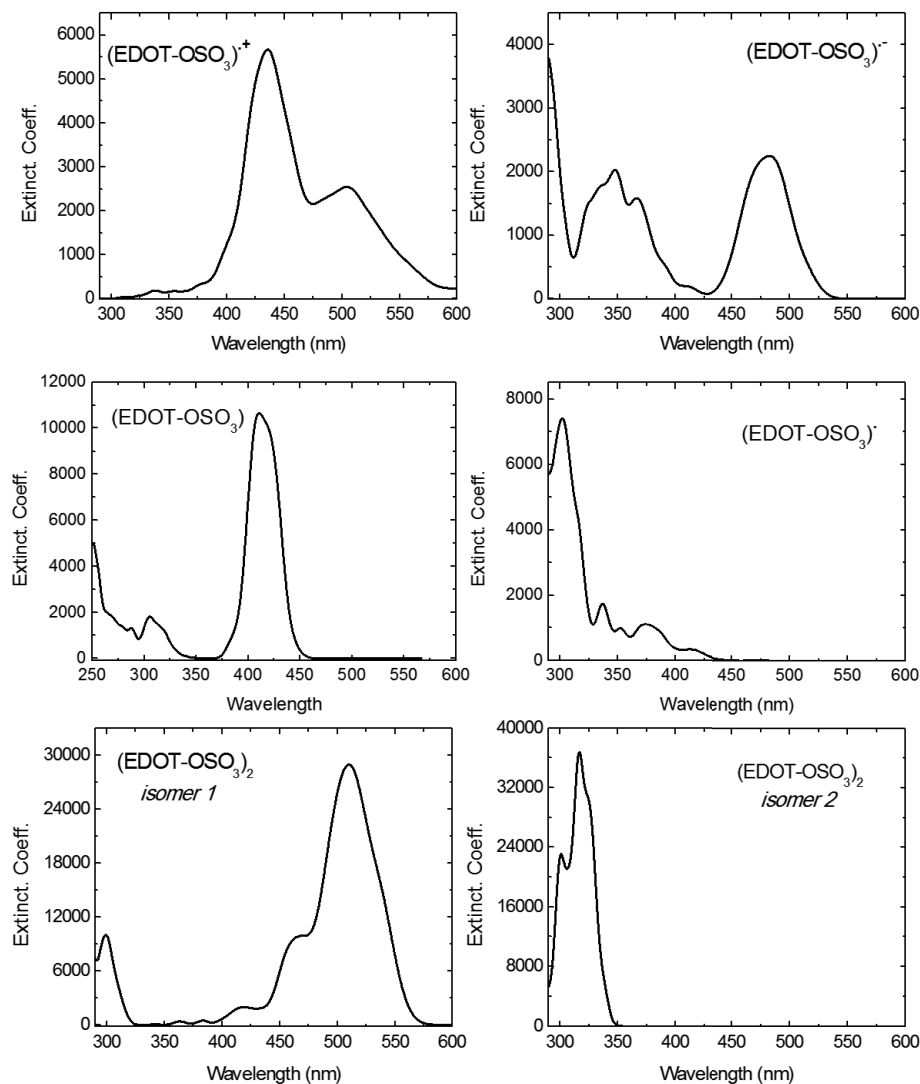


Figure 3.23: Simulated absorption spectra of all molecules of Table 3.3 at ambient temperature by using MC/DFT (B3LYP) method.

3.3.5 Species identification

In the experimental study, we showed that the first transient species, A, is produced by the reaction between EDOT monomer and sulfate radical. So, it should be one of the two radicals previously introduced: $\text{EDOT}^{\cdot+}$ or $(\text{EDOT-OSO}_3)^{\cdot-}$ produced in the reactions 3.13 or 3.14. The experimental absorption spectrum of species A shows mainly two peaks at 295 and 360 nm.

As shown by the mechanism proposed in spectrokinetics analysis, the species B dimerizes and a species C is formed according to reaction 3.11. This species shows a large band of absorption at 500 nm and a weak band at around 300 nm (Figure 3.17 and 3.21). Among the simulated absorption spectra of neutral adduct dimers, only $(\text{EDOT-OSO}_3)_2$ spectrum shows the same bands. This result is not unexpected. Indeed by starting from the two adduct sulfate radicals, $(\text{EDOT-OSO}_3)^{+\cdot}$ and $(\text{EDOT-OSO}_3)^{\cdot-}$, the dimer $(\text{EDOT-OSO}_3)_2$ can be produced in the two reactions 3.20 and 3.21.

Finally, the species D is formed on the ms time scale. The deconvoluted absorption spectrum is characterized by three bands at 300, 360 and 500 nm. This spectrum can not definitely be identified. However it can be suggested that it is the overlapping of two species, the adduct dimer absorbing at 500 nm and the more stable configuration of adduct dimer absorbing at 300 and 360 nm. Moreover the static absorption spectrum recorded after the pulse radiolysis experiment shows two bands at around 300 and 360 nm (Figure 3.24).

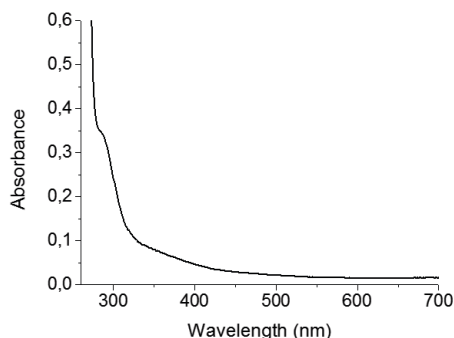


Figure 3.24: Static absorption spectrum after pulse radiolysis irradiation of an aqueous solution containing 5 mM in EDOT, 20 mM in $\text{K}_2\text{S}_2\text{O}_8$ and 0.5 M in *tert*-butanol. The path length was 0.2 cm and the reference was distilled water.

This could be explained by the totally conversion of adduct dimers into more stable adduct dimer. Note that the intensity of the two peaks is at 300 and 360 inverted due to the presence of characteristic peaks of EDOT monomers and $\text{S}_2\text{O}_8^{2-}$ anions which extend to 280 and affects the spectrum.

If the last species is the more stable dimer, absorbing at 300 and 360 nm this means that the species D observed at 1 ms is an intermediate one which probably reacts after this time to give the final dimer. It could be interesting to observe the kinetics at time longer than 1 ms, time limit of the streak camera.

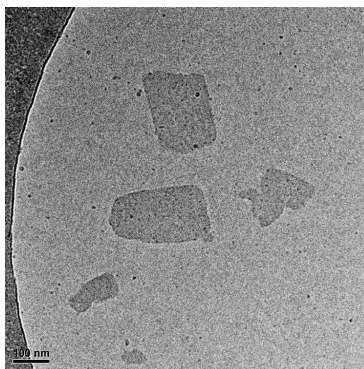


Figure 3.26: Cryo-TEM image of PEDOT synthesized by electron beam irradiation (84 kGy) in the presence of $K_2S_2O_8$. Platelet-shaped nanoparticles are observed

molecules which could be trapped in the polymer containing solid phase. The ATR-FTIR spectra were recorded in the wave number range $1800-600\text{ cm}^{-1}$. In Figure 3.27, ATR-FTIR spectrum of the obtained powder supposed to contain PEDOT was compared with those of EDOT monomer, *tert*-butanol and pure potassium persulfate salt ($K_2S_2O_8$) and PEDOT-OH.

One can note, in the spectrum of the powder obtained by electron beam irradiation, the absence of the characteristic bands of *tert*-butanol in the PEDOT spectrum. In particular, the intense peak at 912 cm^{-1} visible in alcohol spectrum has disappeared, proving the quantitative elimination of the alcohol from the sample thanks to lyophilization. However the presence of three large intense bands around 1265 , 1054 and 700 cm^{-1} demonstrate the presence of persulfate salt $K_2S_2O_8$ salt. The main conclusion here is that lyophilization, which enables *tert*-butanol extraction, does not lead to $K_2S_2O_8$ elimination. Due to the very small amount of powder which was collected after each irradiation, washing of the sample, in order to remove $K_2S_2O_8$ salt, was impossible in our experimental conditions. Nevertheless, we can note that complete elimination of inorganic salts from polymer nanoparticles is not so easy.

In the spectrum of obtained powder, in addition to intense absorption bands of $K_2S_2O_8$, one can observe the presence of many bands which fit well with those of PEDOT polymers previously synthesized by radiolysis by using hydroxyl radicals as oxidizing species, even if these bands appear slightly displaced, (Figure 3.27) may be due to the functionalization of PEDOT polymers by OSO_3 groups. The spectrum of the powder obtained after electron beam irradiation displays vibrations at 1484 , 1446 and 1363 cm^{-1} which are attributable to C=C and C-C stretching modes in the thiophene ring. The vibrations observed at 1301 , 1236 , 1168 and 1054 cm^{-1} are assigned to

the bottom dark areas having no thickness correspond to the substrate. The topography of the sample, displayed as the bright areas, correspond to the thicker regions made up of more or less flat platelet-shaped nanoparticles. This AFM observation agrees well with the particles morphology previously observed in aqueous solution by Cryo-TEM (Figure 3.26). The image depicts an agglomeration of globular nanoparticles with size ranging between 50 and few hundred nm, while some plates appear huge, while some plates appear huge, with a micrometric size.

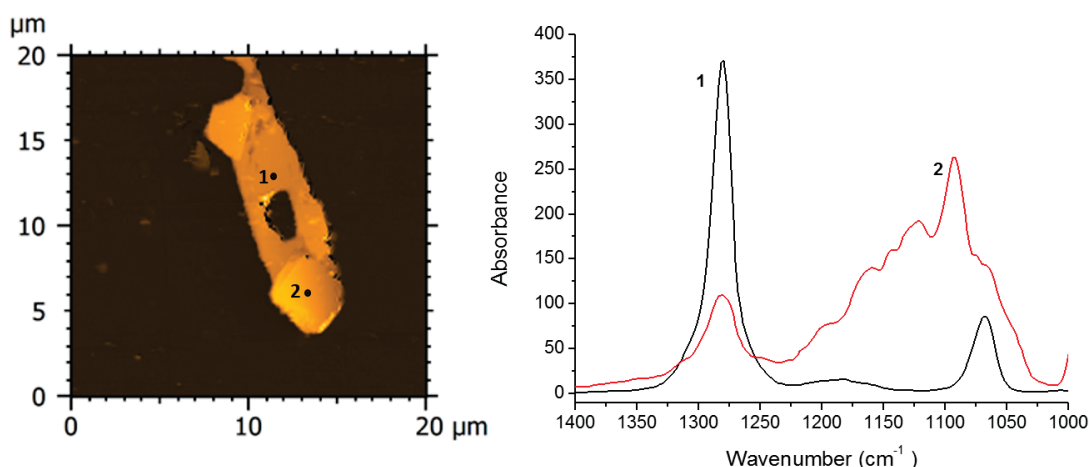


Figure 3.28: AFM-IR characterization of PEDOT polymers synthesized by electron beam irradiation (84 kGy) of the powder obtained by the irradiation of an aqueous solution containing 5 mM in EDOT, 20 mM in persulfate, 5 M in *tert*-butanol on the left and AFM topographic images in contact mode (on the left), and local AFM-IR spectra recorded when the tip is located in positions 1 and 2 of images (on the right).

Since no *tert*-butanol remains in the sample after lyophilisation, as demonstrated by ATR-FTIR spectroscopy, we conclude that the nanoplates, which were observed by cryo-TEM and which are also observed by AFM, do not contain alcohol. Also their morphology is not affected by the presence of *tert*-butanol.

In order to check the chemical nature of these plates, the sample was observed by AFM-IR from 1400 to 1000 cm^{-1} . Since changing the wavelength on a fixed position of the tip gives a local infrared spectrum, we also checked the chemical homogeneity of the platelet-shaped particles by recording infrared spectra at different positions.

The local IR-spectrum (black one) recorded in position 1, which corresponds to a thin zone, fits well with that of pure $\text{K}_2\text{S}_2\text{O}_8$ salt (Figure 3.27) since it displays two intense peak 1260 and 1056 cm^{-1} . This means that these regions are mainly made of potassium persulfate. Differently the local IR spectrum (red one) recorded in position

2 (Figure 3.28), which belongs to a thicker zone, displays a more complex structure. Indeed the two bands characteristic of $K_2S_2O_8$ are still present, but additional absorption peaks and shoulder, which are the signature of PEDOT polymers already described and in agreement with literature [26], appear at 1236, 1209, 1168 and 1054 cm^{-1} .

When we carefully observe by AFM, with a good spatial resolution, another area (Figure 3.29), it is possible to detect the presence of closely packed globular nanostructures (few hundred nm to one μm in diameter) which seem to be adsorbed at the surface of the plates. This AFM observation agrees well with the morphology of PEDOT polymers previously synthesized by radiolysis [27] even if the particle size appears larger here. We deduce that these more or less spherical nanoparticles are made up of radiosynthesized PEDOT polymers. Each globular structure should correspond to the self-assembly of independent amorphous PEDOT polymer chains which interact all together by Hydrogen-bonds ([28]).

Even if we did not remove $K_2S_2O_8$ from the irradiated sample in order to obtain PEDOT polymers, we were able to discriminate PEDOT polymers and $K_2S_2O_8$ inorganic salt and to probe the local chemical composition of PEDOT nanostructures thanks to the use of high resolution AFM microscopy, coupled with infrared nanospectroscopy.

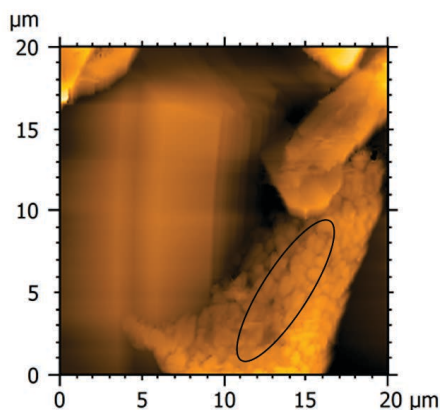


Figure 3.29: AFM-IR characterization of PEDOT polymers synthesized by electron beam irradiation (84 kGy) of the powder obtained by the irradiation of an aqueous solution containing 5 mM in EDOT, 20 mM in persulfate, 5 M in *tert*-butanol.

In order to highlight the role of persulfate in the final morphology of the observed nanoparticles, ethanolic solution of pure $K_2S_2O_8$ was also imaged. The AFM observation (Figure 3.30), after deposition and drying procedure in air, shows the presence of platet-shaped particles in the absence of any adsorbed globular structures (Figure 3.30).

mosphere at 0 °C, an aqueous solution containing 5 mM in EDOT, 20 mM in $\text{K}_2\text{S}_2\text{O}_8$ and 0.5 M in *tert*-butanol at a dose of 168 kGy (4000 pulses, 42 Gy/pulse). This irradiation dose is theoretically high enough to transform all $\text{S}_2\text{O}_8^{2-}$ anions into sulfate radicals. As a consequence, no more $\text{K}_2\text{S}_2\text{O}_8$ particles should remain present in the sample after irradiation. The lyophilized powder obtained after electron beam irradiation at 168 kGy was observed by SEM microscopy (Figure 3.31b). Contrarily to what we had foreseen, some platelet-shaped particles were still observable. But clearly, they were smaller and less numerous than those we got at 84 kGy. Due to the lower effective remaining concentration in potassium persulfate, we predominantly observed rod-shaped particles which had never been detected at lower doses. As it can be seen in Figure 3.31, the relatively low amount of $\text{K}_2\text{S}_2\text{O}_8$ in the sample enables the better observation of PEDOT polymers (some of them are surrounded in the figure for clarity). These polymers appear as aggregated globular structures, not free once again, but in the vicinity of $\text{K}_2\text{S}_2\text{O}_8$ nanorods or plates. Evidently, since the irradiation at 84 kGy was enough to ensure the quantitative polymerization of EDOT, no effect of the dose was expected, at 168 kGy, on the number and the size of PEDOT polymers.

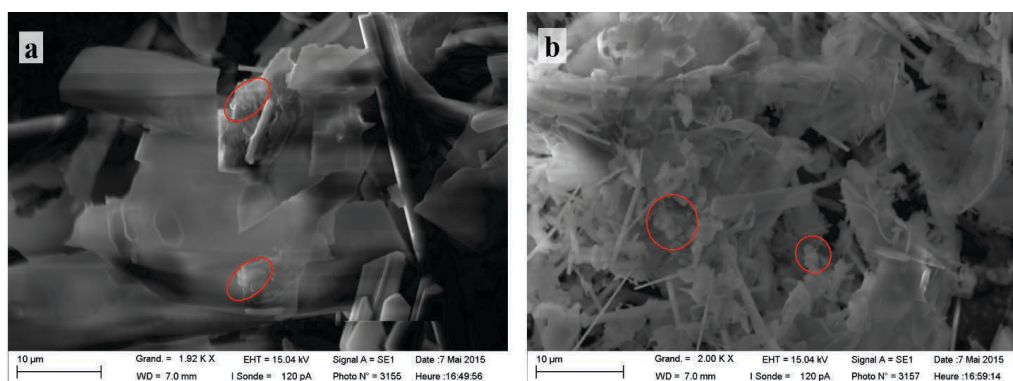


Figure 3.31: SEM images of PEDOT polymers synthesized by electron beam irradiation in the presence of $\text{K}_2\text{S}_2\text{O}_8$ at (a) 84 kGy and (b) 168 kGy

3.4 Conclusion

In this chapter we introduced the study of the growth mechanism of PEDOT by three different oxidizing radicals, such as carbonate, azide and sulfate radicals.

In the case of radicals, such as the azide or the carbonate radicals, the study showed that these radicals are not able to induce EDOT monomers oxidation and then PEDOT polymerization. Indeed at low concentrations, carbonate reacts too slowly with

so they do not more contribute in the time evolution of absorption at 305 nm. Thanks to COPASI simulation it was possible to describe the first steps of Pyrrole oxidation. However, the step following the addition still need to be investigated. Two possible reactions have been proposed here and could be involved: the protonation (R8) or the dimerization (R9). Due to the estimate concentration of H_3O^+ and the species A, these two reaction proceed according to a second order kinetics.

4.4 Theoretical study

In the kinetic study of experimental data, two spectra were isolated. At nanosecond time scale, the spectrum characterized by an intense peak at 305 nm and a weak large band at 400 nm (Figure 4.4) which could be Py^\cdot , $\text{Py}^{\cdot+}$ or, according to Lilie [2], $(\text{PyOH})^\cdot$, resulting from the reaction between hydroxyl radical and Pyrrole monomers. On microsecond time scale, the spectrum of the species A composed by two weak peaks at 270 and 350 nm was not identified (Figure 4.9). Does it correspond to a single species (AH^+ or B) or to a combination of the two species (AH^+ and B)? With the aim to determine the nature A and that of the species absorbing at the microsecond time scale we proceeded to DFT/ TD-DFT calculations to simulate the absorption spectra of all possible species. The structures, formula and current names of the species investigated are reported in Table 4.3.

Py			Py^\cdot			$\text{Py}^{\cdot+}$		
$(\text{PyOH})^\cdot$			$\text{PyHOH}^{+\cdot}$			PyO^\cdot		
$\text{BPy}_{\alpha-\alpha}$			BPyOH			$\text{BPyHOH}^{2+\cdot}$		

Table 4.3: Names, formula and chemical structures of all Pyrrole species studied by simulation.

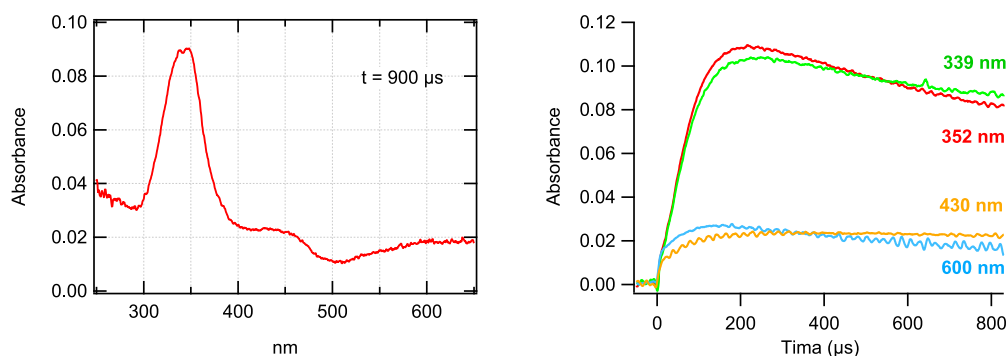


Figure 4.25: Absorption spectra of a N_2O -saturated aqueous solution containing 20 mM in Py at $\text{pH} = 2.8$ recorded at 1 ms after the pulse (on the left). Time evolution of absorbance at 339, 352, 450 and 630 nm over 50 μs (Dose = 43 Gy/pulse; Optical path = 1 cm).

Contrarily to the other experiments, in this case, the absorption spectrum recorded after the experiment shows some of the bands visible in the spectrum recorded at 900 μs . The Figure 4.26 shows the spectrum of solution recorded after the pulse radiolysis experiment. What is amazing is the increase of the absorption and the broadband at 850 nm not visible at 900 μs . This means that the solution continues to react after the pulse irradiation to induce a probable chain length increase. Indeed, after the irradiation, the solution color changes from transparent into black.

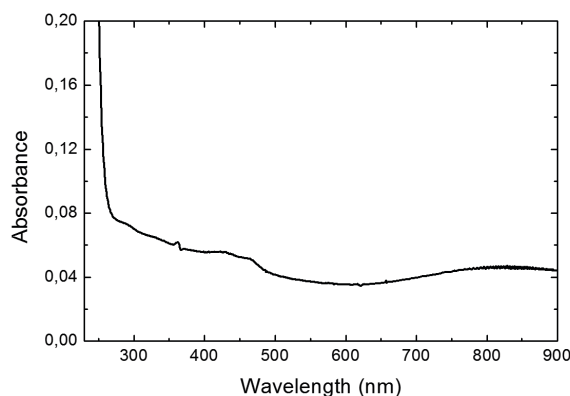


Figure 4.26: Static absorption spectrum of a solution containing 20 mM in Py at $\text{pH} = 2.8$ after the pulse radiolysis experiment (Optical path = 0.2 cm).

This spectrum is in agreement with that found in literature [16], showing an

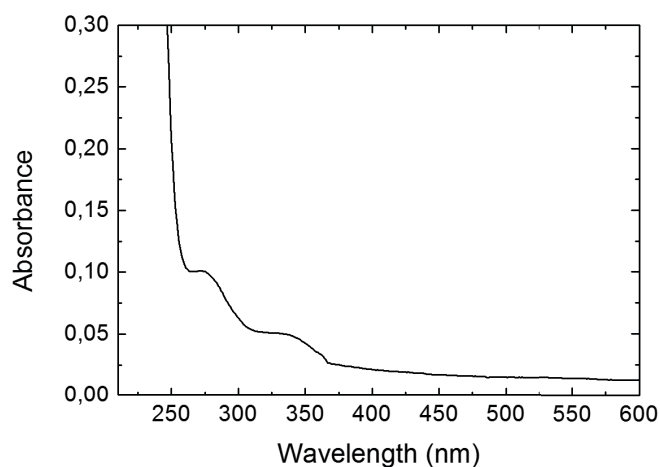


Figure 4.32: Static UV-Vis absorption spectrum of a solution containing 20 mM in Py at pH =13.5 after irradiation (Dose = 40 Gy/pulse; Optical path = 0.2 cm).

Indeed, before irradiation the solution contains 20 mM in Pyrrole. At the end of the experiment, the Py concentration is not significantly affected. Finally the absorption from 350 to 600 nm can be associated to the oligomers probably produced at longer time.

Kinetic simulation in alkaline solution

The aim of the simulation was to definitely identify the mechanism involved in the first steps of Pyrrole oxidation in alkaline solution. Indeed, the data analysis of experiments did not allow to prove completely the action of oxide radical on Pyrrole monomers on nanoscale time range. And it was not possible to determine the species involved in the reaction following the oxidation of Pyrrole.

As previously, the simulation includes all water radiolysis reactions (R1-R6), detailed in Table 4.4.

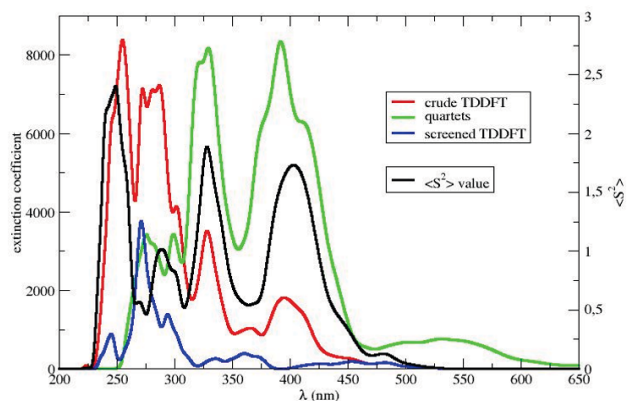


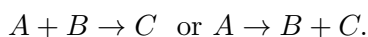
Figure A.3: Absorption spectra of EDOT^{•+} radical cation: TDDFT results for $|M_S| = 0,5$ ("crude" spectrum) and 1,5 ("quartet" spectrum), and screened TDDFT spectrum with the value 0,82 of the screening parameter. The "spectrum" of the $\langle S^2 \rangle$ mean value for the crude TDDFT spectrum is also shown

On this figure we join the "spectrum" of the $\langle S^2 \rangle$ values, namely the equivalent of the absorption spectrum, with the oscillator strength replaced by the $\langle S^2 \rangle$ value. This $\langle S^2 \rangle$ spectrum was normalized, so as to give the value 0,75 to the low energy band (2228 nm, see Table A.1). It can be seen that:

- the band at 400 nm in the crude spectrum can be attributed to quartet states, as shown by the large value of $\langle S^2 \rangle$ in this zone (1,72) and by a band in the quartet spectrum. As a consequence this band is completely dropped by the spin screening.
- the same holds for the band at 330 nm, also displaying a large value of $\langle S^2 \rangle$ (1,88) and clearly present in the quartet spectrum.

In Figure A.3 we displayed the spectrum of EDOT^{•+} cation radical obtained with the value 0,82 which ensures the best comparison with the experimental spectrum.

Thermochemistry In a previous work, our group had shown that PCM (Polarized Continuum) methods, like SMD, can be very unreliable and hazardous when used for chemical reactions of the type [5]



This is due to the poor treatment of the translation rotation entropy, which is

Titre : Etude du mécanisme de croissance de polymères conducteurs par radiolyse

Mots clés : radiolyse impulsienne, polymères conducteurs, spectroscopie

Les polymères conducteurs (PC) sont des matériaux organiques semi-conducteurs très utilisés dans diverses applications technologiques. Les différentes méthodologies de synthèse des PC ont toujours pour finalité la fabrication de nouvelles structures polymères stables dans différents environnements, et dont les propriétés optiques et conductrices seraient ajustables.

Parmi tous les polymères conducteurs, le poly(3, 4-éthylènedioxythiophène) (PEDOT) et le polypyrrole (PPy) sont déjà utilisés dans plusieurs applications pour leurs propriétés chimiques et physiques. Les PC, comme le PEDOT et le PPy, sont habituellement synthétisés par voie chimique ou électrochimique, la polymérisation étant systématiquement initiée par une étape d'oxydation des monomères. La radiolyse de l'eau représente une méthode simple et efficace qui permet la polymérisation à température et pression ambiantes, sans aucun dopant externe, mais qui à notre connaissance n'avait jamais été utilisée seule pour la synthèse de PC.

Au sein de notre laboratoire, une méthodologie alternative basée sur l'interaction rayonnement-matière a récemment été utilisée avec succès

pour la synthèse de PC nanostructurés en solution aqueuse. Le présent travail est plus spécifiquement consacré à la synthèse de PEDOT et PPy en solution aqueuse et à l'étude de leur mécanisme de croissance par radiolyse pulsée. Grâce à l'accélérateur d'électrons ELYSE, l'utilisation de la radiolyse pulsée couplée à la spectroscopie d'absorption résolue dans le temps a permis d'étudier la cinétique des réactions à l'échelle de la nanoseconde et de la milliseconde. Les spectres d'absorption des espèces transitoires impliquées dans le mécanisme réactionnel ont été identifiés grâce à des calculs de chimie quantique. Tout d'abord, la réaction du radical hydroxyle avec les monomères EDOT et Py a été étudiée, ainsi que la polymérisation induite par le rayonnement. Ensuite, l'étude a été transposée à d'autres radicaux oxydants tels que $\text{CO}_3^{\cdot-}$, N_3^{\cdot} et $\text{SO}_4^{\cdot-}$ à différents pH. Enfin, le faisceau d'électrons a été utilisé comme source de rayonnement ionisant (accumulation de pulses) afin de synthétiser in situ les polymères conducteurs PEDOT et PPy. Ces résultats démontrent que le mécanisme de croissance des PC n'est pas un mécanisme en chaîne, mais un mécanisme par stades.

Title : Study of growth mechanism of conducting polymers by pulse radiolysis

Keywords : Pulse Radiolysis, Conducting Polymers, Spectroscopy

Today conductive polymers have many applications in several devices. For these reasons they have received much attention in recent years. The methods of polymerization are limited to two principal ways: chemical and electrochemical synthesis. On the other hand, the complex properties of polymers can be controlled only if a good knowledge of polymerization process is acquired. Water radiolysis represents an easy and efficient method of synthesis comparing to chemical and electrochemical polymerization routes. It enables the polymerization under soft conditions: ambient temperature and pressure, without any external dopant.

Among all conductive polymers, poly(3,4-ethylenedioxythiophene) (PEDOT, a derivate of polythiophene) and polyPyrrole (PPy) have gained some large scale applications for their

chemical and physical properties. The aim of the present work was the synthesis of PEDOT and PPy in aqueous solution and the study of their growth mechanism by pulsed radiolysis. Thanks to the electron accelerator ELYSE, the use of pulsed radiolysis coupled with time-resolved absorption spectroscopy allowed to study the kinetics of polymerization. The first transient species involved in the mechanism were identified by time resolved spectroscopy and the rate constants were determined. First, the reaction of hydroxyl radicals onto EDOT and Py monomers was studied, as well as the corresponding radiation induced polymerization. Then, the study was transposed to others oxidizing radicals such as $\text{CO}_3^{\cdot-}$, N_3^{\cdot} and $\text{SO}_4^{\cdot-}$ at different pHs. Finally, the electron beam was originally used as a simple electron irradiator in order to in situ synthesise PEDOT and PPy.

